

DETECTION OF GAS IN SANDSTONE RESERVOIR USING AVO ANALYSIS IN
PRINOS BASIN

By

CHOUSTOULAKIS E. EMMANOUIL

SCIENTIFIC ADVISOR: PROF. VAFIDIS ANTONIOS

A THESIS

Submitted in partial fulfillment of the requirements

for the degree of

MASTER OF SCIENCE IN PETROLEUM ENGINEERING

TECHNICAL UNIVERSITY OF CRETE

November, 2015

This thesis, "DETECTION OF GAS IN SANDSTONE RESERVOIR USING AVO ANALYSIS IN PRINOS BASIN", is hereby approved in partial fulfillment of the requirements for the Degree of MASTER OF SCIENCE IN PETROLEUM ENGINEERING.

DEPARTMENT: School of Mineral Resources Engineering

Signatures:

Prof. Antonios Vafidis
(Scientific Advisor-Applied Geophysics Laboratory)

Prof. Dionissios T. Hristopulos
(Member Committee- Geostatistics Laboratory)

Prof. Nikolaos Varotsis
(Member Committee-PVT and Core Analysis Laboratory)

Date _____

Abstract

This thesis was focused on an integrated approach of gas detection in the sandstone reservoir of Prinos oil field, located in the northern Aegean Sea between the island of Thasos and city of Kavala on the mainland. The rock properties variation with depth in the study area, were inferred from suite of quality controlled well seismic logs, while the geological structure of the model was based on an East-West 2D geological plan of Prinos basin. Furthermore, the top layer of the reservoir was considered to be 50% saturated with gas, so, its elastic parameters were accordingly adjusted. The above information were given as input to a synthetic data simulator (Applied Geophysics Laboratory of the Technical University of Crete) in order to build low frequency synthetic seismograms. Additionally, a signal processing graphical interface was build, in order to properly process the synthetic data before the application of the AVO analysis. The GUI can support the whole preprocessing scheme prior to the AVO analysis, from the commissioning of the SGY data, until the generation of the stacked and migrated sections, while the results can be represented graphically at any point. Finally, an analytical AVO analysis flow was adapted for the processed seismic data which successfully detected the presence of gas in the shallow gas saturated layer. The AVO analysis flow included rock physics analysis, intercept-gradient crossplots, far versus near stack attributes, detailed investigation of distance to amplitude analysis and AVO inversion for the elastic parameters of the model.

Acknowledgements

First and foremost, I would like to thank my supervisor, Dr. Antonis Vafidis, Professor in Applied Geophysics Lab in Department of Mineral Resources Engineering of Technical University of Crete whose help, guidance and supervision from preliminary to concluding levels, enabled me to fulfill this thesis.

I also thank Dr. George Kritikakis, Lab and Teaching Staff of Applied Geophysics Laboratory for his significant contribution and help.

I am also grateful to all my lecturers in the master of Petroleum engineering, most especially, Prof. Nikos Pasadakis without whom this master course would have never been viable and Dr. Vasilios Gaganis for his support, constructive feedback and communicability of knowledge. I would always be indebted to you all.

Many thanks goes to my course mates in the Petroleum Engineering course and especially to my study group mates, Katerina Stathopoulou and Aggeliki Vlassopoulou for their collaboration and support through this work.

I thank my examination committee: Professors Dionissios Christopoulos and Nikolaos Varotsis for their time and input.

The last but the most important, I want to express my heartfelt appreciation to my parents, Emmanouil Choustoulakis and Argiro Kalisperaki, my brothers Nikos Choustoulakis, Kyriakos Choustoulakis, Aris Choustoulakis and my girlfriend, Marilena Anastasaki. Without your love, support and understanding, I couldn't be able to get my work done.

Table of Contents:

1.	<i>Introduction.....</i>	1
2.	<i>Prinos Basin</i>	2
	2.1 Geological Setting.....	3
	2.2 Stratigraphy.....	4
	2.3 Traps and Reservoir	6
	2.4 Oil generation and migration	7
3.	<i>Synthetic data simulator</i>	8
	3.1 Heterogeneous Approach.....	9
	3.2 Elastic wave propagation	11
	3.3 Accuracy, convergence and stability.....	12
4.	<i>AVO Analysis Theory</i>	16
	4.1 AVO analysis principles	16
	4.2 Transforming From the Offset to the Angle Domain.....	20
	4.3 Ray Tracing.....	22
	4.4 Seismic Data Pre-Processing for AVO Analysis	24
	4.5 Far versus near-stack attributes	27
	4.6 AVO attributes combining intercept and gradient	28
	4.7 AVO Analysis Application on Gas Detection.....	30
	4.8 AVO Response Classification.....	35
5.	<i>Seismic Data Processing Analysis</i>	38
	5.1 Prinos Basin Geological Model Representation.....	41
	5.2 Velocity and Bulk Density Estimation.....	47
	5.3 Synthetic Seismic Data Acquisition	54
	5.4 Seismic Data Processing	62
	5.4.1 Preprocessing.....	66
	5.4.2 Spherical divergence correction.....	70
	5.4.3 Spiking and Predictive deconvolution	71
	5.4.4 FX deconvolution	74
	5.4.5 F-K Filtering.....	76
	5.4.6 CMP sorting	78
	5.4.7 Velocity Analysis	79
	5.4.8 NMO correction	82
	5.4.9 Radon Transform.....	83
	5.4.10 Stacking.....	85
	5.4.11 Post-stack Processing	87
	5.4.12 Migration.....	88
6	<i>Seismic Processing Graphical Interface</i>	93
	6.1 Plotting Different Gather Types.....	95
	6.2 Signal Processing Analysis	100
	6.3 Stack section	106
	6.4 Migration.....	108
	6.5 Plotting tools	111
7	<i>AVO Analysis Application</i>	114
	7.1 Ray tracing	114
	7.2 Rock Physics of AVO.....	118
	7.3 AVO crossplot analysis.....	120
	7.4 Near Far Stack.....	123
	7.5 PG crossplot	127
	7.6 Detailed investigation of distance to amplitude analysis.	131
	7.7 AVO inversion of elastic parameters	133
8	<i>Summary and Conclusion</i>	135

9	References	136
	Appendix A	140
	Matlab Codes:	140
	AVA inversion.....	140
	AVO classification.....	141
	Common Offset gather creation.....	144
	Digitize function	144
	Excel creation	151
	Geometrical Spreading	153
	PG Crossplots of Synthetic Data	153
	Raytracing Algorithm	157
	Record's Length Calculation	159
	Rock Physics.....	162
	Spline Layers	169
	Appendix B	173
	List of Figures	173
	Chapter 2.....	173
	Chapter 3.....	173
	Chapter 4.....	173
	Chapter 5.....	174
	Chapter 6.....	176
	Chapter 7.....	177
	Appendix C	179
	List of Tables	179

1. Introduction

In recent years, as the easy to find conventional hydrocarbon reserves in the earth's crust are being exploited, the oil industries tend to search in more difficult terrains and much deeper waters to match the growing demand for fossil fuels. As such, exploration for oil and gas over time has advanced from being qualitative to quantitative. Quantitative studies of the subsurface in general and hydrocarbon fields in particular, require a lot of integrated data and analysis from geologists, geophysicists, petrophysicists, and reservoir engineers.

Fueled by progressive technological advances and breakthroughs in the oil and gas industry, the possible computing power has also followed suite, such, that reservoir characterization has extended from deterministic to probabilistic. Accurate characterization requires a combination of 3D and 4D seismic volume interpretations, seismic inversion and amplitude analyses, rock physics and AVO (amplitude versus offset) analysis. Earlier, geophysical data were mainly used in exploration, and to a smaller extent in the development of discoveries. In more recent times geophysical and petrophysical data is integrated in reservoir characterization schemes, and serves as a link between geologic reservoir properties (such as porosity, sorting, clay content, lithology and saturation) and seismic properties (like P-wave and S-wave velocities V_p/V_s ratio, acoustic impedance, elastic moduli, bulk density) (Avseth *et al.*, 2010). Reservoir characterization therefore simply refers to quantitatively assigning reservoir properties which usually show a non-uniform and non-linear spatial distribution.

This study will focus on an integrated approach to reservoir characterization of the Prinos oil field, located in the northern Aegean Sea, between the island of Thasos and city of Kavala on the mainland. A suite of quality controlled well seismic logs, along with a 2D geological model will be used to infer the rock property variations with depth in the study area. The rock properties will then be used to build low frequency synthetic seismograms, using a synthetic data simulator, (*Applied Geophysics Laboratory of the Technical University of Crete*) and later perform AVO modeling. However, the synthetic data needs special pre-treatment prior to the application of the AVO analysis. In order to cope with such a demanding and complex procedure, a graphical interface is built which can undertake the whole preprocessing scheme prior to the AVO analysis. The study begins with the geological and stratigraphical setting of Prinos basin.

2. *Prinos Basin*

The Prinos basin is the only geological area in Greece, where oil and gas are being produced for more than thirty years. Exploration for hydrocarbons in this particular offshore area has started in the beginning of the seventies. The first seismic campaign took place in the sea of Thrace in 1970 and the first oil discovery in Prinos basin occurred in 1973. The search for oil in this basin is still under continuation. The taphrogenetic basin of Prinos has been widely studied, due to its hydrocarbon reservoirs. The combined geological information, derived from the analysis of lithological, stratigraphic and geochemical data of the basin, suggested a structural and depositional model, strongly related to the Miocene tectonics and sedimentation [Proedrou, P., and Papaconstantinou, C.M., 2004].

The largest part of the basin is located offshore between the island of Thassos and the opposite mainland to the west. Only the north-eastern portion of it lies onshore in the Delta Nestos plain (**Figure 2.1**). The total area covers 800km². The sea depth doesn't exceed fifty meters. In this chapter the general geologic and geotectonic characteristics of Prinos basin, in the wide geological area, are being presented.

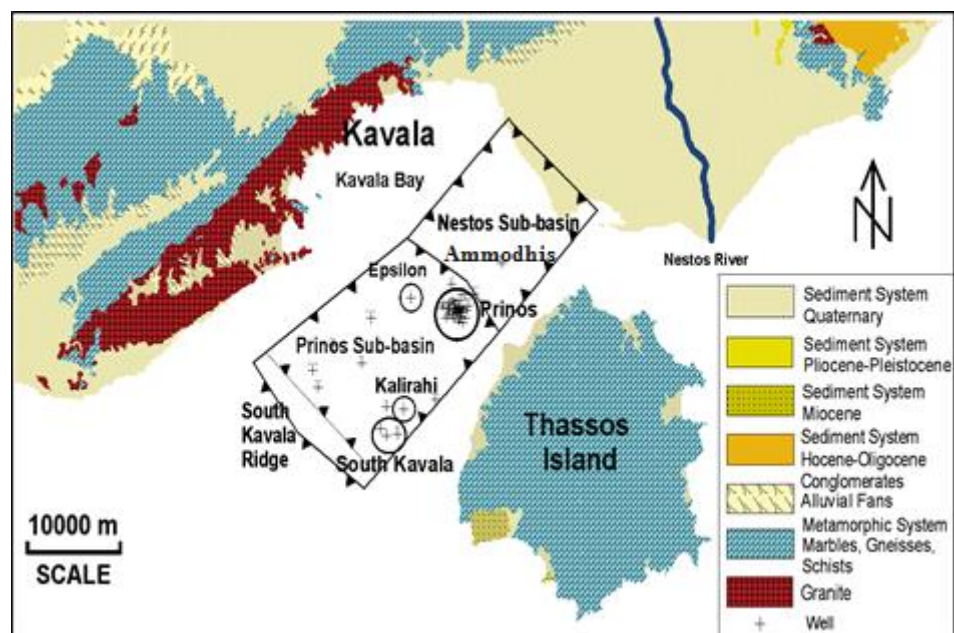


Figure 2.1 Prinos – Kavala Basin. Prinos field, Prinos North field, Epsilon field and South Kavala gas field are the only productive hydrocarbon fields in Greece. The oil generation and the migration paths are shown (improved version published after Kioumourtzi et al., 2007).

2.1 Geological Setting

Prinos - Kavala basin has been formed during Palaeogene period at the southern margin of the Rhodope Massif, controlled by NE-SW and NW-SE faults, at the area that nowadays is surrounded by Thassos Island and the mainland of NE Greece. It is a result of the post-alpine tectonism that started in early to middle Miocene and led to the breaking of the Aegean plate and to the subsidence of the pre-alpine Rhodope massive under the sea level. This gravity tectonics was responsible for the genesis of grabens and horsts in North Aegean. The NE part of Prinos basin was probable close by the first time of its formation, while the SW basement started to uplift by messinian period, forming the south Kavala ridge (**Figure 2.1**). The basin was gradually isolated from the open sea and changed into a lagoon. A number of gravity, often echelon, faults with NE-SW and NW-SE direction formed the taphrogenetic basin of Prinos. Its length is approximately 38 km, from Nestos river delta in NE, to offshore south Kavala ridge in SW. Its width is approximately 20 km, from Thassos Island in SE, to the opposite mainland in NW. It is subdivided into two sub-basins, separated by a topographic basement high, in Ammodhis area (**Figure 2.1**).

The Nestos sub-basin is located at the north part and the Prinos sub-basin, deeper than the previous, at the south part. The taphrogenetic basin is structured by roll-over anticlines, formed by NW-striking and SW-dipping faults which are related to the trapping mechanism (**Figure 2.2**). These faults, still active today, activated during sedimentation (syngenetic faults) and resulted in the dome-like anticlines of Prinos, North Prinos, Epsilon, Ammodhis and South Kavala.

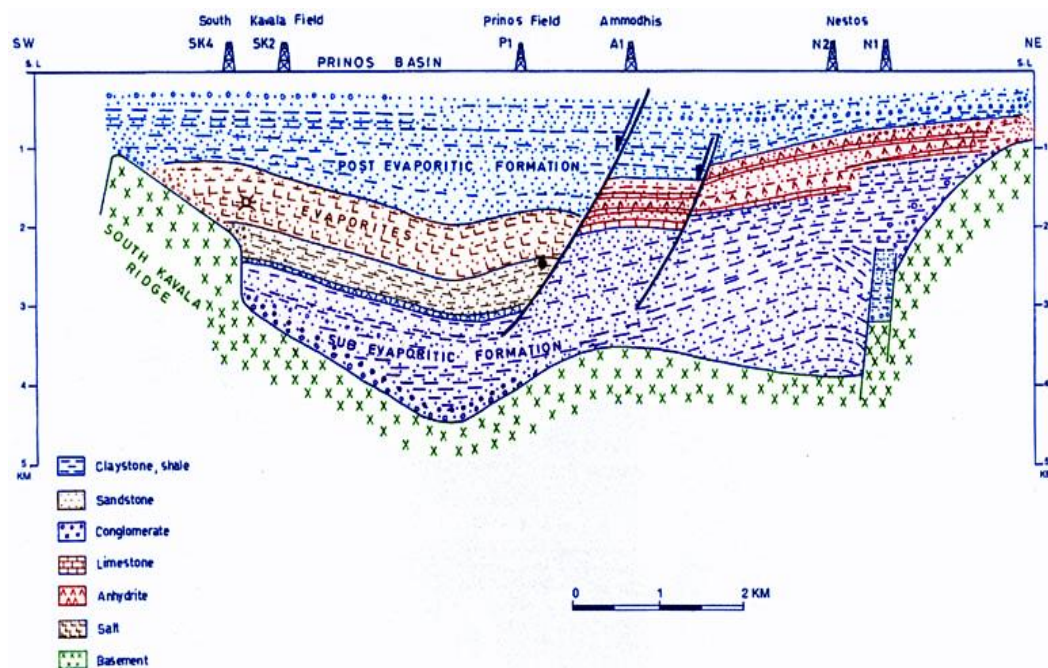


Figure 2.2 Simplified cross section of the Prinos basin parallel to the long axis. The roll-over syngenetic faulting formed the dome-like anticlines. Depths in kilometres below mean sea level. Figure from Proedrou and Sidiropoulos (1992).

2.2 Stratigraphy

The stratigraphy model of the taphrogenetic basin has been presented by Pollak and Proedrou (1979) (**Figure 2.3**). According to this, the generalized stratigraphic column is divided into three series:

- The Pre-Evaporitic Series.
- The Evaporitic Series.
- The Post-Evaporitic Series.

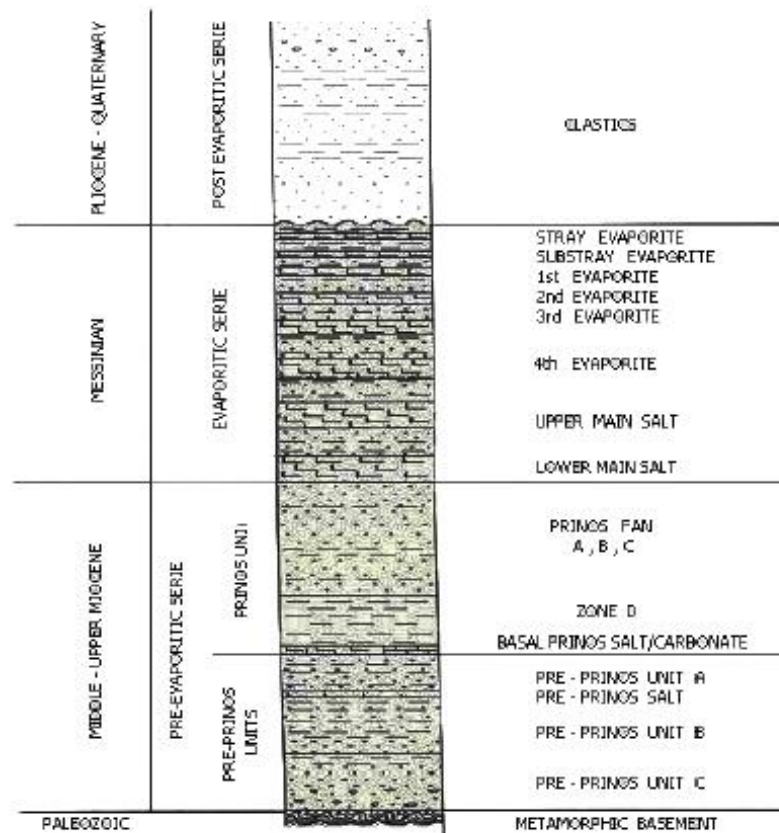


Figure 2.3. Generalized chronostratigraphic column of Prinos basin. Figure from Proedrou and Sidiropoulos (2004).

The Palaeozoic basement is composed of metamorphic rocks: gneiss, quartzite and dolomitic marble. The Pre-Evaporitic Series, closely related to Miocene tectonics, begins with continental deposits: conglomerates with large basement components, sandstones, feldspatic, mainly immature, claystones and thick coal seams. These continental deposits originated from the NE and SW parts of the basin, decrease in thickness towards the centre of the sub-basins. They are followed by marine deposits of shales with interbedded sandstones, coarser at the periphery of the basin, which overlay the older ones with an unconformity. Above these units, a zone of limestone, dolomite and anhydrite layers alternated with clastics follows. Towards the centre of the basin, to the deeper parts, the anhydrite is replaced by a few metres thick layers of salt. At the top of the Pre-Evaporitic Series, at Prinos sub-basin, there is an extended deposition of dark gray claystone, the zone D. It is petro-liferous and strong carbonaceous, with sandstone intercalations. The following Prinos sub-marine fan, consists entirely of turbiditic fan deposits, which were deposited along the downthrown side of a fault escarpment. The present facies, are representative of the turbidite facies classification of Walker and Mutti (1973). At Nestos sub-basin, the equivalent zone is the pro-deltaic varves (*Proedrou and Papaconstantinou, 2004*).

The Evaporitic Series, closely related to Messinian “Salinity Crisis” of the Mediterranean Sea (*Hsu, 1972*), consists of two facies, in each of the two sub-basins. In the northern one, anhydrite and limestone layers 3-5 m thick, alternate each other and with sandstone, claystones and marls, too. The series in the southern part, consists of 7-8 salt layers with increasing thickness towards the base of the section, which alternate with clastics and has a total thickness up to 800 m. The salt is white, gray, crystalline, often intercalated by anhydrite and dolomite layers (*Proedrou and Papaconstantinou, 2004*). The Post-Evaporitic Series is pure clastic and marine origin, as indicated by the presence of a great number of Pliocene foraminifera and algae. Towards the top, coarse clastic sediments with abundant rests of molluscs point out to a deltaic, according the seismic, prograding sequence. A transgression followed with deposition of marine clastic sediments (*Proedrou and Papaconstantinou, 2004*). These three series reflect the different sedimentological conditions of each period and generally, increase in thickness towards the centre of the sub-basins.

2.3 Traps and Reservoir

The most typical anticlines for the broad basin are the Prinos and Prinos North oil fields as rollover anticlines in front of syngenetic northwest-southeast striking downthrown faults. To the same case belongs the south Kavala gas field being formed as a combination of a rollover anticline and a stratigraphic pinch-out of the south western flank against the basement (*P. Proedrou 2001*). In contrast, the Ammodhis structures, as well as the Epsilon structure are rollover anticlines surrounded by mainly down-thrown faults. Stratigraphic traps are traced along the basin margins and mainly along the western margin, where the basin flank is dipping gently. A peculiarity states the Kallirachi trap building up between two major down-thrown faults in conjunction. The first fault is marginal and syngenetic with the basin formation, while the second one as internal fault, is postdepositional. The stratigraphic horizons are dipping from the fault conjunction to the centre of the basin (**Figure 2.4**).

Reservoirs are mainly sandstones and secondly siltstones, that resulted of the uppermost Miocene depositions from deltaic, marine and turbiditic environments. The evaporites cover the whole basin, keeping hydrocarbons below them, except from an upward movement of hydrocarbons in South Kavala and Ammodhis fields, probable due to fault activation. Generally, porosity and permeability is decreasing with increasing depth, due to weight overlay, clay content and dolomitization (*Proedrou and Papaconstantinou, 2004*).

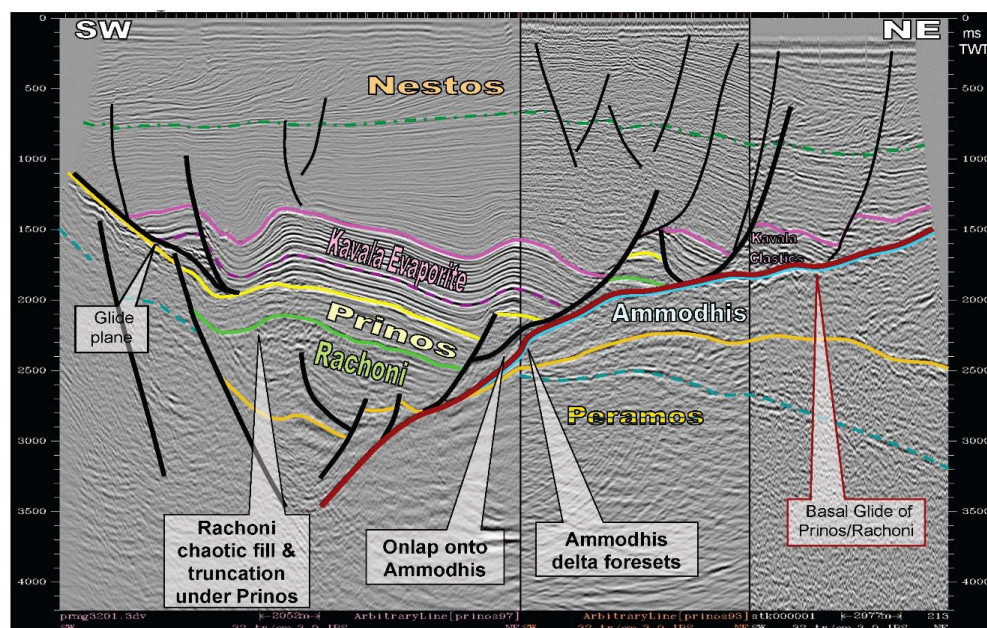


Figure 2.4 NW-SE seismic section across the Prinos basin. The anticlinal structure with the downthrown faults are well illustrated from the seismic reflectors [*Stuart Harker 2004-2008*].

2.4 Oil generation and migration

Marine claystones of Middle to Upper Miocene age and messinian claystones deposited under highly reducing conditions interrupted by hyperhaline episodes are considered to be the source of oil in the basin. Coal deposits may have a good potential for gas generation. The oil source - rock is characterized by a waxy sapropelic oil prone kerogen with terrestrially derived organic matter frequently dominant. Maturity measurements show vitrinite reflectance up to 1.10 for depths up to 3500 meters. The central part of the basin, with a depth of approximately 5500m was never reached by drilling. Generally there is a rapid increase of thermal maturity towards the basement throughout the basin suggesting that a heat source is originating from it (*Robertson Research INT. 1981*).

According to the oil maturation plots oil reached the threshold of maturity during latest Miocene in the deepest part of the basin. Generation continued throughout the Pliocene and recent. The present top of the maturation window starts at depths of 2500m. The equivalent top for gas window is at depth of 4000m (*Proedrou, Sidiropoulos 1992*). Only in Nestos area where the geothermal gradient is very high the zone of peak gas generation is reached at 3500m. The Prinos, North Prinos, Epsilon and Ammodhis oils are of the same quality. They belong to an aromatic - asphaltic type with a sulfur content. The gases are dissolved in the wet phase and consist from methane to pentane with H₂S and CO₂ in various percentages.

The sweet hydrocarbons more probably have been generated from the earlier deposited miocene claystones in an open marine phase. This early phase produced more mature hydrocarbons without any H₂S contribution. The coal has more probably also contributed to the gas generation. In contrast the Prinos, North Prinos, Epsilon and Ammodhis fields contain a more immature oil with high content in H₂S and CO₂ that mainly was originated from the under reducing conditions deposited claystones (*Rigakis et al 2001*).

Concerning the oil migration it breaks out from the deepest parts of the southern half of the basin and spreads out radial to the periphery and to the central basin Highs where the trapping mechanisms were present (**Figure 2.4**). The gas migration from the deepest part of the Nestos subbasin is very local and due to the absence of good quality and sufficient volume reservoirs has been dispersed.

3. Synthetic data simulator

A basic tool in exploration seismology is the synthetic seismogram which is generated by solving an elastic wave equation. The analytical solution is not always known. Therefore, various approximation methods have been suggested for the computation of synthetic seismograms.

- In a series method, the solution of the propagation problem is represented by an infinite series (Asymptotic Ray Theory). The coefficients of a finite number of terms (most often the leading term only) are then determined numerically to yield an approximation to the true solution. One of the disadvantages of ART is that a large number of rays is necessary to generate a synthetic seismogram.
- In transform methods, if the independent variables in the wave equation are separable by applying transforms partial differential equations can be reduced to ordinary differential equations which can be solved analytically or numerically. Having found the solution of the ordinary differential equations, the inverse transforms must be evaluated.
- In segmentation methods, the given interval is segmented into subintervals and the differential equation is approximated with reference to those segments. Depending on the size of the segments and the, approximation procedure for the solution, there are several methods. One subgroup consists of the finite difference and finite element methods waves.

In finite differences (FD), both the spatial and time variables are discretized by superimposing a rectangular grid on the model. Finite difference approximations to the differential equations that describe the wave propagation, give rise to difference equations. Numerical solutions are obtained from the difference equations solved on the discrete grid subject to some initial condition.

Kelly et al. (1976) pointed out that two formulations can be distinguished: The ***homogeneous*** approach solves the wave equation in each homogeneous layer separately. Boundary conditions must be explicitly imposed on the interfaces between different layers. The ***heterogeneous*** formulation directly solves the wave equation for the whole model. The wave equation in this case allows the physical properties to vary both laterally and vertically. In the ***heterogeneous*** approach, boundary conditions are satisfied implicitly and more complicated geometries can be accommodated with no extra effort.

3.1 Heterogeneous Approach

The heterogeneous approach has certain advantages over the homogeneous since it can be applied to any model geometry without requiring major changes in the program code. In approximating the second order wave equation, numerical differentiation of the elastic parameters is necessary. Here, the equivalent first order hyperbolic system will be examined

A first order system in two dimensions can be expressed as

$$\partial_t U(x, z, t) = A \partial_x U(x, z, t) + B \partial_z U(x, z, t) \quad (3.1)$$

Where U is a vector function of x , z and t . In problems of seismic wave propagation, U includes any relevant components of displacement (or their time derivatives) and stress, A , B are matrices, containing the properties of the medium as functions of x and z , with $0 < x < H_x$, $0 < z < H_z$. The symbol ∂ denotes partial derivative with respect to a spatial or temporal coordinate s . This system is solved numerically for $t > 0$, subject to initial conditions: $U(x, z, t = 0)$.

A system is called hyperbolic if, for all real α , β with $\alpha^2 + \beta^2 = 1$, there exists a nonsingular transformation matrix Q , such that

$$Q(\alpha A + \beta B)Q^{-1} = D \quad (3.2)$$

where D is a diagonal matrix with real elements. All of these conditions are satisfied if the matrices A and B , are real and symmetric.

To set up the finite-difference method, two integers are selected $J > 0$, $M > 0$ and the time step $K > 0$. If H_x and H_z are the endpoints of the grid and $h = H_x/J = H_z/M$, the mesh points (x_j, z_m, t_n) are defined by

$$\begin{aligned} x_j &= jh \quad \text{for each } j = 0, 1, \dots, J \\ z_m &= mh \quad \text{for each } m = 0, 1, \dots, M \\ t_n &= nk \quad \text{for each } n = 0, 1, \dots \end{aligned}$$

Various difference approximations for hyperbolic systems are well established and have been applied in different fields. The best known method for first-order hyperbolic systems is the Lax-Wendroff method (Lax and Wendroff, 1964, Mitchell, 1981) where a difference equation is determined so that it has accuracy of second order. A Lax-Wendroff scheme for a first order hyperbolic system in two space dimensions with the matrices of coefficients A and B varying both in space and time given by Mitchell (1981) has been modified so that it maintains second order accuracy where the matrices A and B depend on the space variables. The modified Lax-Wendroff scheme is based on the Taylor expansion of U at time $t+k$ for $k > 0$ carried to second order.

$$U(x, z, t+k) = U(x, z, t) + k \frac{\partial U}{\partial t} + \frac{1}{2} k^2 \frac{\partial^2 U}{\partial t^2} + O(k^3) \quad (3.3)$$

which becomes, after replacing the time derivatives by space derivatives from equation (3.1) and keeping up to second order terms in k

$$U(x, z, t+k) = U(x, z, t) + k \left(A \frac{\partial U}{\partial x} + B \frac{\partial U}{\partial z} \right) + \frac{k^2}{2} \left[A \frac{\partial}{\partial x} \left(A \frac{\partial U}{\partial x} + B \frac{\partial U}{\partial z} \right) + A \frac{\partial}{\partial z} \left(A \frac{\partial U}{\partial x} + B \frac{\partial U}{\partial z} \right) \right] \quad (3.4)$$

A modified Lax-Wendroff scheme [Griffiths, Abramovici, 1987; Vafidis, 1988], when applied to equation 3.4, results in:

$$\begin{aligned} U_{j,m}^{n+1} = & \left\{ I - \frac{p^2}{4} \left[\tilde{A}_{j,m} (\tilde{A}_{j+1,m} + 2\tilde{A}_{j,m} + \tilde{A}_{j-1,m}) + \tilde{B}_{j,m} (\tilde{B}_{j,m+1} + 2\tilde{B}_{j,m} + \tilde{B}_{j,m-1}) \right] \right. \\ & + \frac{p^2}{4} \left[\tilde{A}_{j,m} (\tilde{B}_{j+1,m} - 2\tilde{B}_{j,m} + \tilde{B}_{j-1,m}) + \tilde{B}_{j,m} (\tilde{A}_{j,m+1} - 2\tilde{A}_{j,m} + \tilde{A}_{j,m-1}) \right] \Big\} U_{j,m}^n \\ & + \frac{p}{2} \left\{ \tilde{A}_{j,m} \left[I + \frac{p}{2} (\tilde{A}_{j+1,m} + 2\tilde{A}_{j,m}) \right] + \frac{p}{2} \tilde{B}_{j,m} (\tilde{A}_{j,m} - \tilde{A}_{j,m-1}) \right\} U_{j+1,m}^n \\ & + \frac{p}{2} \left\{ \tilde{B}_{j,m} \left[I + \frac{p}{2} (\tilde{B}_{j,m+1} + \tilde{B}_{j,m}) \right] + \frac{p}{2} \tilde{A}_{j,m} (\tilde{B}_{j,m} - \tilde{B}_{j-1,m}) \right\} U_{j,m+1}^n \\ & - \frac{p}{2} \left\{ \tilde{A}_{j,m} \left[I - \frac{p}{2} (\tilde{A}_{j,m} + \tilde{A}_{j-1,m}) \right] + \frac{p}{2} \tilde{B}_{j,m} (\tilde{A}_{j,m+1} - \tilde{A}_{j,m}) \right\} U_{j-1,m}^n \\ & - \frac{p}{2} \left\{ \tilde{B}_{j,m} \left[I - \frac{p}{2} (\tilde{B}_{j,m} + \tilde{B}_{j,m-1}) \right] + \frac{p}{2} \tilde{A}_{j,m} (\tilde{B}_{j+1,m} - \tilde{B}_{j,m}) \right\} U_{j,m-1}^n \\ & + \frac{p^2}{8} (\tilde{A}_{j,m} \tilde{B}_{j,m} + \tilde{B}_{j,m} \tilde{A}_{j,m}) \{ U_{j+1,m+1}^n - U_{j-1,m+1}^n - U_{j+1,m-1}^n + U_{j-1,m-1}^n \} \end{aligned} \quad (3.5)$$

where $p=k/h$. The differencing star of this scheme is shown in **Figure 3.1**. It is a nine-point numerical scheme explicit in the vector U . Given the vector U at a given time, it is a simple matter to compute U at any other time by the above forward time marching process.

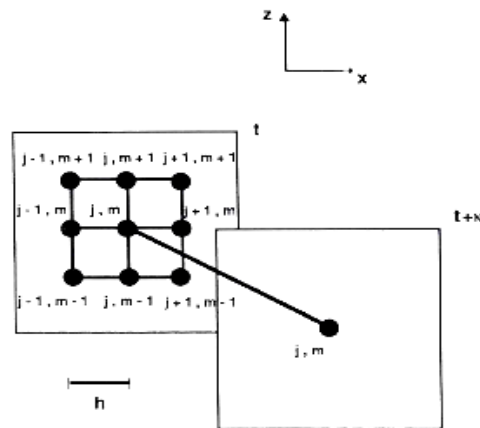


Figure 3.1 The differencing star for the modified Lax-Wendroff scheme.

3.2 Elastic wave propagation

The basic equation for two-dimensional SH-wave propagation in a heterogeneous isotropic medium, in absence of body forces, is:

$$\rho(x, z) \partial_t u(x, z, t) = \partial_x (\mu(x, z) \partial_x u(x, z, t)) + \partial_z (\mu(x, z) \partial_z u(x, z, t)) \quad (3.6)$$

where $u(x, z, t)$ is the displacement, $\mu(x, z)$ the shear modulus, and $\rho(x, z)$ the density.

Instead of solving numerically the second-order hyperbolic wave equation one can use an equivalent first-order system. In matrix form the system is:

$$\partial_t \begin{bmatrix} \dot{u} \\ \sigma_{xy} \\ \sigma_{zy} \end{bmatrix} = \begin{bmatrix} 0 & p^{-1} & 0 \\ \mu & 0 & 0 \\ 0 & 0 & 0 \end{bmatrix} \partial_z \begin{bmatrix} \dot{u} \\ \sigma_{xy} \\ \sigma_{zy} \end{bmatrix} + \begin{bmatrix} 0 & 0 & p^{-1} \\ 0 & 0 & 0 \\ \mu & 0 & 0 \end{bmatrix} \partial_x \begin{bmatrix} \dot{u} \\ \sigma_{xy} \\ \sigma_{zy} \end{bmatrix}$$

$$\text{or} \quad \partial_t U = A \partial_x U + B \partial_z U \quad (3.7)$$

where the dot denotes time derivative and $\sigma_{xy}(x, z, t)$, $\sigma_{zy}(x, z, t)$ are the stress components.

The system in equation (3.7) can also be written in the form

$$\begin{bmatrix} \rho & 0 & 0 \\ 0 & \mu^{-1} & 0 \\ 0 & 0 & \mu^{-1} \end{bmatrix} \partial_t \begin{bmatrix} \dot{u} \\ \sigma_{xy} \\ \sigma_{zy} \end{bmatrix} = \begin{bmatrix} 0 & 1 & 0 \\ 1 & 0 & 0 \\ 0 & 0 & 0 \end{bmatrix} \partial_x \begin{bmatrix} \dot{u} \\ \sigma_{xy} \\ \sigma_{zy} \end{bmatrix} + \begin{bmatrix} 0 & 0 & 1 \\ 0 & 0 & 0 \\ 1 & 0 & 0 \end{bmatrix} \partial_z \begin{bmatrix} \dot{u} \\ \sigma_{xy} \\ \sigma_{zy} \end{bmatrix} \quad (3.8)$$

Now, the earth's response is resolved into components in the horizontal (x) and the vertical (z) directions only. To calculate the elastic response of a model in rectangular (x, z) coordinates, the corresponding first-order system was solved numerically. This system consists of the basic equations of motion in the x- and z-direction.

$$\begin{aligned} \rho(x, z) \partial_t \dot{u}(x, z, t) &= \partial_x \sigma_{xx}(x, z, t) + \partial_z \sigma_{xz}(x, z, t) \\ \rho(x, z) \partial_t \dot{w}(x, z, t) &= \partial_x \sigma_{xz}(x, z, t) + \partial_z \sigma_{zz}(x, z, t) \end{aligned} \quad (3.9)$$

and the stress-strain relations after taking the first time derivatives

$$\begin{aligned} \partial_t \sigma_{xx}(x, z, t) &= (\lambda(x, z) + 2\mu(x, z)) \partial_x \dot{u}(x, z, t) + \lambda(x, z) \partial_z \dot{w}(x, z, t) \\ \partial_t \sigma_{xz}(x, z, t) &= \mu(x, z) \partial_x \dot{w}(x, z, t) + \mu(x, z) \partial_z \dot{u}(x, z, t) \\ \partial_t \sigma_{zz}(x, z, t) &= \lambda(x, z) \partial_x \dot{u}(x, z, t) + (\lambda(x, z) + 2\mu(x, z)) \partial_z \dot{w}(x, z, t) \end{aligned} \quad (3.10)$$

where $u(x, z, t)$ and $w(x, z, t)$ are the displacements in the x - and z -directions, respectively, σ_{xx} , σ_{xz} , σ_{zz} , the stress components, $\mu(x, z)$ and $\lambda(x, z)$ the Lamé parameters, $p(x, z)$ the density and the dot denotes time derivative. In this formulation there are no space derivatives of the Lamé coefficients.

Equations (3.9) and (3.10) can be written in the following matrix form

$$\partial_t \begin{bmatrix} \dot{u} \\ \dot{w} \\ \sigma_{xx} \\ \sigma_{zz} \\ \sigma_{xz} \end{bmatrix} = \begin{bmatrix} 0 & 0 & p^{-1} & 0 & 0 \\ 0 & 0 & 0 & 0 & p^{-1} \\ \lambda + 2\mu & 0 & 0 & 0 & 0 \\ \lambda & 0 & 0 & 0 & 0 \\ 0 & \mu & 0 & 0 & 0 \end{bmatrix} \partial_x \begin{bmatrix} \dot{u} \\ \dot{w} \\ \sigma_{xx} \\ \sigma_{zz} \\ \sigma_{xz} \end{bmatrix} + \begin{bmatrix} 0 & 0 & 0 & 0 & p^{-1} \\ 0 & 0 & 0 & p^{-1} & 0 \\ 0 & \lambda & 0 & 0 & 0 \\ 0 & \lambda + 2\mu & 0 & 0 & 0 \\ \mu & 0 & 0 & 0 & 0 \end{bmatrix} \partial_z \begin{bmatrix} \dot{u} \\ \dot{w} \\ \sigma_{xx} \\ \sigma_{zz} \\ \sigma_{xz} \end{bmatrix} \quad (3.11)$$

One of the key factors in forward modelling is the implementation of the source. Since the treated problems are two-dimensional, line sources were considered. To avoid the large values of the response in the source region Alterman's and Karal's method (1968) was used. The solution to the two-dimensional elastic or acoustic system for a homogeneous, infinitely extended, medium with a line source, is well known. Convolution of the impulse response with the source excitation results in an integral that can be evaluated numerically. A Gaussian function whose frequency response is practically band limited defines the source excitation.

3.3 Accuracy, convergence and stability

To guarantee that solutions to the difference equations remain bounded as the computations proceed, and that as the grid spacing becomes smaller and smaller those solutions approach the solution of the differential equation the accuracy the convergence and stability must be checked.

Accuracy

A criterion for the local accuracy of a finite difference formula is defined by the difference, E , between the exact solutions of the differential, W , and the difference, U , equations at a grid point $(jh, mh, (n+1)k)$ as

$$E_{j,m}^n = W_{j,m}^n - U_{j,m}^n \quad (3.12)$$

The Taylor series of W^n is

$$W^{n+1} = W^n + kW_t^n + \frac{k^2}{2} W_{tt}^n + O[k^3] \quad (3.13)$$

Replacing the time derivatives from the differential system (3.1) we get

$$W^{n+1} = W^n + \kappa (AW_x + BW_z)^n + \frac{k^2}{2} \left[A(AW_x + BW_z)_x^n + B(AW_x + BW_z)_z^n \right] + O[\kappa^3] \quad (3.14)$$

The Lax-Wendroff scheme (3.5) after approximating the difference operators by keeping the leading terms only

$$\begin{aligned}
 (\Delta_x + \nabla_x)U^n &= 2hU_x^n, (\Delta_z + \nabla_z)U^n = 2hU_z^n, (\Delta_x A \nabla_x + \nabla_x A \Delta_x)U^n = 2h^2 (AU_x^n)_x \\
 (\Delta_z B \nabla_z + \nabla_z B \Delta_z)U^n &= 2h^2 (BU_z^n)_z, (\Delta_x + \nabla_x)(\Delta_z + \nabla_z)U^n = 4h^2 U_{xz}^n \\
 [(\Delta_z A) \nabla_x + (\nabla_z A) \Delta_x]U^n &= 2h^2 A_z U_x^n, [(\Delta_x B) \nabla_z + (\nabla_x B) \Delta_z]U^n = 2h^2 B_x U_z^n
 \end{aligned} \tag{3.15}$$

Gives

$$\begin{aligned}
 U^{n+1} &= U^n + ph(AU_x + BU_z)^n + \frac{p^2 h^2}{2} \left[A(AU_x)_x + A(BU_{xz} + B_x U_z)^n \right. \\
 &\quad \left. + B(AU_{xz} + A_z U_x)^n + B(BU_z)_z \right]
 \end{aligned} \tag{3.16}$$

Substituting the equations (3.13) and (3.16) in equation (3.12), the truncation error is of third order in time. Similarly, by expanding the Taylor series in the space domain, one can obtain accuracy of the order (h^2, k^2) or $(2, 2)$. The truncation error of MacCormack schemes has the form

$$E = k \left[\pm \frac{1}{6} A_o (A_x U_x)_x kh + O(h^4) + O(kh^2) + O(k^2) \right] \tag{3.17}$$

Convergence

The various difference schemes are only useful for solving PDE, if they are convergent and stable. Convergence exists if the theoretical solution to a difference equation approaches the solution of the corresponding differential equation as the mesh is refined. The Courant-Friedrichs-Lewy (1928) (CFL) condition must be satisfied for explicit difference replacements to the hyperbolic differential equations for the systems to be convergent. The CFL condition states that the domain of dependence of the difference equation must include the domain of dependence of the differential equation. If the CFL condition is not satisfied the solution of the difference equation is independent of the initial data of the problem which lies outside the domain of dependence of the difference equation but lies inside the domain of dependence of the differential equation. Alteration of this initial data modifies the solution of the differential equation but leaves the solution of the difference equation unaltered. The domain of dependence of a hyperbolic system can be found by the method of characteristics (Mitchell, 1981). The domain of dependence of an explicit difference system is confined by the grid points which influence the value of U at a certain point and depends on the mesh ratio p .

As an example the simple SH wave equation with $\mu(x,z)=p(x,z)=1$ will be considered. The domains of dependence of the system (3.7) and the explicit difference system (3.5) will be examined with respect to the Cauchy initial value problem where the initial conditions are

$$U(x, z, 0) = C(x, z) \quad -\infty < x, z < +\infty \tag{3.18}$$

The domain of dependence for the equivalent wave equation (3.6) with constant coefficients is calculated by using the method of characteristics. The domain of dependence in the (x, z) plane of the differential system for a point $P(X, Z, T)$ is the circle

$$(x-X)^2 + (z-Z)^2 \leq T^2 \quad (3.19)$$

which is cut from the (x, z) plane by the circular (characteristic) cone (Mitchell, 1981) with apex $\pi/4$, vertex at P and axis parallel to the t axis. The explicit difference formula (3.5) allows the value of the vector U at the grid point $P(X, Z, T)$ to be expressed uniquely in terms of the values of C at certain points of the initial plane $t=0$, $U_{j,m}^0 = C(jh, mh)$. The grid points which influence the value of U at P lie inside a pyramid which cuts out from the initial plane $t=0$ one square as the domain of dependence. The CFL condition for the difference scheme (3.5) to be convergent for all initial smooth data is that the square of dependence of this difference scheme must contain the circle of dependence of the corresponding differential equation in its interior. The domain of dependence will be given without loss of generality for a point lying on the t -axis. Then the domain of dependence for the differential equation is a circle of radius $T=nk$ and the square of dependence for the difference equation with sides $2nh$ (Figure 3.2) must satisfy the CFL condition,

$$nk \leq nh \text{ or } p=k/h \leq 1 \quad (3.20)$$

In two dimensions the convergence condition is less restrictive than the stability condition. Convergence analysis for the more general hyperbolic wave system with A, B not constant becomes cumbersome. Convergence can also be guaranteed when a scheme is stable and the truncation error tends to zero with $h, k \rightarrow 0$.

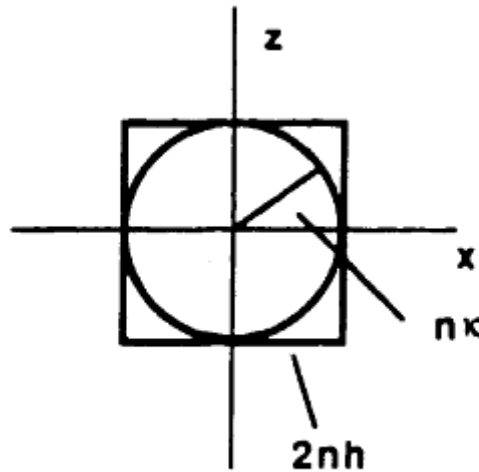


Figure 3.2 The domains of dependence on the plane x - z : a square for Lax-Wendroff scheme and a circle for the simplest $(\rho(x,z)-\mu(x,z)=1)$ SH wave equation.

Stability

The problem of stability consists of finding conditions under which the difference between the theoretical and numerical solutions of the difference equation remains bounded as time progresses. A finite difference scheme is unstable when its error grows without a bound. The easiest way of investigating stability is to use the Fourier series approach pioneered by von Neumann. In this discussion boundary or initial conditions are not going to be taken into consideration.

A stability analysis of a hyperbolic system in two space dimensions is difficult, even with A and B constant. The stability of a difference scheme at a grid point in the field will be the same as the stability of the corresponding difference equation where the values of the coefficients have been 'frozen' to the values attained at that grid point. This local stability condition\ usually a limitation on the-size of the mesh ratio p , will vary from point to point in the field and the overall stability condition must be the largest mesh ratio which satisfies the local stability condition at every grid point in the region. The von Neumann necessary condition for the stability of a system requires the magnitude of the maximum eigenvalue of the amplification matrix to be less than one. The amplification matrix for the Lax-Wendroff scheme with A, B constant

$$G = I - p^2 \left[A^2 (1 - \cos \xi) + B^2 (1 - \cos n) + \frac{1}{2} (AB + BA) \sin \xi \sin n \right] + ip [A \sin \xi + B \sin n] \quad (3.21)$$

is used to evaluate the eigenvalues. Lax and Wendroff(1964) proved that if

$$|a_m| = \max_{A,B} (|a_A|, |a_B|) \quad (3.22)$$

where a_A, a_B are the eigenvalues of the matrices A, B respectively, then the Lax-Wendroff scheme with A,B constant is stable if

$$p|a_m| \leq \frac{1}{2\sqrt{2}} \quad (3.23)$$

For the MacCormack scheme, since the matrix A (or B) can be diagonalized, the von Neumann condition is both necessary and sufficient for stability. If a is an eigenvalue of A the stability condition for this scheme is given by

$$p|a_m| \leq \frac{2}{3} \quad (3.24)$$

The MacCormack scheme stability condition is almost half as restrictive as the Lax-Wendroff. The number of time steps required for the generation of a synthetic trace of a given duration is therefore halved so that the method becomes less expensive.

4. AVO Analysis Theory

The variation of reflection and transmission coefficients with angle of incidence (AVA) (and corresponding increasing offset) is often referred to as offset-dependent reflectivity and is the fundamental basis for amplitude-versus-offset (AVO) analysis. There are two kinds of AVO phenomena according to the types of seismic data. One is P-wave AVO and the other is multicomponent AVO corresponding to single component P-wave seismic data and multicomponent seismic data, respectively. Today, AVO analysis is widely used in hydrocarbon detection, lithology identification, and fluid parameter analysis, due to the fact that seismic amplitudes at the boundaries are affected by the variations of the physical properties just above and just below the boundaries. In recent years, a growing number of theories and techniques in seismic data acquisition, processing, and seismic data interpretation have been developed, updated, and employed. AVO analysis in theory and practice is becoming increasingly attractive [Feng and Bancroft 2006].

4.1 AVO analysis principles

Although, in exploration geophysics, there are rarely simple isolated interfaces, the understanding of offset-dependent reflectivity will be explained at just such an interface. In **Figure 4.1** the angles for incident, reflected and transmitted rays synchronous at the boundary are related according to Snell's law by:

$$p = \frac{\sin \theta_1}{V_{P1}} = \frac{\sin \theta_2}{V_{P2}} = \frac{\sin \phi_1}{V_{S1}} = \frac{\sin \phi_2}{V_{S2}} \quad (4.1)$$

Where V_{P1} = P-wave velocity in medium 1, V_{P2} = P-wave velocity in medium 2, V_{S1} = S-wave velocity in medium 1, V_{S2} = S-wave velocity in medium 2, θ_1 =incident P-wave angle, θ_2 = transmitted P-wave angle, ϕ_1 = reflected S-wave angle, ϕ_2 = transmitted S-wave angle, and p is the ray parameter.

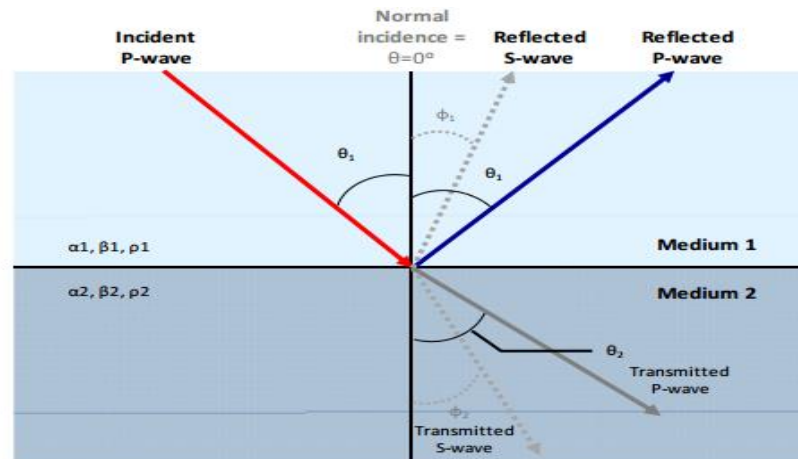


Figure 4.1 Reflection and transmission at an interface for an incident P-wave.

For an interface between two infinite elastic half-spaces, there are sixteen reflection and transmission coefficients (**Figure 4.2**). In the *Aki Richards* notation (4.2), the coefficients are represented by two letters (e.g. $\tilde{P}\tilde{S}'$). The first letter indicates the type of the incident wave and the second letter represents the type of derived wave. The acute accent (') indicates an upgoing wave while a downgoing wave has a grave accent (`). Thus $\tilde{P}\tilde{S}$ is the downgoing P-wave to upgoing S-wave coefficient. With this notation, the scattering matrix is

$$Q = \begin{pmatrix} \tilde{P}\tilde{P} & \tilde{S}\tilde{P} & \tilde{P}\tilde{P} & \tilde{S}\tilde{P} \\ \tilde{P}\tilde{S} & \tilde{S}\tilde{S} & \tilde{P}\tilde{S} & \tilde{S}\tilde{S} \\ \tilde{P}\tilde{P} & \tilde{S}\tilde{P} & \tilde{P}\tilde{P} & \tilde{S}\tilde{P} \\ \tilde{P}\tilde{S} & \tilde{S}\tilde{S} & \tilde{P}\tilde{S} & \tilde{S}\tilde{S} \end{pmatrix} = \underset{\sim}{P}^{-1} \underset{\sim}{R} \quad (4.2)$$

where $\underset{\sim}{P}$ is the matrix

$$\begin{pmatrix} -\sin \theta_1 & -\cos \varphi_1 & \sin \theta_2 & \cos \varphi_2 \\ \cos \theta_1 & -\sin \varphi_1 & \cos \theta_2 & -\sin \varphi_2 \\ 2p_1V_{s1} \sin \varphi_1 \cos \theta_1 & p_1V_{s1}(1-2\sin^2 \varphi_1) & 2p_2V_{s2} \sin \varphi_2 \cos \theta_2 & p_2V_{s2}(1-2\sin^2 \varphi_2) \\ -p_1V_{p1}(1-2\sin^2 \varphi_1) & p_1V_{s1} \sin 2\varphi_1 & p_2V_{p2}(1-2\sin^2 \varphi_2) & -p_2V_{s2} \sin 2\varphi_2 \end{pmatrix} \quad (4.3)$$

and $\underset{\sim}{R}$ is the matrix

$$\begin{pmatrix} \sin \theta_1 & \cos \varphi_1 & -\sin \theta_2 & -\cos \varphi_2 \\ \cos \theta_1 & -\sin \varphi_1 & \cos \theta_2 & -\sin \varphi_2 \\ 2p_1V_{s1} \sin \varphi_1 \cos \theta_1 & p_1V_{s1}(1-2\sin^2 \varphi_1) & 2p_2V_{s2} \sin \varphi_2 \cos \theta_2 & p_2V_{s2}(1-2\sin^2 \varphi_2) \\ p_1V_{p1}(1-2\sin^2 \varphi_1) & -p_1V_{s1} \sin 2\varphi_1 & -p_2V_{p2}(1-2\sin^2 \varphi_2) & p_2V_{s2} \sin 2\varphi_2 \end{pmatrix} \quad (4.4)$$

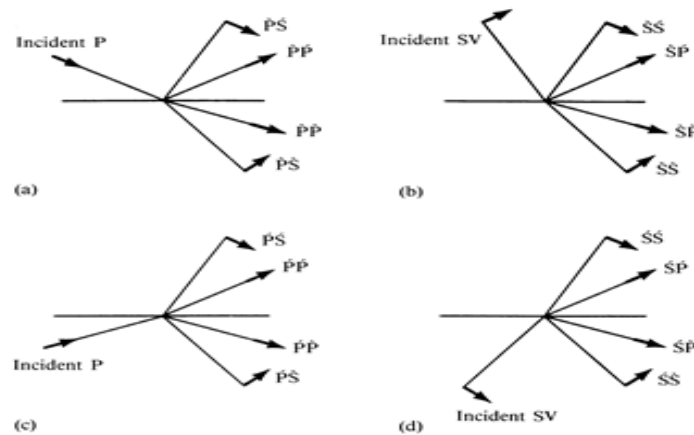


Figure 4.2 Notation for the sixteen possible reflection/transmission coefficients for P-SV waves at an interface between two different solid half-spaces. Short arrows show the direction of particle motion (from Aki and Richards, 1980).

Koefoed (1955) first pointed out the practical possibilities of using AVO analysis as an indicator of V_P - V_S variations and empirically established five rules, which were later verified by *Shuey (1985)* for moderate angles of incidence:

- a) When the underlying medium has the greater longitudinal [P-wave] velocity and other relevant properties of the two strata are equal to each other, an increase of Poisson's ratio for the underlying medium causes an increase of the reflection coefficient at the larger angles of incidence.
- b) When, in the above case, Poisson's ratio for the incident medium is increased, the reflection coefficient at the larger angles of incidence is thereby decreased.
- c) When, in the above case, Poisson's ratios for both media are increased and kept equal to each other, the reflection coefficient at the larger angles of incidence is thereby increased.
- d) The effect mentioned in (a) becomes more pronounced as the velocity contrast becomes smaller.
- e) Interchange of the incident and the underlying medium affects the shape of the curves only slightly, at least up to values of the angle of incidence of about 30 degrees.

Bortfeld (1961) linearized the Zoeppritz equations by assuming small changes in layer properties ($\Delta\rho/\rho$, $\Delta V_P/V_P$, $\Delta V_S/V_S \ll 1$).

This approach was also followed by *Richards and Frazier (1976)* and *Aki and Richards (1980)* who derived a form of approximation simply parameterized in terms of the changes in density, P-wave velocity, and S-wave velocity across the interface:

$$R_{\rho\rho}(\theta) \approx \frac{1}{2}(1 - 4\rho^2 V_s^2) \left(\frac{\Delta\rho}{\rho} \right) + \frac{1}{2\cos^2(\theta)} \cdot \frac{\Delta V_\rho}{V_\rho} - 4V_s^2 \rho^2 \frac{\Delta V_s}{V_s} \quad (4.5)$$

Where $\Delta\rho = \rho_2 - \rho_1$, $\Delta V_P = V_{P2} - V_{P1}$, $\Delta V_S = V_{S2} - V_{S1}$, $\rho = (\rho_2 + \rho_1)/2$, $V_P = (V_{P2} + V_{P1})/2$, $V_S = (V_{S2} + V_{S1})/2$, $\theta = (\theta_1 + \theta_2)/2$ and p is the ray parameter as defined by equation (4.1). By simplifying the Zoeppritz equations, *Shuey (1985)* presented another form of the *Aki and Richards (1980)* approximation,

$$R(\theta) \approx R_o + \left[A_o R_o + \frac{\Delta\sigma}{(1-\sigma)^2} \right] \sin^2 \theta + \frac{1}{2} \frac{\Delta V_P}{V_P} (\tan^2 \theta - \sin^2 \theta) \quad (4.6)$$

Where R_o is the normal-incidence P-P reflection coefficient, A_o is given by:

$$A_o = B_o - 2(1 + B_o) \frac{1 - 2\sigma}{1 - \sigma} \quad (4.7)$$

$$\text{and } B_o = \frac{\Delta V_P / V_P}{\Delta V_P / V_P + \Delta\rho / \rho} \quad (4.8)$$

Where $\Delta\sigma$ is the average Poisson's ratio and is defined as $\Delta\sigma = \sigma_2 - \sigma_1$ and $\sigma = (\sigma_2 + \sigma_1)/2$.

With various assumptions, the (4.6) can be simplified as:

$$R(\theta) = R_p + G \sin^2 \theta \quad (4.9)$$

This equation is linear if R is plotted as a function of $\sin^2 \theta$. Then a linear regression analysis can be performed on the seismic amplitudes to estimate intercept, R_p , and gradient G . Before performing the linear regression, firstly the data should be transformed from constant offset form to constant angle form.

The quantity A_o , given by equation (4.6), specifies the variation of $R(\theta)$ in the approximation range $0 < \theta < 30^\circ$ for the case of no contrast in Poisson's ratio. The first term gives the amplitude at normal incidence, the second term characterizes $R(\theta)$ at intermediate angles, and the third term describes the approach to the critical angle. The coefficients of Shuey's approximation form the basis of various weighted stacking procedures. Weighted stacking, here also called Geostack (Smith and Gidlow, 1987), is a means of reducing prestack information to AVO attribute traces versus time. This is accomplished by calculating the local angle of incidence for each time sample, then performing regression analysis to solve for the first two or all three coefficients of an equation of the kind:

$$R(\theta) \approx A + B \sin^2 \theta + C \sin^2 \theta \tan^2 \theta \quad (4.10)$$

where A is the “zero-offset” stack, B is commonly referred to as the AVO “slope” or “gradient” and the third term becomes significant in the far-offset stack. At the same time, the “fluid factor” concept was introduced by Smith and Gidlow (1987) to highlight gas-bearing sandstones. Hiltermann (1989) derived another convenient approximation:

$$R(\theta) \approx R_o \cos^2 \theta + 2.25 \Delta \sigma \sin^2 \theta \quad (4.11)$$

Thus, at small angles R_o dominates the reflection coefficient whereas $\Delta \sigma$ dominates at larger angles. In this way, we can think of a near-offset stack as imaging P-wave impedance contrasts while the far-offset stack images Poisson's-ratio contrasts. The analysis of amplitude variation with offset (AVO) was a significant component in the development of direct hydrocarbon indicators (DHIs), and AVO techniques are identified by Hiltermann (2001) as the second era of amplitude interpretation, following the brightspot era.

4.2 Transforming From the Offset to the Angle Domain

As mentioned on chapter 4.1, both Zoeppritz equations and Shuey's equation are dependent upon the angle of incidence at which the seismic ray strikes the horizon of interest. However, the seismic data is recorded as a function of offset. While offset and angle are roughly similar, there is a nonlinear relationship between them, which must first be accounted for in processing and analysis schemes which require that angle be used instead of offset. This type of analysis is termed AVA (amplitude versus angle) rather than AVO. An example of such a transform is shown in **Figure 4.3**.

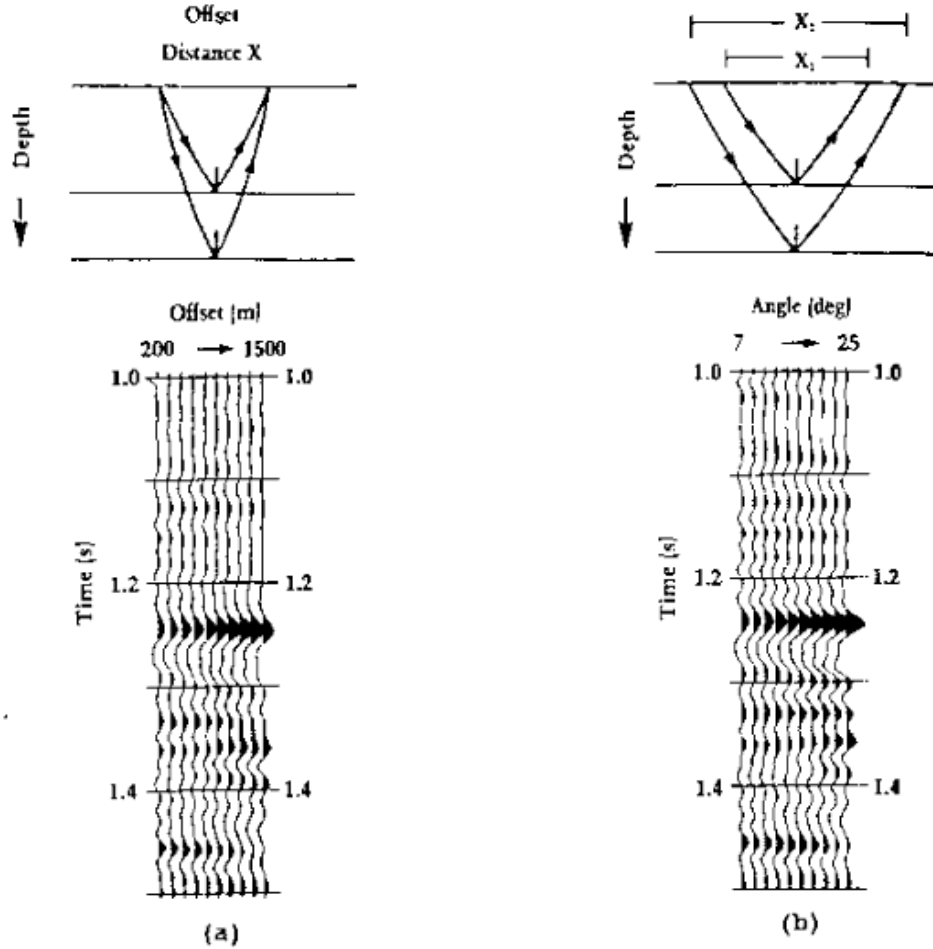


Figure 4.3 (a) shows AVO response and (b) shows transform of (a) in AVA (amplitude versus angle) response [NTNU, AVO theory, 2004].

An offset gather is shown in **Figure 4.3 (a)**, and the equivalent angle gather is shown in **Figure 4.3 (b)**. At the top of each gather a schematic of the raypath's geometry is shown for the reflected events in a particular trace of each gather. As it is observed from **Figure 4.3**, the angle of incidence for a constant offset trace decreases with depth, whereas the angle remains constant with depth for a constant angle trace. The operation for computing this transform is quite straightforward. To transform from constant offset to constant angle, the relationship between X and θ needs to be known. For a complete solution, a full ray tracing must be done. However, a good approximation is to use straight rays. In this case it is found that:

$$\tan \theta = \frac{X}{2Z} \quad (4.12)$$

Where θ =angle of incidence, X =offset and Z =depth.

If the velocity down to the layer of interest is known:

$$Z = \frac{V \cdot t_o}{2} \quad (4.13)$$

Where V =Velocity either RMS or Average and t_o = total zero-offset travel time.

Substituting equation (4.12) into (4.13) gives:

$$\tan \theta = \frac{X}{V \cdot t_o} \quad (4.14)$$

which gives the mapping from offset to angle. By inverting equation (4.14), the mapping from angle to offset derives:

$$X = V \cdot t_o \tan \theta \quad (4.15)$$

Equation (4.15) thus allows the mapping of the amplitudes on an offset gather to amplitudes on an angle gather. **Figure 4.4** shows a theoretical set of constant angle curves superimposed on an offset versus time plot. As it is observed from **Figure 4.4** the curves increase to larger offsets at deeper times. This means that a constant angle seismic trace would contain amplitudes collected from longer offset on the **AVO** gather as time increases.

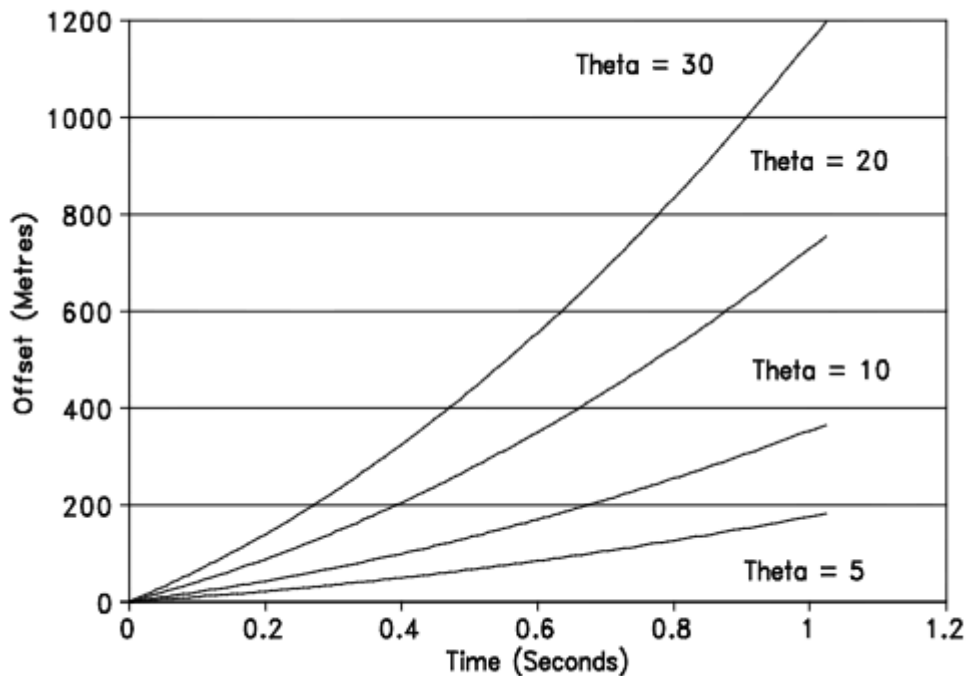


Figure 4.4 A plot of constant angle curves superimposed on constant offset traces.

4.3 Ray Tracing

The ray-tracing problem in AVO is that for a given source and receiver location, and a given reflection layer, the raypath which connects the source and receiver should be defined, while obeying Snell's Law in each layer. The following derivation follows that of *Dahl and Ursin (1991)*. Define the ray-parameter, p , as:

$$p = \frac{\sin \theta_1}{V_{P1}} \quad (4.16)$$

where θ_1 is the emergence angle for energy from the source and V_{P1} is the P-wave velocity of the first layer. Snell's Law indicates that for any layer:

$$p = \frac{\sin \theta_i}{V_{Pi}} \quad (4.17)$$

If the emergence angle is known, the offset, y , at which the reflected energy will come back to the surface can be calculated:

$$y(p) = \sum_k \frac{D_k V_k p}{\sqrt{1 - V_k^2 p^2}} \quad (4.18)$$

In this equation, D_k is the thickness of the k th layer, and the sum is over all layers down to the reflecting interface.

In the ray-tracing problem, the desired offset y_d is known, it is the distance between the source and receiver for the trace in question. The problem is to find the value of p that gives the correct value of y in equation (4.18). Unfortunately, there is no explicit solution to this problem. The approach used in AVO is an iterative solution, sometimes called a "shooting method". The first step is to make a guess at the correct value of p , say p_o . With this value of p , the initial value of y can be calculated, from equation (4.18):

$$y_o = \sum_k \frac{D_k V_k p_o}{\sqrt{1 - V_k^2 p_o^2}} \quad (4.19)$$

Usually, y_o will not be the same as the desired value y_d . The error is $\Delta y = y_d - y_o$.

An improved value for p is then given by:

$$p' = p_o + \frac{\partial p}{\partial y} \Delta y \quad (4.20)$$

where $\partial p / \partial y$ is calculated from equation (4.18) as:

$$\frac{\partial p}{\partial y} = \left[\sum_k \frac{D_k V_k}{(1 - V_k^2 p_o^2)^{3/2}} \right]^{-1} \quad (4.21)$$

The new value, p' , when used in equation (4.18) should give a value of y closer to the desired y_d than the initial guess. Ray tracing consists of continually applying equations (4.19) to (4.21) until a “convergence condition” is reached.

The convergence condition in AVO is reached when either of the following is true:

- 1) The maximum number of iterations is reached. For synthetic modelling in AVO, the maximum number of iterations is set to 100. This value should never be reached under normal circumstances.
- 2) The offset error Δy becomes “small enough”. In AVO, the tolerance is set to the greater of 1% of the desired offset or 1 distance unit. If, for example, the desired offset is 1000 m, the iterations will stop when the error is less than 10m. If the desired offset is 10m, the iterations will stop when the error is less than 1m.

The algorithm described by equations (4.19) to (4.21) is so efficient that for the vast majority of cases, convergence is reached in two or three iterations. Unfortunately, certain pathological conditions can occur from time to time, which cause the algorithm to get stuck. The worst case occurs when a single layer between the surface and the target interface has a P-wave velocity much higher than average. In this case, the propagation angle θ_i in equation (4.17) is close to 90° . This also means that the ray-path is close to critical but not quite. Instability can then arise, which causes the error, Δy , to converge very slowly. A typical cause of anomalously high velocity layers is, in fact, errors in the log.

4.4 Seismic Data Pre-Processing for AVO Analysis

AVO processing should **preserve or restore relative trace amplitudes** within CMP gathers. This implies two goals:

- Reflections must be correctly positioned in the subsurface
- Data quality should be sufficient to ensure that reflection amplitudes contain information about reflection coefficients.

Even though the unique goal in AVO processing is to preserve the true relative amplitudes, there is no unique processing sequence. It depends on the complexity of the geology, whether it is land or marine seismic data and whether the data will be used to extract regression-based AVO attributes or more sophisticated elastic inversion attributes. *Cambois (2001)* defines AVO processing as any processing sequence that makes the data compatible with Shuey's equation. If that is the model used for the AVO inversion. Camhois emphasizes that this can be a very complicated task.

Factors that change the amplitudes of seismic traces can be grouped into Earth effects, acquisition-related effects, and noise (*Dey-Sarkar and Suatek, 1993*). Earth effects include i) spherical divergence, ii) absorption, iii) transmission losses, iv) interbed multiples, v) converted phases, vi) tuning, vii) anisotropy, and viii) structure. Acquisition-related effects include **source and receiver arrays and receiver sensitivity**. Noise can be **ambient or source generated, coherent or random**. Processing attempts to compensate for or remove these effects, but can in the process change or distort relative trace amplitudes. This is an important trade-off we need to consider in pre-processing for AVO.

a) Spiking deconvolution and wavelet processing

In AVO analysis we normally want zero-phase data. However, the original seismic pulse is causal, usually some sort of minimum phase wavelet with noise. Deconvolution is defined as convolving the seismic trace with an inverse filter in order to extract the impulse response from the seismic trace. This procedure will restore high frequencies and therefore improve the vertical resolution and recognition of events. The wavelet shape can vary vertically (with time), laterally (spatially), and with offset. However, AVO analysis is normally carried out within a limited time window where one can assume stationarity. Lateral changes in the wavelet shape can be handled with surface-consistent amplitude balancing (*e.g., Cambois and Magesan, 1997*). Offset-dependent variations are often more complicated to correct for, and are attributed to both offset-dependent absorption, tuning effects, and NMO stretching. NMO stretching acts like a low-pass, mixed-phase, nonstationary filter, and the effects are very difficult to eliminate fully (*Cambois, 2001*).

b) Spherical divergence correction

Spherical divergence, or geometrical spreading, causes the intensity and energy of spherical waves to decrease inversely as the square of the distance from the source (*Newman, 1973*). This technique will be further analysed in the next chapter.

c) Surface-consistent amplitude balancing

Source and receiver effects as well as water depth variation can produce large deviations in amplitude that do not correspond to target reflector properties. Commonly, statistical amplitude balancing is carried out both for time and offset. However, this procedure can have a dramatic effect on the AVO parameters. It easily contributes to intercept leakage and consequently erroneous gradient estimates (*Cambois, 2000*). *Cambois (2001)* suggested modeling the expected average amplitude variation with offset following Shuey's equation, and then using this behaviour as a reference for the statistical amplitude balancing.

d) Multiple removal

One of the most deteriorating effects on pre-stack amplitudes is the presence of multiples. There are several methods of filtering away multiple energy, but not all of these are adequate for AVO pre-processing. The method known as f - k multiple filtering, done in the frequency-wavenumber domain, is very efficient at removing multiples, but the dip in the f - k domain is very similar for near-offset primary energy and near-offset multiple energy. Hence, primary energy can easily be removed from near traces and not from far traces, resulting in an artificial AVO effect. More robust demultiple techniques include linear and parabolic Radon transform multiple removal (*Hampson, 1986; Herrmann et al., 2000*).

e) NMO (normal moveout) correction

A potential problem during AVO analysis is error in the velocity moveout correction. When extracting AVO attributes, one assumes that primaries have been completely flattened to a constant traveltime. This is rarely the case, as there will always be residual moveout. The reason for residual moveout is almost always associated with erroneous velocity picking, and great efforts should be put into optimizing the estimated velocity field (*e.g., Adler, 1999; Le Meur and Magneron, 2000*). However, anisotropy and non-hyperbolic moveouts due to complex overburden may also cause misalignments between near and far offsets. Ursin and Ekren (1994) presented a method for analyzing AVO effects in the offset domain using time windows. This technique reduces moveout errors and creates improved estimates of AVO parameters. One should be aware of AVO anomalies with polarity shifts (class lip, see definition below) during NMO corrections, as these can easily be misinterpreted as residual moveouts (*Ratcliffe and Adler, 2000*).

f) Pre-stack migration

Pre-stack migration might be thought to be unnecessary in areas where the sedimentary section is relatively flat, but it is an important component of all AVO processing. Pre-stack migration should be used on data for AVO analysis whenever possible, because it will collapse the diffractions at the target depth to be smaller than the Fresnel zone and therefore increase the lateral resolution (*Berkhout, 1985; Mosher et al., 1996*). Normally, pre-stack time migration (PSTM) is preferred to prestack depth migration (PSDM), because the former tends to preserve amplitudes better. However, in areas with highly structured geology, PSDM will be the most accurate tool (*Cambois, 2001*). An amplitude-preserving PSDM routine should then be applied (*Bleistein, 1987; Schleicher et al., 1993; Hanitzsch, 1997*). Migration for AVO analysis can be

implemented in many different ways. *Resnick et al. (1987)* and *Allen and Peddy (1993)* among others have recommended Kirchhoff migration together with AVO analysis.

Below are presented three different proposed pre-processing schemes for AVO analysis of a 2D seismic line.

Yilmaz (2001)

- (1) Pre-stack signal processing (source signature processing, geometric scaling, spiking deconvolution and spectral whitening).
- (2) Sort to CMP and do sparse interval velocity analysis.
- (3) NMO using velocity field from step 2.
- (4) Demultiple using discrete Radon transform.
- (5) Sort to common-offset and do DMO correction.
- (6) Zero-offset FK time migration.
- (7) Sort data to common-reflection-point (CRP) and do inverse NMO using the velocity field from step 2.
- (8) Detailed velocity analysis associated with the migrated data.
- (9) NMO correction using velocity field from step 8.
- (10) Stack CRP gathers to obtain image of pre-stack migrated data. Remove residual multiples revealed by the stacking.
- (11) Unmigrate using same velocity field as in step 6.
- (12) Post-stack spiking deconvolution.
- (13) Remigrate using migration velocity field from step 8.

Ostrander (1984):

- (1) Spherical-divergence correction.
- (2) Exponential-gain correction.
- (3) Minimum-phase spiking deconvolution.
- (4) Velocity analysis.
- (5) NMO correction.
- (6) Trace equalization.
- (7) Horizontal trace summing.

Chiburis (1984):

- (1) Mild f-k multiple suppression.
- (2) Spherical divergence and NMO correction.
- (3) Whole-trace equalization.
- (4) Flattening on a consistent reference event.
- (5) Horizontal trace summing.
- (6) Peak amplitude picked interactively.
- (7) Smoothed least-squares curve fitting.
- (8) Despiking of outliers.
- (9) Results clipped and smoothed.
- (10) Curve refitting.

4.5 Far versus near-stack attributes

Several AVO attributes can be created from limited-range stack sections. The far stack minus the near stack (FN) is a "rough" estimate of an AVO gradient, and in particular it is found to be a good attribute from which to detect class II AVO anomalies (Ross and Kinman, 1995). For class II type prospects, the far stack alone can be a good attribute for improved delineation. However, for class IIP anomalies, both the near and the far stack can be relatively dim, but with opposite polarities. Then the difference between far and near will manifest the significant negative gradient that is present. In contrast, a conventional full stack will completely zero-out a class IIP anomaly. Ross and Kinman (1995) suggested the following equation for the FN attribute depending on whether there is a class II or class IIP anomaly:

$$FN = \sum_{\theta=\theta_f}^{\theta_{\max}} F - c \sum_{\theta=0}^{\theta_n} N \quad (4.22)$$

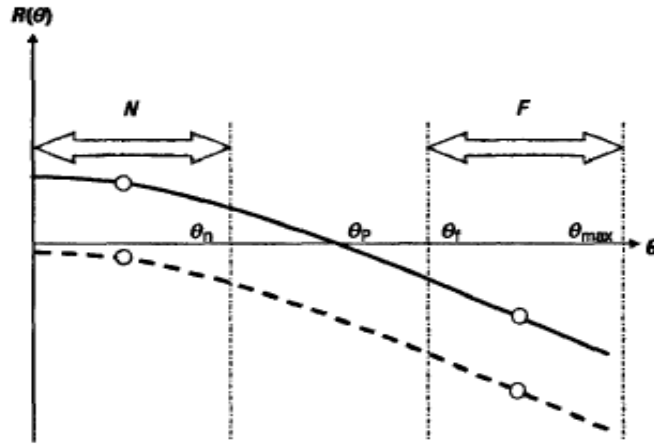


Figure 4.5 Schematic illustration of class II and class IIP and definitions of parameters used in equation (4.22). The angle θ_p is the angle of polarity change. Separation of near and far stack away from the angle of phase reversal will increase the dynamic range of the FN attribute. (Modified from Ross and Kinman, 1995.)

Where $c = 0$ if class II, and $c = 1$ if class IIP. The variables F and N are the far- and near-stack amplitudes, respectively. The angles θ_n , θ_f , and θ_{\max} are the limitations of angle ranges applied to calculate average amplitudes of N and F , as depicted in **Figure 4.5**. The mid-offset range where the phase reversal occurs is avoided. This gives larger average amplitudes of N and F , and hence increases the dynamic range of equation (4.22). Cross-plots of near (N) versus far minus near (FN) will indicate similar trends to a cross-plot of intercept versus gradient. However, one should make sure that the near stack and the far stack are balanced correctly, so the amplitude changes from near stack to far stack are representative for true AVO effects. Also, one should make sure the horizons are time-aligned correctly during the subtraction procedure. Other attributes include far minus near times far ($FNXF$) and far minus near times near ($FNXN$). The first is a good attribute to enhance class II AVO anomalies, where the near stack is weak and the far is a strong negative. The second is a good attribute to enhance hydrocarbon-related class III AVO anomalies, and at the same time reduce the corresponding brine-saturated class II AVO response.

4.6 AVO attributes combining intercept and gradient

AVO analysis is not very much more complicated than stacking the data. **Figure 4.6** shows a set of traces in a gather. These traces have been selected so that they all are representative of a line of observations extending vertically from a particular point on the surface to some pre-selected depth (in two-way, acoustic travel time). They have been adjusted so that corresponding samples on different traces reference the same two-way travel time. They are arranged in order with the trace coming from the shot-receiver pair closest to the gather lying on the left. Remember that all of the traces in a gather have the same X-Y location. Also, the graph shown on **Figure 4.6** plots the value of the amplitude for each trace at time t_2 on the ordinate (or Y- axis) against $\sin^2\theta$ on the abscissa (or X- axis), where θ is the angle between the shot (or receiver) and the line of the trace.

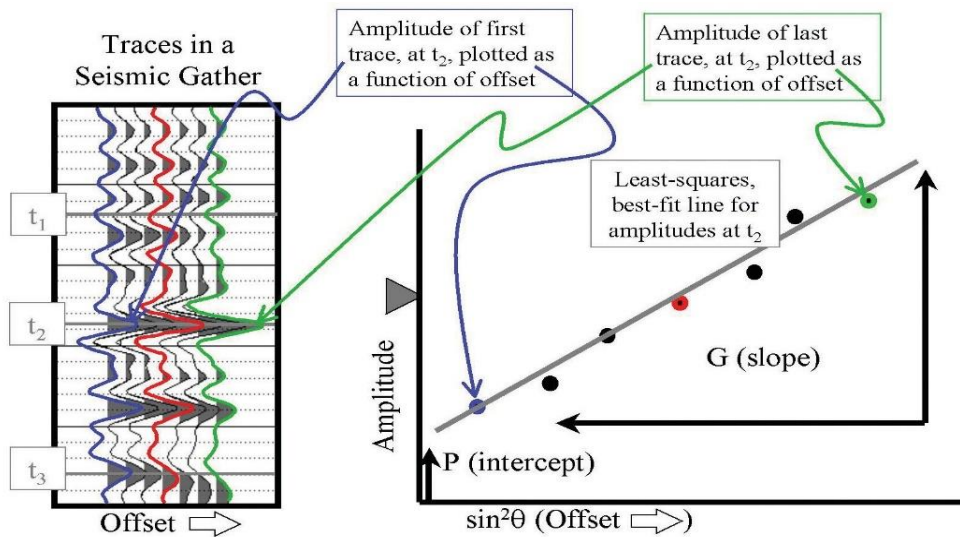


Figure 4.6 A basic AVO analysis after appropriate geometric corrections the individual traces for one gather are displayed in the panel on the left; the colours correspond to different reflectors. A graph may be constructed at any point in time (e.g. t_1 , t_2 or t_3) to analyse the amplitude variation with offset of the traces at that time; the graph at the right shows one such plot for time t_2 . The gray line is a least-squares, best-fit to the natural distribution; values for P and G are extracted from analysis of the best-fit line. Triangle shows the average amplitude of all of the traces at t_2 .

Higher angles obviously are associated with far offsets. For reasons that are discussed elsewhere, $\sin^2\theta$ transforms the relationship between amplitude and offset into a more-linear one. Because the relationship, as graphed, is nearly linear, a simple, least-squares, best-fit line can be used to describe the distribution of the amplitudes (shown on **Figure 4.6** as a gray line going through the data points). This line can be completely and uniquely characterized by two parameters: the value where it intersects the ordinate (called “ P ”), and its slope (called “ G ”). To the extent that the line fully describes the distribution of the amplitudes, these two parameters (P and G) fully describe the line and, therefore, the amplitude variation with offset (AVO). P is often referred to as the “zero-offset” amplitude, or the “Normal Incident” amplitude. In addition to “Slope,” G is often referred to as the “Gradient” or the “AVO Gradient.”

There are other pieces of information or AVO parameters which may be extracted from the traces or from the graph of their amplitudes. Sometimes a subset of the traces such as those reflected through a small angle (or from a short offset distance) are stacked independently of the others and, in this case, referred to as “Nears.” Other groupings, such as those reflected through a large angle or an intermediate angle, are called “Fars” or “Mids.” Summarizing, the most commonly used parameters in AVO analysis are the values of Ps and Gs, which together completely define the gathers; the stack, which averages all of the information from the gathers; and the nears, mids and fars, which average subsets of the information in the gathers.

As it has been mentioned, the Ps and Gs effectively contain all of the information from the gathers. It’s instructive, therefore, to start with the Ps and Gs and then see how other products relate to them. **Figure 4.7** is a plot of all of the values of P and of G from a seismic dataset, crossplotted against each other; we refer to this plot as representing AVO space. The left-hand panel of **Figure 4.7** is obviously of little value; it shows that there is some regularity to the data, but little more. The right-hand panel of **Figure 4.7** shows the same data color-coded to highlight the amplitudes of the stacked dataset. The distribution of the colours should come as no surprise: A negative amplitude is a trough and a bunch of trace amplitudes distributed so as to yield a strongly negative P with a strongly negative gradient (G) that will have the highest average negative amplitudes (large, dark-blue troughs on the stack). Superimposed on the right-hand panel are the three regions defined by Rutherford and Williams’ AVO classes.

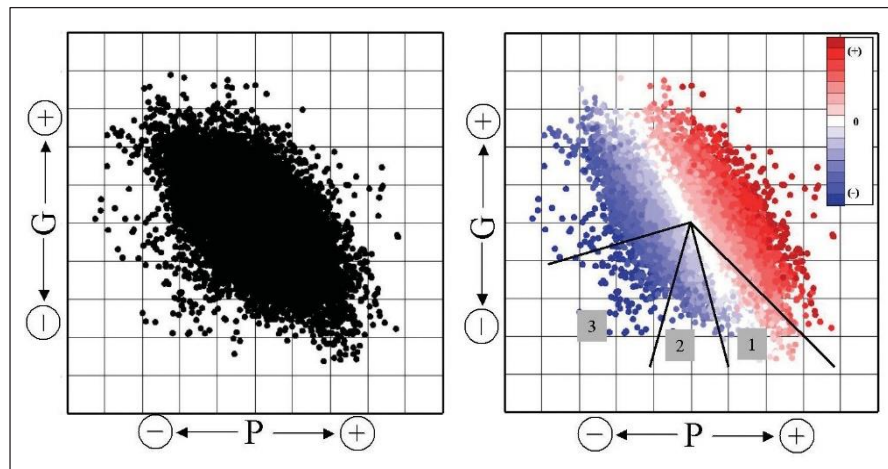


Figure 4.7 On the left, a cross-plot shows P versus G for every time sample for every gather in a volume of seismic data. The data have been normalized to constrain P and G to the same range of values. On the right, the same cross-plot has been color-coded to show the stacked amplitude of each point; light to dark blues are low to high amplitude troughs, and pink to dark reds are low to high amplitude peaks. The three regions denoted 1, 2 and 3 are defined by the three AVO classes of Rutherford and Williams.

4.7 AVO Analysis Application on Gas Detection

By far, gas-sand detection is the most promising application of AVO analysis. It is hoped that the characteristically low V_P/V_S ratio of gas sands should allow their differentiation from other low-impedance layers, such as coals and porous brine sands (Castagna et al., 1993). Rutherford and Williams (1989) defined three distinct classes of gas-sand AVO anomalies. Their Class 1 occurs when the normal-incidence P-wave reflection coefficient is strongly positive and shows a strong amplitude decrease with offset and a possible phase change at far offset (**Figure 4.8**).

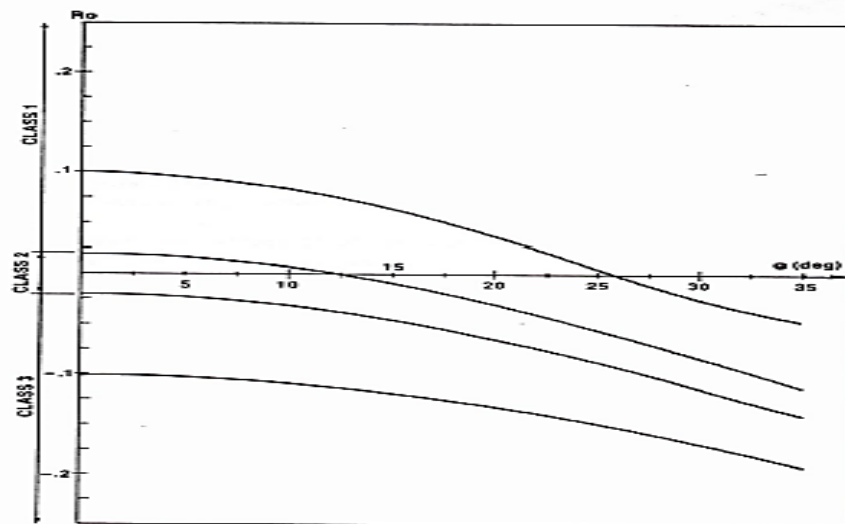


Figure 4.8 Zoeppritz P-wave reflection coefficients for a shale/gas-sand interface for a range of R_0 values. The Poisson's ratio and density of the shale were assumed to be 0.38 and 2.4 g/cm³, respectively. The Poisson's ratio and density of the gas sand were assumed to be 0.15 and 2.0 g/cm³, respectively (Rutherford and Williams, 1989).

Class 2, for small P-wave reflection coefficients, shows a very large percent change in AVO. In this situation, if the normal-incidence reflection coefficient is slightly positive, a phase change at near or moderate offsets will occur. Class 3 anomalies (Rutherford and Williams, 1989) have a large negative normal-incidence reflection coefficient, which becomes more negative as offset increases (these are classical bright spots). A simple rule of thumb that generally applies to shale over gas-sand reflections is that the reflection coefficient becomes more negative with increasing offset (Castagna and Backus, 1993).

But on the principles of AVO crossplotting, Castagna and Swan (1997) suggest that hydrocarbon-bearing sands overlain by shale should be classified according to their location in the A-B plane, rather than by their normal-incidence reflection coefficient alone. Class I sands (Castagna et al., 1997) are of higher impedance than the overlying unit. They occur in quadrant IV of the A-B plane. The normal incidence reflection coefficient is positive while the AVO gradient is negative. And the reflection coefficient decreases with increasing offset. Class II sands (Castagna et al. 1997) have about the same impedance as the overlying unit. They exhibit highly variable AVO behaviour and may occur in quadrants II, III, or IV of the A-B plane. Class III sands (Castagna and Swan, 1997) here are of lower impedance than the overlying unit and are frequently bright. (

Figure 4.9).

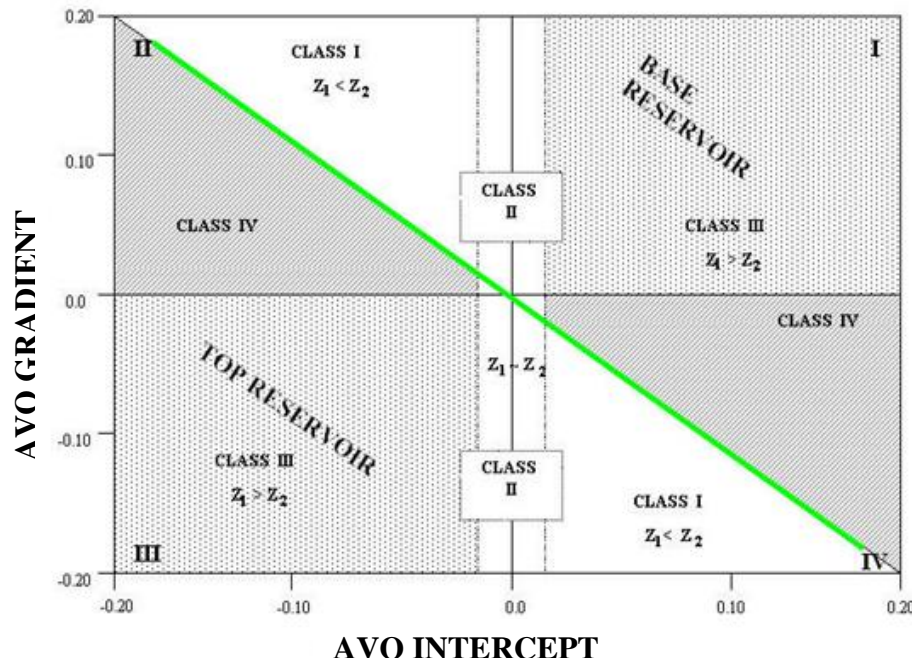


Figure 4.9 This newer classification is identical to that of Rutherford and Williams (1989) for Class I (high-impedance-contrast) and Class II (low-impedance-contrast) sands. However, it differs in that Class III (low-impedance-contrast) is subdivided into two classes, III and IV. The Class IV sands are highly significant in that they exhibit AVO behaviour contrary to established rules of thumb and occur in many basins throughout the world, including the Gulf of Mexico (Castagna and Swan, 1997). (Numbers in the corners are quadrant numbers).

The key value of AVO crossplot interpretation is the ability to differentiate population outliers relative to background trend points within crossplot space. Incorporating direct hydrocarbon indicators (DHIs) via crossplotting can play a significant role in minimizing the risk associated with an exploration play. The stability of the background trend (fluid angle) can have an impact on what is being interpreted as anomalous, be it fluid or lithology induced outliers. For a given anomaly (population outliers) an interpretation of an increase in V_p/V_s (due to a superimposed background trend) can be just as feasible as a decrease in V_p/V_s (due to a fluid response or coal) dependent upon the choice of background trend. The Castagna and Swan crossplot template, seen in **Figure 4.10**, is often used in the literature to explain crossplot behavior observed in seismic data.

As it is observed from **Figure 4.10** A versus B trends for various constant ratios of compressional (V_p) to shear wave (V_s) velocity. Notice that the AVO gradient (B) and the AVO intercept (A) are generally negatively correlated, and that the A versus B trends become more positive as V_p/V_s increases. Also, note that the trend becomes positive at high V_p/V_s ratios. Thus, the normal response for (nonhydrocarbon-related) reflections at very high background V_p/V_s is an amplitude increase versus offset. Large reflection coefficients associated with shale over porous brine-sand interfaces will exhibit “false positive” AVO anomalies in the sense that they will have larger AVO gradients than weaker reflections lying along the same background trend. When interpreted in terms of deviation from the background A versus B trend, such reflections are correctly interpreted as not being anomalous.

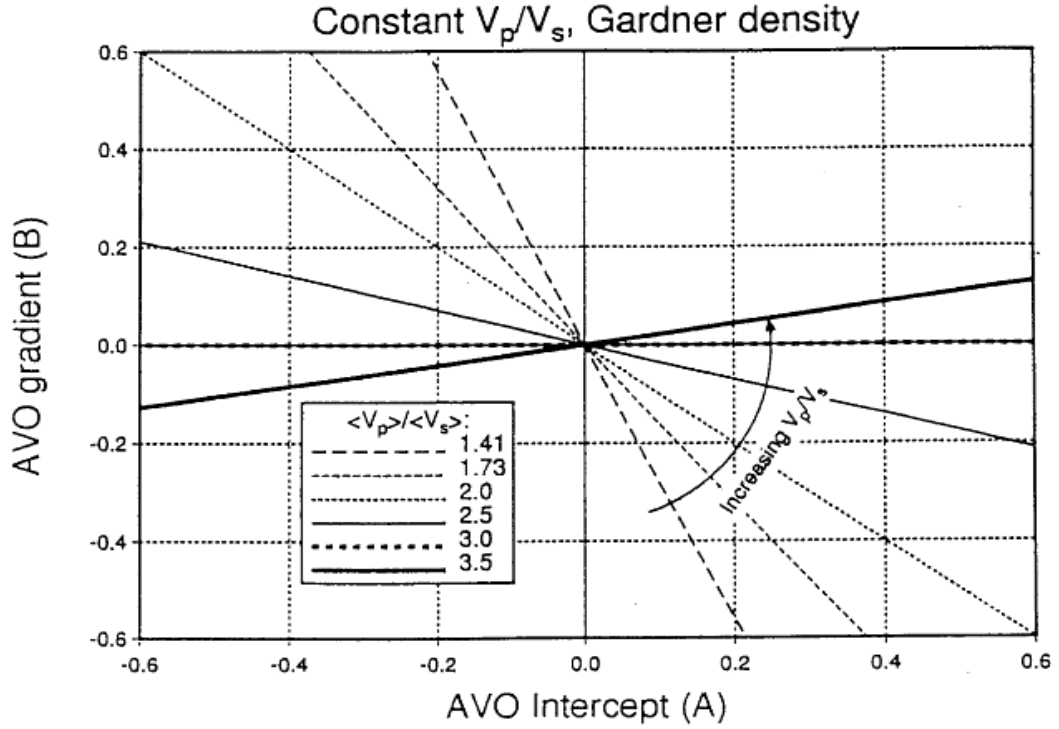


Figure 4.10 Zero-offset reflection coefficient (A) versus the AVO gradient (B) assuming constant V_p/V_s and Gardner's relation. The background trend rotates counter clockwise as V_p/V_s increases.

It is assumed that the “background” consists of brine saturated sandstones and shales and, to first order, that density is a constant factor times the velocity raised to some arbitrary power g . Gardner et al. (1974) showed that g is about equal to $1/4$ for most sedimentary rocks. For small changes in velocity, we have

$$\frac{\Delta\rho}{\langle\rho\rangle} \sim g \frac{\Delta V_p}{\langle V_p\rangle} \quad (4.23)$$

Combining equations 4.23 and 4.8 yields a general equation for “background” reflections in the A–B plane:

$$B = \frac{A}{1+g} \left[1 - 4 \frac{\langle V_s \rangle}{\langle V_p \rangle} \left(\frac{2}{m} + g \frac{\langle V_s \rangle}{\langle V_p \rangle} \right) \right] \quad (4.24)$$

If it is assumed that V_p/V_s is constant and equals to m then:

$$m = V_p / V_s = \langle V_p \rangle / \langle V_s \rangle = \Delta V_p / \Delta V_s \quad (4.25)$$

Now, instead of assuming constant density, the Gardner's relation is used (4.23). Setting $g=1/4$ and $m = \langle V_p \rangle / \langle V_s \rangle$ yields from 4.24

$$A = \frac{5}{8} \Delta V_p / \langle V_p \rangle \quad (4.26)$$

$$B = \frac{4}{5} \left[1 - 9 \left(\frac{\langle V_s \rangle}{\langle V_p \rangle} \right)^2 \right] A \quad (4.27)$$

Of course, the most interesting deviation from background petrophysical relationships results from replacement of brine in the pore space by hydrocarbons, particularly gas, for which the effects are most pronounced. Assuming no associated geological or chemical effects, the mechanical replacement of gas for brine using Gassmann's equations reduces V_P/V_S ratio and causes ΔV_P and Δp to become more negative. Thus, by equations (4.7) and (4.8), for a top-of-sand reflection, partial gas saturation causes both A and B to become more negative than for the corresponding fully brine-saturated sand. This is illustrated in **Figure 4.11**, which shows calculated AVO intercepts and gradients for pairs of shale/gas sand and shale/brine sand reflectors. The shale over brine-sand reflection coefficients vary from strongly positive to strongly negative, but were selected to have the same average P-wave velocity. Intercepts and gradients were then calculated using Gardner's relation and the mudrock trend, and were found to lie along the straight line predicted by equation (6.11). Gassmann's equations were then used to substitute gas for brine in the sands. The reflection coefficients for the corresponding gas sands also fall along a straight line to the lower left of the background trend. Each tie line moves toward more negative A and B from brine sand to gas sand.

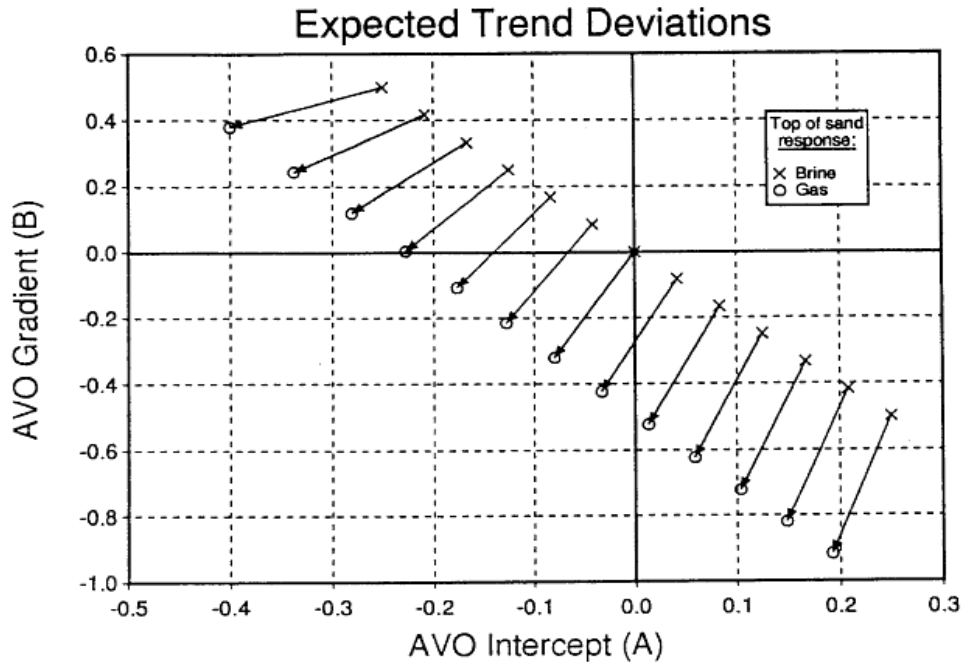


Figure 4.11 Deviations from the background petrophysical trends, as would be caused by hydrocarbons or unusual lithologies, cause deviations from the background A versus B trend. This figure shows brine sand-gas sand tie lines for shale over brine-sand reflections falling along a given background trend. In general, the gas sands exhibit more negative As and Bs than the corresponding brine sands (assuming the frame properties of the gas sands and the brine sands are the same). Note that the gas sands form a distinct trend which does not pass through the origin.

The most famous theory in the detection of gas in sandstone reservoirs using AVO analysis is that of Fatti et al. (1994). They employed a technique called Geostack (Smith and Gidlow, 1987). The fluid factor (Smith and Gidlow, 1987) here is defined as:

$$\Delta F = R_{PP} - 1.16 \frac{W}{V} R_{SS} \quad (4.28)$$

Where R_{PP} = zero-offset P-P reflection coefficient, W = average S-wave velocity, V = average P-wave velocity, R_{SS} = zero-offset S-wave reflection coefficient. The success of the ΔF traces in indicating the presence of gas depends on the amount of separation on the crossplot of W versus V for gas sandstones, on the one hand, and water sandstones and shales on the other hand (**Figure 4.12**).

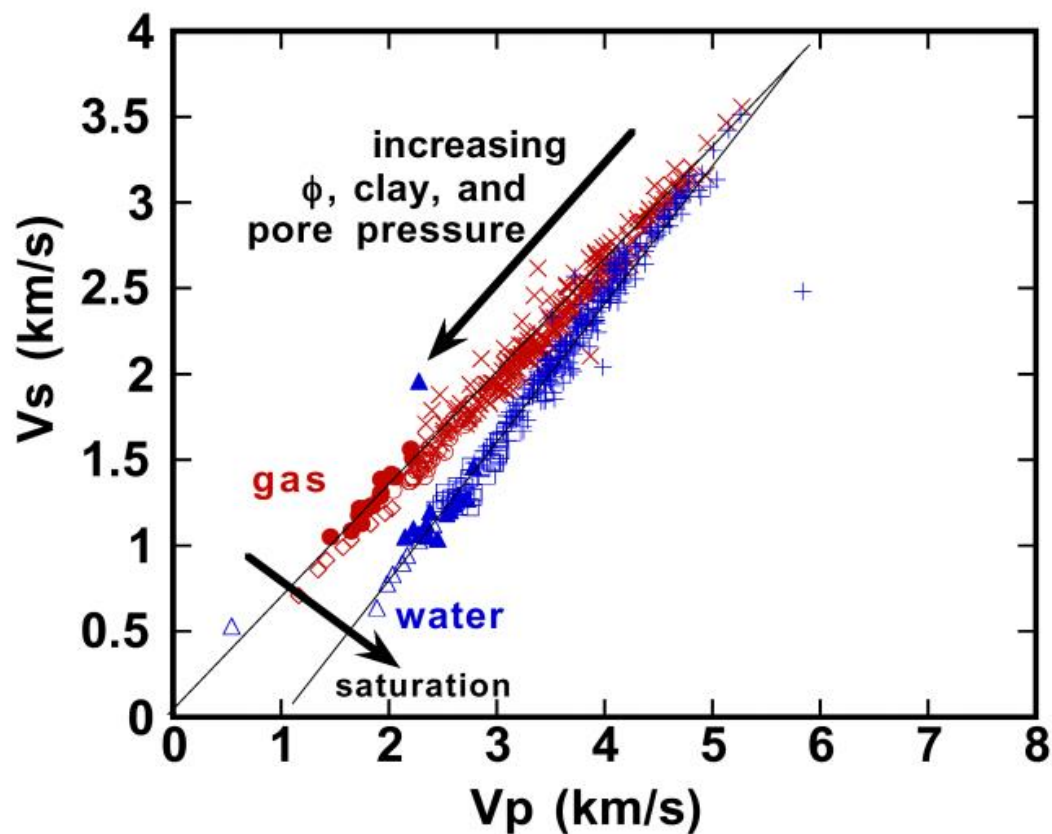


Figure 4.12 Diagrammatic crossplot of P-wave velocity against S-wave velocity [Stanford Rock Physics Laboratory]

4.8 AVO Response Classification

Rutherford and Williams's classification of the reflection coefficient curves has become the industry standard and it is associated respectively with 1970s classification of bright spot, phase reversal, and dim out. The classification was developed for reflections from hydrocarbon saturated formations. According to Rutherford and Williams's classification, the slope of the reflection coefficient curve is negative for all classes. The reflection amplitude decreases with the angle of incidence. However, the absolute amplitude can increase with angle of incidence as depicted for Class II and III AVO gas saturated anomalies. Castagna et al. (1998) found that certain Class III gas saturated anomalies can have slowly decreasing amplitudes with offset. These were named Class IV AVO anomalies (**Figure 4.13**). However, the main diagnostic feature for the Class IV anomalies is still the large amplitude associated with the hydrocarbons.

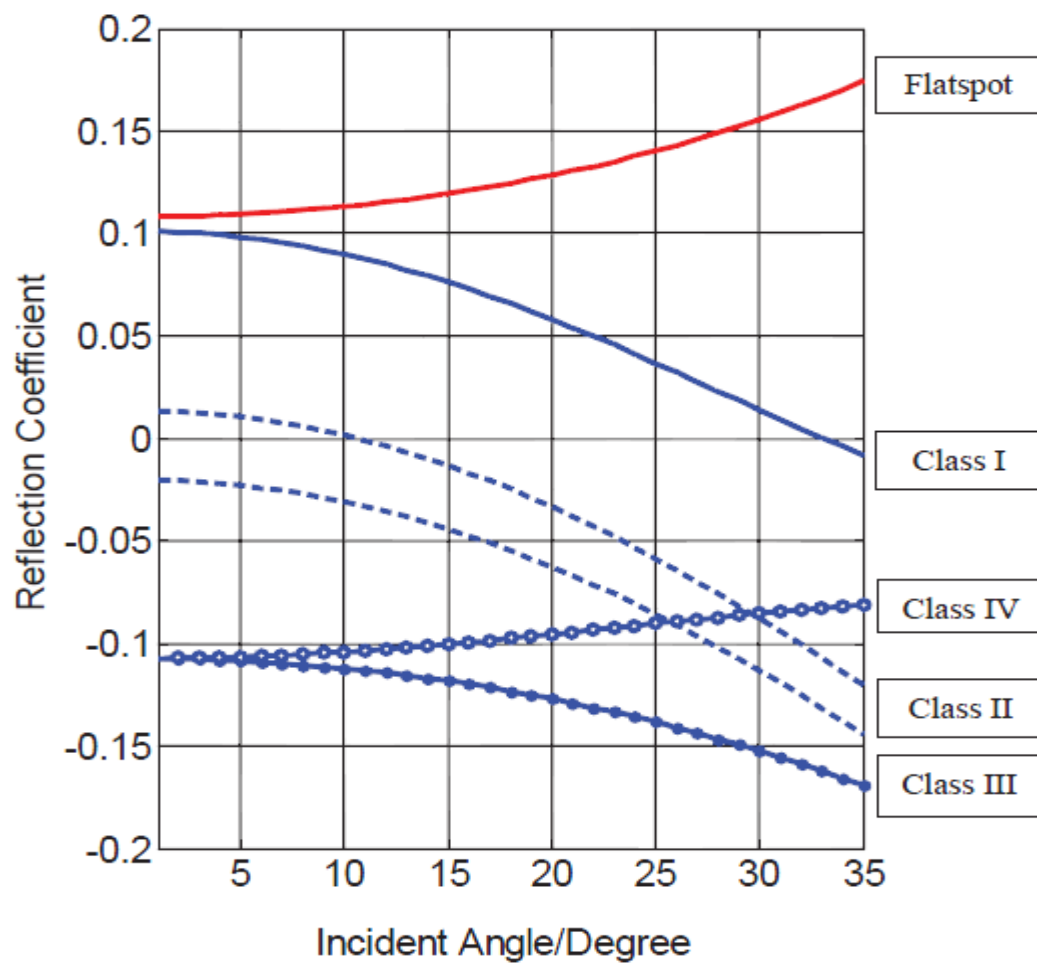


Figure 4.13 The four usual AVO classifications defined by Rutherford, et al. (1989) and Castagna, et al. (1998), and typical flatspot behaviour.

A brief description of the characteristics for each AVO class is given below, while in **Table 1** and **Figure 4.14** their characteristics are summarized.

Class I (Dim out) anomalies have the following properties:

- ❖ Amplitude decreases with increasing angle, and may reverse phase on the far angle stack
- ❖ Represents relatively hard sands with hydrocarbons.
- ❖ These sands tend to plot along the background trend in intercept-gradient cross-plots
- ❖ Amplitude on the full stack is smaller for the hydrocarbon zone than for an equivalent wet saturated zone.
- ❖ Wavelet character is peak-trough on near angle stack
- ❖ Wavelet character may or may not be peak-trough on the far angle stack.

Class II (Phase reversal) anomalies have the following properties:

- ❖ There is little indication of the gas sand on the near angle stack.
- ❖ Representing transparent sands with hydrocarbons. Often shows up as dim spots or weak negative reflectors on the seismic
- ❖ The gas sand event increases amplitude with increasing angle. This attribute is more pronounced than anticipated because of the amplitude decrease of the shale-upon-shale reflections.
- ❖ The gas sand event may or may not be evident on the full stack, depending on the far angle amplitude contribution to the stack.
- ❖ Wavelet character on the stack may or may not be trough-peak for a hydrocarbon charged thin bed.
- ❖ Wavelet character is trough-peak on the far angle stack.
- ❖ Inferences about lithology are contained in the amplitude variation with incident angle.
- ❖ AVO alone, unless carefully calibrated, cannot unambiguously distinguish a clean wet sand from a gas sand, because both have similar (increasing) behavior with offset.

Class III (Bright spot) anomalies have the following properties:

- ❖ Hydrocarbon zones are bright on the stack section and on all angle limited stacks.
- ❖ Represents relatively soft sands with high fluid sensitivity
- ❖ The hydrocarbon reflection amplitude, with respect to the background reflection amplitude, is constant or increases slightly with incident angle range. Even though the amplitude of the hydrocarbon event can decrease with angle, as suggested for the Class 4 AVO anomalies, the surrounding shale-upon-shale reflections normally decrease in amplitude with angle at a faster rate.
- ❖ Wavelet character is trough-peak on all angle stacks. This assumes that the dominant phase of the seismic wavelet is zero and the reservoir is below tuning thickness.

Class IV anomalies have the following properties:

- ❖ Mainly gas sands with low impedance
- ❖ They have negative intercept but positive gradient.
- ❖ The reflection coefficients decrease with increasing offset.

Class	Relative impedance	Quadrant	$R(0)$	G	AVO product	Amplitude Over Offset
I	High-impedance sand	4th	+	-	Negative	Decreases
II	No or low contrast	4th	+	-	Negative	Increases
IIp	No or low contrast	3rd	-	-	Positive	Decreases
III	Low impedance	3rd	-	-	Positive	Increases
IV	Low impedance	2nd	-	+	Negative	Decreases

Table 1. AVO classes, after Rutherford and Williams (1989), extended by Castagna and Smith (1994), and Ross and Kinman (1995).

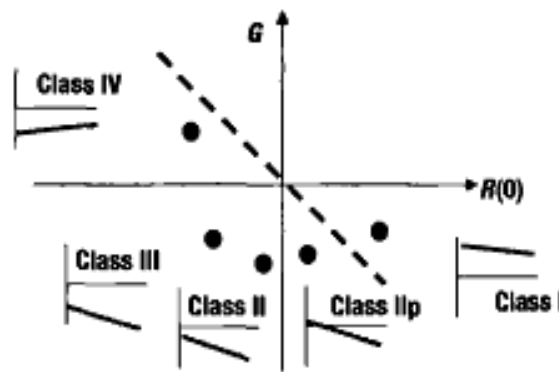


Figure 4.14 Rutherford and Williams AVO classes, originally defined for gas sands (classes I, II and III), along with the added classes IV (Castagna and Smith, 1994) and IIp (Ross and Kinman, 1995). Figure is adapted from Castagna et al. (1998).

5. Seismic Data Processing Analysis

The seismic survey is one form of geophysical survey that aims at measuring the earth's properties by means of physical principles such as magnetic, electric, gravitational, thermal, and elastic theories. It is based on the theory of elasticity and therefore tries to deduce elastic properties of materials by measuring their response to elastic disturbances called seismic waves.

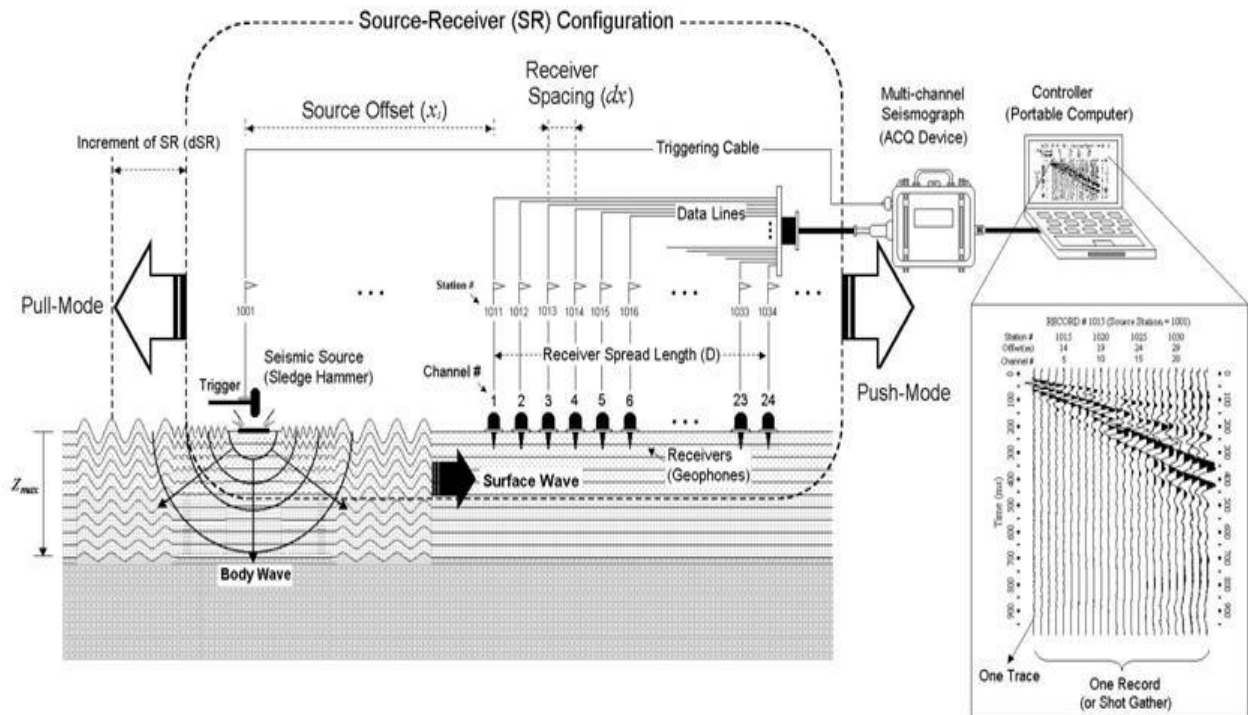


Figure 5.1 Schematic of overall field setup for a seismic survey [Park Seismic].

A seismic source, such as sledgehammer or an explosion, is used to generate seismic waves, sensed by receivers deployed along a preset geometry (called receiver array), and then recorded by a digital device called seismograph (**Figure 5.1**). Based on a typical propagation mechanism used in a seismic survey, seismic waves are grouped primarily into direct, reflected, refracted, and surface waves (**Figure 5.2**).

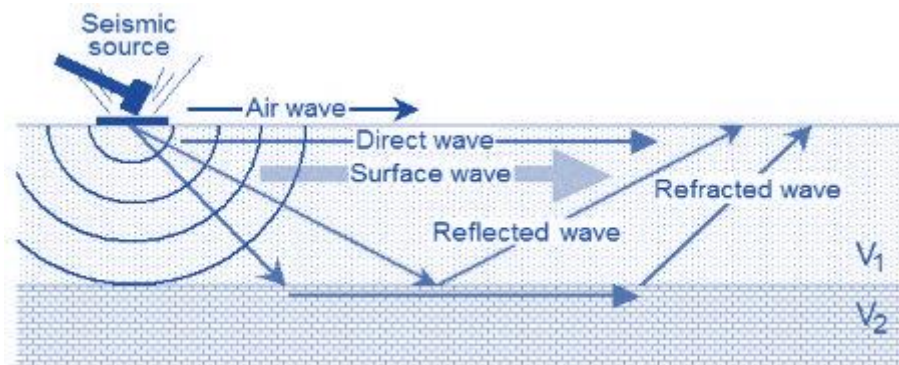


Figure 5.2 Major types of seismic waves based on propagation characteristics [Park Seismic].

There are three major types of seismic surveys: refraction, reflection, and surface-wave, depending on the specific type of waves being utilized. Each type of seismic survey utilizes a specific type of wave and its specific arrival pattern on a multichannel record (**Figure 5.3**).

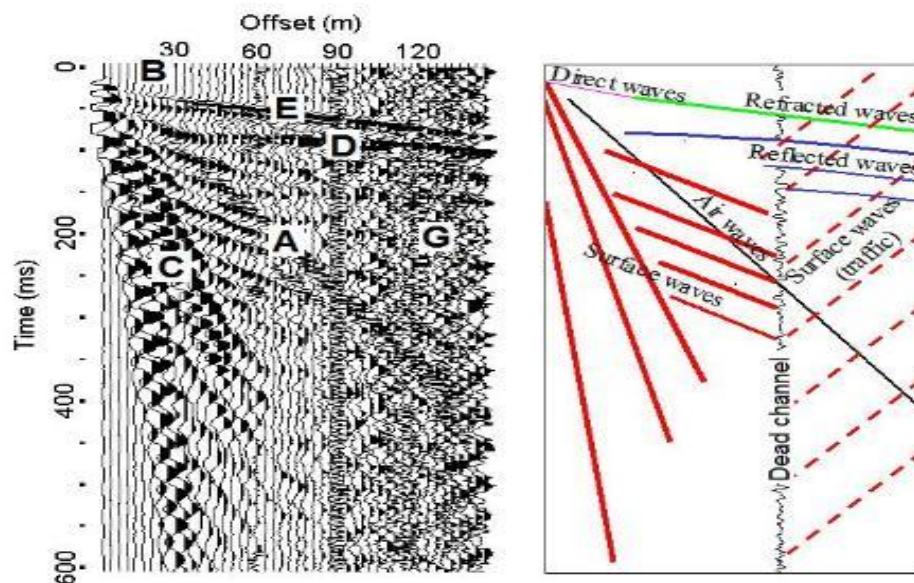


Figure 5.3 A field record and interpretation of different seismic events based on the arrival pattern [Park Seismic].

Seismic waves for the survey can be generated in two ways: actively or passively. They can be generated actively by using an impact source like a sledgehammer or passively by natural (for example, tidal motion) and cultural (for example, traffic) activities. Most of the seismic surveys historically implemented have been the active type. Seismic waves propagating within the vertical plane holding both source and receivers are also called inline waves, whereas those coming off the plane are called offline waves (**Figure 5.4**).

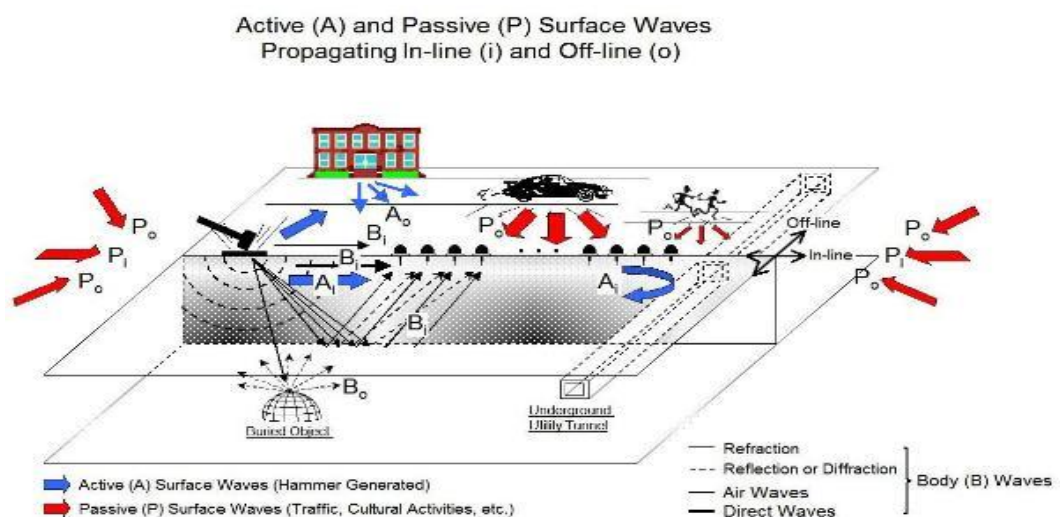


Figure 5.4 Illustration of active versus passive waves and inline versus offline waves.

Seismic signals are generated by a source (transmitter), such as an explosion, which then propagate through earth layers. Some of these signals will be reflected, refracted and lost due to attenuation as shown in **(Figure 5.2)**. At the surface, the reflected signals are then recorded by a receiver. The strength of the reflected signal depends on the impedance contrast between adjacent layers. In summary, a seismic survey analysis scenario involves collection of data by an array of receivers (geophones for land and hydrophones for marine), transmission over a narrow band channel, and storage of data for processing, and interpretation.

A seismic trace represents a combined response of a layered ground and a recording system to a seismic source wavelet. Any display of a collection of one or more seismic traces is termed a **seismogram**. Assuming that the pulse shape remains unchanged as it propagates through such a layered ground, the resultant seismic trace may be regarded as the convolution of the input impulse with a time series known as a **reflectivity function**, which is composed of **spikes** (delta functions). Each spike has an amplitude related to the reflection coefficient at a layer boundary and a traveltime equivalent to the two-way reflection time from the surface to that boundary.

Furthermore, the reflection time series represents the impulse response of the layered ground, which is basically the output for a spike input. Since the source wavelet has a finite length, individual reflections from closely-spaced boundaries may overlap in time on the resultant seismogram (seismic section). **Figure 5.5** represents a typical seismic convolution model.

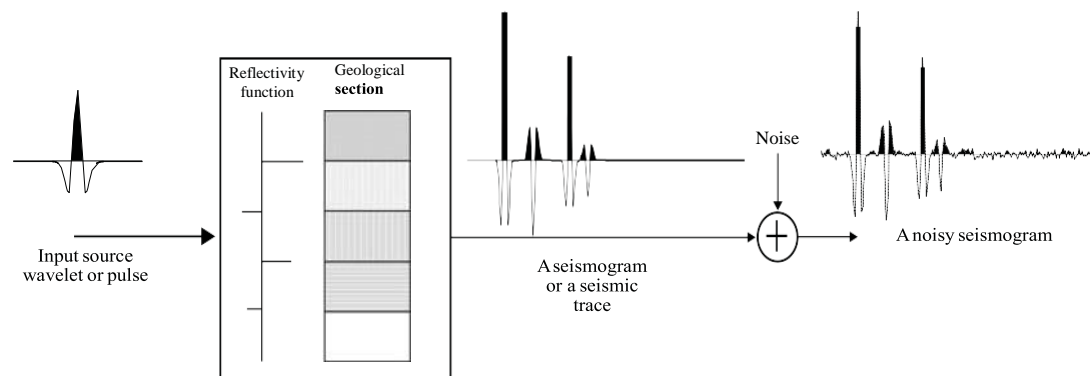


Figure 5.5 Convolution seismic data model. A seismic pulse is convolved with the reflection coefficient log (reflectivity function) to get a seismic trace. The reflection coefficient log is related to the geological section of the subsurface through the reflection coefficient of each geological boundary and the two-way travel time [Mousa, Al-Shuhail, 2011].

5.1 Prinos Basin Geological Model Representation

The synthetic dataset that will be analyzed in this thesis consists of a hypothetical two-dimensional (2-D) land line using the geological setting of Prinos basin. The construction of the layer's structure below the subsurface of Prinos basin, along with the synthetic seismic dataset were based on the synthetic data simulator algorithm that was described on chapter 3. The whole procedure was implemented in Matlab environment and will be more explicitly described, step by step, below.

Geological model creation

As a first step, the geological model under examination needs to be defined. In **Figure 5.6** a 3-D representation of Prinos basin, along with its stratigraphy column is presented [Michelakis 2010]. Due to the high complexity of the 3-D model, only a single plan was chosen for the implementation of the seismic survey. Specifically, a plan of the model with East-West orientation was extracted, as shown in **Figure 5.7-Figure 5.8**.

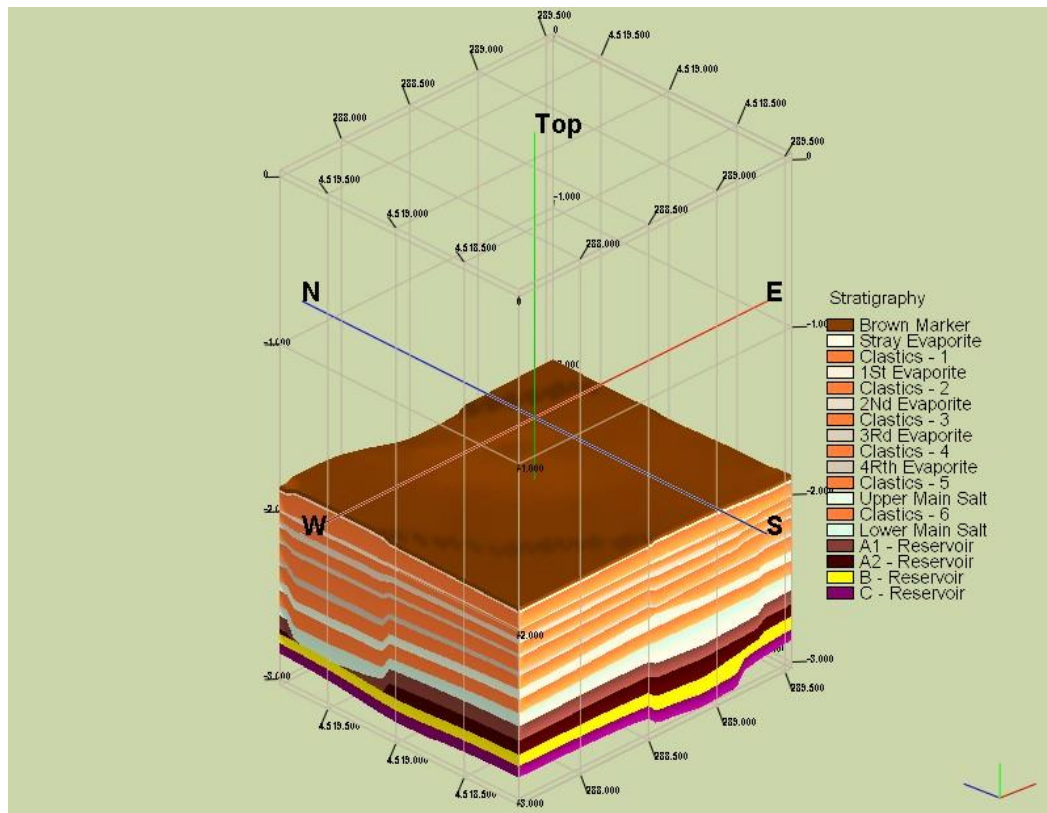


Figure 5.6 3-D geological model representation of Prinos basin [Michelakis 2010].

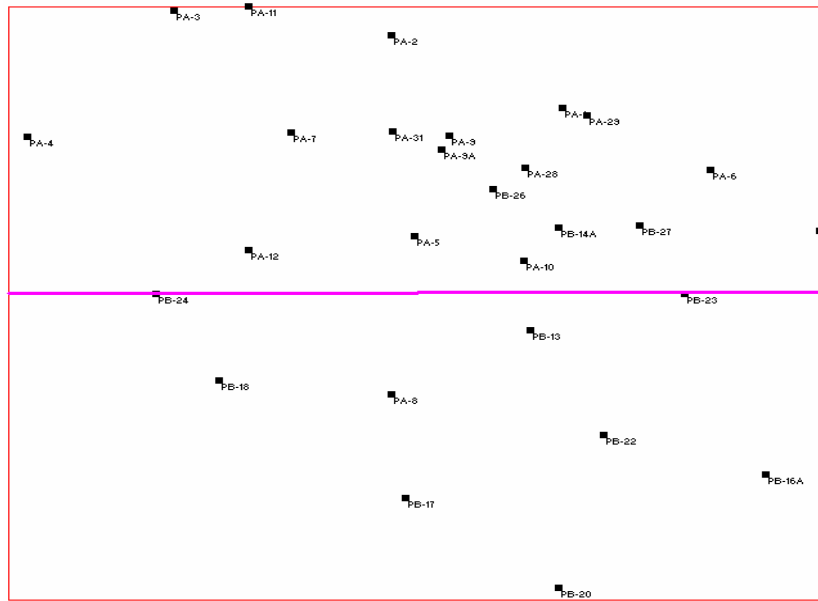


Figure 5.7 Geological plan of Prinos basin with East-West orientation.

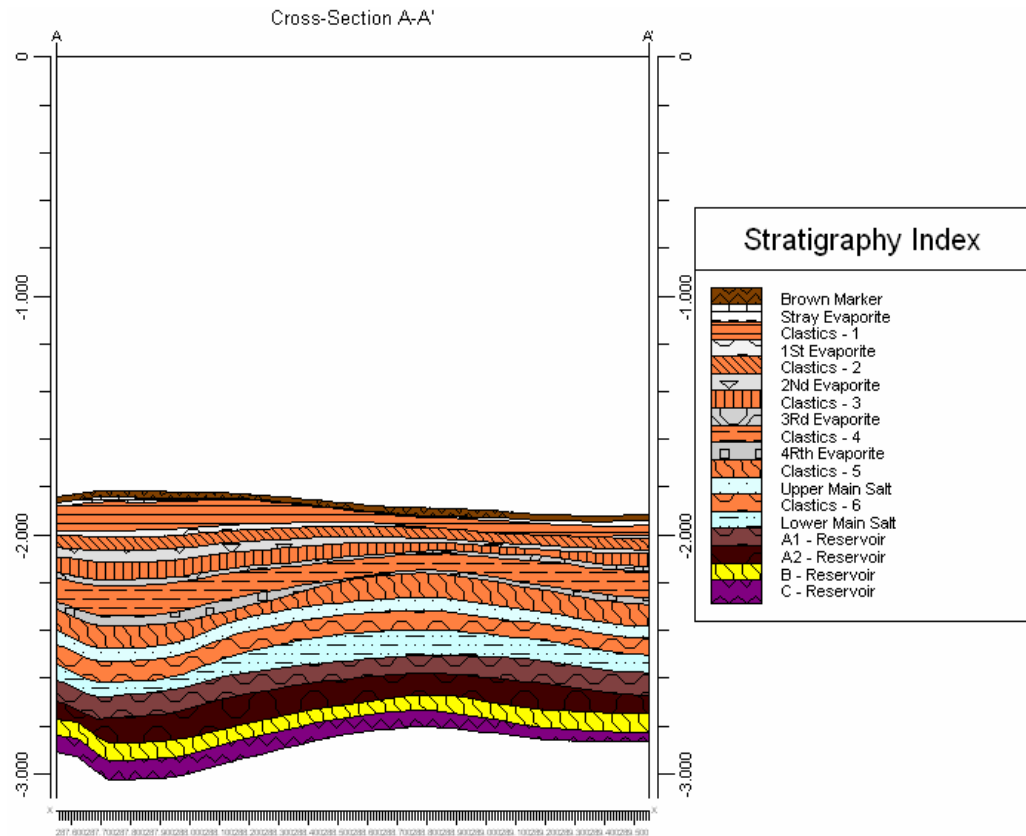


Figure 5.8 2-D representation of the East-West geological plan.

In order to digitize the 2-D geological plan shown in **Figure 5.8**, a function was created in Matlab. This function was called **digitize**. By loading the picture and providing the limits of both X and Y axis (in this case Y=3100m, X=1900m), a picking procedure would allow the user to define the coordinates for each picked point, by extension for each layer. In **Figure 5.9** the picking procedure is presented for some random layers.

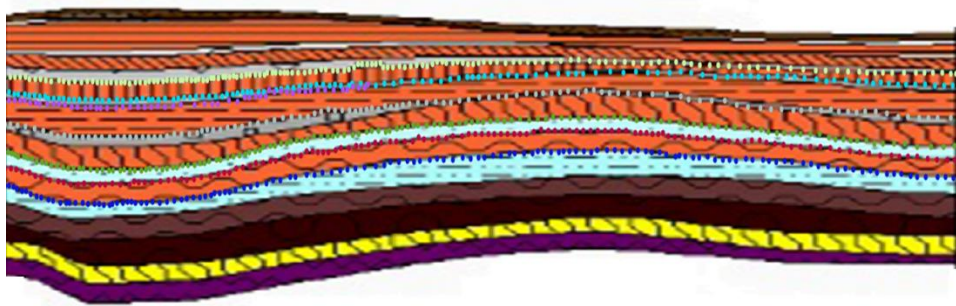


Figure 5.9 Picking procedure for the layers' digitization.

After applying the picking procedure, the coordinates of each layer are interpolated using the “**spline**” function with respect to the X axis, in order to smoothen the results and avoid the randomness related to the picked values. The result for a spline interval of 5 m is presented in **Figure 5.10**.

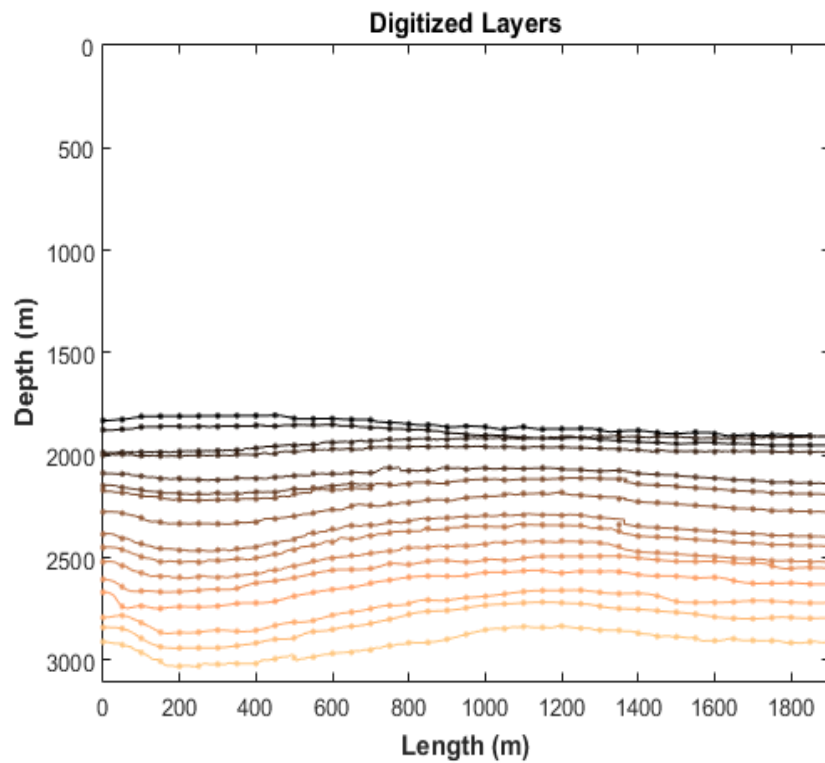


Figure 5.10 Digitized layers after applying spline procedure with spline interval equal to 5m.

The layers are also presented in a more comprehensible form, using the “**area**” function of Matlab (**Figure 5.11**).

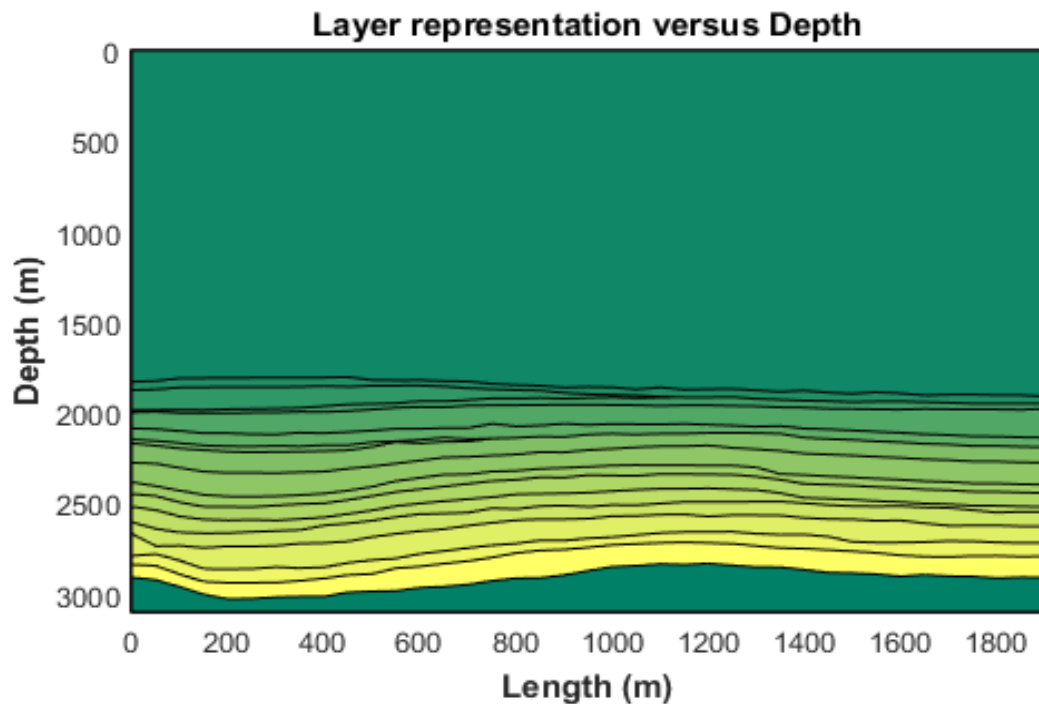


Figure 5.11 Layer representation versus depth using the “**area**” function.

The geological model presented so far is still of high complexity but it can be further simplified, since most of the top formations shown in **Figure 5.11** share the same geological properties. Specifically, the top formations are, mainly, evaporites that act as the “**cap-rock**” of the reservoir with similar geophysical attributes. On the other hand, the last five layers constitute the basic layers of the Prinos basin reservoir. As a result, the top layers were considered as one simple layer of evaporites, the last four layers were digitized and inserted to the simulator separately, while the last layer was considered as the base of the reservoir. Summarizing, the final model, as implemented in the simulator, consists of six basic formations: Evaporite formation, Sand A1, Sand A2, Sand B, Sand C and the Base formation (**Figure 5.12**). The overall evaluation of the formation of Prinos basin, as derived from a well resistivity log analysis is presented in **Table 2** [Fronimos 1998].

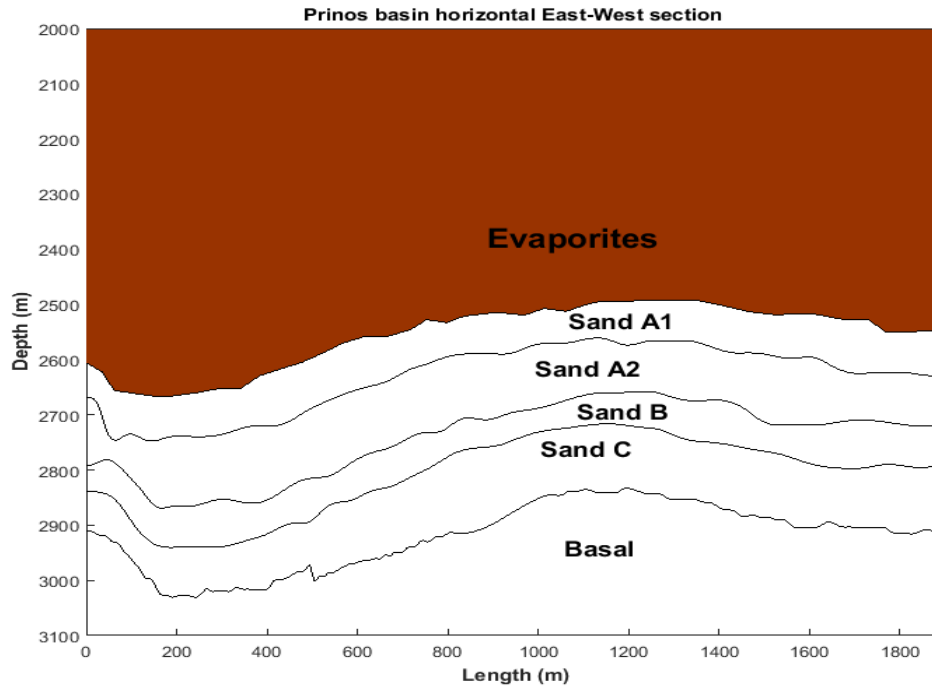


Figure 5.12 The simplified geological model of Prinos' basin East-West plan. The model consists of six formations, Evaporites, sand A1, sand A2, sand B, sand C and the Basal formation.

Horizon	Rt	Rxo	ϕ (%)	F	Sw(%)	So(%)	Sxo(%)	Sor(%)	di
Sand A1	3,6	1,8	17,0	28,0	39,4	60,6	59,8	40,2	50
Sand A2	4,5	1,0	19,5	20,8	30,4	69,6	69,2	30,7	35
Sand B	3,5	1,4	18,0	24,7	37,6	62,4	63,7	36,3	30
Sand C	3,6	0,9	19,5	20,8	34,0	66,0	72,9	27,1	25

Table 2. Summary of well log analysis for Prinos basin [Fronimos 1998], where Rt=formation's electrical resistivity, Rxo= resistivity of flushed zone, ϕ =porosity, F=formation's factor, Sw=water saturation, So=oil saturation, Sxo=water saturation of flushed zone, Sor=oil saturation of flushed zone and di=diameter of flushed zone.

A brief analysis of the results presented in **Table 2** is carried out below:

Sand A1 displays the lowest porosity value and the lowest oil saturation value (along the other reservoir formations), 17.0% and 60.6% respectively. At the same time, it shows the lowest hydrocarbon mobility, indicating a formation with low permeability. Finally, the flushed zone has the biggest diameter compared to the other formations. The above results indicate a non-homogenous transitional formation from the cap-rock to the reservoir. This theory testifies the decreased mobility of the hydrocarbons, the low porosity and the great infiltration zone.

Sand A2 displays the highest porosity value and at the same time the greatest oil saturation value (along the other reservoir layers), 19.5% and 69.65% respectively. The hydrocarbon mobility level is good enough (saturation level inside the flushed zone 30.7%) and the diameter of the flushed zone is the greatest among the other formations. It should also be pointed out that it shows the highest value of electrical resistivity.

Sand B displays a porosity value equals to 18.0%. The hydrocarbon saturation level (62.4%) is the lowest among the rest of the reservoir formations. The hydrocarbon mobility is also the lowest among the rest of the formations, while the diameter of the flushed zone is 30 in. The above information confirms that formation Sand B is slightly more compact than Sand A2, while this difference becomes even more pronounced when Sand B is compared to Sand C.

Sand C displays the same porosity value with Sand A2 (19,5%) and oil saturation slightly lower (66,0% over 69,6%). The characteristic that differentiates this formation from the others, is the very high permeability and mobility ratio of the hydrocarbons. The oil saturation inside the infiltration zone along with the diameter of the infiltration zone are the lowest ones with values (27.1%) and (25in) respectively.

5.2 Velocity and Bulk Density Estimation

The bulk density and velocity of the Prinos basin can be sufficiently approximated using cross-property relations. Associations between electrical conductivity and seismic velocity, stiffness moduli, and density can be obtained by expressing the porosity in terms of those properties [Carcione, Ursin & Nordskog 2007]. As an example, the physical properties of three different mediums given in **Table 3** were examined with the velocity/porosity relations represented in **Figure 5.13** and **Figure 5.14**, corresponding to shale and sandstone, respectively [Carcione, Ursin & Nordskog 2007].

Medium	K (Gpa)	μ (Gpa)	ρ (g/cm ³)
Shale grain	25	20	2.6
Sand grain	39	40	2.6
Brine	2.25	0	1.0

Table 3. Material properties of a North Sea Well. K and μ are the bulk and shear moduli respectively, while ρ is the medium's density.

The plots show that the data follow closely Gassmann's velocity model in both shaly and sandy sections. As a result the Gassmann's velocity curve was considered to be a reliable and accurate tool and was used for the estimation of the matrix velocity V_p for Prino's basin. In **Figure 5.15** the matrix velocity of the shale and sandstone is given as a function of porosity, where in **Figure 5.23** the curves of **Geometric**, **Raymer** and **Gassmann** were digitized and fitted in first order polynomials.

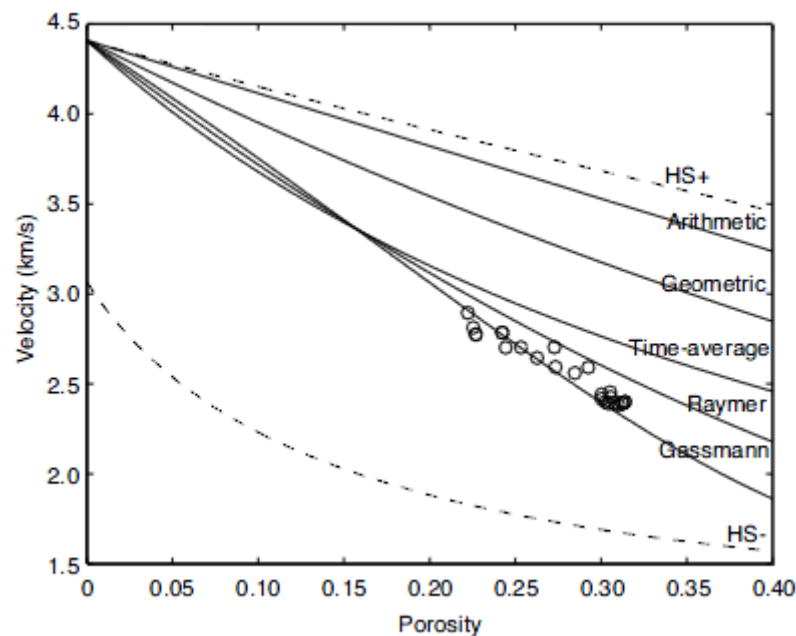


Figure 5.13 Different models of the P-wave velocity as a function of porosity and real data (circles), corresponding to the shaly section of the well.

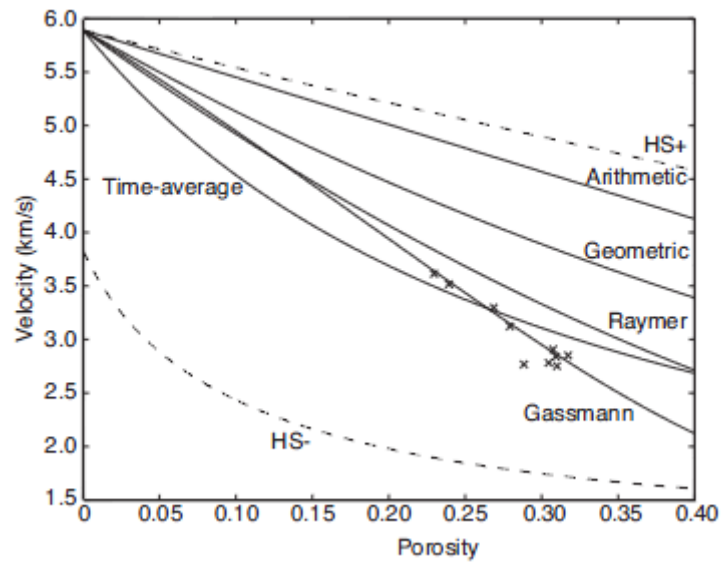


Figure 5.14 Different models of the P-wave velocity as a function of porosity and real data (crosses), corresponding to the sandy section of the well.

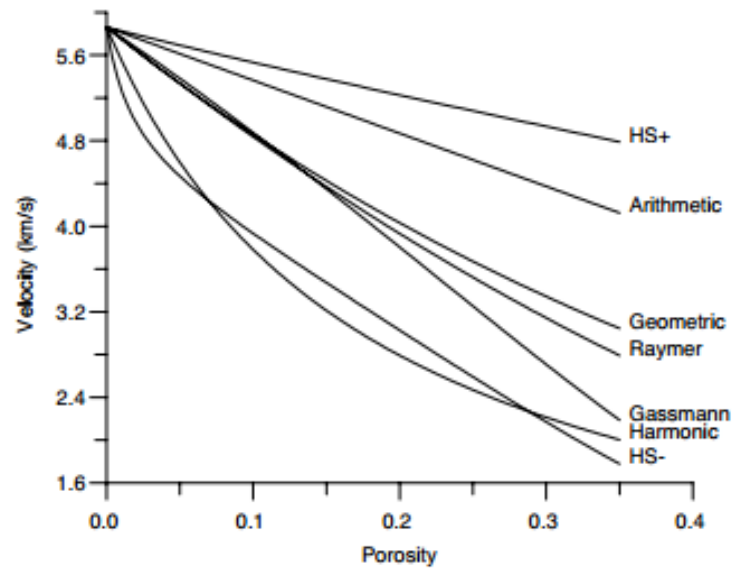


Figure 5.15 P-wave velocity as a function of porosity corresponding to different models of the reservoir (sandstone saturated with oil). The harmonic average is the time-average equation.

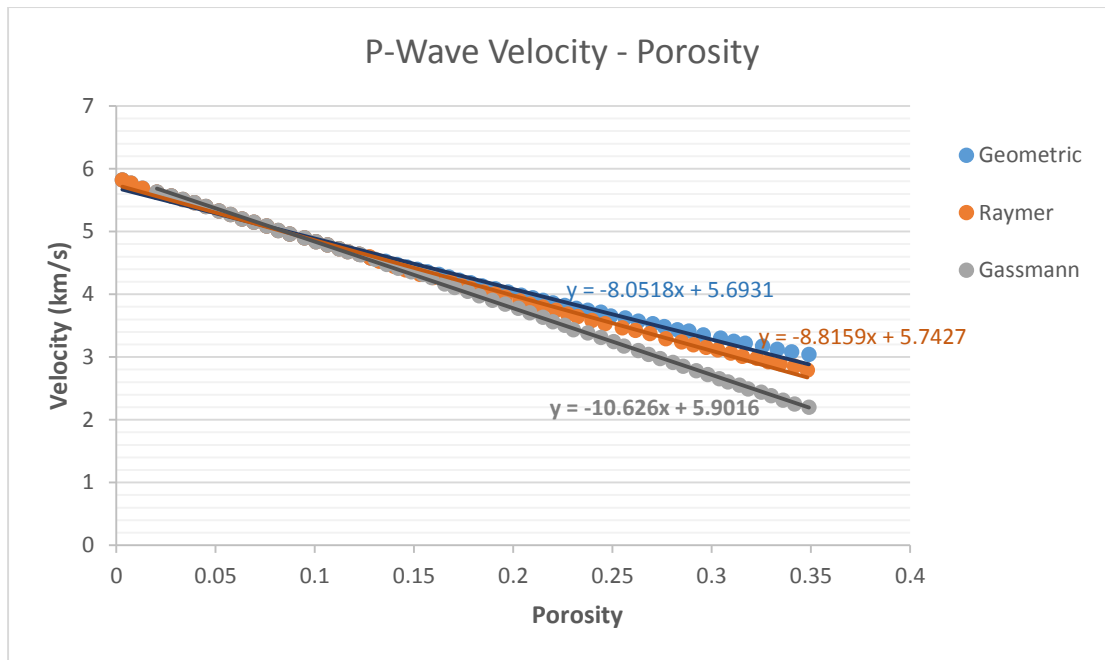


Figure 5.16 P-wave velocity as a function of porosity using Geometric, Raymer and Gassmann curve fitting.

The matrix velocity was calculated for each of the three linear equations respectively as shown in **Table 4**. As mentioned above, though, the Gassmann's equation $V_p = -10.6 \cdot \phi + 5.9$ is considered the most accurate one and only the specific results were kept for the rest of the analysis.

Formation	Porosity (%)	Gassmann Velocity (km/	Raymer Velocity (km	Geometric Velocity (km
Sand A1	0.17	4.14	4.244	4.324
Sand A2	0.195	3.846	4.024	4.123
Sand B	0.18	3.989	4.156	4.244
Sand C	0.195	3.83	4.024	4.123

Table 4. P-Velocity estimation using Gassmann's, Raymer's and Geometric curves.

Within a sequence of fully brine-saturated rocks of similar age and composition, often a first order linear relationship between V_p and V_s can be assumed, without lithologic differentiation. Many different empirical relationships between P-wave and S-wave velocity have been derived so far, but we will examine three of the most popular ones. Castagna et al (1985) derived a simple empirical relationship, called the “**mudrock line**”, which can be written:

$$\begin{aligned}
 \text{Mudrock line:} & \quad V_s = 0.86V_p - 1.17 \\
 \text{Castagna et al. (1993):} & \quad V_s = 0.80V_p - 0.86 \\
 \text{Han (1986):} & \quad V_s = 0.79V_p - 0.79
 \end{aligned}
 \tag{5.1}$$

where velocity is in km/s.

The above linear approximations are fitted to observations and presented graphically in **Figure 5.17**.

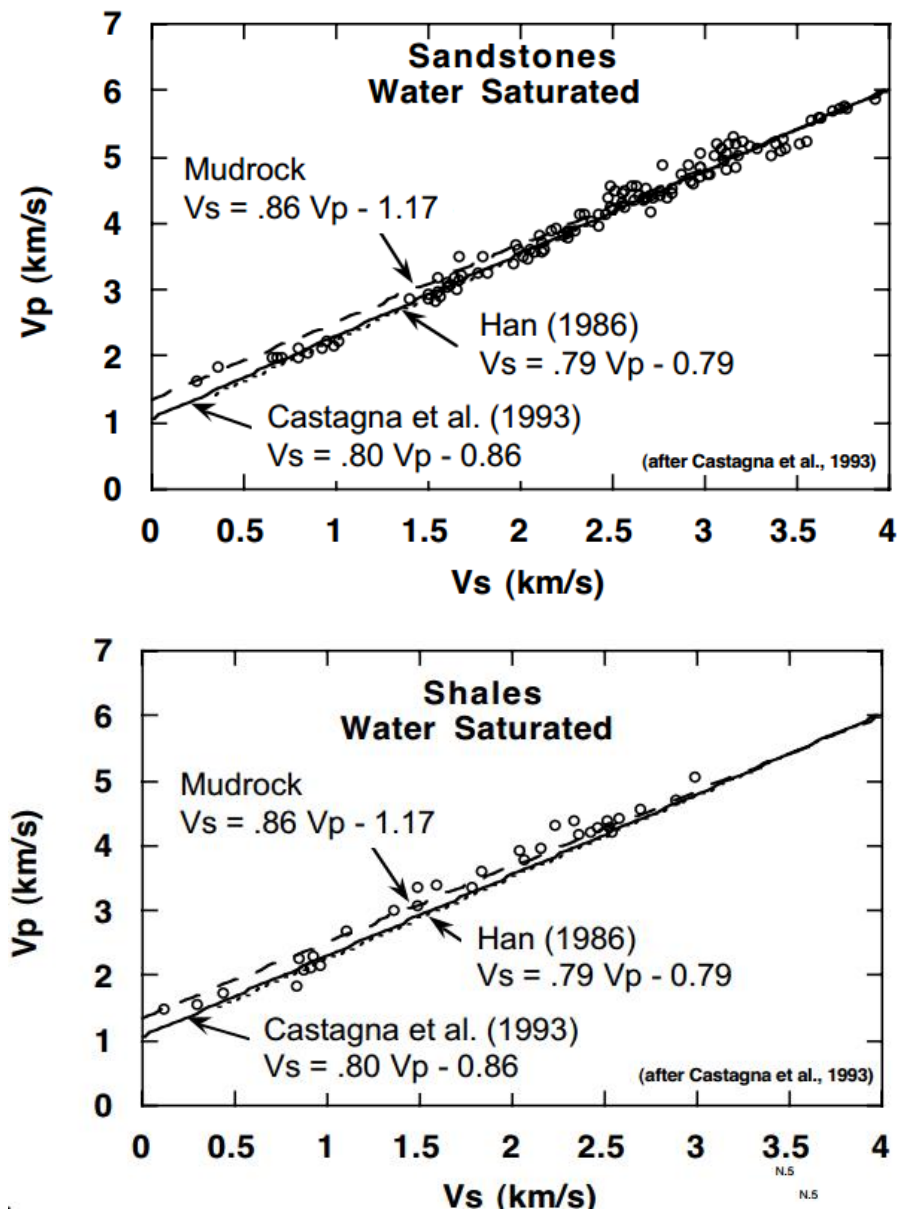


Figure 5.17 V_p versus V_s crossplotting from shale and sandstone formations [Castagna, Batzlek and Kan, 1993].

Using the linear equations presented above, the shear velocities can be approximated as:

Formation	P-Velocity (km/s)	S-Velocity (km/s) [Mudrock]	S-Velocity (km/s) [Castagna]	S-Velocity (km/s) [Han]
Sand A1	4.14	2.396	2.452	2.481
Sand A2	3.846	2.143	2.2168	2.248
Sand B	3.989	2.266	2.3312	2.361
Sand C	3.83	2.128	2.204	2.236

Table 5. Shear velocity approximation using Mudrock, Castagna's and Han's empirical equations.

The results from the mudrock line approximation are considered more accurate, so the final values for the shear velocity are those derived from the Lindseth approximation.

Finally, for the approximation of the medium's density two different approaches are tested. Gardner's equation can approximate the density from the matrix Velocity V_p as:

$$\rho = \alpha V_p^b \quad (5.2)$$

Where ρ is the bulk density in g/cc, V_p is the P-wave velocity in ft/s, $a=0.23$ and $b=0.25$. This empirical relationship is based on field and laboratory measurements of saturated sedimentary rocks from a wide variety of basins and depths.

Lindseth (1979), also, proposed an empirical relation between acoustic impedance and density which is used to extract the density from the reflectivity:

$$V_p = 0.308\rho V_p + 3460 \quad (5.3)$$

Where ρ is the bulk density in g/cc, V_p is the P-wave velocity in ft/s.

Using both equations (5.2) and (5.3) we get the following density values (Table 6):

Formation	P-Velocity (ft/s)	Density (g/cc) [Gardner]	Density (g/cc) [Lindseth]
Sand A1	13583	2.483	2.420
Sand A2	12631	2.438	2.357
Sand B	13091	2.460	2.389
Sand C	12566	2.435	2.353

Table 6. Density estimation from P-velocity using Gardner and Lindseth approximations.

The Lindseth equation is considered more accurate, so the final values for the bulk density are those derived from the Lindseth approximation.

All the velocity approximations used so far are accurate only for water or brine saturated sands. However, the scope of this thesis is the detection of gas in the sandstone reservoir of Prinos. In order to introduce gas in the synthetic data, the first layer of the reservoir is considered to be 50% gas saturated. According to *Domenico (1974)*, only a small amount of gas in the pore space will produce a large decrease of velocity (**Figure 5.19a**) and a large change in reflectivity (**Figure 5.19b**). Thus, for the reservoir of Prinos with average depth ≈ 3 km, the red dashed curve shown in **Figure 5.19a**, can give a good estimation of the P-wave velocity drop for a 50% gas saturation. The curve was fitted in a 3rd order polynomial, as shown in **Figure 5.19**, giving a mathematical relationship between the gas saturation and the P-wave velocity drop for our model. Taking the above relationship one step further, the curve was plotted again, but this time the velocity drop was expressed as a percentage ratio, as shown in **Figure 5.20**. Hence, judging from **Figure 5.20**, for a 50% gas saturation the P-wave velocity is expected to drop about 8%. Based on the above assumption, the P-wave velocity of the first layer of the reservoir was reduced from 4140 m/s to 3809 m/s.

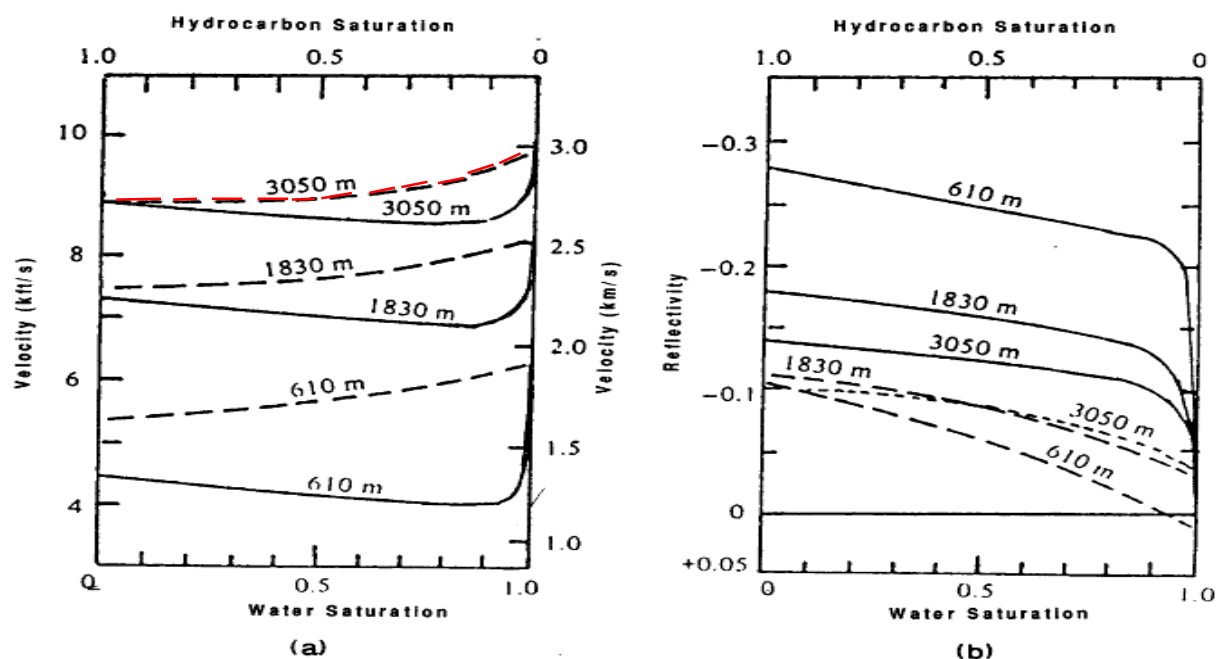


Figure 5.18 Effect of gas/water or oil/water saturation on velocity. Solid curves are for gas, dashed for oil. a) P-wave velocity versus saturation and b) reflection coefficient for gas/oil sands overlain by shale. [Sheriff and Geldart, 1995]

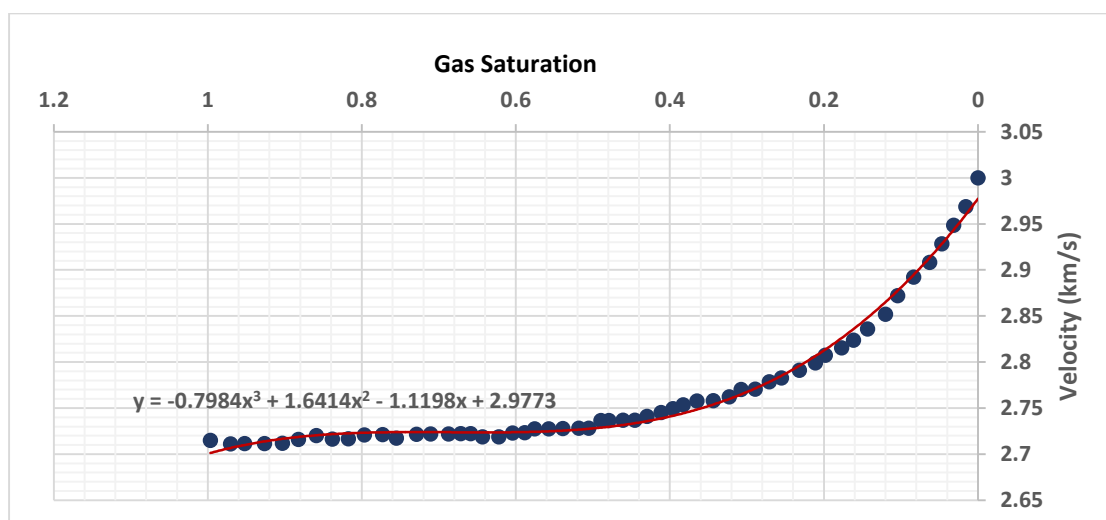


Figure 5.19 P-wave velocity versus gas saturation at 3050 m.

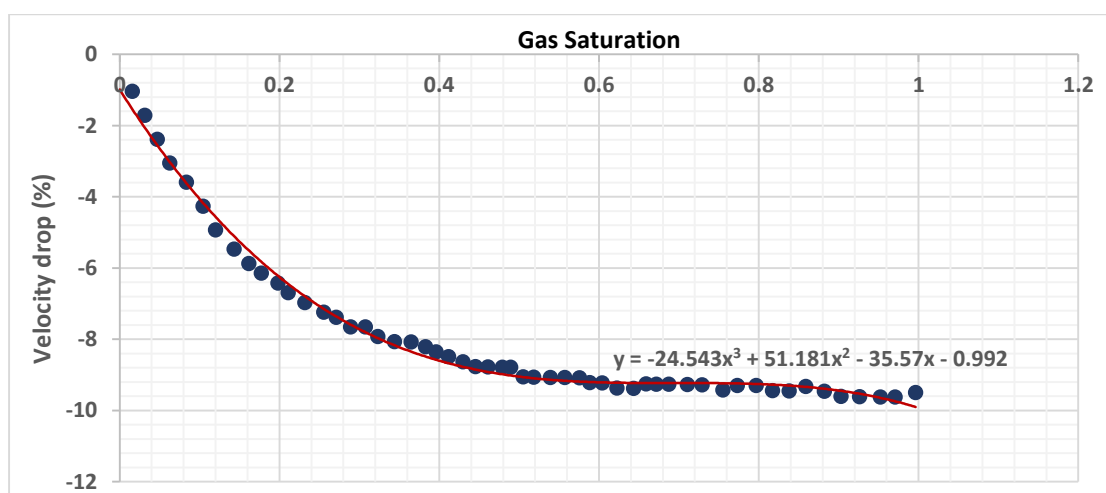


Figure 5.20 Percentage P-wave velocity drop versus gas saturation at 3050m.

Now, as regards the shear waves, they are almost insensitive to a rock's fluid content. Shear-wave velocity remain virtually unchanged whether the formation contains gas, oil or water. In other words, the amount of gas and the mode of gas saturation in the pore space dramatically affects the P-wave velocity, but not the S-wave velocity, as shown in **Figure 5.21**. So, shear wave velocity for the gas saturated layer remained 2396 m/s.

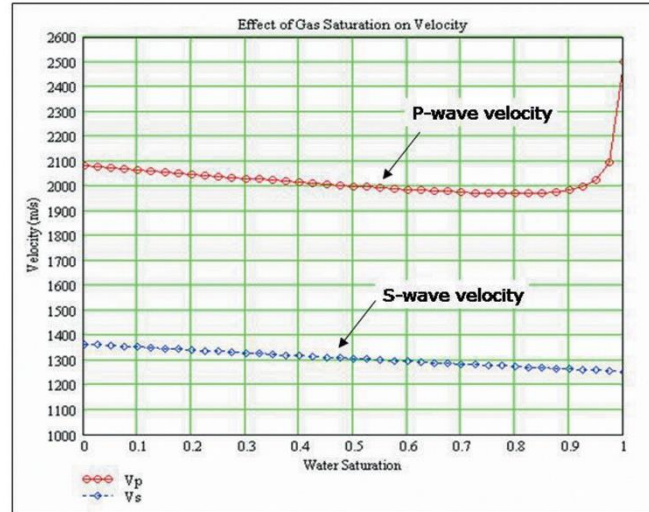


Figure 5.21 Gas saturation effect on P-wave and S-wave velocity. [Russell B. & Hampson D., 2006]

Finally, the density for the gas saturated layer was calculated with the use of the Lindseth equation (5.3) and derived 2.238 kg/m³.

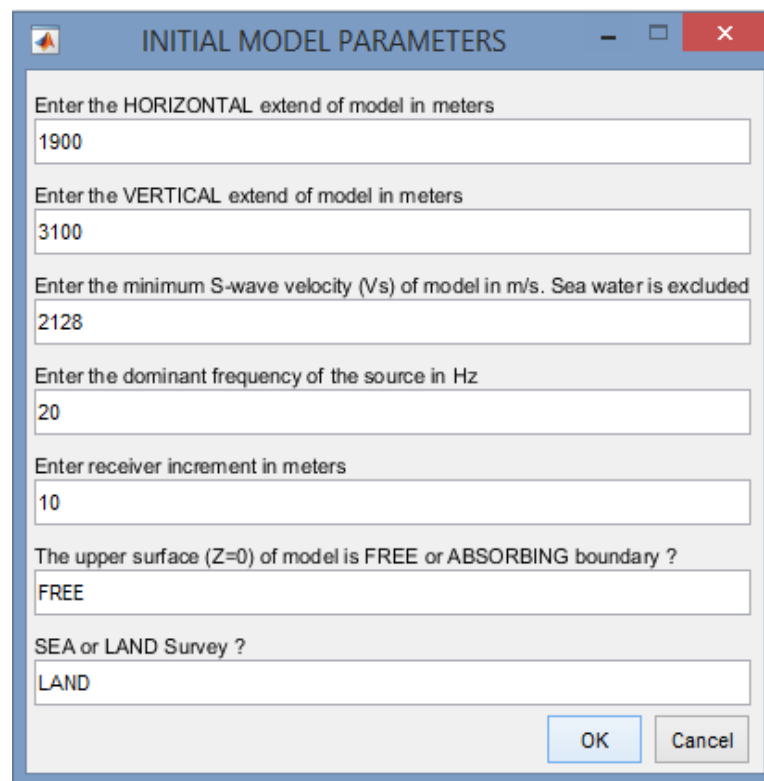
The final properties for each layer of the model are summarized in **Table 7**.

Formation	P-Velocity (m/s)	S-Velocity (m/s)	Density (g/cc)
Sand A1	3809	2396	2.238
Sand A2	3846	2143	2.357
Sand B	3989	2266	2.389
Sand C	3830	2128	2.353

Table 7. Elastic parameters for the 4-layer medium.

5.3 Synthetic Seismic Data Acquisition

The synthetic seismic dataset's construction was based on the synthetic data simulator which was implemented in Matlab by the Applied Geophysics Laboratory of the Technical University of Crete. The algorithm, as described in chapter 3, can simulate the propagation of seismic waves (P-SV) in two dimensions, using the finite differences method. Firstly, the function **PSV_SYNTHETICS_VER10** was called and the option **CREATE MODEL** was chosen in order to create the seismic survey. The simulator was initiated using the values shown in **Figure 5.22**. The horizontal extend of the model is 1.9 km, the depth of the section is 3.1 km, the minimum shear velocity is 2128 m/s as shown earlier in **Table 7**, the source's frequency was considered to be 20 Hz and the receiver's increment was set to 10 m. Furthermore, the upper surface of the model was considered as a free boundary and the whole survey was considered to be a land survey.



A screenshot of a MATLAB dialog box titled "INITIAL MODEL PARAMETERS". The dialog box contains several input fields and a dropdown menu. The fields are labeled as follows: "Enter the HORIZONTAL extend of model in meters" (value: 1900), "Enter the VERTICAL extend of model in meters" (value: 3100), "Enter the minimum S-wave velocity (Vs) of model in m/s. Sea water is excluded" (value: 2128), "Enter the dominant frequency of the source in Hz" (value: 20), "Enter receiver increment in meters" (value: 10), "The upper surface (Z=0) of model is FREE or ABSORBING boundary ?" (value: FREE), and "SEA or LAND Survey ?" (value: LAND). At the bottom right, there are "OK" and "Cancel" buttons.

Parameter	Value
HORIZONTAL extend of model in meters	1900
VERTICAL extend of model in meters	3100
minimum S-wave velocity (Vs) of model in m/s	2128
dominant frequency of the source in Hz	20
receiver increment in meters	10
upper surface (Z=0) boundary	FREE
Survey type	LAND

Figure 5.22 Initial model parameters.

In order to avoid any kind of stability or numeric dispersion errors when solving the differential wave equation with the finite difference method, the following constraints should be applied:

- For the grid's dimensions, the following calculation took place:

$$Dh = \frac{a_{\min}}{15 \cdot f_{\max}} = \frac{2128}{15 \cdot 20} \approx 7.1 \quad (5.4)$$

By taking into account the receiver's interval, the final grid size was derived as:

$$Grid = \frac{\Delta x}{\text{ceil}\left(\frac{\Delta x}{Dh}\right)} = \frac{10}{\text{ceil}\left(\frac{10}{7.1}\right)} = \frac{10}{2} = 5 \quad (5.5)$$

So the final grid size is set to 5 m. It is obvious at this point that the higher the frequency of the source, the smallest the grid size and, as a result, the higher the complexity of the simulation would be.

- For the system's stability, the following condition should be met:

$$\frac{\Delta t}{Grid} \cdot a_{\max} \leq \frac{2}{3} \Rightarrow \Delta t \leq \frac{2}{3} \cdot \frac{Grid}{a_{\max}} \quad (5.6)$$

Where a_{\max} is the maximum P-velocity 4750 m/s and Δx is the receiver's increment 10 m, so the above condition is translated to:

$$\Delta t \leq \frac{2}{3} \cdot \frac{5}{4750} \Rightarrow \Delta t \leq 7 \cdot 10^{-4} s$$

- For the numeric dispersion (the change of wave's propagation velocity with frequency), the following condition should be met:

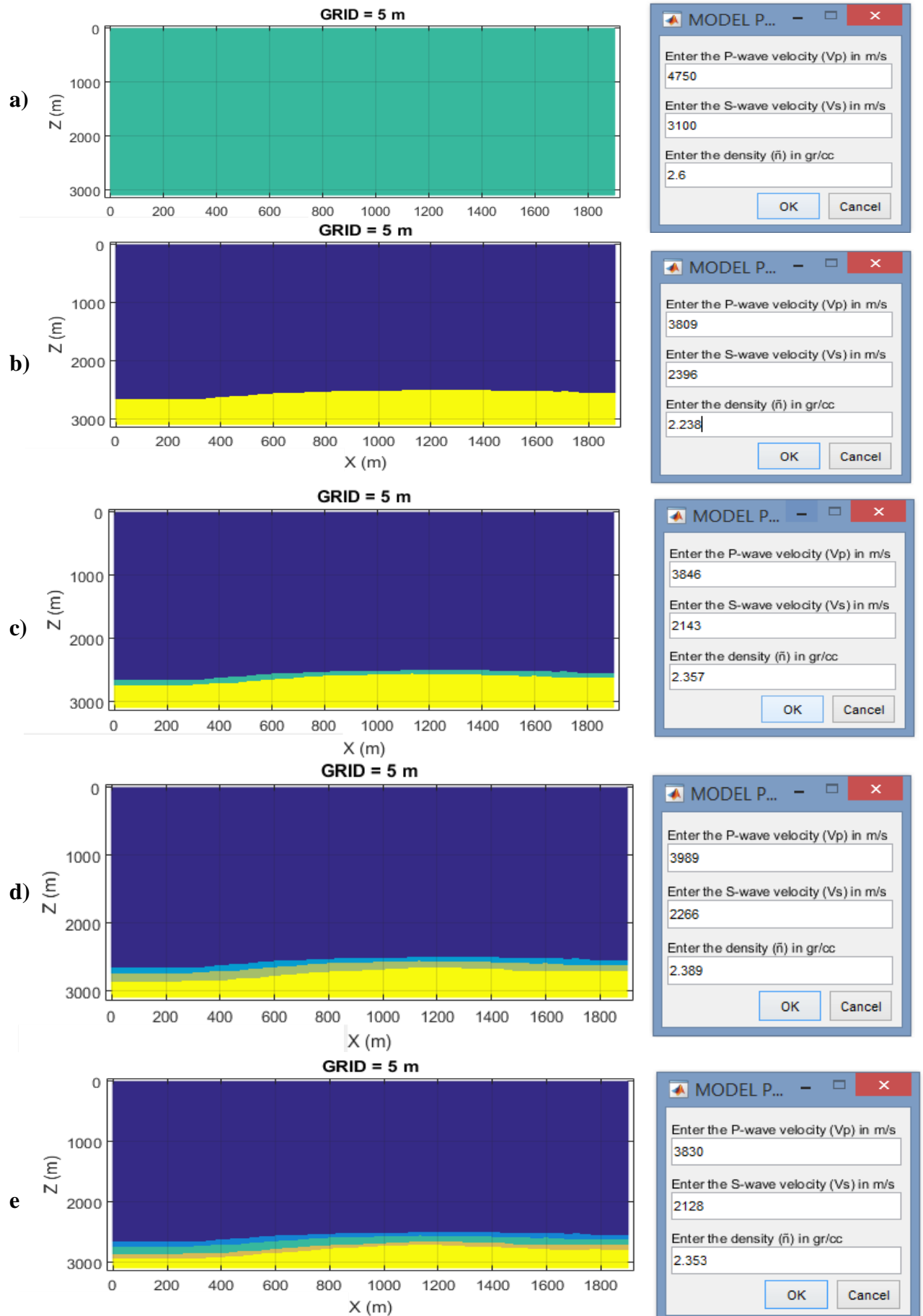
$$\frac{\lambda_{\min}}{Grid} > 5 \quad (5.7)$$

Where $\lambda_{\min} = \frac{a_{\min}}{f_{\max}}$, a_{\min} is the minimum S-velocity 2128 m/s and f_{\max} is the dominant

frequency of the source 20Hz, so the condition is fulfilled as:

$$\frac{\lambda_{\min}}{Grid} = \frac{2128 / 20}{5} = 21.28 > 5$$

As a next step, the geometry and the properties of each layer should be introduced to the simulator. The formation above the reservoir was considered as a thick layer of evaporites with $V_p=4750$ m/s, $V_s=3100$ m/s and $\rho=2.6$ g/cc which acts as a cap-rock. Below the reservoir there is another evaporite formation with $V_p=4750$ m/s, $V_s=2900$ m/s and $\rho=2.7$ g/cc which acts as the base of the reservoir. The geophysical properties of the reservoir between those two formations were calculated in the previous chapter and are introduced to the simulator one by one as shown in **Figure 5.23**.



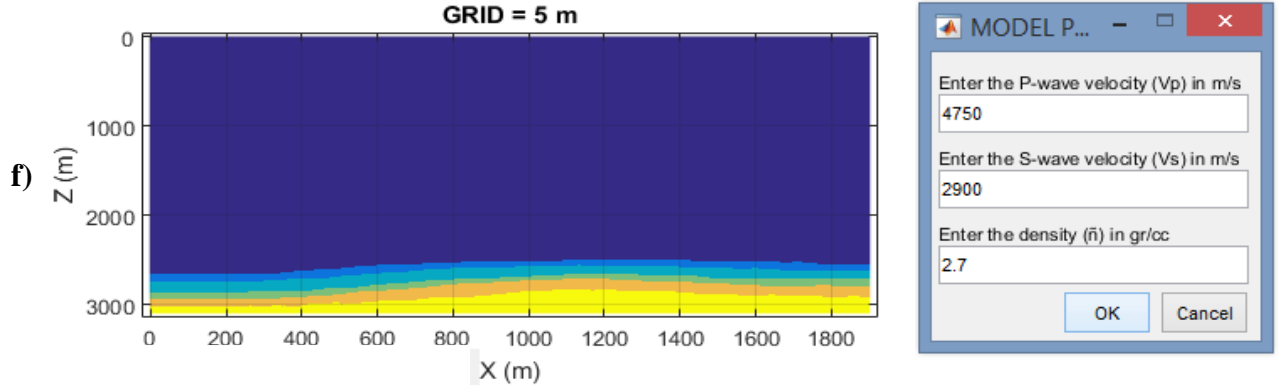


Figure 5.23 Representation of the layers import in the simulator. a) The background evaporite horizon. b-e) The horizons sand A1, sand A2, sand B and sand C respectively. f) To the bed evaporite horizon.

The geophysical properties of the Prinos basin with respect to depth are summarized in **Figure 5.24**, where the Poisson's ratio is calculated as:

$$PR = \frac{V_s^2 - 0.5 \cdot V_p^2}{V_s^2 - V_p^2} \quad (5.8)$$

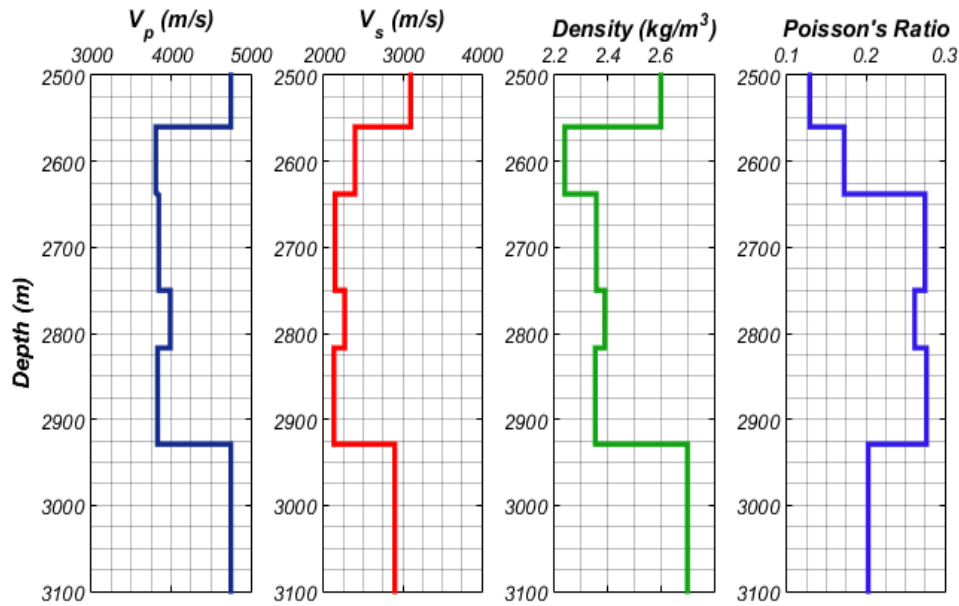


Figure 5.24 V_p , V_s , density and Poisson's ratio versus depth for the Prinos basin.

After the definition of the geophysical and geological properties of the basin, the seismic survey's set up should be defined. The number of the shots is a crucial factor for the quality and the duration of the seismic data acquisition. In this simulation the number of the sources was chosen to be 48 with a 40 m interval in order to cover the whole extension of the basin $(48-1) \times 40 = 1880\text{m}$. All the sources were horizontally spread and set at $3 \times \text{Grid} = 15\text{m}$ below the surface, while the first source was initiated at 10m in the horizontal plane as shown in **Figure 5.25**.

SOURCE PARAMETERS

Source dominant frequency is 20 Hz

Source increment and coordinates must be multiple of 5 m

Enter the No of shots
48

Enter the shot increment
40

Enter the Z coordinate of source (m)
15

Enter the X coordinate of 1st source
10

OK Cancel

Figure 5.25 The Source parameters introduction.

The receivers were also horizontally spread but their position was considered to be fixed during the simulation, so the receiver's increment was set to zero. The first receiver was initiated at 0 m on the horizontal plane, while all the receivers were set at 0m depth. The number of the receivers was set to 191 in order to cover the whole extension of the reservoir $(191-1)*10\text{m}=1900\text{m}$, as shown in **Figure 5.26**.

RECEIVER ...

Receiver increment = 10 m

Coordinates must be multiple of 5 m

Enter the Number of receivers
191

Enter the Z coordinate of receivers (m)
0

Enter the X coordinate of 1st receiver
0

Enter the Receiver increment in meters
0

OK Cancel

Figure 5.26 Introduction of the receiver's parameters.

The final overall setting of the experiment is shown in **Figure 5.27**.

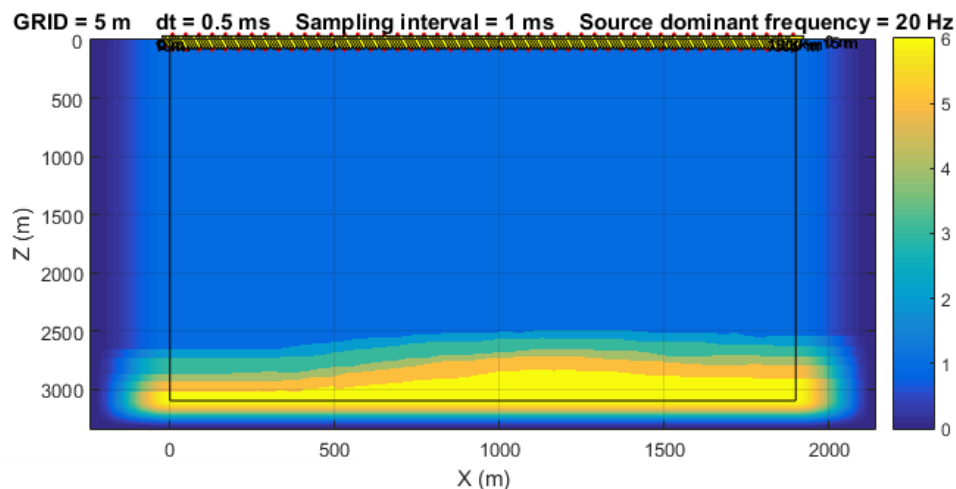


Figure 5.27 The final setup of the experiment.

The final step includes the approximation of the record length of the simulation. In order to calculate the optimal record length for the simulation, a function was created in Matlab, with the name **Record_Length**. This function averages each layer's depth into its mean value and calculates the travel time for a raypath to reach the deepest reflection and return to the geophone with the greatest offset. The velocity value was calculated as the weighted average velocity between the layers and the returning distance of the ray was calculated using the Pythagorean Theorem as shown in **Figure 5.28**. The record length was derived as $t=d_2/V_p+d_3/V_p=1327\text{ms}$. In order to avoid any record loss, an extra time margin was added to the simulation and the final record length was set to 1600 ms.

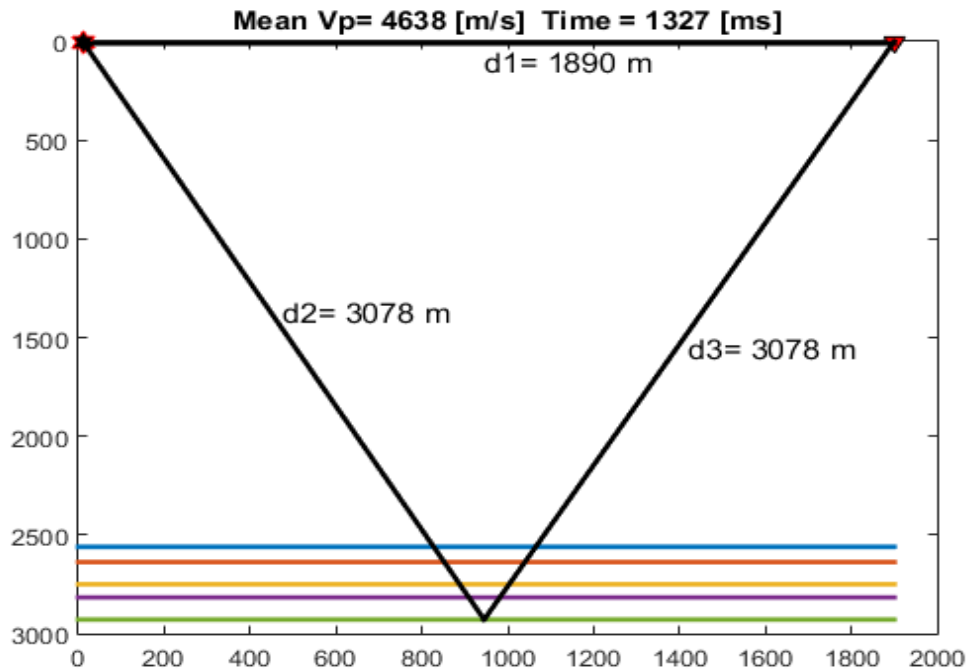


Figure 5.28 Presentation of the record's length calculation procedure.

The output of the simulation in time domain is presented in **Figure 5.29**

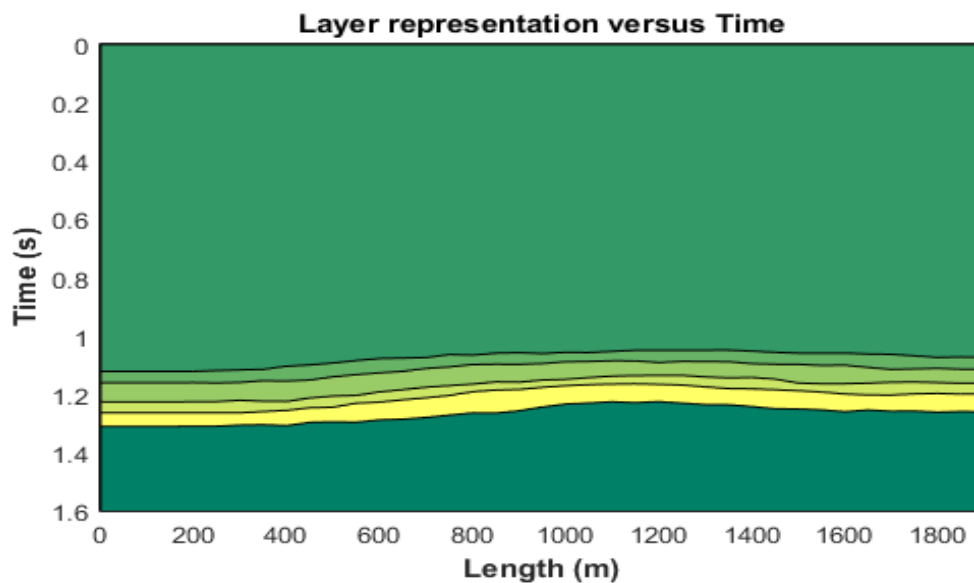


Figure 5.29 Prinos basin layers representation in time using the “area” function.

The transition from depth to time domain was achieved using the following equation:

$$t_n = t_{n-1} + 2 \cdot \frac{dS_n}{Vp_n} \quad (5.9)$$

Where t_n is the two way travel time at the n^{th} layer, t_{n-1} is the two way travel time till the previous layer, dS_n is the thickness of the n^{th} layer and Vp_n is the matrix velocity of the n^{th} layer. As an example, the calculation for the first three layers is presented in **Figure 5.30**.

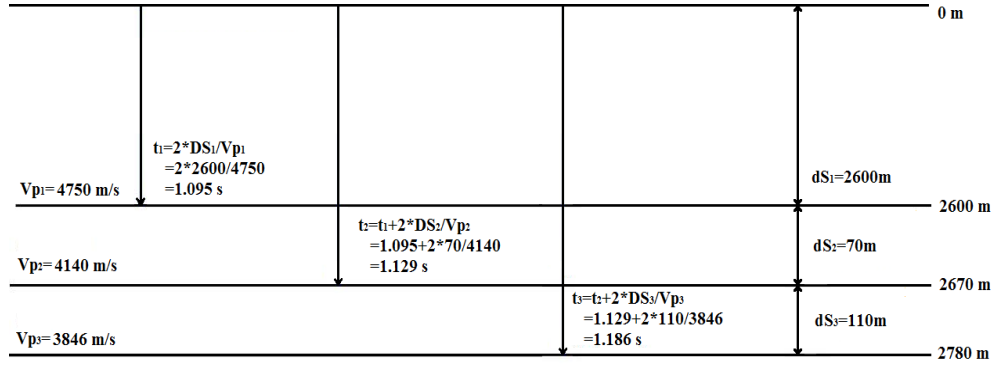


Figure 5.30 An example of the time calculation for the first three layers of the reservoir.

The synthetic data of the simulation was converted to a SEG-Y file in Matlab with the use of the function **SYNTHETIC2SGY** [TUC Applied Geophysics Lab]. The following are some important parameters about the SEG-Y file:

- Number of shots = 48.
- Number of channels per shot = 191.
- Receiver type = Vertical-component geophones.
- Number of traces in line = 9168.
- Receiver interval = 10 m.
- Shot interval = 40 m.
- 1st shot location = 10 m.
- 1st receiver location = 0 m.
- Time sampling interval = 1 ms.
- Number of time samples per trace = 1602.
- Data format = SEG-Y.
- Source frequency 20 Hz.

The stacking chart plot of the synthetic data is presented in **Figure 5.31**. The red dots represent the different explosions (sources) while the blue rectangles represent the receivers. As shown in **Figure 5.31**, 48 different explosions took place in varying x-axis locations (40 m interval), while the 191 receivers were recording each shot in the same fixed position. The number of traces per line is derived $191 \times 48 = 9168$. The number of traces per shot equals the receivers' number (191) and is presented graphically in **Figure 5.32**.

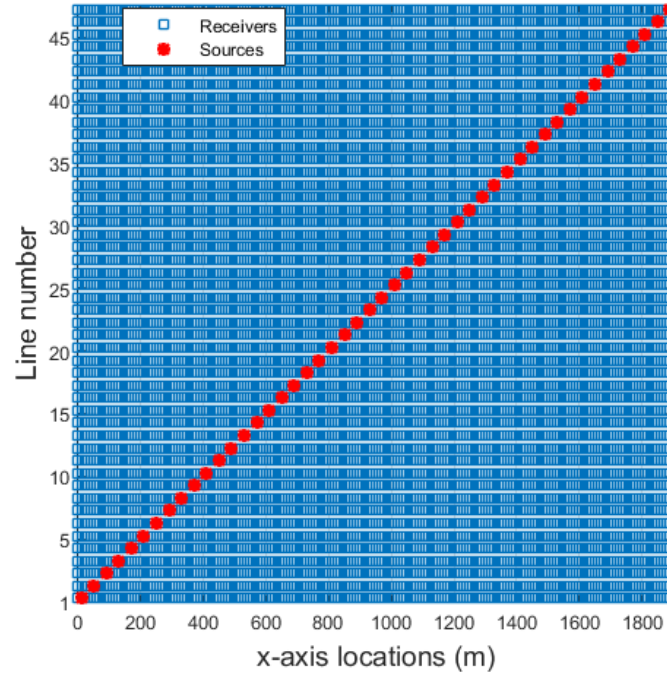


Figure 5.31 The stacking chart plot of the seismic data.

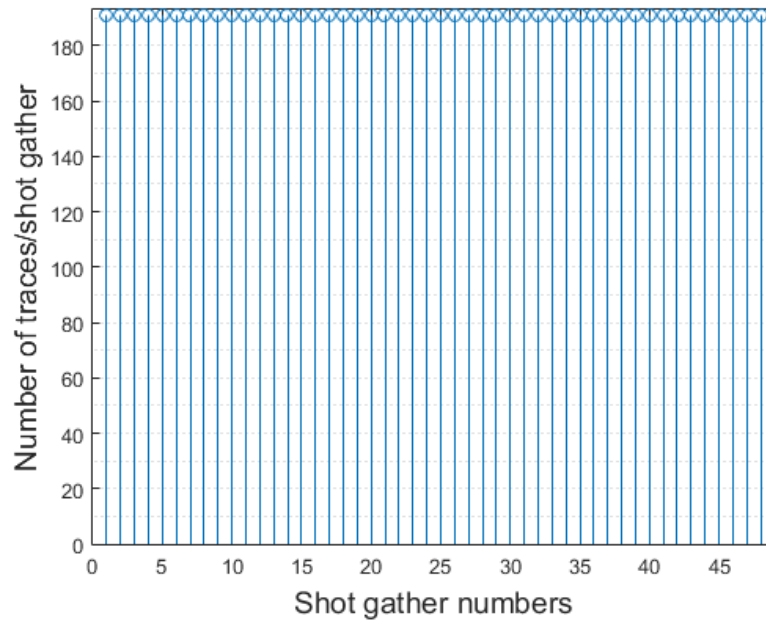


Figure 5.32 The number of traces per shot.

5.4 Seismic Data Processing

Seismic data processing can be considered as a sequence of cascaded operations that attenuate/remove noise accompanying seismic data as well as make geometrical corrections such that the final image will truly show a map (seismic image) of the subsurface. Processing of seismic data includes, but is not limited to: filtering, common mid-point (CMP) sorting, velocity analysis, normal move-out (NMO) correction, and stacking. Each seismic trace has three primary geometrical factors which determine its nature: **a) shot position, b) receiver position, and c) the position of the subsurface reflection point**. The last factor is the most critical [Mousa, Al-Shuhail, 2011].

Before processing, the position of the subsurface reflection point is unknown but a good approximation can be made by assuming that this reflection point lies vertically under the position on the surface mid-way between the shot and the receiver for that particular trace. This point is referred to as *common mid-point* (CMP) or *common depth-point* (CDP). Traces reflected from the same CMP define a CMP gather. The CMP gather is important for seismic data processing because the subsurface velocity can be derived using it. In general, the reflection seismic energy is very weak and it is essential to increase the signal-to-noise ratio (SNR) of most data. Once the velocity is known, the traces in CMP gathers can be corrected for NMO, which is basically a way of correcting for time differences which occur due to offset in a CMP gather, i.e., to get the equivalent of a *zero-offset* trace. This implies that all traces will have the same reflected pulses at the same time, but with different random and coherent noise. So, combining all the traces in a CMP gather will average out noise and the SNR increases. This process is known as stacking.

In general, the main objectives of seismic data processing are to improve the seismic resolution and increase the SNR of the data. These objectives are achieved through three primary stages. In their usual order of application, they are:

1. **Deconvolution**, which increases the vertical resolution
2. **Stacking**, which increases the SNR; and
3. **Migration**, which increases the horizontal resolution.

In addition to these primary stages, secondary processes may be implemented at certain stages to condition the data and improve the performance of these three processes.

Figure 5.33 shows a conventional seismic data processing flow.

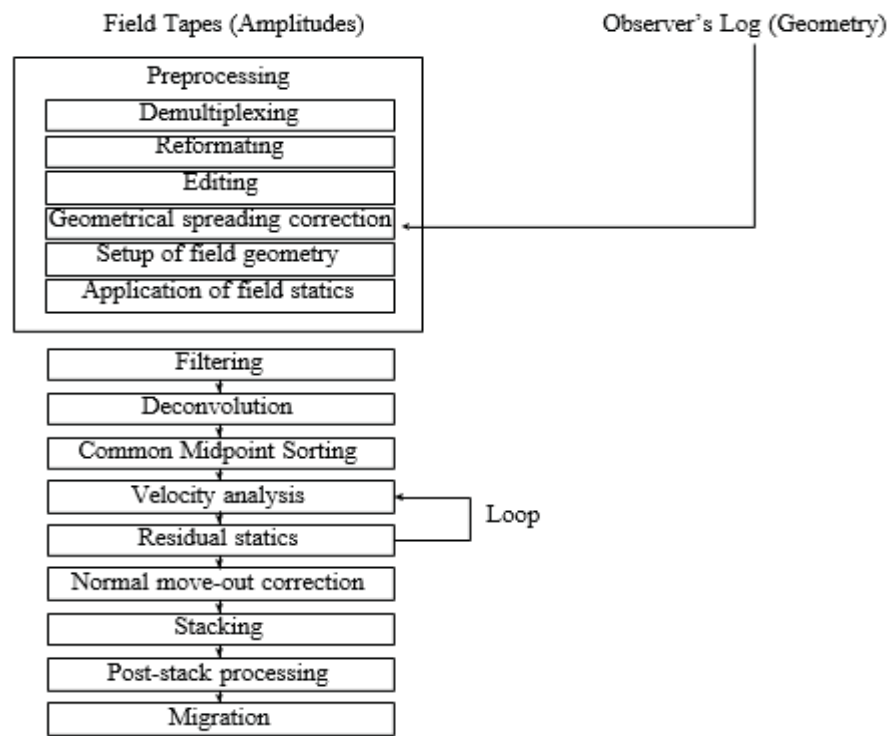


Figure 5.33 A conventional seismic data processing flow [Mousa, Al-Shuhail, 2011].

Surface seismic reflection surveys commonly use the common midpoint (CMP) method. In this method, points in the subsurface are covered more than once by primary reflections from different source-receiver pairs. **Figure 5.34** and **Figure 5.35** show the difference between shot gather and CMP configurations. Traces reflected from the same midpoint form a CMP gather while the number of traces in a gather is called the fold of that gather. Common CMP folds are 80, 120, 240, and 480. It is notable here that the CMP spacing is half of the trace (receiver) spacing in a survey. Seismic data is acquired in the shot gather mode while most seismic data processing is performed in the CMP-offset mode.

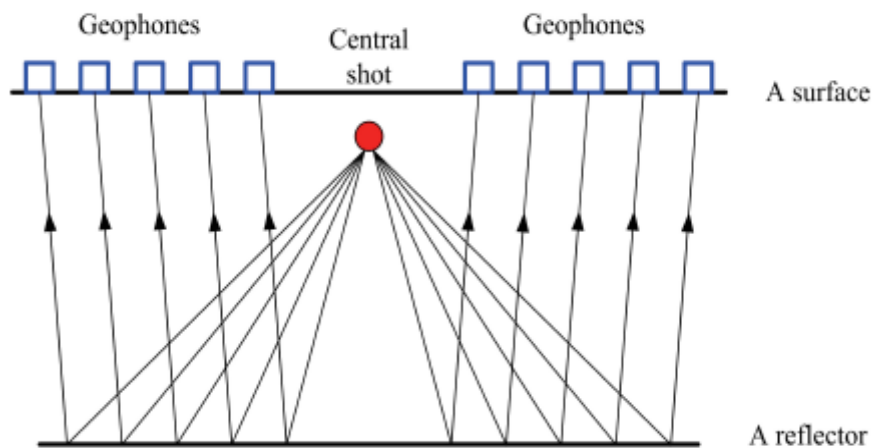


Figure 5.34 Two-sided common shot gather configuration with five receivers from each side of the shot record [Mousa, Al-Shuhail, 2011].

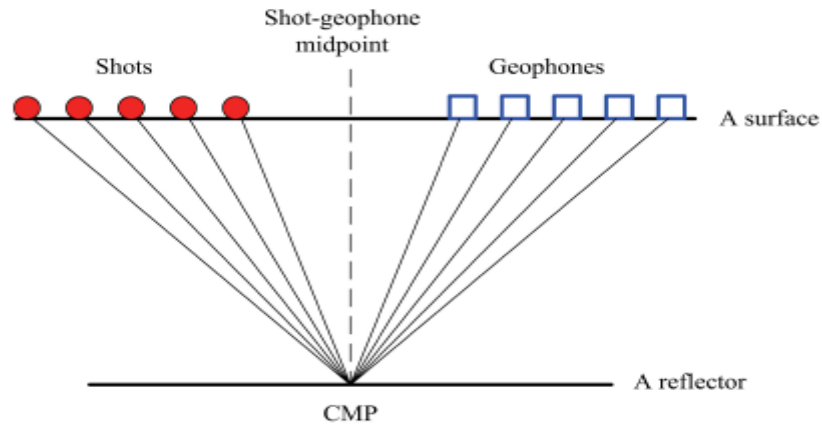


Figure 5.35 Common mid-point gather (CMP) configuration. Each of the shot-receiver combinations is centred around the same mid-point.

The number of times that the same subsurface reflecting element is delineated on a seismogram or on separate seismograms is called the number of **fold coverage**. Practically, the fold coverage coincides with the number of traces in a CMP gather, as each trace of a CMP gather is a record of the same subsurface reflecting element. The fold's approximation is given by equation (5.10).

$$\text{Fold} = \frac{\text{Receiver's interval} \times \text{Number of receivers}}{2 \times \text{Shot interval}} \quad (5.10)$$

According to equation 5.10, for the current seismic survey the fold coverage should be $10 \times 191 / 2 \times 40 \approx 24$. However, as shown on **Figure 5.36** the fold doesn't have a constant value, but is varying from 1 to 48. This can be attributed to the fact that the equation 5.10 is valid only when the recording channels are moving along with the sources during the survey, instead of remaining in the same fixed position, as is the case of the current setup. As mentioned previously, the CMP interval is half of the receiver's spacing, i.e. $\text{CMP interval} = 10/2 = 5$ m. Thus, the CMP number gives $(1900/5) - 1 = 379$ CMP gathers.

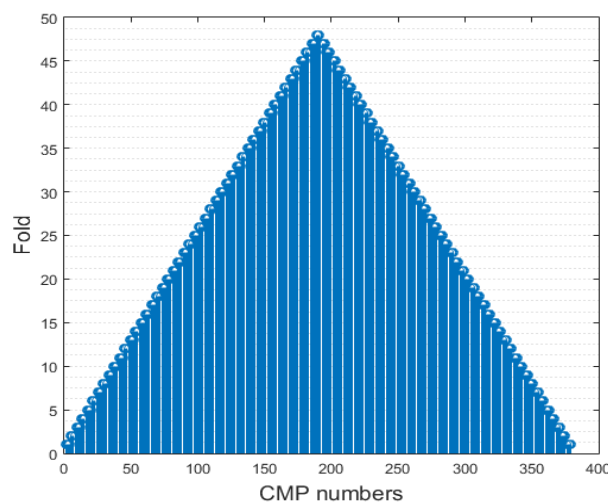


Figure 5.36 The fold (number of traces per CMP) versus the CMP numbers.

Before starting the processing analysis of the synthetic data, a simple demonstration of the source's expected waveform is presented. As stated previously, the dominant frequency of the source is 20 Hz with sampling interval 1ms. Using the data above, along with the approximated reflectivity series of the Prino's subsurface (which will be further analyzed in chapter 7), a first representation of the synthetic seismic data is given on **Figure 5.37**.

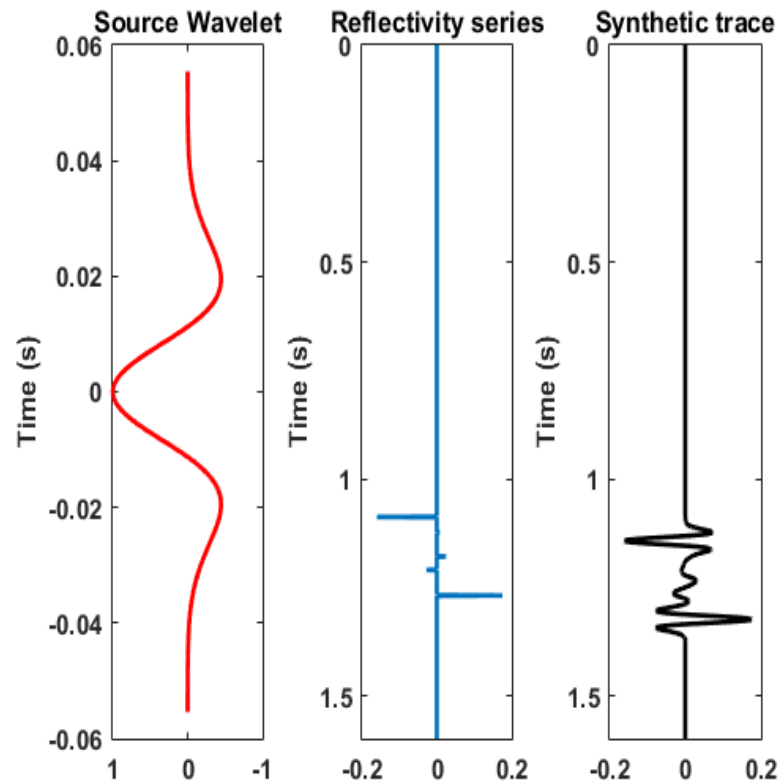


Figure 5.37 Representation of source wavelet, reflectivity series and their convolution in time.

In the following section, the processing steps presented in **Figure 5.33** are elaborated, beginning with the preprocessing procedure.

5.4.1 Preprocessing

The synthetic data is acquired firstly in the shot gather mode with the use of the function **SEG_Y_FindShots(seg_y, binsize)** [Chad Hogan, 2008]. As an example, the shot gather number 8 is presented in

Figure 5.38. It is obvious that the synthetic data presents very weak amplitudes and needs further processing in order to better delineate the reflectors.

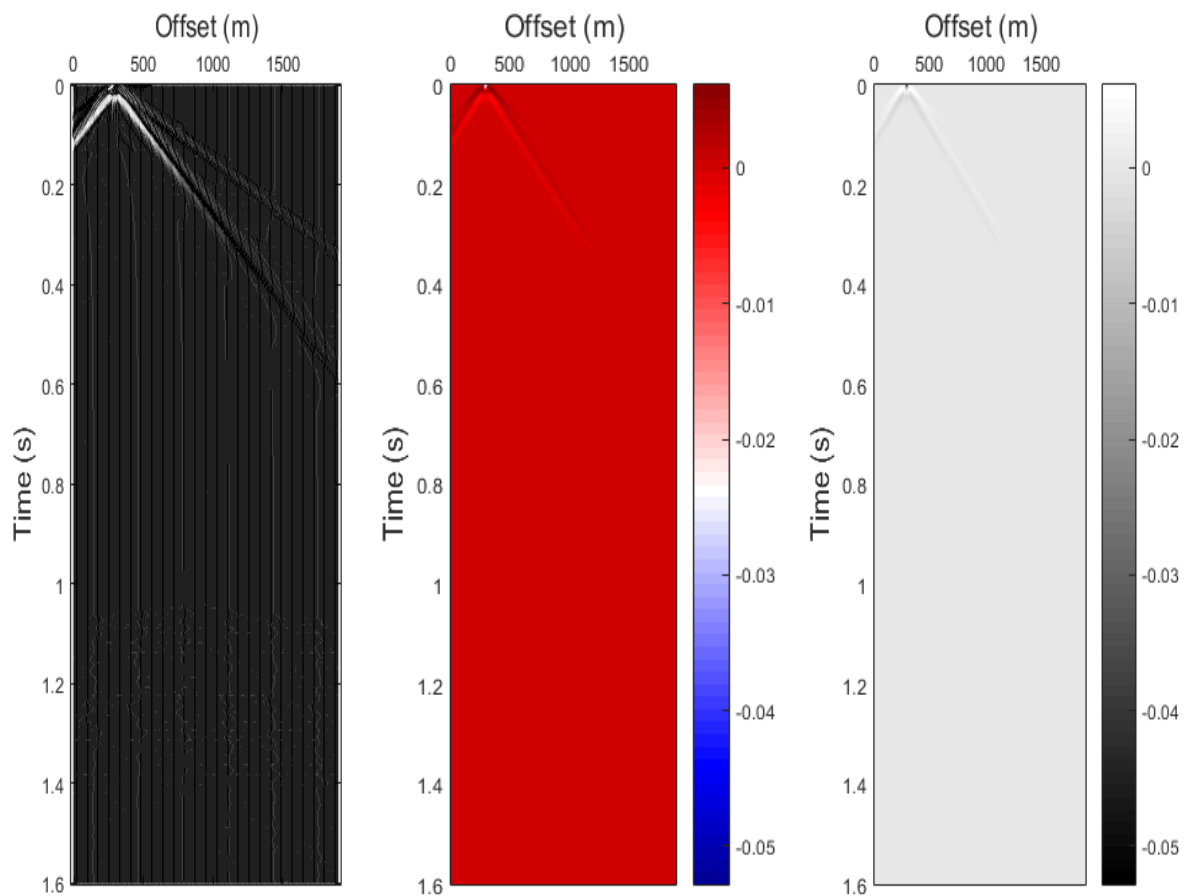


Figure 5.38 Various displays for shot gather number 8.

The pre-processing involves a series of steps to condition the data and prepare it for further quality control and processing including:

- i) demultiplexing
- ii) reformatting
- iii) trace editing
- iv) gain application
- v) setup of field geometry
- vi) application of field static

The reformatting and trace editing procedures are necessary only in real seismic data, where bad recordings and noise are involved. In the synthetic data the only pre-processing step that that would be meaningful is the amplitude correction or gain. At the pre-processing stage, correction of amplitudes may be needed due to geometric divergence, as well as absorption losses. Also, whenever displaying seismic data, weak signals may need boosting by adding more gain to the data. Amplitude correction schemes can be either dependent or independent of data. Both techniques are applied for shot gather number 8 and are displayed in **Figures 5.39** and **5.40**.

The data-independent scheme corrects the amplitudes applying a common scaling function to all the traces such as the gain through multiplication by a power of time using:

$$f_{corrected}(t) = f(t)t^a \quad (5.11)$$

where $f(t)$ is the seismic trace amplitude to be corrected, t is the time independent variable, and a is the power of time which controls the change in the amplitude of $f(t)$.

Another commonly used technique is the exponential gain function correction:

$$f_{corrected}(t) = f(t)e^{\beta t} \quad (5.12)$$

where β is the parameter which controls the exponential function.

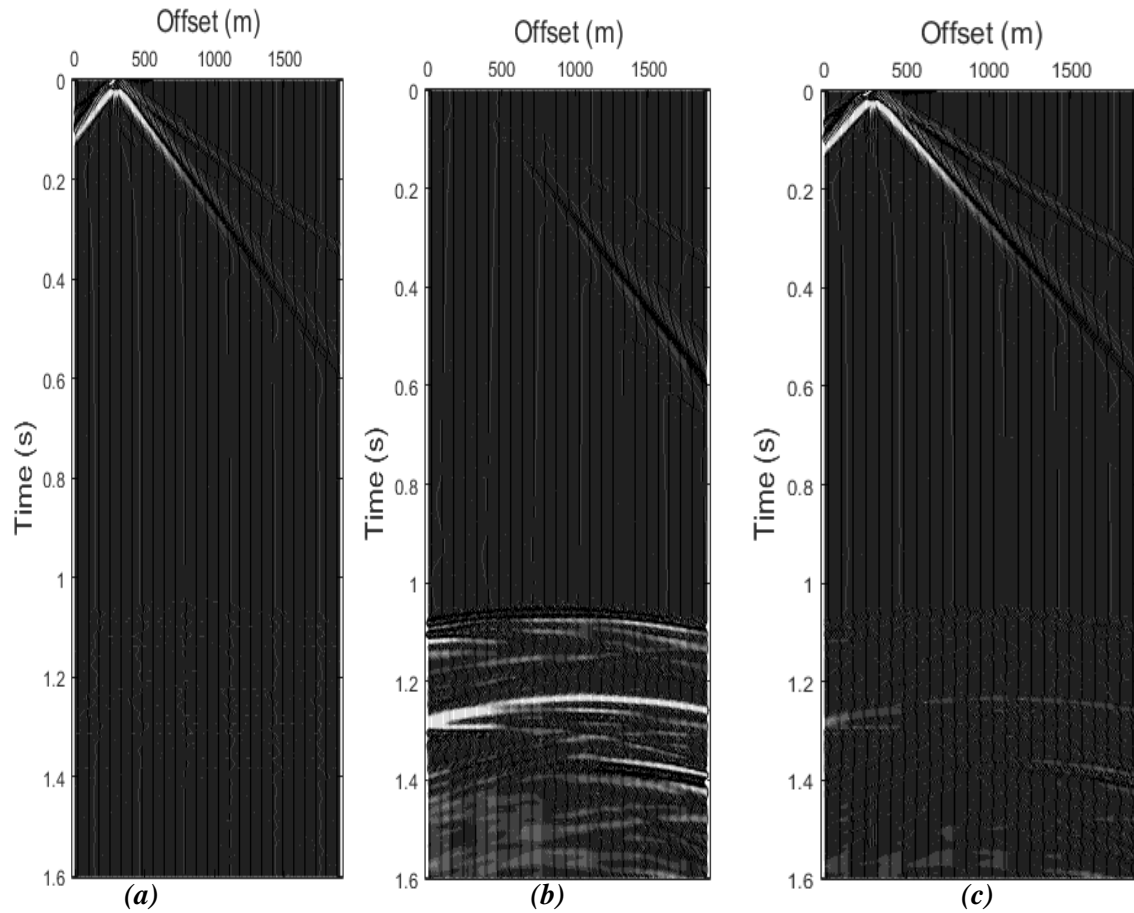


Figure 5.39 Seismic data shot gather number 8: (a) before, (b) after applying amplitude correction gain method of Equation 5.11 with $a=3$ and (c) amplitude correction gain method of Equation 5.12 with $\beta=3$.

The data-dependent scheme, on the other hand, relies on multiplying each time sample by a scalar derived from a window of data around the sample. Such a technique is known as automatic gain control (AGC). Some of the famous AGC techniques include:

- **RMS amplitude AGC:** This method requires segmenting each trace into fixed time gates and then:
 - i. Calculate the RMS value in each gate.
 - ii. Divide the desired RMS scalar by the RMS value of step 1 and multiply it by the amplitude of the sample at each gate center.
 - iii. Interpolate between these gate centers and multiply the result by the amplitude of samples corresponding in time.
- **Instantaneous AGC:** this is a bit different from the RMS AGC:
 - i. Calculate the absolute mean value for in a given gate of length w .
 - ii. Divide the desired RMS scalar by the mean value of step 1 and multiply it by the amplitudes of all the samples in the gate.
 - iii. Slide the gate down by one sample and repeat steps 1-2 until all the amplitudes of all trace samples that have been corrected are calculated.

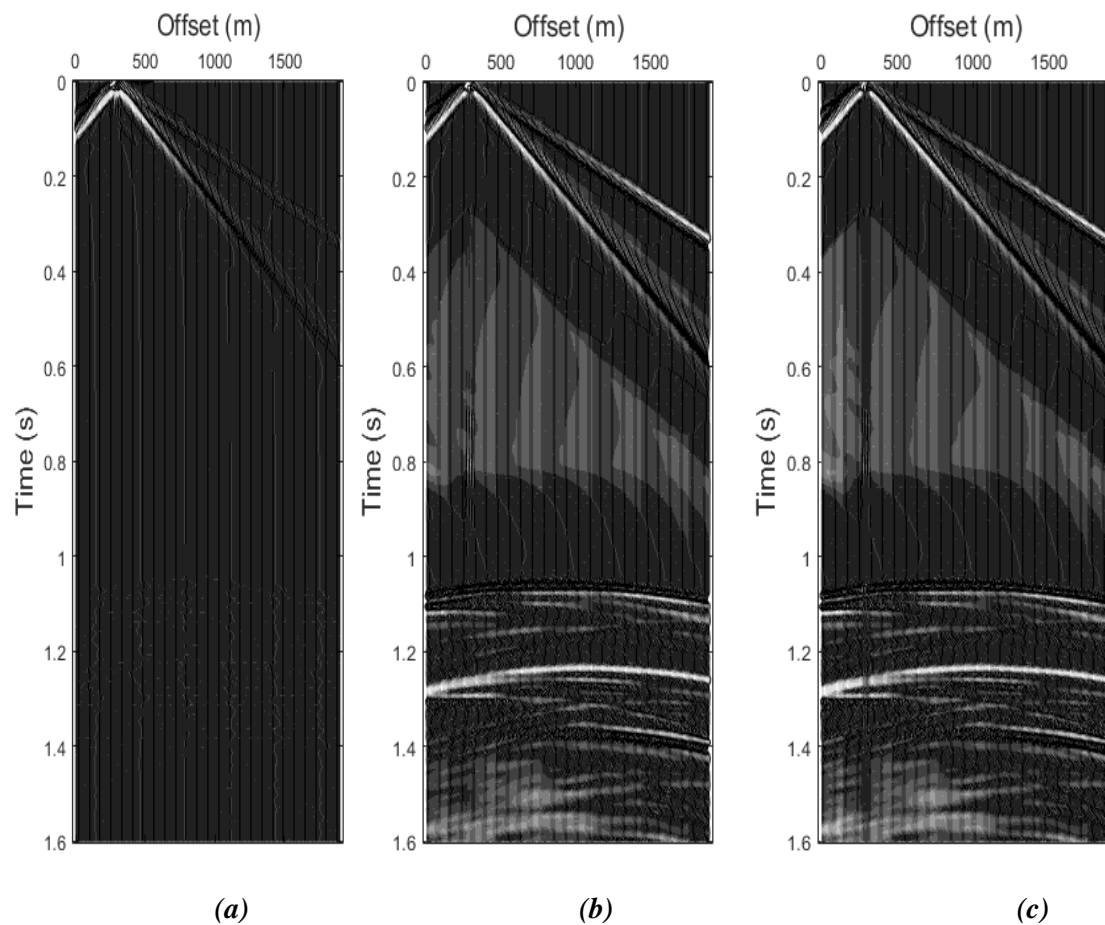


Figure 5.40 Seismic data shot gather number 8: (a) before, (b) after applying the AGC using the RMS and (c) instantaneous based methods.

In order to better understand the differences between the data-dependent and independent gain schemes, the amplitude envelope of gain is presented in **Figure 5.41**, separately before and after the application of each process.

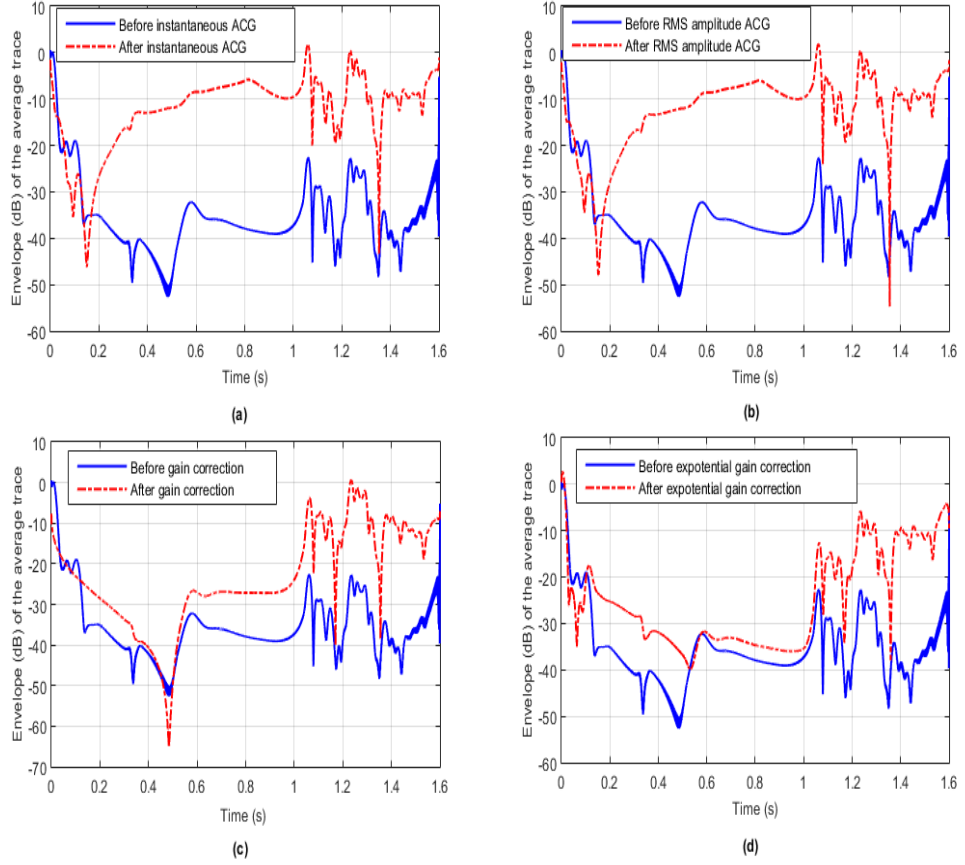


Figure 5.41 The amplitude envelope gain in dB of the average trace for a) instantaneous ACG, b) RMS amplitude ACG, c) power gain correction with $a=3$ and d) exponential gain correction with $b=3$.

It is obvious from **Figure 5.41** that the data-dependent gain increases the amplitude of the average trace, both in early and in late times, while in the case of the power and exponential gains the amplitudes are increased mainly in the later times. Also, the data-dependent gain has greater and more abrupt impact on the average trace's amplitude. Finally, there is a difference between the power and the exponential gain, with the latter giving a smoother and lower amplitude boosting.

For the data independent scheme the function `iac(Dshot,t,pow,T)` was used, while for the time-dependent scheme the function `AGCgain(Dshot,dt,agc,T)` was used. Finally, for the amplitude's envelope plotting the function `seis_env_dB(Dshot,Dg,t)` was applied.

5.4.2 Spherical divergence correction

As the wave moves away from the source, the area that its energy covers becomes larger and, thus, its intensity decreases. This is referred to as "*spherical divergence*" or "*geometrical spreading*", is independent of frequency and plays a major role in sound propagation situations. For the application of geometrical spreading a single "representative" velocity function is usually used for a data according to the formula $\text{gain} = 1/(\text{velocity multiplied by two-way travel time})$. The above procedure was applied in the synthetic seismic data and the result before and after the application of geometrical spreading is shown in **Figure 5.42**.

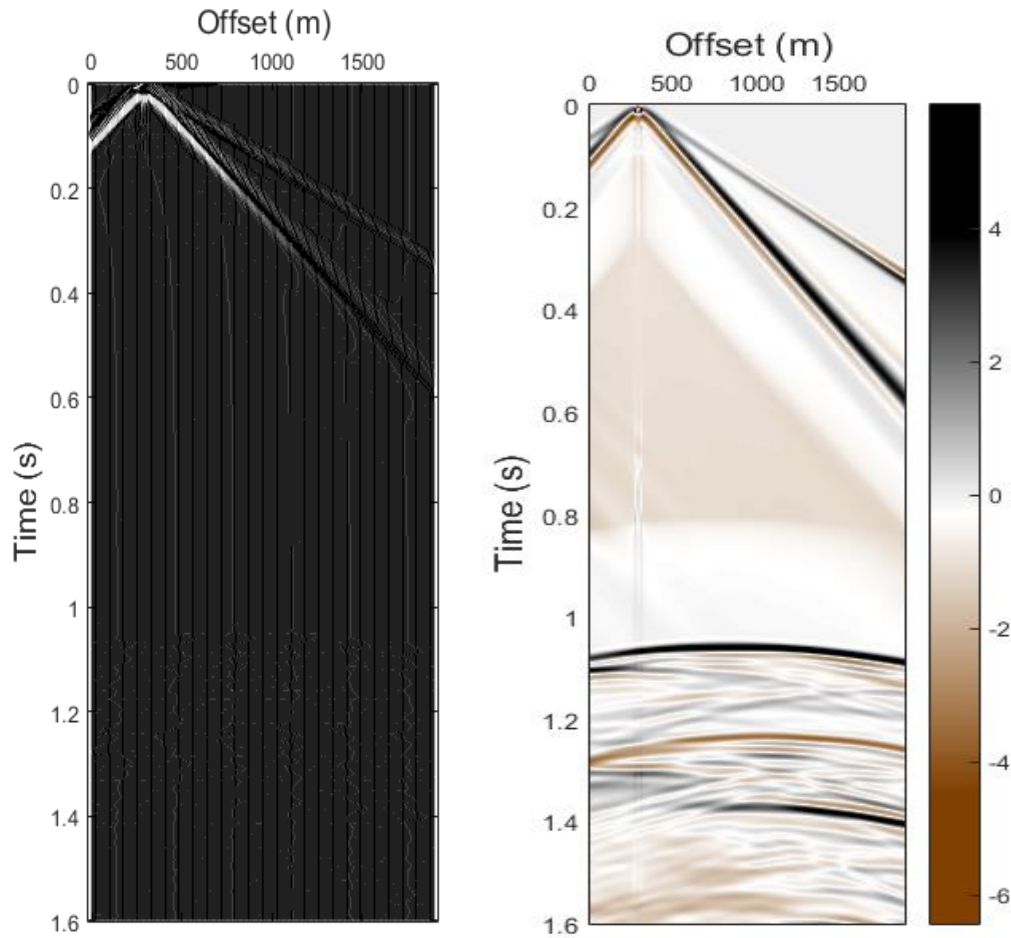


Figure 5.42 Seismic data shot gather number 8: (a) before and (b) after applying geometrical spreading correction.

In **Figure 5.43** the amplitude envelope for the average trace is presented before and after the application of geometrical spreading. It is clear that the geometrical spreading correction in contrary with the gain procedures that were previously presented, reduces the amplitudes in early times and enhances the deeper signal without over-boosting the noise in the deepest part of the record.

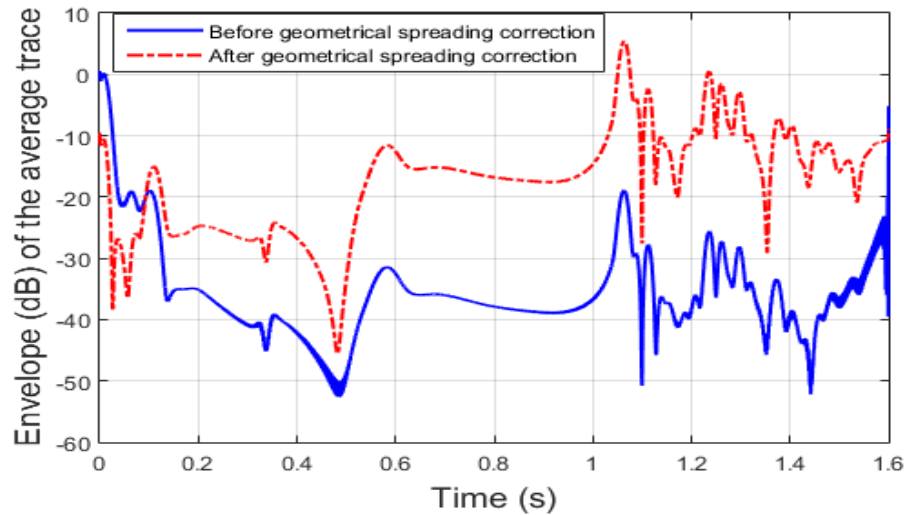


Figure 5.43 The amplitude envelope gain in dB for the average trace before and after the application of geometrical spreading correction.

5.4.3 Spiking and Predictive deconvolution

Predictive deconvolution predicts the values, after a specified prediction distance, of each point in the seismic wavelet and then subtracts these values from the wavelet. Predictive deconvolution therefore simply shortens the length of the wavelet by truncation. Any prediction distance can be used. If the prediction distance is unity ($\alpha = 1$), then this is known as a "spiking deconvolution", and the filtered output will simply be a wavelet that has been shortened to an impulse. In the ideal case, the impulse will be directly proportional to the reflection coefficient. If the prediction distance is any other value, then the wavelet will (in an ideal, noise-free environment) be truncated after the prediction distance.

To perform predictive deconvolution in practice, the following parameters need to be set:

- **Autocorrelation window (w):** This sets up the part of seismic trace from which we will select the elements of the autocorrelation matrix in the normal equations.

The autocorrelation window should include the part of the record that contains useful reflection signal and should exclude coherent (e. g., ground roll) or incoherent noise (e.g., later parts of the record). The length of the autocorrelation window should be greater than eight times the largest operator length which will be used for that data set.

- **Filter length (N):** This sets up the length of the spiking filter $h(n)$.

The filter (operator) length should be equal to the wavelet length. The first transient zone of the trace autocorrelation is the part that mostly represents the autocorrelation of the source wavelet. The first transient zone is the first part of the autocorrelation that contains high amplitudes. The operator length should be selected so that it is approximately equal to the length of the first transient zone of the trace autocorrelation.

- **Percent prewhitening (ϵ):** This sets up the amount of white random noise that needs to be included into the autocorrelation matrix to stabilize the solution of the normal equations.

The magnitude of prewhitening is measured as a percentage of the zero-lag autocorrelation value $r(0)$. In practice, typically 0.1% to 0.3% prewhitening is standard in processing. In **Figure 5.44** the autocorrelogram of the shot gather number 8 is displayed along with the output of the shot gather after applying spiking deconvolution. The chosen value for the autocorrelation window is 0.2 s, while the prewhitening value was set to 0.1%. It is clear that the data became spikier, something that can also be proved by analyzing the data in the spectrum domain via the power spectral density of the average traces as seen in **Figure 5.45**.

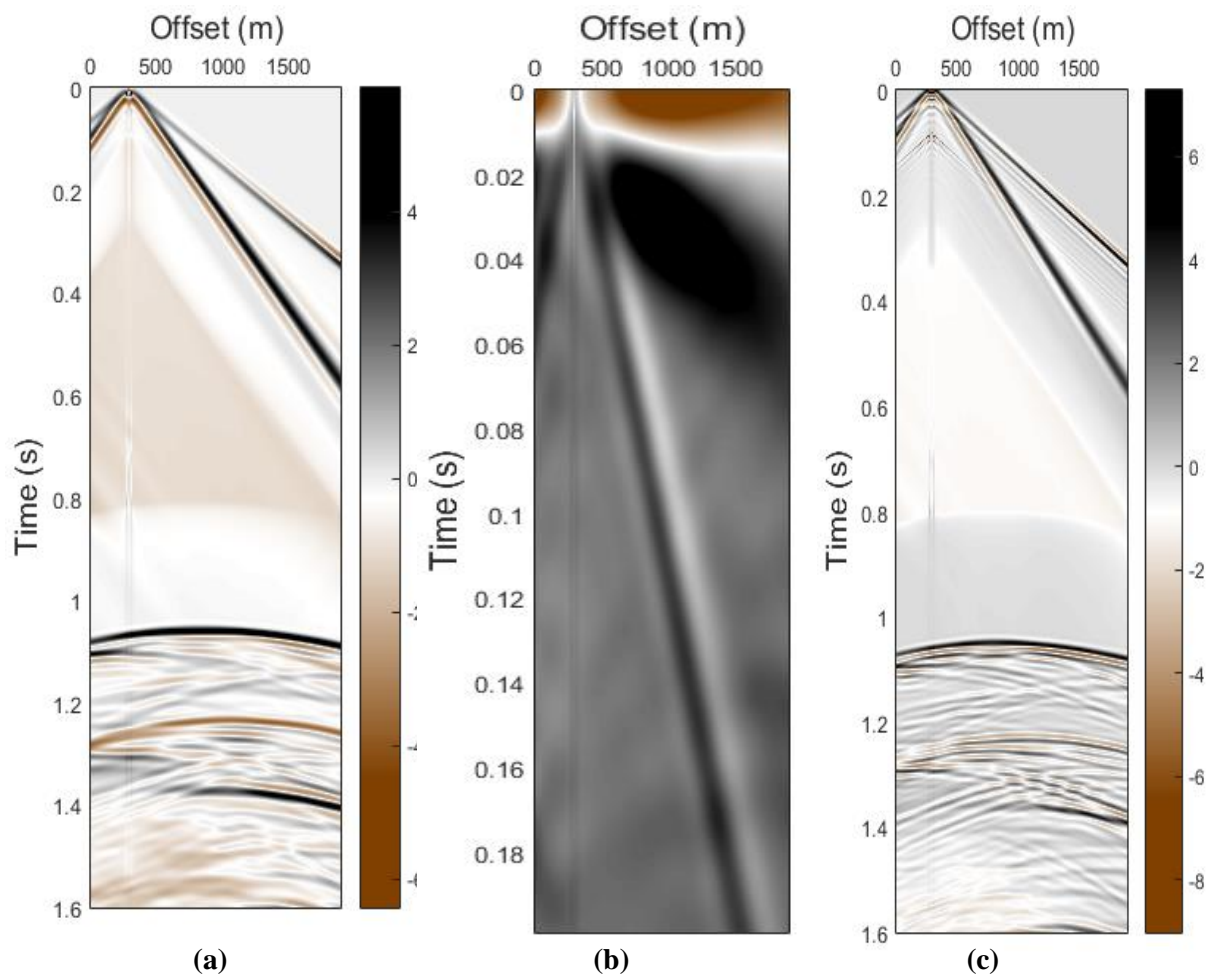


Figure 5.44 Shot gather 8 (a) before applying spiking deconvolution (b) its autocorrelogram for window 0.2 s and (c) after applying spiking deconvolution.

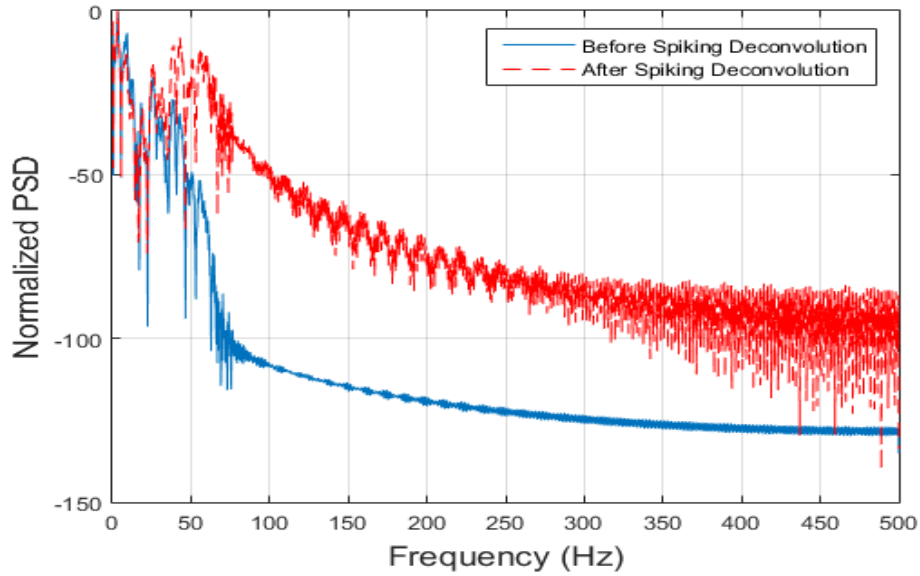


Figure 5.45 PSD of the average trace of shot gather 8 before and after spiking deconvolution.

The same procedure is repeated, but this time using the predictive deconvolution scheme. The results are presented graphically in **Figures 5.46** and **5.47**.

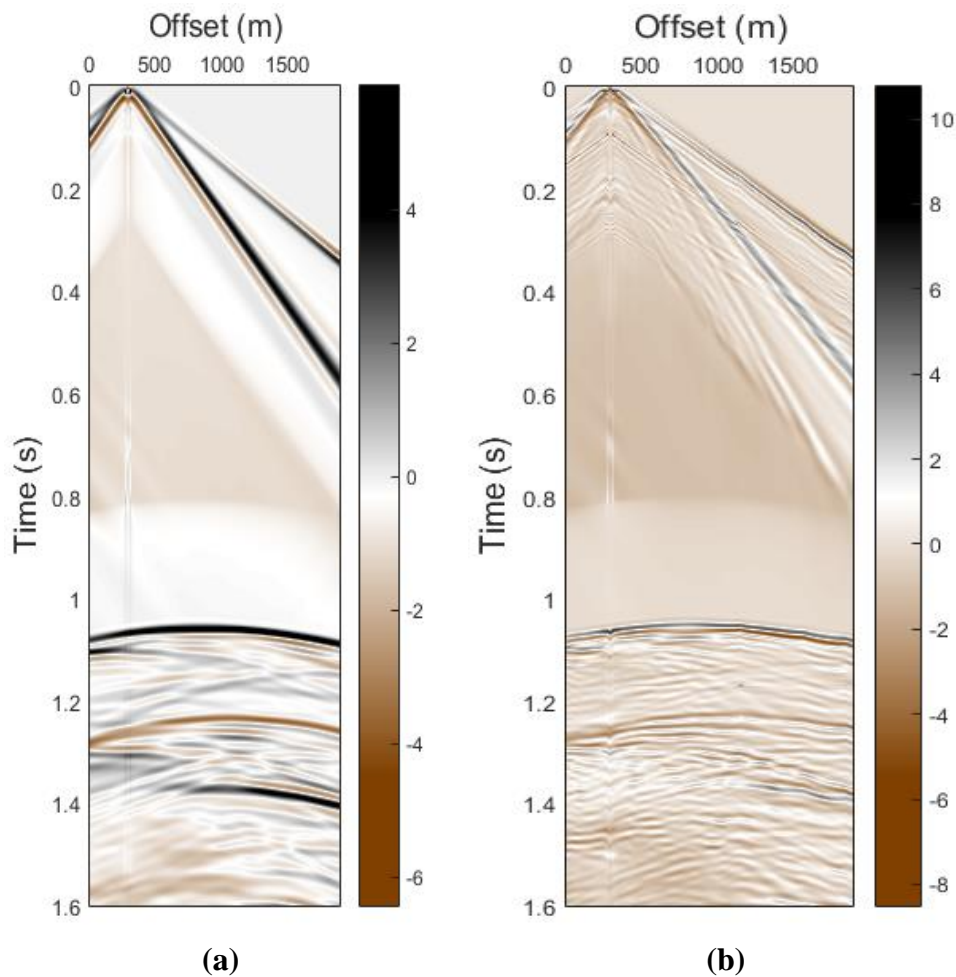


Figure 5.46 Shot gather 8 (a) before and (b) after applying predictive deconvolution with autocorrelation window 0.2 s and operator's length 0.08 s.

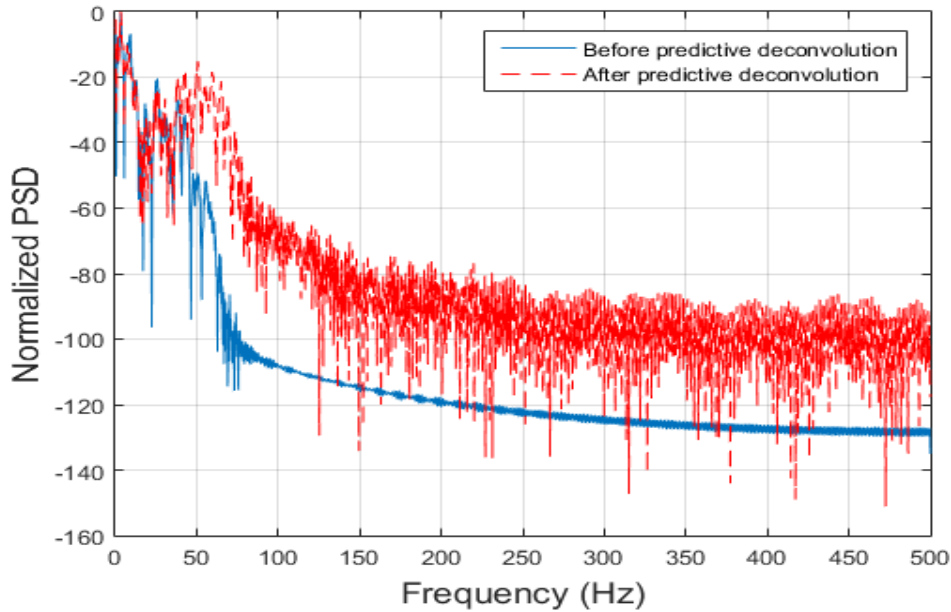


Figure 5.47 PSD of the average trace of shot gather 8 before and after predictive deconvolution.

5.4.4 FX deconvolution

This is the most common modern technique for attenuating random noise, since it has few artifacts and can be run in 2D or 3D modes. Small temporal (e.g. 10 traces) and spatial (e.g. 20ms) windows of input data are Fourier transformed to the FX domain. Deconvolution operators are designed in the lateral (X) dimension to predict the coherent parts of the signal. Subtracting the coherent parts will leave the incoherent parts i.e. random noise which can then be inverse transformed and subtracted from the signal. The next window would then be selected, ensuring some overlap with the previous window. An example is given in **Figure 5.48**, showing how random noise can be eliminated with FX – Deconvolution. The function that was used is the `fx_decon(D,dtsec,lf, mu,flow,fhigh)` [Sacchi, *SeismicLab*, 2008]. In **Figure 5.49** fx deconvolution is applied on the shot gather number 8, without having any significant effect, since the data is synthetic and the random noise is already in low levels.

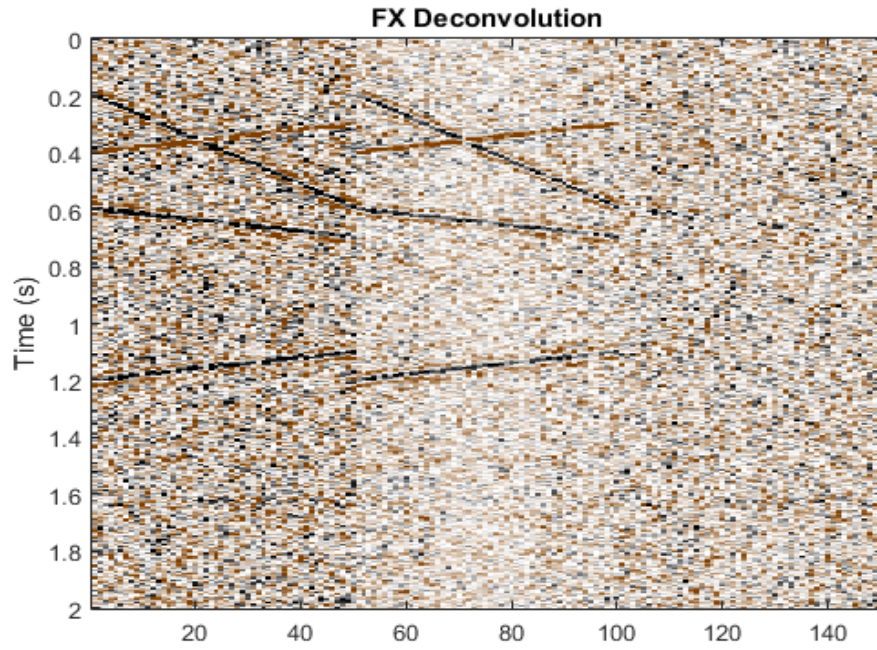


Figure 5.48 Display of seismic data form left to right, before FX deconvolution, after FX deconvolution and estimated noise.

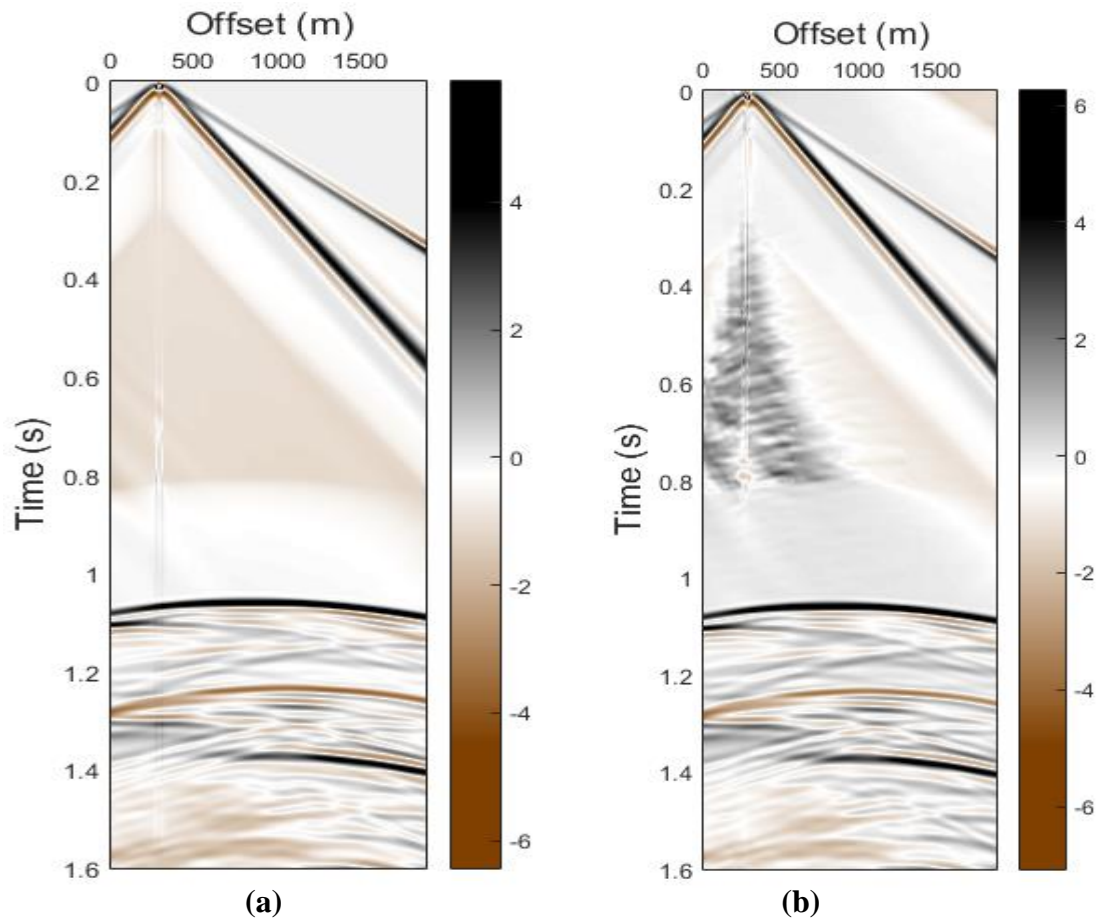


Figure 5.49 Shot gather number 8 (a) before and (b) after the application of fx deconvolution.

5.4.5 F-K Filtering

Filtering is used to attenuate components of the seismic signals based on some measurable property. Since the land seismic data set contains, mainly, ground roll noise, frequency linear filters can be applied, so that band-pass filters (BPFs) to attenuate their effect. In particular, BPFs enhance the overall gain of each seismic shot gather, and increases the SNR ratio by attenuating low and high frequency noise records, including the ground roll noise.

There are different means for such useful analysis, such as the frequency-space ($f-x$) or the frequency-wavenumber ($f-k$) spectra, each of which can be used to obtain meaningful interpretation and, therefore, apply a suitable filtering technique. Both techniques demand transition from time to frequency domain and, as a result, the use of the Fourier transform is necessary. In **Figure 5.50** both $f-x$ and $f-k$ magnitude spectra of shot gather number 8 are presented.

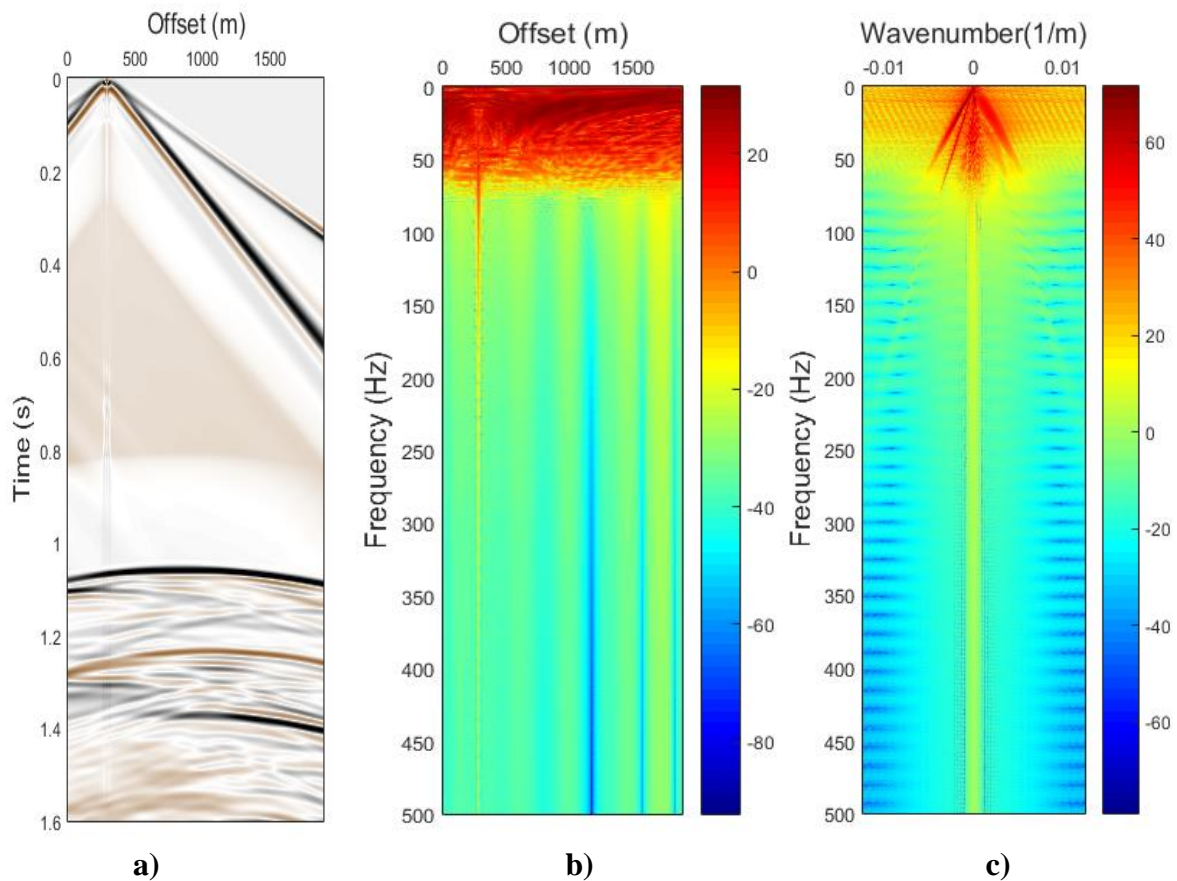


Figure 5.50 a) Seismic data shot gather number 8 after geometrical spreading b) Its $f-x$ and c) its $f-k$ magnitude spectra. The color bars in b) and c) indicate the magnitude values in dB.

F-k filtering is a 2-D data processing technique that is based on a relationship between two domains: a time-space ($t-x$) domain and its Fourier dual, an $f-k$ domain. This technique filters coherent noise for wavefield separation to produce better quality data. In short, $f-k$ filtering relies on signal and noise separation via the 2-D Fourier transform. The region in the $f-k$ domain where noise is present is set to zero and the signal region is set to one. Then the filtered shot record is restored by the inverse Fourier transform. Using the information of the $f-k$ magnitude's spectra shown in **Figure 5.50** (c), a

polygonal zone band-pass filter (BPF) is designed for frequencies lower than 100 Hz, as shown in **Figure 5.51**.

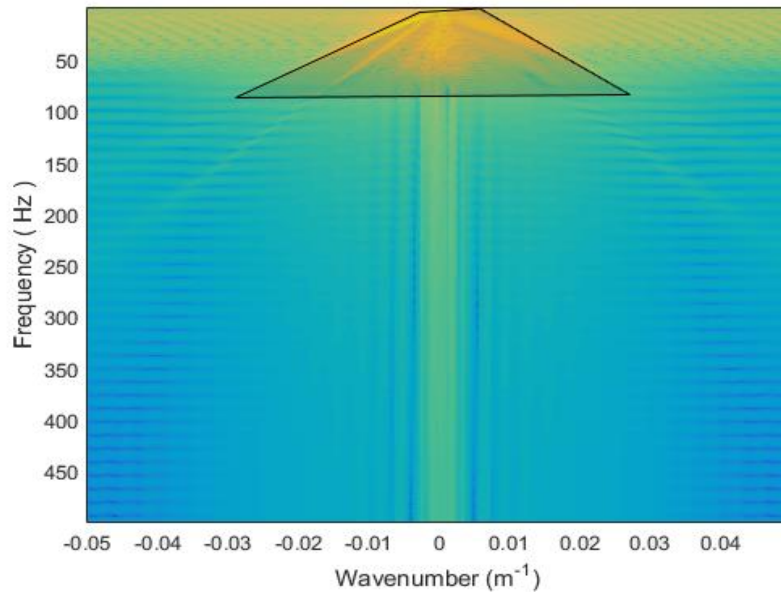


Figure 5.51 Design of the polygonal zone band-pass filter.

The above BPF is applied on the shot gather number 8 and the results are presented graphically after applying the inverse Fourier transform (**Figure 5.52**).

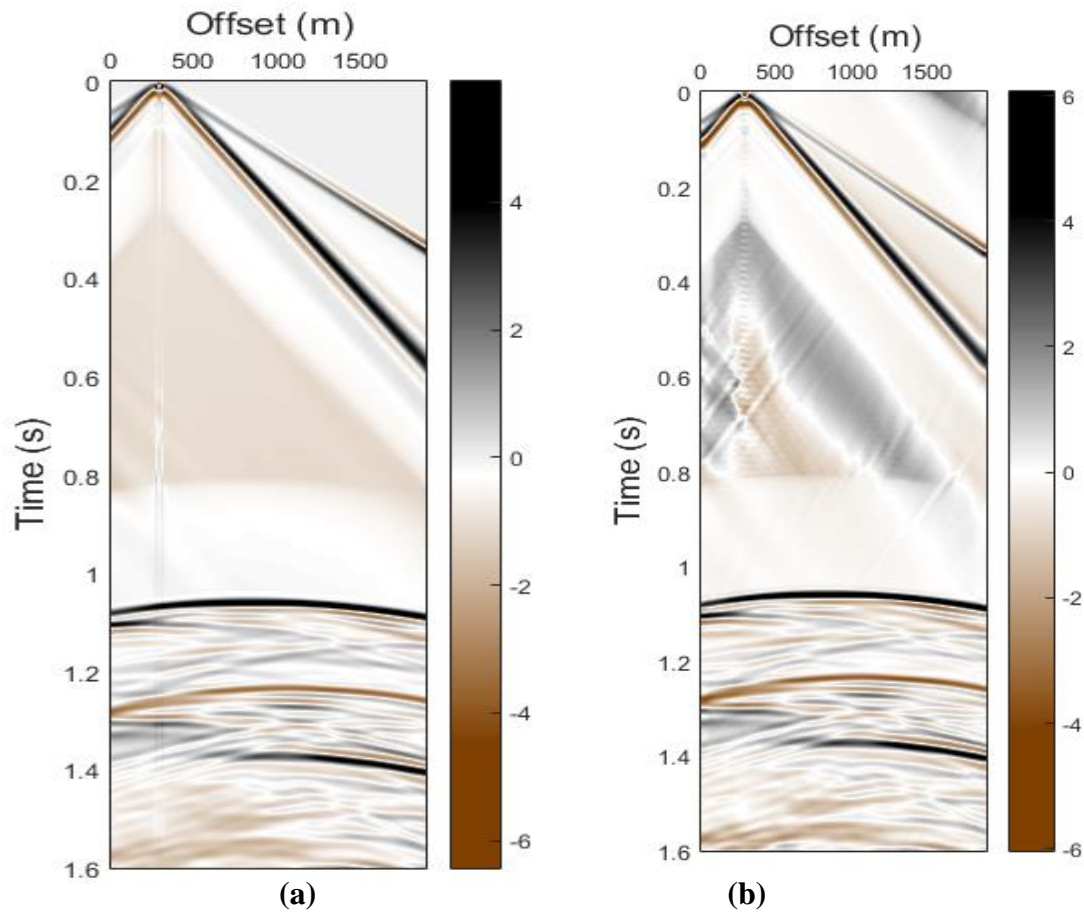


Figure 5.52 Shot gather number 8 (a) before and (b) after the application of the f - k BPF.

5.4.6 CMP sorting

In order to convert the synthetic data from Common Shot to CMP gathers the function **SEG_Y_FindCMPs(seg_y, binsize)** was used [Chad Hogan, 2008]. In **Figure 5.53** the CMP gather number 100 is plotted before and after the application of geometrical spreading. Due to the fact that the receiver's array was stationary through the recording procedure there are traces with both negative and positive offsets.

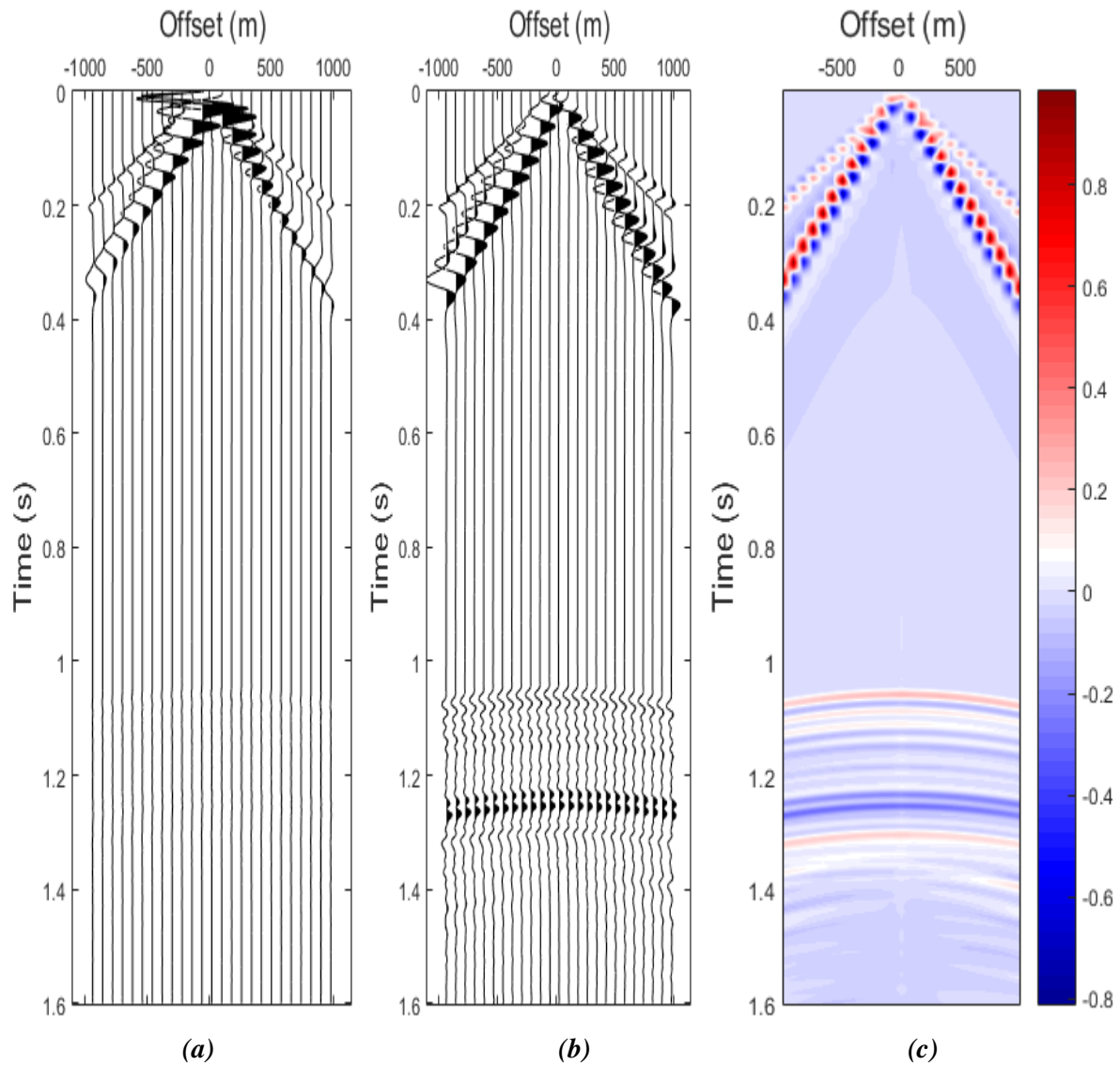


Figure 5.53 CMP number 100 (a) before geometrical spreading (b) after geometrical spreading (c) in colored display.

5.4.7 Velocity Analysis

Velocity analysis is performed on selected CMP gathers to estimate the stacking, root-mean squared (RMS), or NMO velocities to each reflector. Velocities are interpolated between the analyzed CMPs. The aim of the velocity analysis is to find the velocity that flattens a reflection hyperbola, which returns the best result when stacking is applied. There is a distinction between:

- V_{stack} : the velocity that returns the best stacking result.
- V_{rms} : the actual RMS-velocity of a layer.

For a horizontal layer and small offsets, both velocities are similar. When the reflectors are dipping then v_{stack} is not equal to the actual velocity, but equal to the velocity that results in a similar reflection hyperbola.

There are different ways to determine the velocity:

- (t^2-x^2) -Analysis.
- Constant velocity panels (CVP).
- Constant velocity stacks (CVS).
- Analysis of velocity spectra.

In **Figure 5.54** the velocity spectra technique is analysed. Specifically, the un-normalized cross-correlation along hyperbolic paths is calculated in order to extract stacking velocities from a CMP gather with the use of the function `velan(D,dtsec,h,vmin,vmax,nv,R,L)` [Sacchi, *SeismicLab*, 2008].

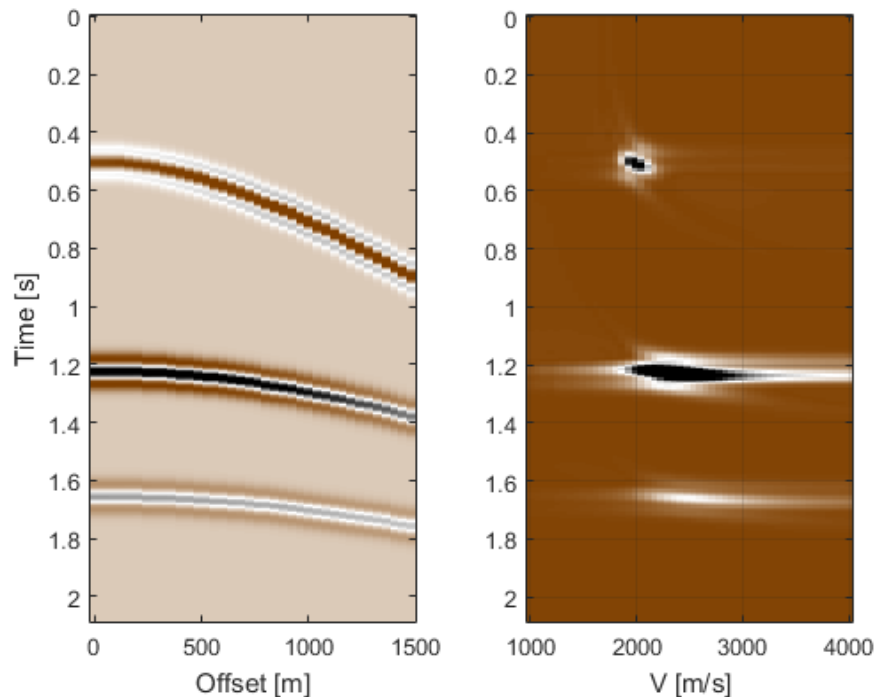


Figure 5.54 Velocity spectra of a hyperbolic reflectors.

In the case of the synthetic data the velocity spectra procedure is unnecessary, since the interval velocity of each medium is known and the RMS velocities can be derived from it. The equation that connects RMS with interval velocities is:

$$V_{RMS}^2 = \frac{\sum_{i=1}^N V_i^2 \Delta t_i}{\sum_{i=1}^N \Delta t_i} \quad (5.13)$$

As was shown in the beginning of this chapter, the synthetic data was separated in distance intervals of 5m each. The horizontal extend of the model is 1900m, resulting in $1900/5=380$ intervals with 380 different values of travel times. Using equation (5.13) the RMS velocities of the reflectors for each of this intervals was calculated and interpolated using the Matlab functions **meshgrid** and **griddata**. The results for some random interval's locations are presented in **Figures 5.55** and **5.56**. **Figure 5.57** shows the RMS velocity analysis for all the 380 locations using different interpolation techniques.

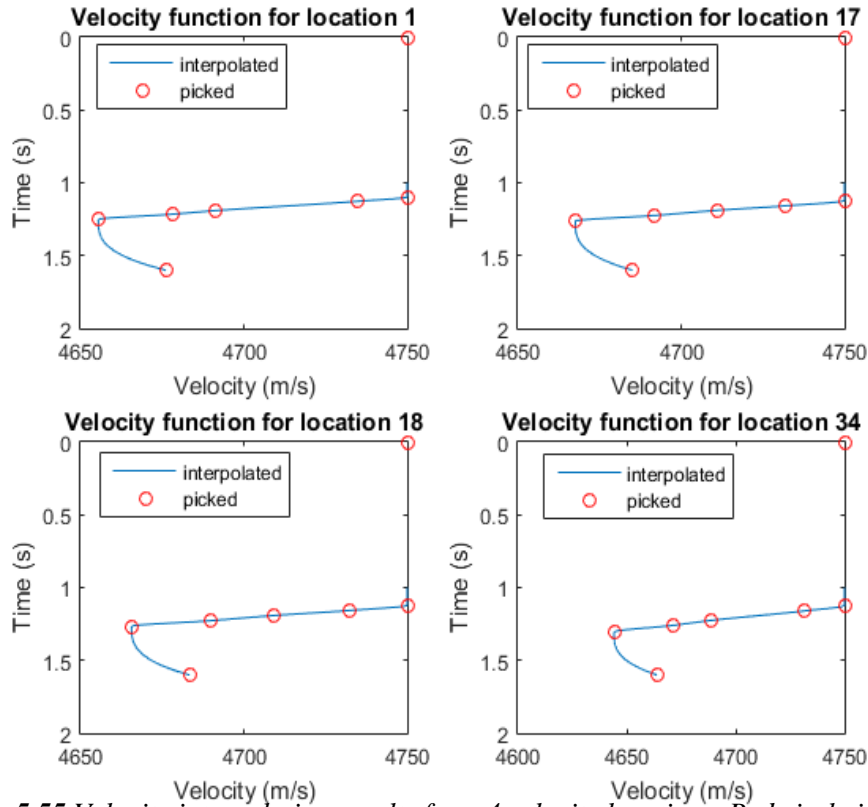


Figure 5.55 Velocity interpolation results from 4 velocity locations. Red circle is the picked velocity, while blue line is the interpolated velocity using shape-preserving cubic interpolation.

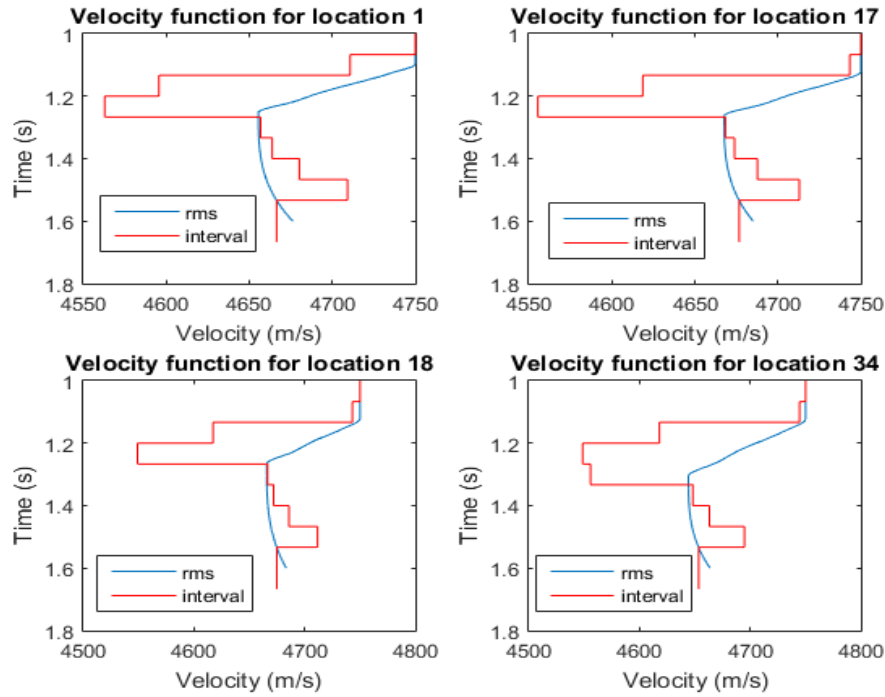


Figure 5.56 Comparison between interpolated v_{rms} (blue) and block constant v_{int} (red) on 4 velocity analysis locations.

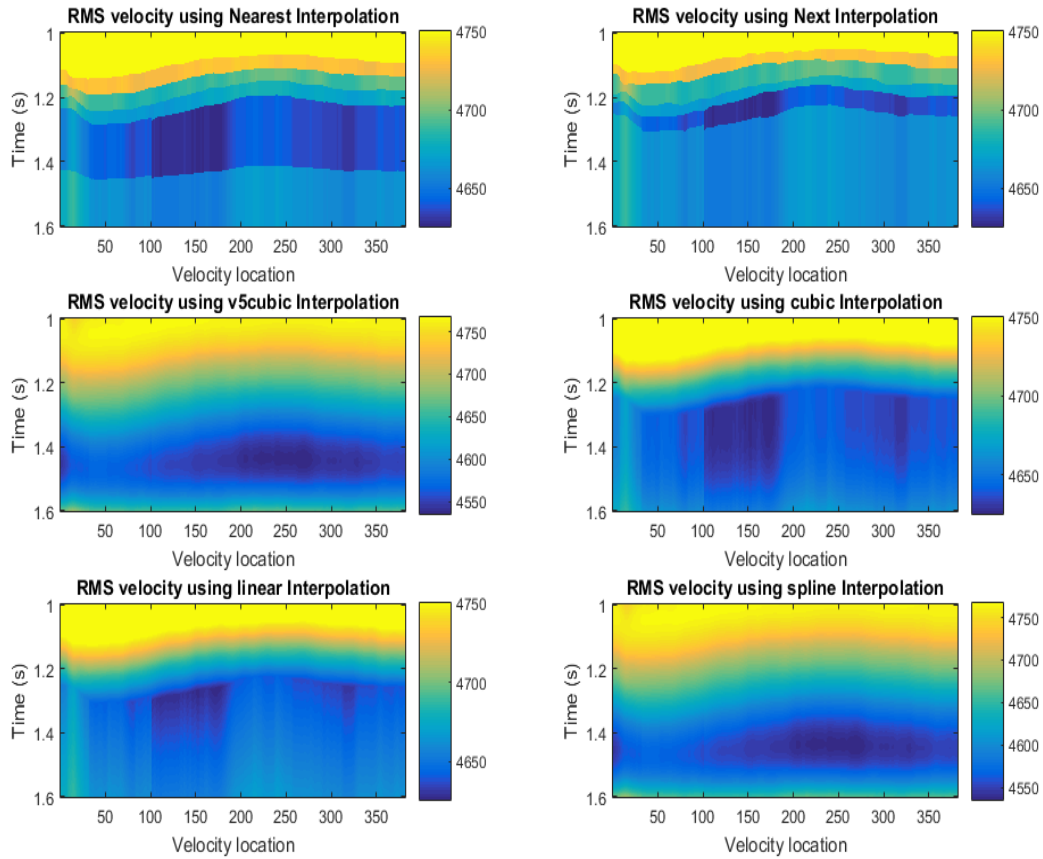


Figure 5.57 Interpolated v_{rms} for all velocity analysis locations.

5.4.8 NMO correction

The process of NMO correction aims to remove the move-out effect on travel time along the offset dimension. The stacking velocities are used to flatten the reflections in each CMP gather. **Figure 5.58** displays a representative example for the CMP gather 150 before and after the application of NMO correction.

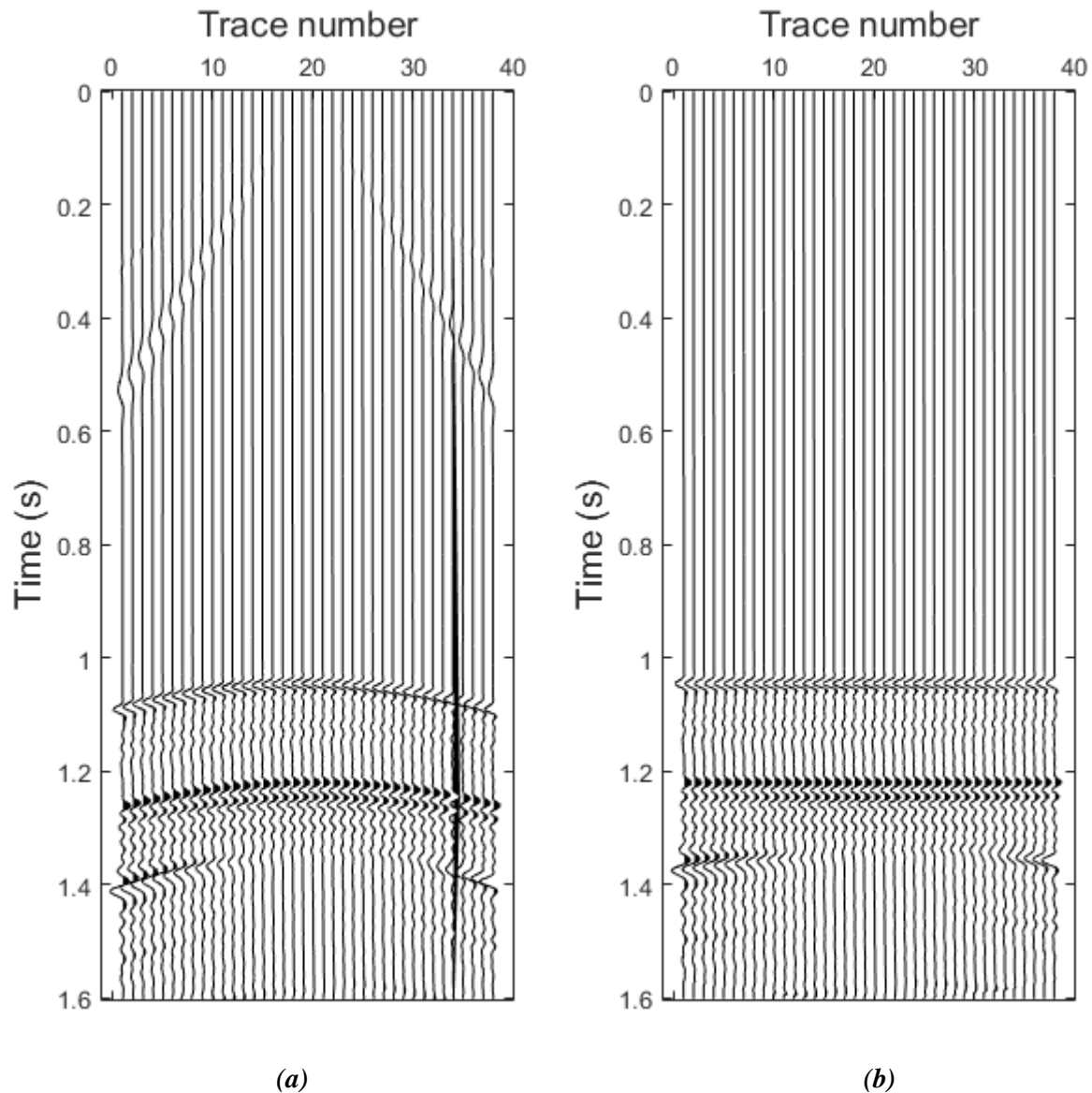


Figure 5.58 CMP gather number 150 (a) before and (b) after the NMO correction.

NMO is a dynamic correction, which means that the values of a single trace are shifted with different amounts. This results, for larger offsets, in a stretching of the data and an artificial increase of the wavelength. This effect is relatively large for horizontal reflections with low velocities. To reduce the effect of the stretching on the result of the stacking procedure, the part with severe stretching of the data is muted from the data (“stretch-mute”). In **Figure 5.59** the effect of stretching on the data is demonstrated.

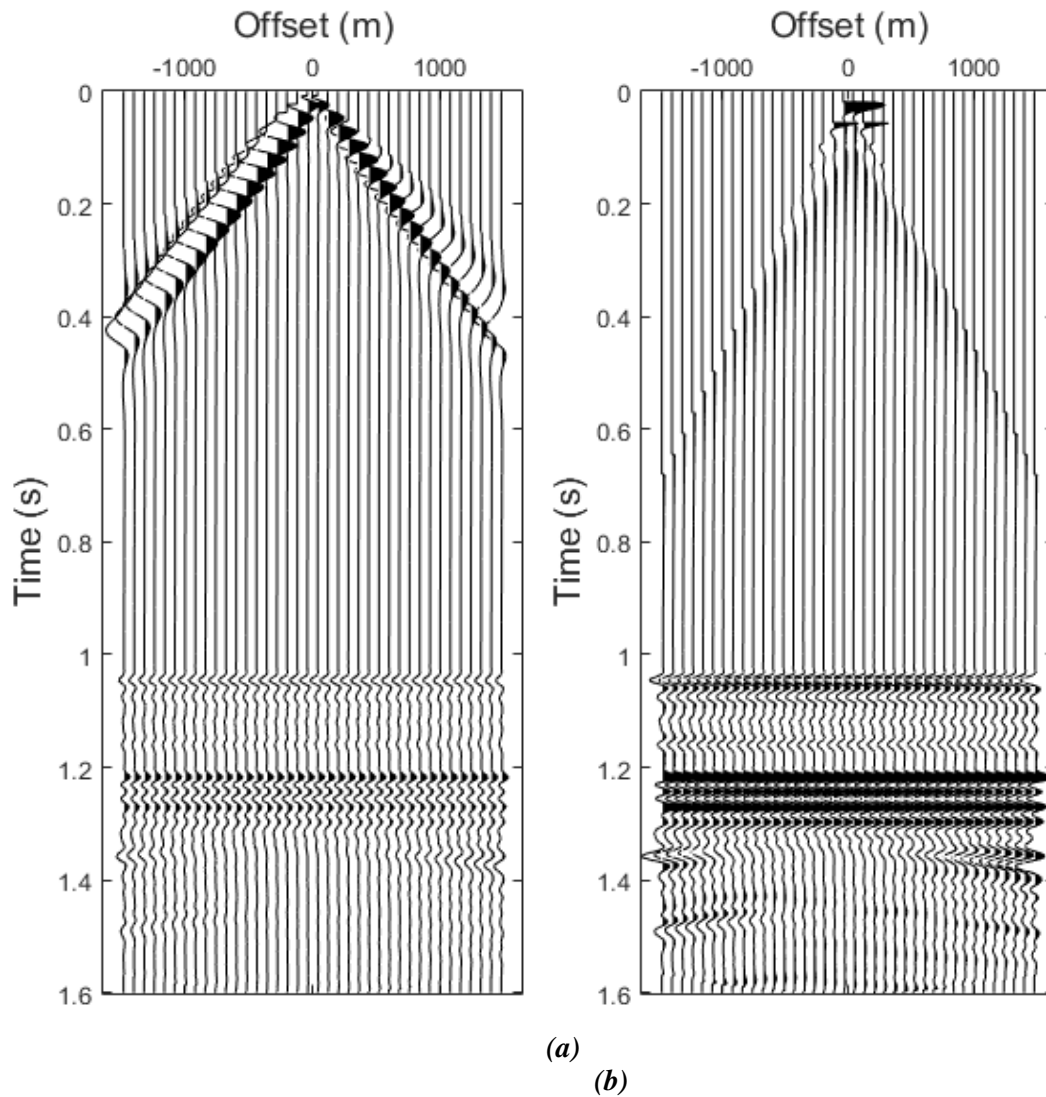


Figure 5.59 CMP gather number 150 NMO corrected for stretching (a) 50% and (b) 10%.

5.4.9 Radon Transform

Radon transform is a generic mathematical procedure in which the input data in the frequency domain are decomposed into a series of events in the Radon domain. Whichever curve type is chosen, will map to a point. Note this is similar to Fourier decomposition but using more complex functions than sinusoids. Common geophysical usage, however, refers to the particular case where the input data is decomposed into parabolas (or sometimes hyperbolas) since this transform can be computed efficiently. The Radon domain can be more accurate for filtering curved rather than dipping events as compared to the FK domain. Thus, the technique is now commonly used for multiple suppression. Parameters required for the Radon transform are the number and spacing of parabolas (often referred to as P traces) and the maximum frequency of transformation. **Figures 5.60 and 5.61** present two examples for elimination of multiples using the Parabolic Radon Transform function **pradon_demultiple**, [University of Alberta, SeismicLab, 2008].

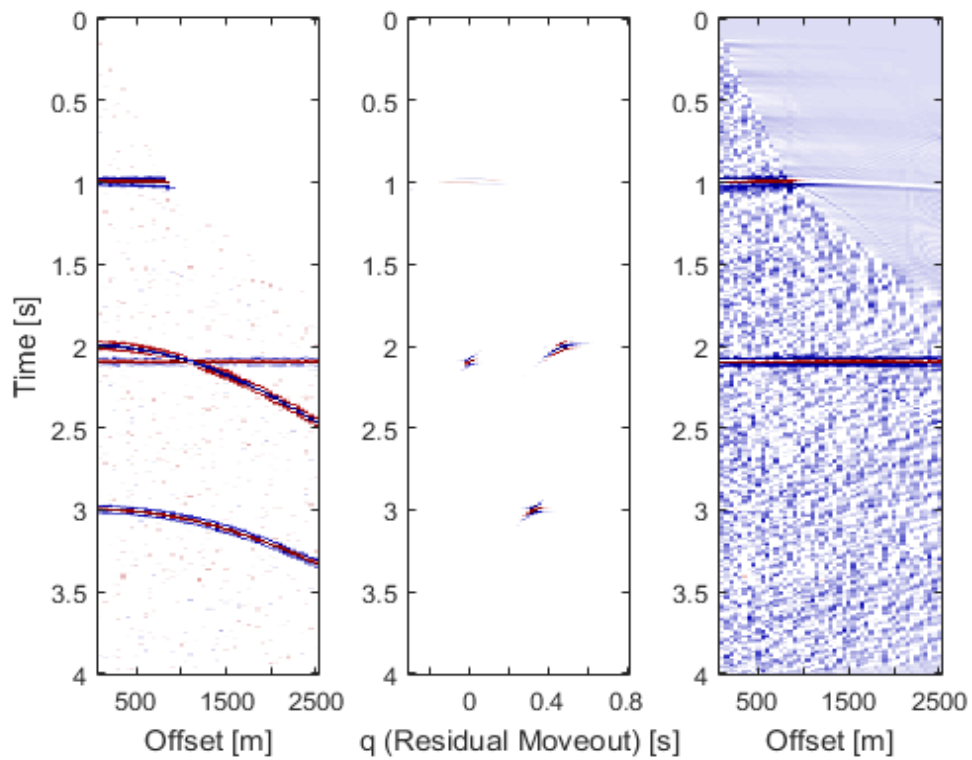


Figure 5.60 Parabolic Radon transform used on synthetic data for the elimination of multiples.

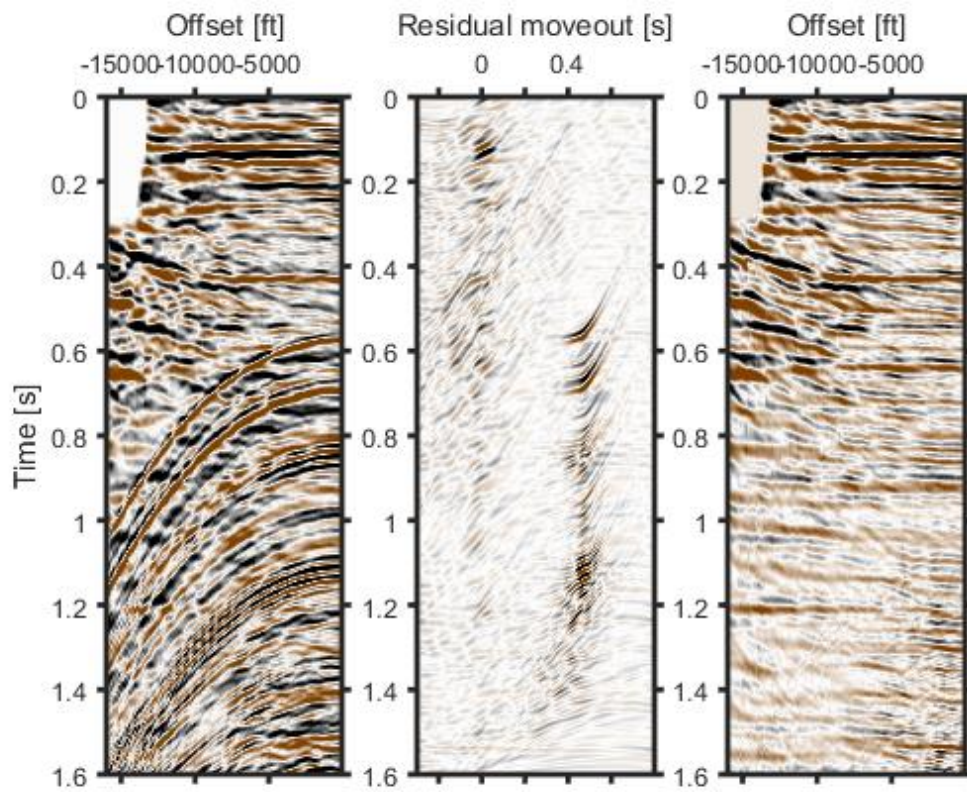


Figure 5.61 Parabolic Radon transform used on real seismic data for the elimination of multiples.

The same function is applied for the CMP gather 200 of the synthetic seismic data and the results are presented graphically in **Figure 5.62**.

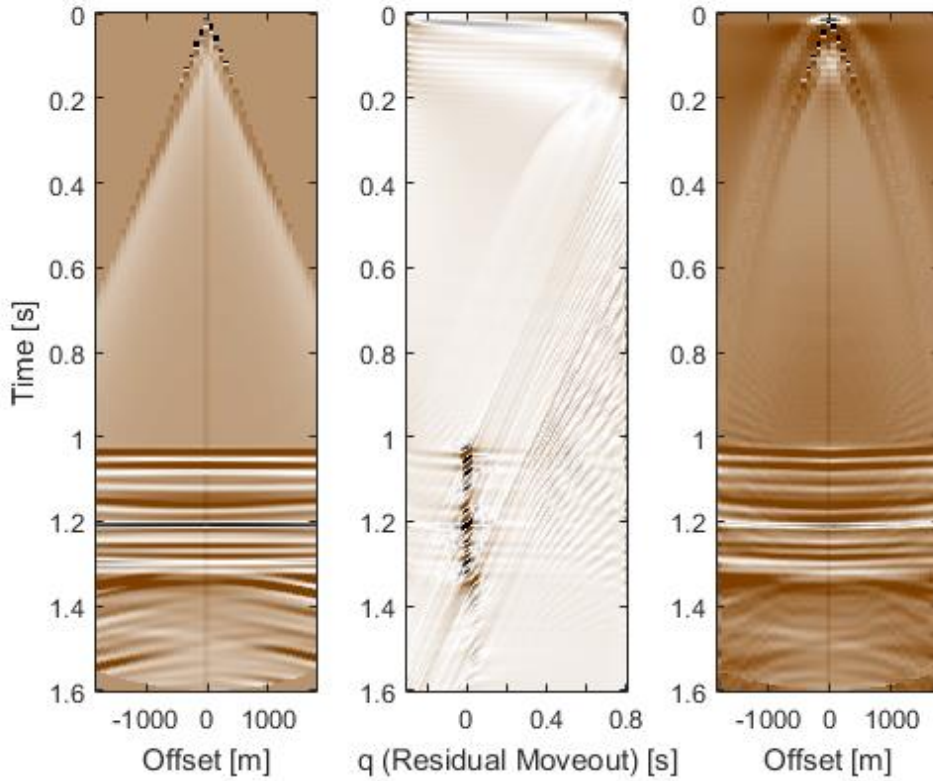


Figure 5.62 Parabolic Radon transform used on CMP gather 200 for multiple's elimination.

5.4.10 Stacking

The NMO-corrected traces in each CMP gather are summed over the offset (stacked) to produce a single trace. Stacking M traces in a CMP increases the SNR of this CMP by \sqrt{M} . The output of the full stack section for the 379 CMP gathers is presented in **Figures 5.63** and **5.64**. Two abnormal hyperbolic reflections can be observed in the stacked section, starting from the upper left part of the section and ending to the lower right part of it. These reflections are attributed to the special geometry of the reservoir which inclines and declines abruptly, misleading the simulator to the creation of erroneous records. Furthermore, the intermediate layers of the reservoir are not clearly distinguishable and may need further post-stack processing in order to boost their amplitudes.

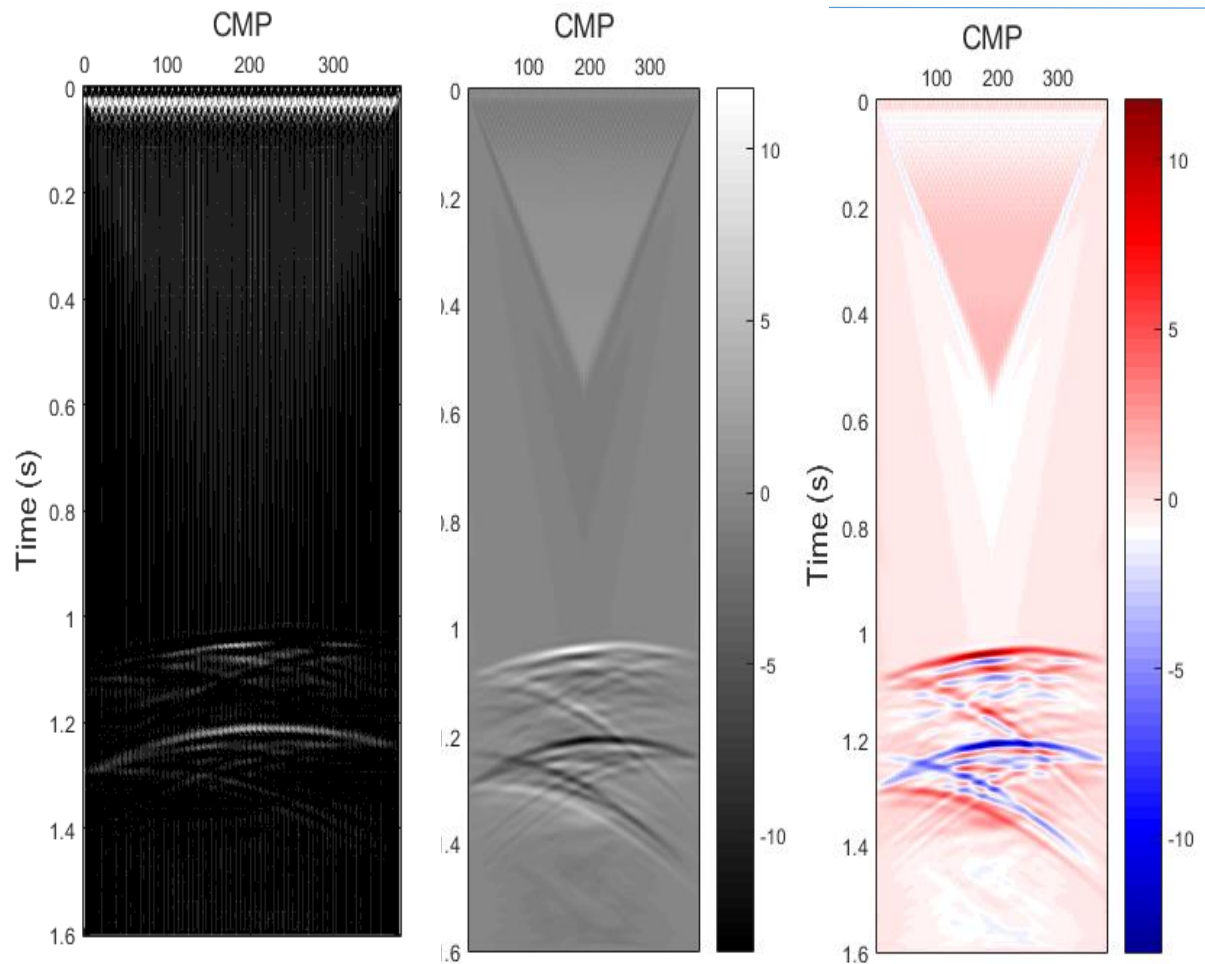


Figure 5.63 Different displays for the full stack section.

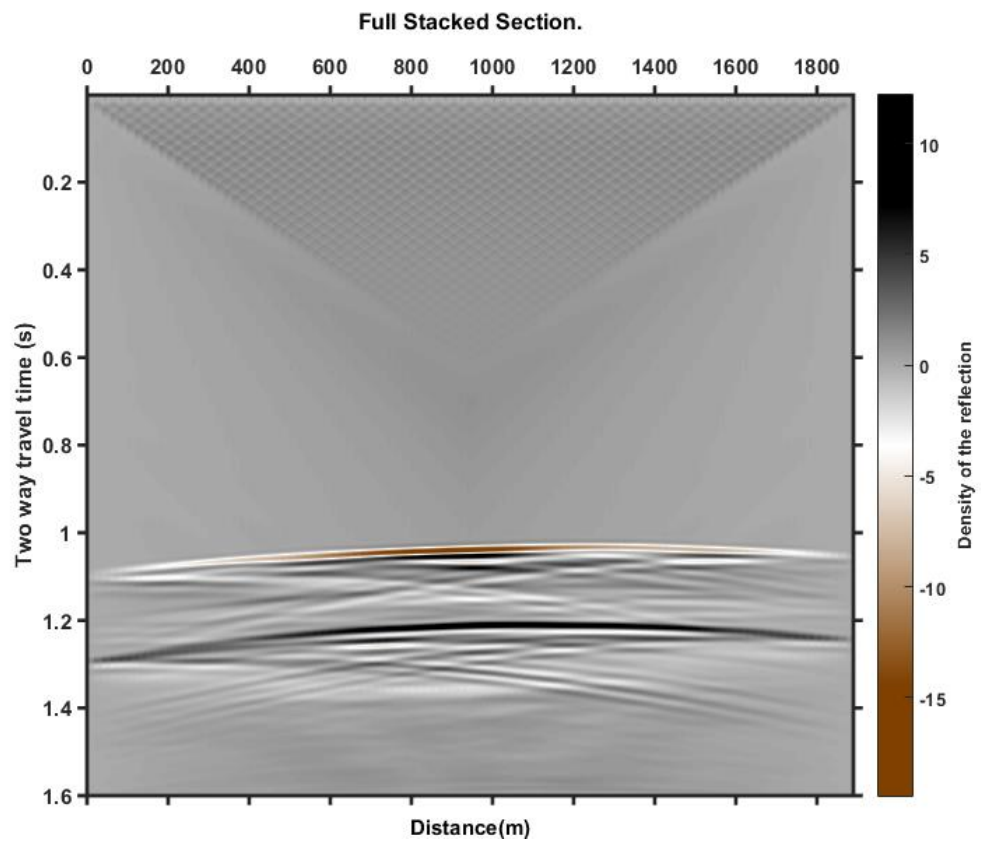


Figure 5.64 Full stack section of synthetic data.

5.4.11 Post-stack Processing

Post-stack processing includes time-variant band-pass filtering, dip filtering and other processes to enhance the stacked section. After applying post-stack FK filtering, Radon transform and spiking deconvolution to the seismic stacked section the intermediate reflectors were significantly enhanced, as shown in **Figure 5.65**.

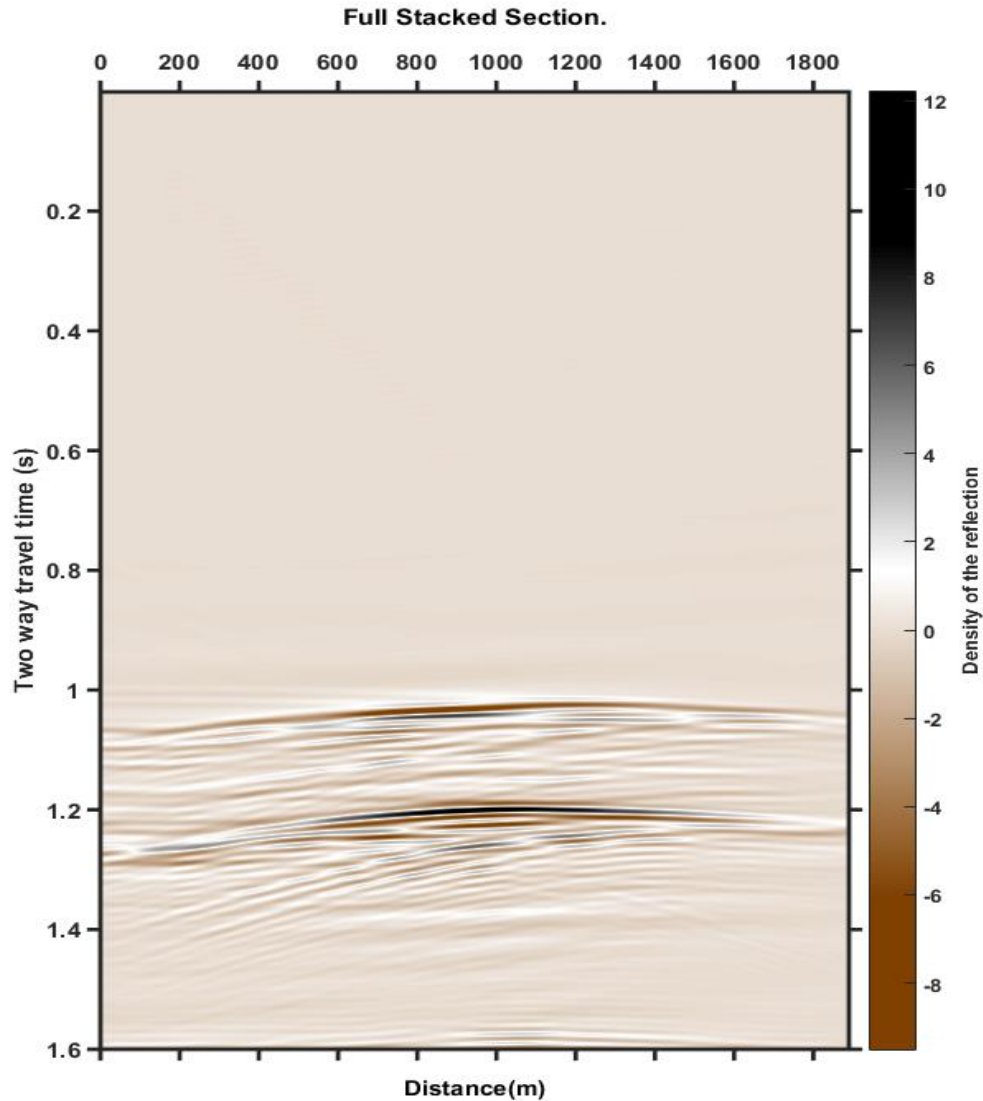


Figure 5.65 Full stack section of synthetic data after post-stack application of FK filtering, Radon transform and spiking deconvolution.

5.4.12 Migration

Seismic migration is the process by which seismic events are geometrically re-located in space or time to the subsurface location the event occurred, rather than the surface location that it was recorded, thereby creating a more accurate image of the subsurface. Dipping reflections are moved to their true subsurface positions and diffractions are collapsed by migrating the stacked section. A form of migration is one of the standard data processing techniques for reflection-based geophysical methods.

Figure 5.66(a) provides an example of a point's reflection, in order to better understand how migration technique is applied. For this example the minimum travel time is given by:

$$t_0 = \frac{2z}{c} \quad (5.14)$$

where z is the depth of the scatter and c is the velocity of the propagating wave, which is assumed to be constant. Also, the source and the receiver are assumed to be co-located (zero-offset).

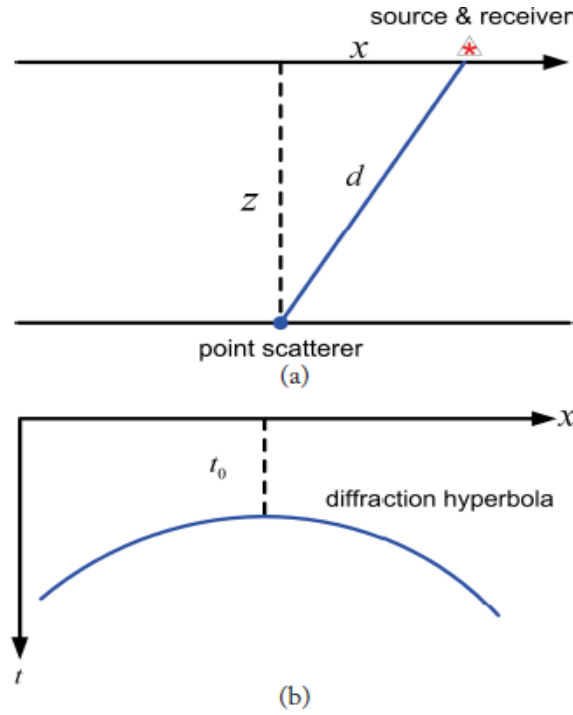


Figure 5.66 (a) A point scatterer (secondary source), and (b) a curved reflector which is produced based on the point scatterer.

The travel time as a function of distance, x , is given by:

$$t(x) = \frac{2\sqrt{x^2 + z^2}}{c} \quad (5.15)$$

By squaring, rearranging, and using (5.14), equation (5.15) can be expressed as:

$$\frac{t(x)^2}{t_0^2} - \frac{4x^2}{c^2 t_0^2} = 1 \quad (5.16)$$

This shows that the travel time curve for the scattered arrival has the form of a hyperbola with the apex directly above the scattering point, as seen in **Figure 5.66(b)**.

Now, in a hypothetical horizontal reflector that is composed of a series of point scatterers (gaps) (**Figure 5.67(a)**), each point will generate a diffraction hyperbola in a zero-offset section (**Figure 5.67(b)**). Following Huygen's principle, these hyperbolas sum coherently only at the time of the reflection, while the later contributions cancel out (**Figure 5.67(b)**). However, if the reflector vanishes at some point, there will be a diffracted arrival from the endpoint that will show up in zero-offset data. This creates an artifact in the section that might be falsely interpreted as structure. Such sections need to be migrated in order to remove such artifacts.

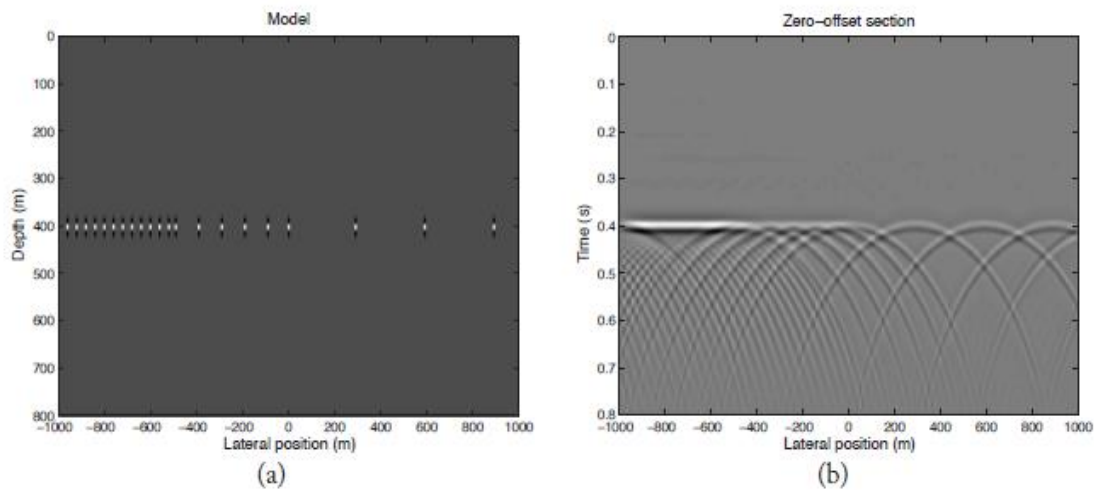


Figure 5.67 (a) An array of point scatterers positioned at different locations, and (b) its resultant curved reflectors interfering with each other.

Migration can be classified as *Pre-stack* migration or *Post-stack* migration. For the former, migration is performed on pre-stacked data either on shot gathers or on CMPs, but requires massive computer storage and processing power.

There are many migration algorithms, but they, mostly, belong to the following four main post-stack migration algorithms:

1. Kirchhoff migration.
2. Frequency-wavenumber-($f - k$) migration.
3. Finite-difference (downward continuation) migration.
4. Phase shift time migration.

All of the above post-stack migration algorithms were implemented in Matlab and applied on the synthetic data (**Figures 5.68-5.71**).

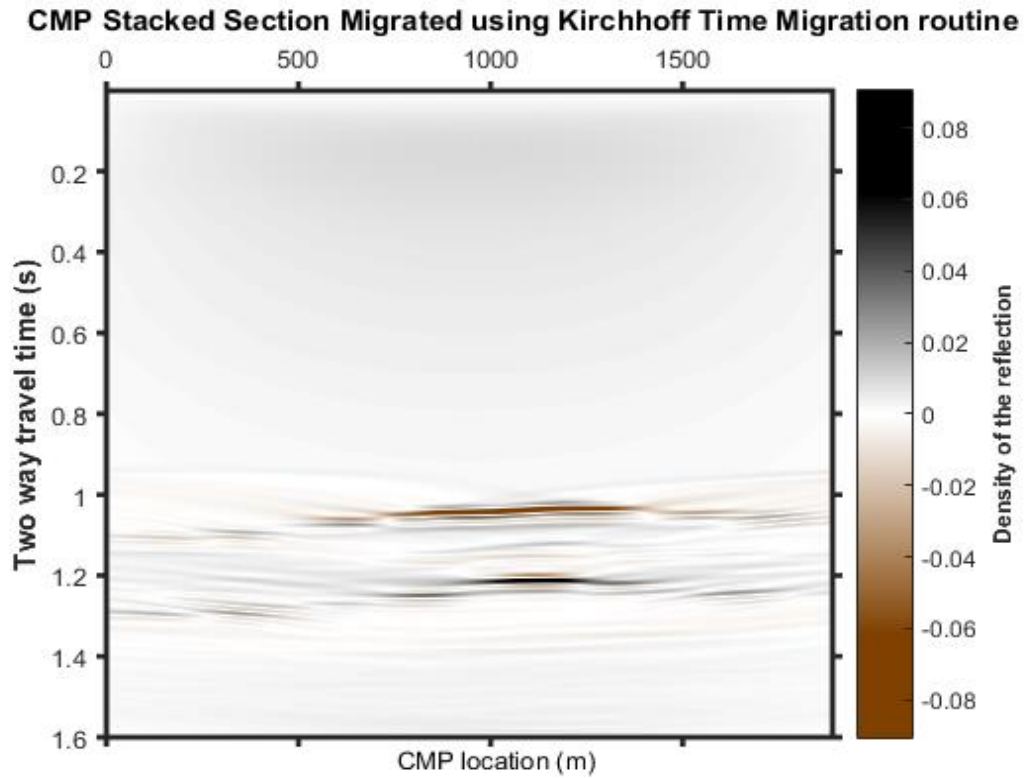


Figure 5.68 Time migrated section using Kirchhoff migration routine.

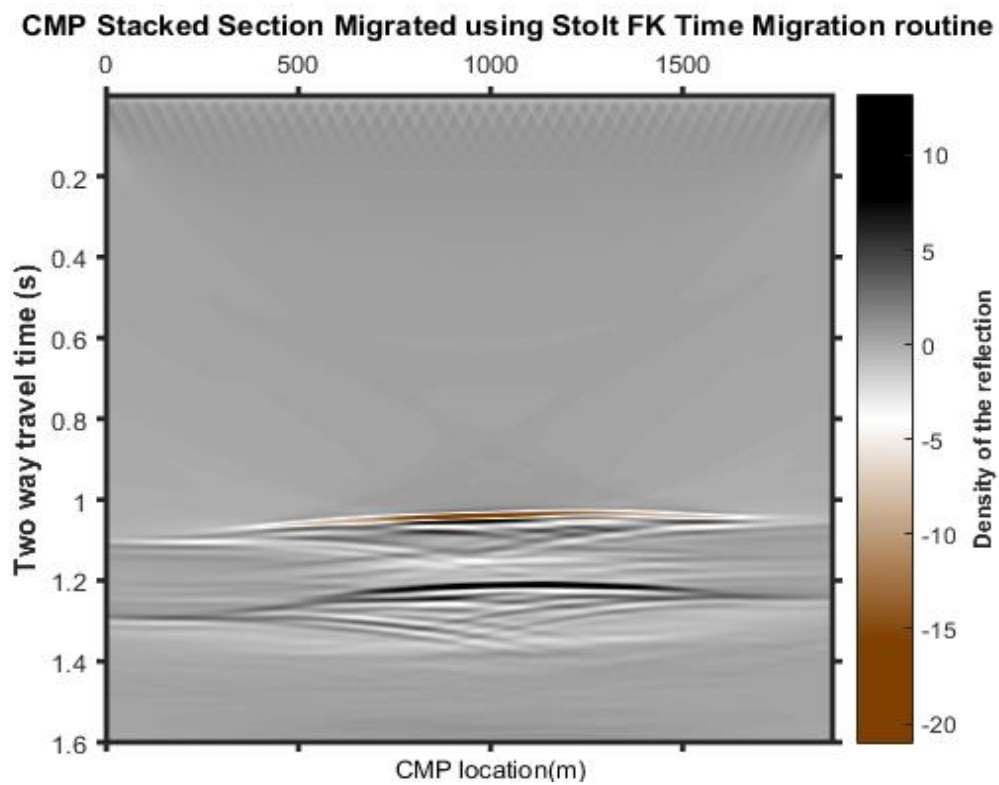
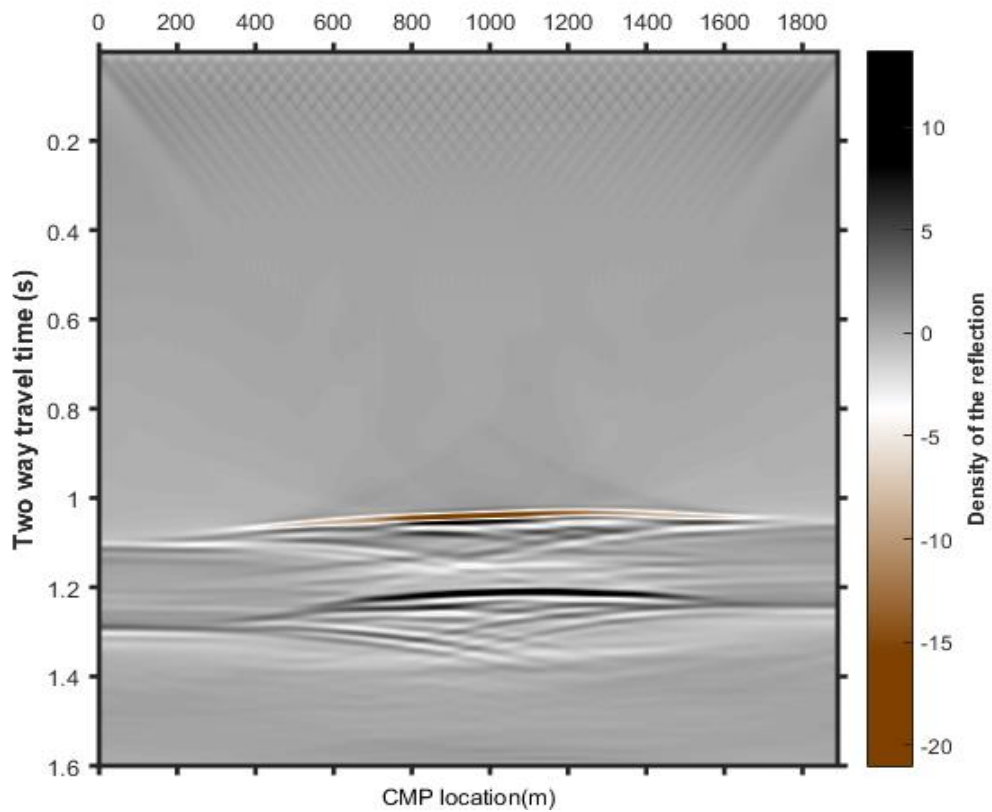
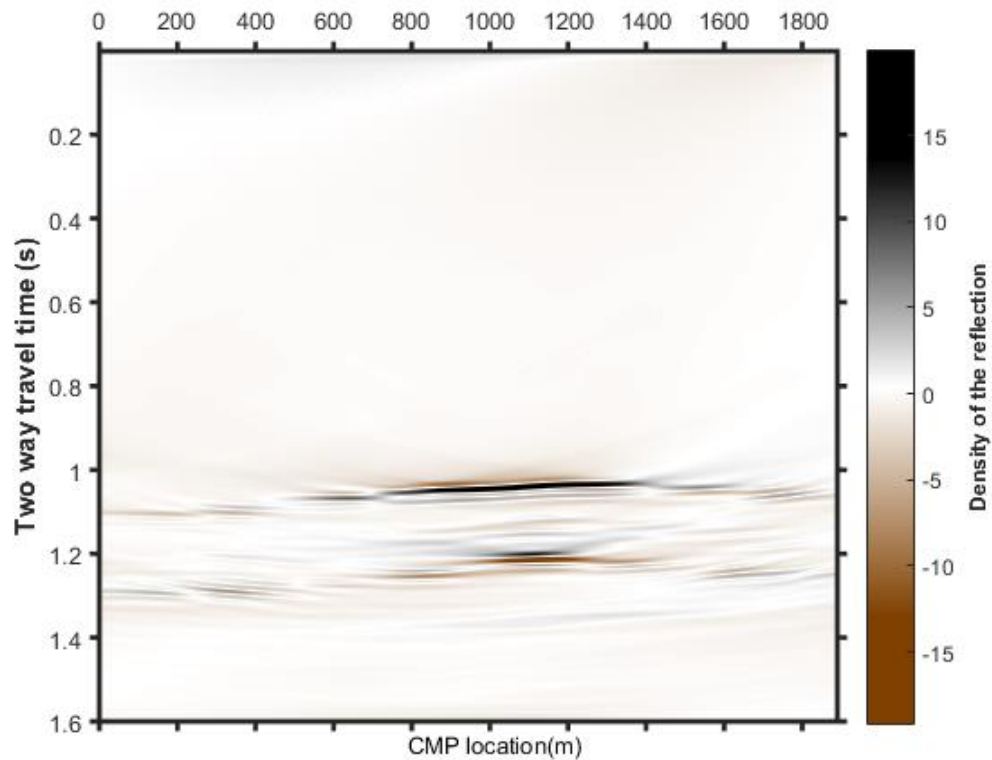


Figure 5.69 Time migrated section using Stolt FK migration routine.

CMP Stacked Section Migrated using Finite Differences Time Migration routine*Figure 5.70 Time migrated section using finite differences migration routine.***CMP Stacked Section Migrated using Gazdag Phase Shift Time Migration routine***Figure 5.71 Time migrated section using Gazdag phase shift migration routine.*

In order to verify the accuracy of the migration, the Kirchhoff time migrated section is superimposed on the reflectors (**Figure 5.72**) and on the rms velocity model (**Figure 5.73**). In both of the cases the migrated section matches the expected values accurately enough.

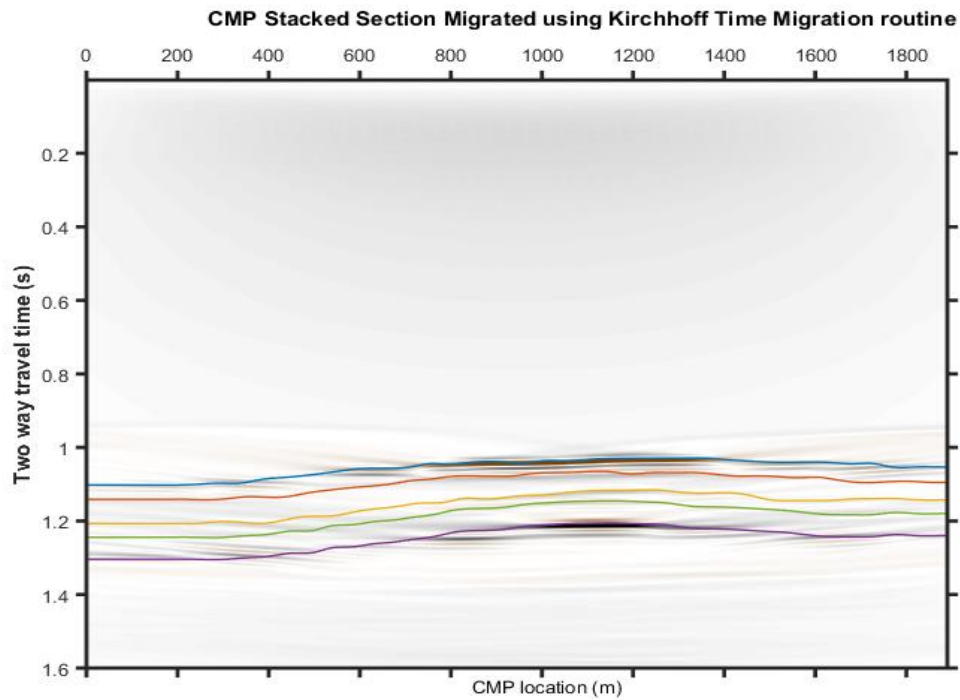


Figure 5.72 Superposition of the reflectors on the migrated section.

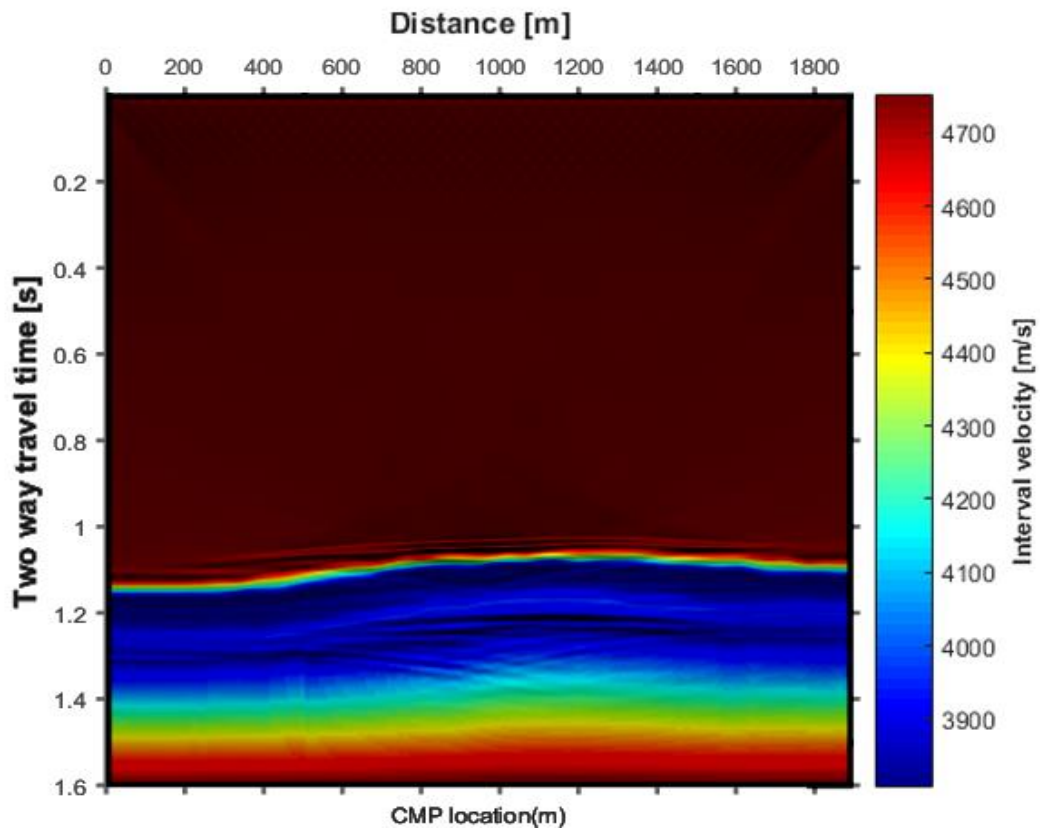


Figure 5.73 Superposition of the interval velocity model on the migrated section.

6 Seismic Processing Graphical Interface

The seismic data processing, described in the previous chapter is usually an extremely demanding and complicated task. Many different processing tests may be needed before achieving the optimal output. In order to simplify the whole procedure, a practical and user-friendly graphical interface (GUI) was designed in Matlab. The GUI can support the whole processing procedure from the commissioning of the SGY data, until the generation of the migrated section, while the results can be represented graphically at any point. In **Figure 6.1** the overall display of the GUI is presented.

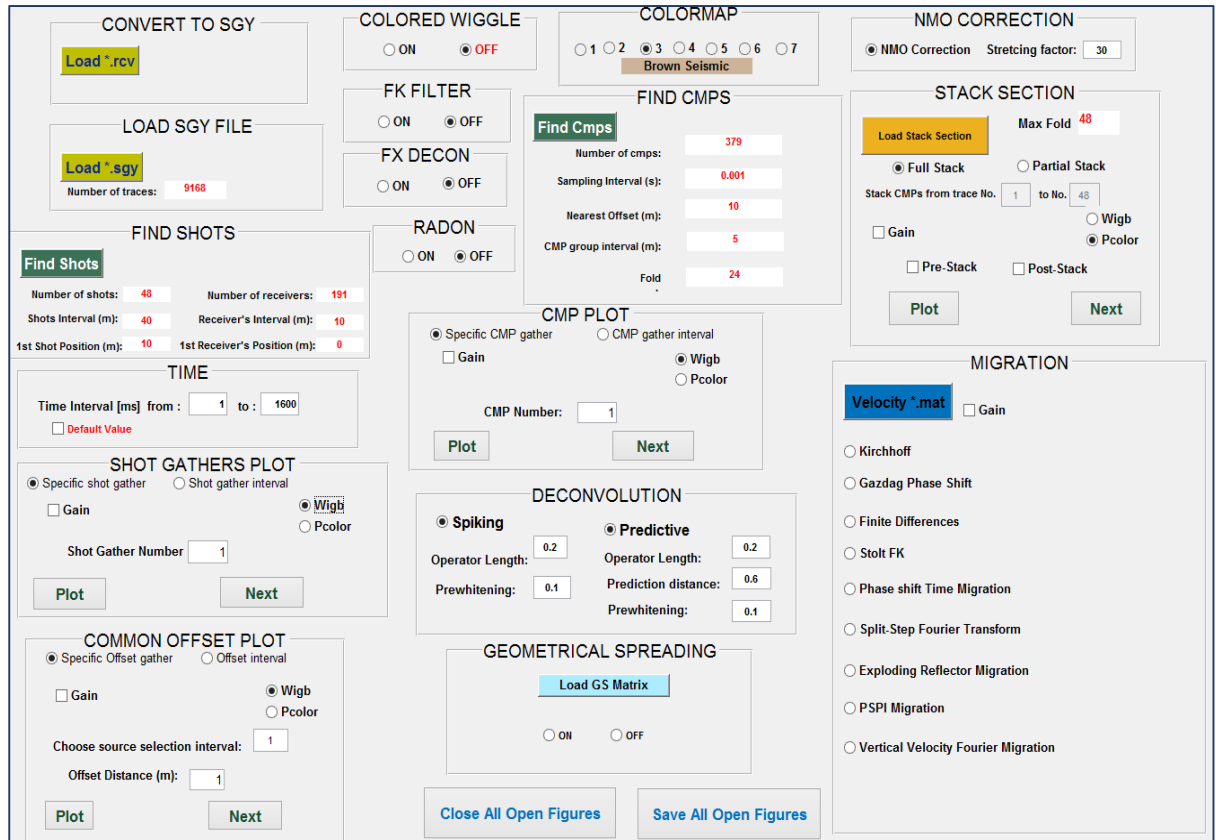


Figure 6.1 Display of the graphical user interface for the seismic processing.

The functionality of the GUI is explained below, separately for each one of its parts, starting from the first function panel “convert to SGY” (**Figure 6.2**). By pushing the button **Load*.rcv** the function **SYNTHETIC2SGY** (TUC, Applied Geophysics Laboratory) is called and the output data of the simulator is converted from .rcv format to an SGY format. As a result the output of the synthetic data simulator can be directly converted to a SGY file for further processing.



Figure 6.2 Convert to SGY function panel.

The next available panel is the “**Load SGY file**”. By pushing the button Load*.sgy the function SEG_Y_OpenFile is called [Hogan, 2008]. The sgy file is read and the number of the traces is given as output. In **Figure 6.3** the output of the panel is given as an example after loading the sgy file of the synthetic data that had been previously created.



Figure 6.3 Load SGY file function panel.

After the sgy has been loaded and read the panel “**Find Shots**” will appear. By pushing the button **Find Shots** the synthetic data (SGY) is analysed and the interface provides as output useful information, such as, the number of shots and receivers, their interval and the position between the first source and receiver.

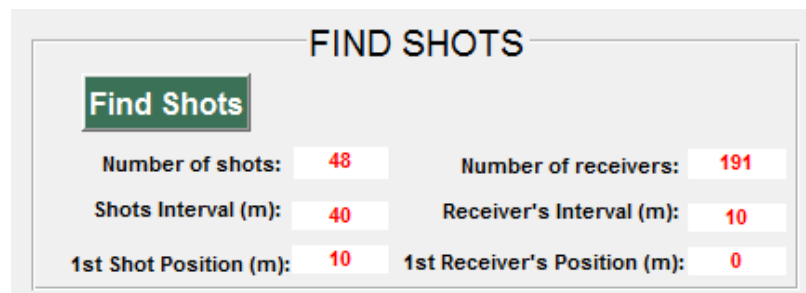


Figure 6.4 Load SGY file function panel.

6.1 Plotting Different Gather Types

Common Shot Gather

In the “Shot Gathers Plot” panel the first graphical representation of the data is available. This block uses the function **SEG_Y_ReadShotGather** (Hogan, 2008) in order to read the data in shot gathers form and plot it either individually (**Specific shot gather**) or massively (**Shot gather interval**) e.g. from shot gather 5 to 8. Furthermore, the data can be plotted either in wiggle or in colored form (**Figure 6.5**), while an amplitude correction scheme can be applied at any point by checking the box **Gain** and choosing the desired gain technique and the Time Window value. In **Figures 6.6** and **6.7** the Shot gather number 20 is plotted as an example in both colored and wiggle plot using an AGC with a Time Window of 0.2

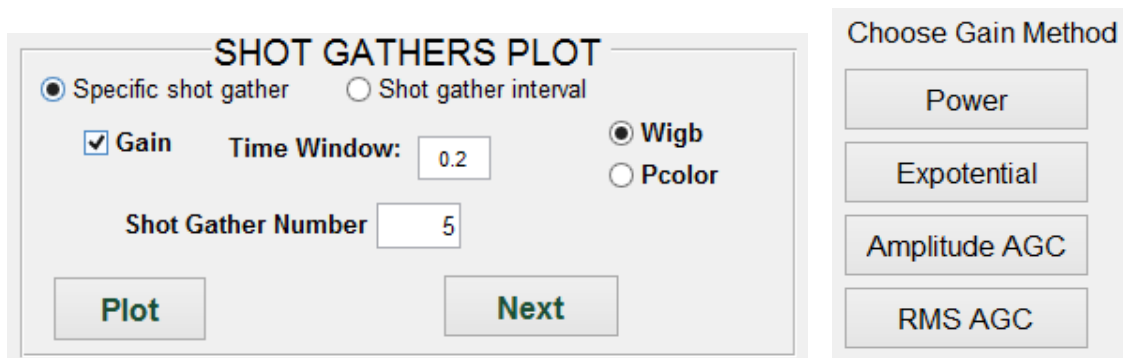


Figure 6.5 Shot gathers plot function panel along with the menu prompt for the gain correction method.

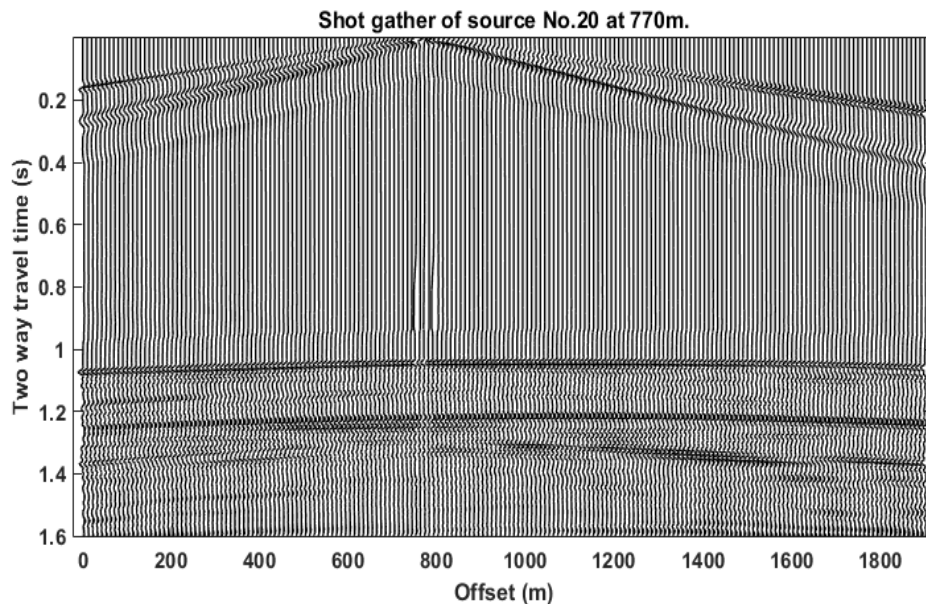


Figure 6.6 Shot gather number 20 in wiggle display.

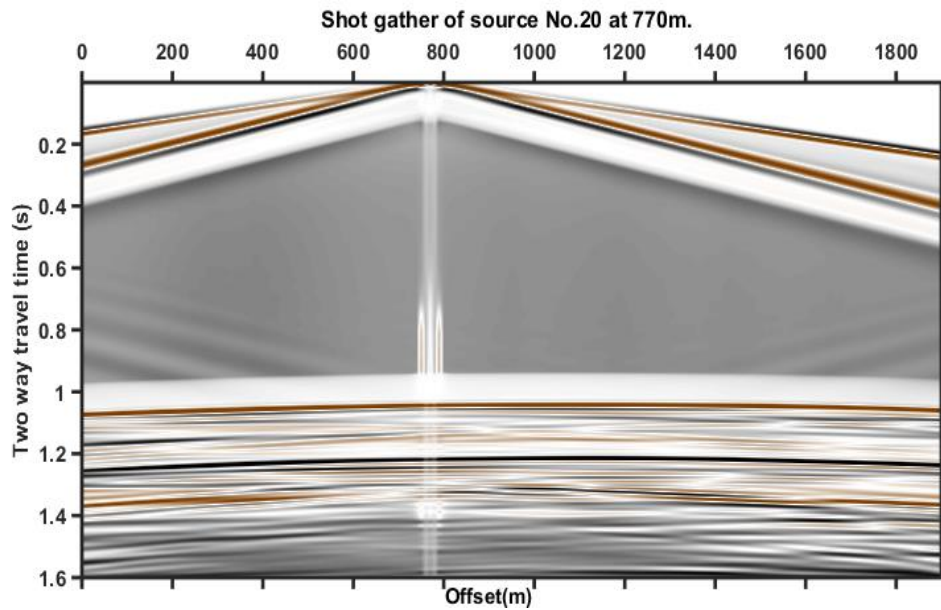


Figure 6.7 Shot gather number 20 in colored display.

In **Figure 6.8** the “**Time block**” is presented. This block is a tool for the plotting of the synthetic data and can limit the time axis to specific time intervals where the reflections may be more distinctive. By checking the box **Default value** the whole time length is given as input. As an example a time interval of [1s-1.4s] is chosen (**Figure 6.8**) and the shot gather number 20 is plotted again for the specific time interval (**Figure 6.9**).

TIME

Time Interval [ms] from : to :

☐ Default Value

Figure 6.8 Time function panel.

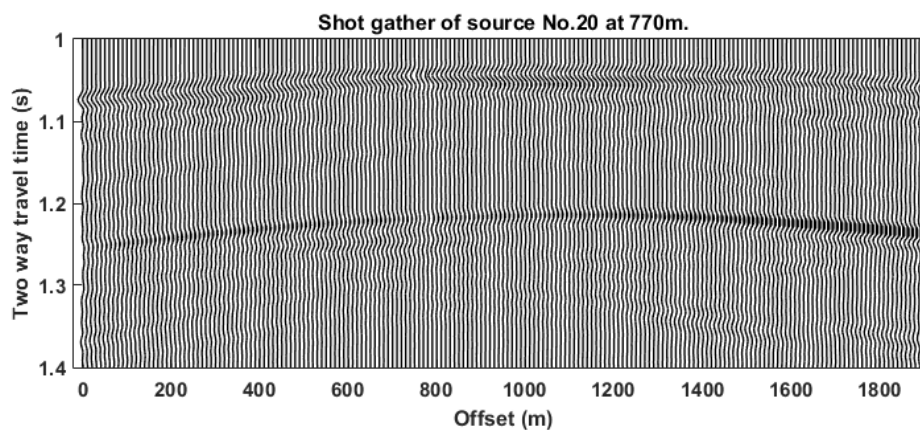


Figure 6.9 Shot gather number 20 for time interval (1s-1.4s).

Common Offset Gather

Similarly, the “**Common Offset Plot**” will display the data in common offset gathers form, giving as input the desired offset distance and the shots interval (**Figure 6.10**). An algorithm was developed for this reason that finds the traces of each shot gather which share the same offset. As an example an offset of 50m was requested with a selection interval of 2 sources and an ACG of 0.2. The result is represented graphically in **Figures 6.11** and **6.12**.

Figure 6.10 Common Offset plot function panel.

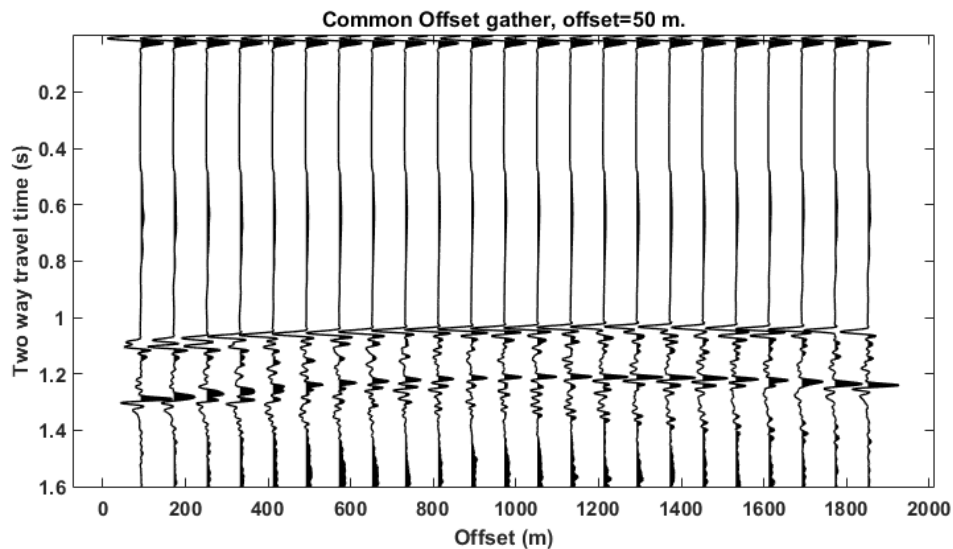


Figure 6.11 Common Offset gather with offset 50 m in wiggle display.

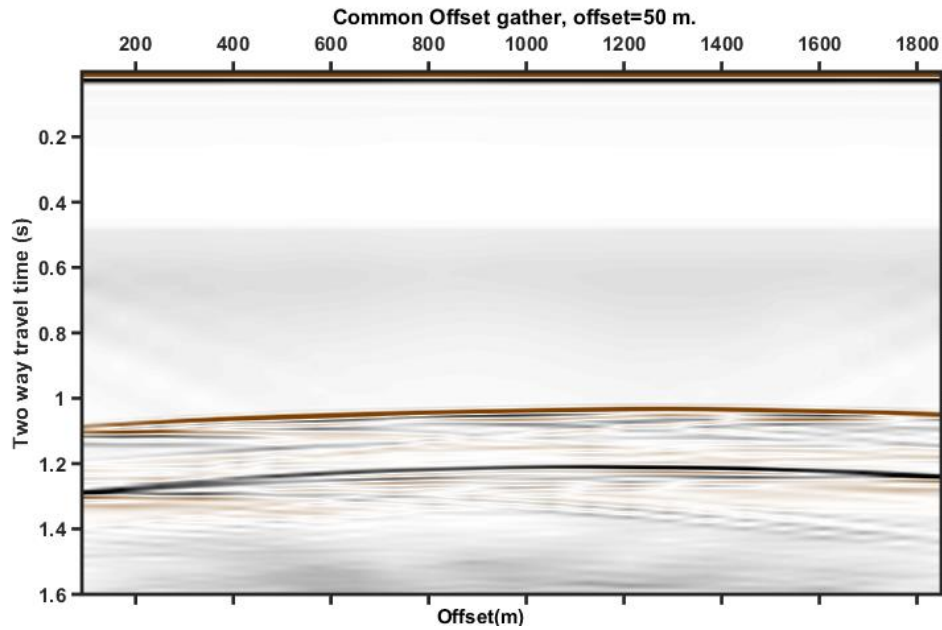


Figure 6.12 Common Offset gather with offset 50 m in colored display.

Common Midpoint Gather

Following, the **“Find Cmps”** panel will convert the data from Common Shot Gather to Common Midpoint Gather with the use of the function **SEG_Y_FindCMPs (Hogan, 2008)**. The panel, after finding the CMPs will display useful information such as the total number of the CMP gathers, the sampling interval, the nearest offset, the CMP group interval and the fold coverage of the CMPs (**Figure 6.13**).

FIND CMPS	
Find Cmps	
Number of cmps:	379
Sampling Interval (s):	0.001
Nearest Offset (m):	10
CMP group interval (m):	5
Fold	24

Figure 6.13. Display of the Find CMPs panel.

As a next step the data can be plotted in the CMP form with the use of the **“Cmp Plot”** panel (**Figure 6.14**). This panel functions in the same way as the other panels that were previously described. As an example the CMP 100 is plotted in **Figures 6.15** and **6.16**.

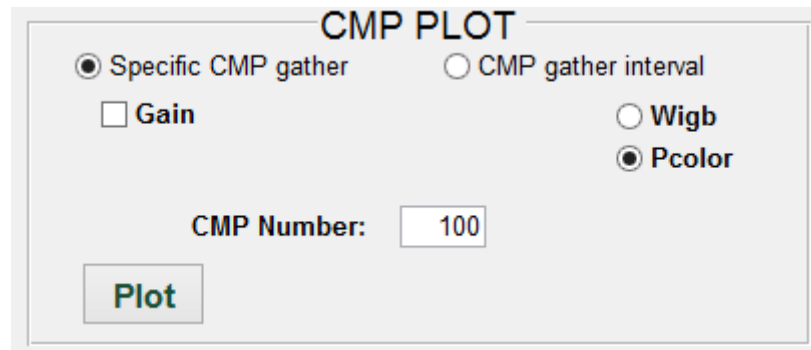


Figure 6.14 Display of the CMP Plot function panel.

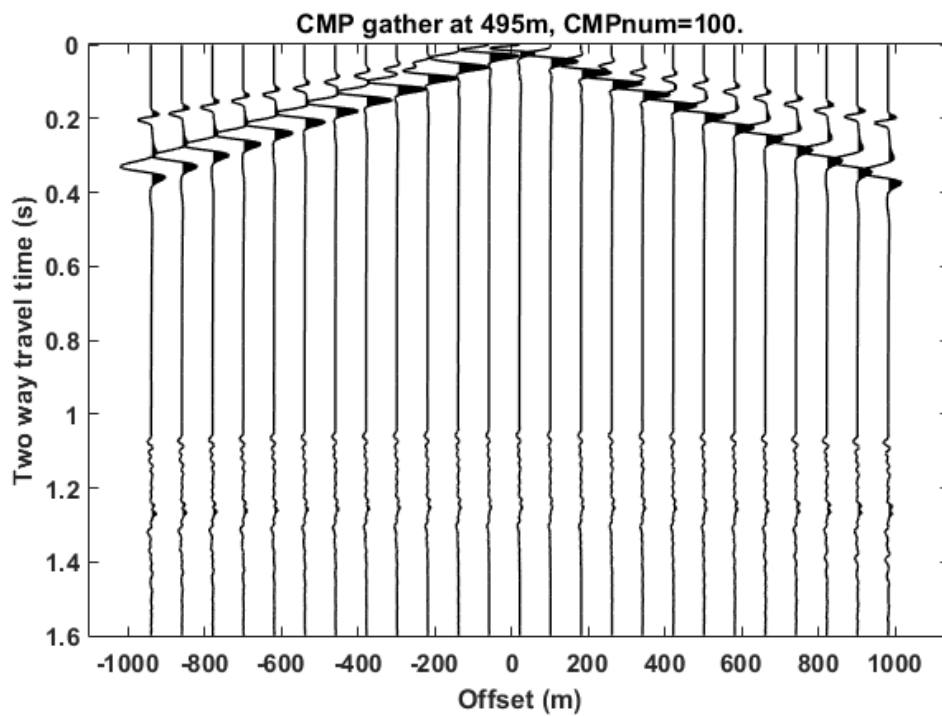


Figure 6.15 Common Midpoint Gather number 100 in wiggle display.

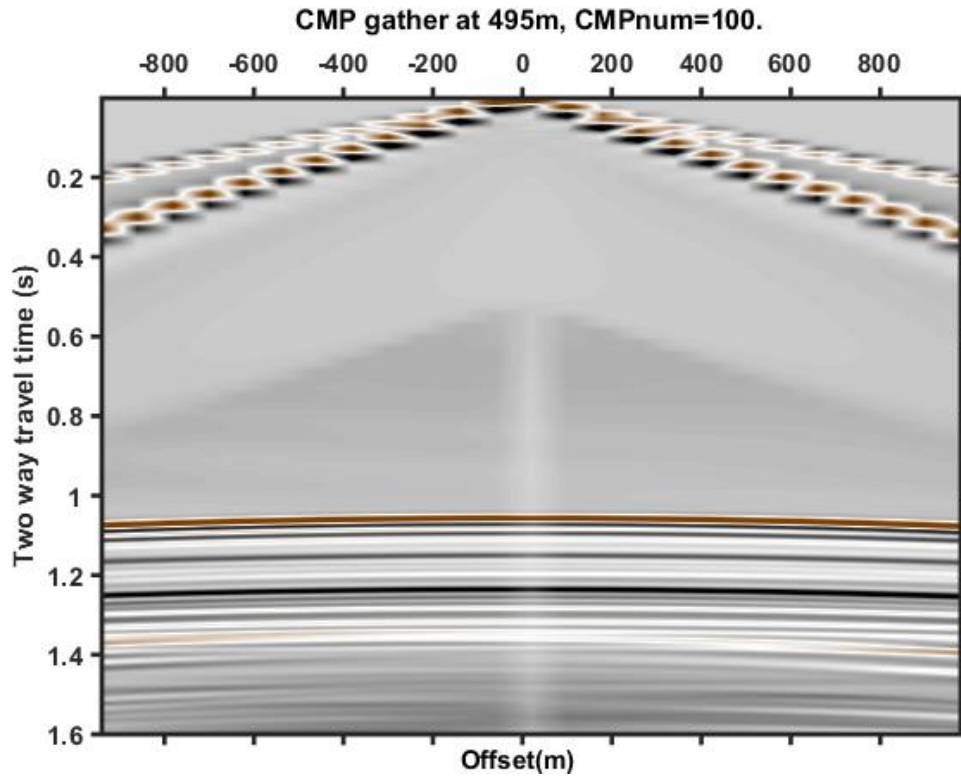


Figure 6.16 Common Midpoint Gather number 100 in colored display.

6.2 Signal Processing Analysis

The next available panels are associated with the signal processing analysis of the seismic data, presented analytically on chapter 5. The first panel, named “**FK filter**” (**Figure 6.17**) applies FK filtering on the data with the use of the function **fk_filter** (Tzanis, 2005). The function allows the user to design a band pass filter of the data on the screen (in frequency domain) and after applying the filter, transforms back the data to time domain with inverse Fourier transform. An example of the FK filter application on CMP gather 100 is shown on **Figures 6.18** and **6.19**.



Figure 6.17 Fk filter function panel.

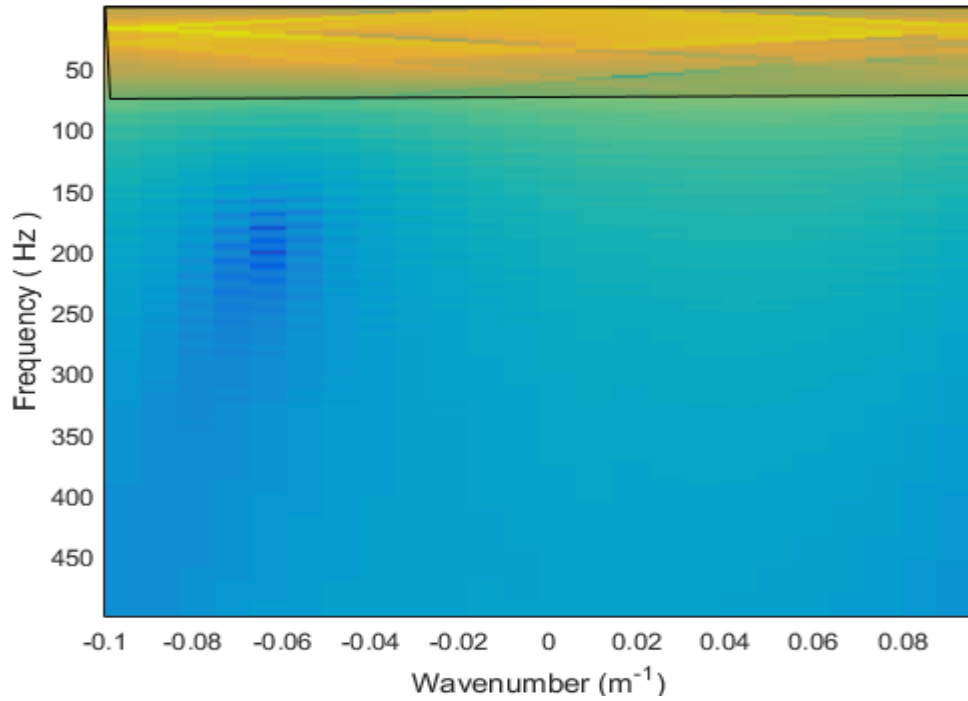


Figure 6.18 Design of the polygonal zone band-pass filter for CMP 100.

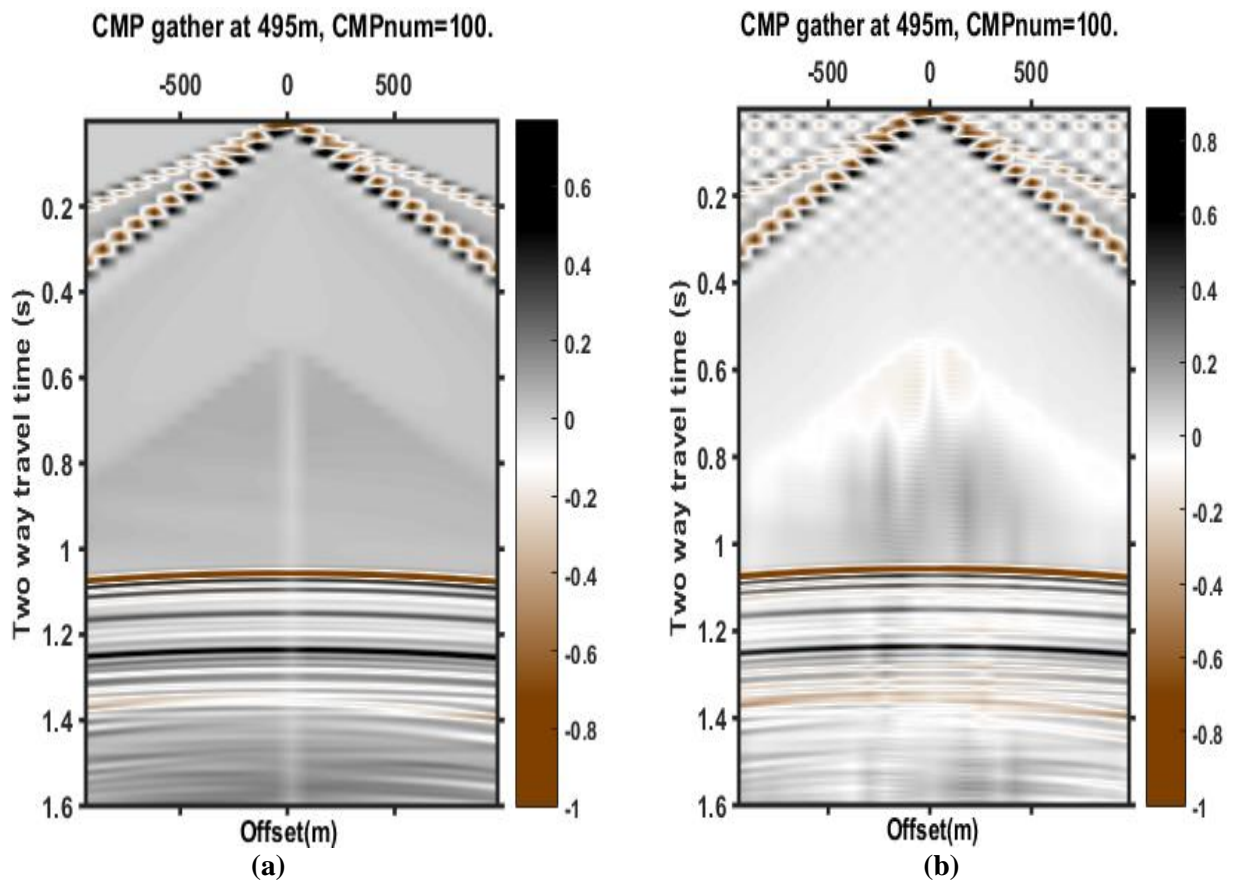


Figure 6.19 CMP gather 100 (a) before and (b) after the fk filtering.

The next panel, named “**FX decon**” (**Figure 6.20**) applies FX deconvolution on the data with the use of the function **fx_decon** (Sacchi, 2008). The inputs of the function are inserted through a dialog box, shown in **Figure 6.21**.

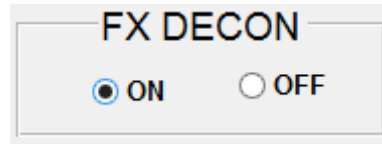


Figure 6.20 FX deconvolution function panel.

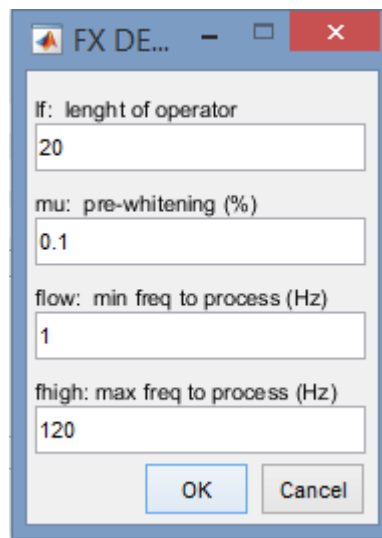


Figure 6.21 Dialog box for FX deconvolution operator's selection.

Following, the panel “**Radon**” (**Figure 6.22**) applies Radon transform on the data with the use of the function **pradon_demultiple**, [University of Alberta, SeismicLab, 2008]. The inputs of the function are inserted through a dialog box, shown in **Figure 6.23**. An example of the FX deconvolution application on CMP gather 100 is shown on **Figure 6.24**.

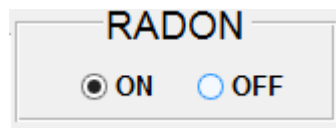


Figure 6.22 Radon transform function panel.

RADON TRANSFORM

qmin: min residual moveout at far offset (secs)
-0.3

qmax: max residual moveout at far offset (secs)
0.8

nq: number of samples of the residual moveout axis
120

flow: min freq to process (Hz)
1

fhigh: max freq to process (Hz)
120

mu: trade-off parameter for LS solution used to retrieve the Radon panel
0.1

q_cut: keep contributions from q_cut to qmax, this is to estimate the multiples that are removed from the primaries
0.05

OK Cancel

Figure 6.23 Dialog box for Radon transform operator's selection.

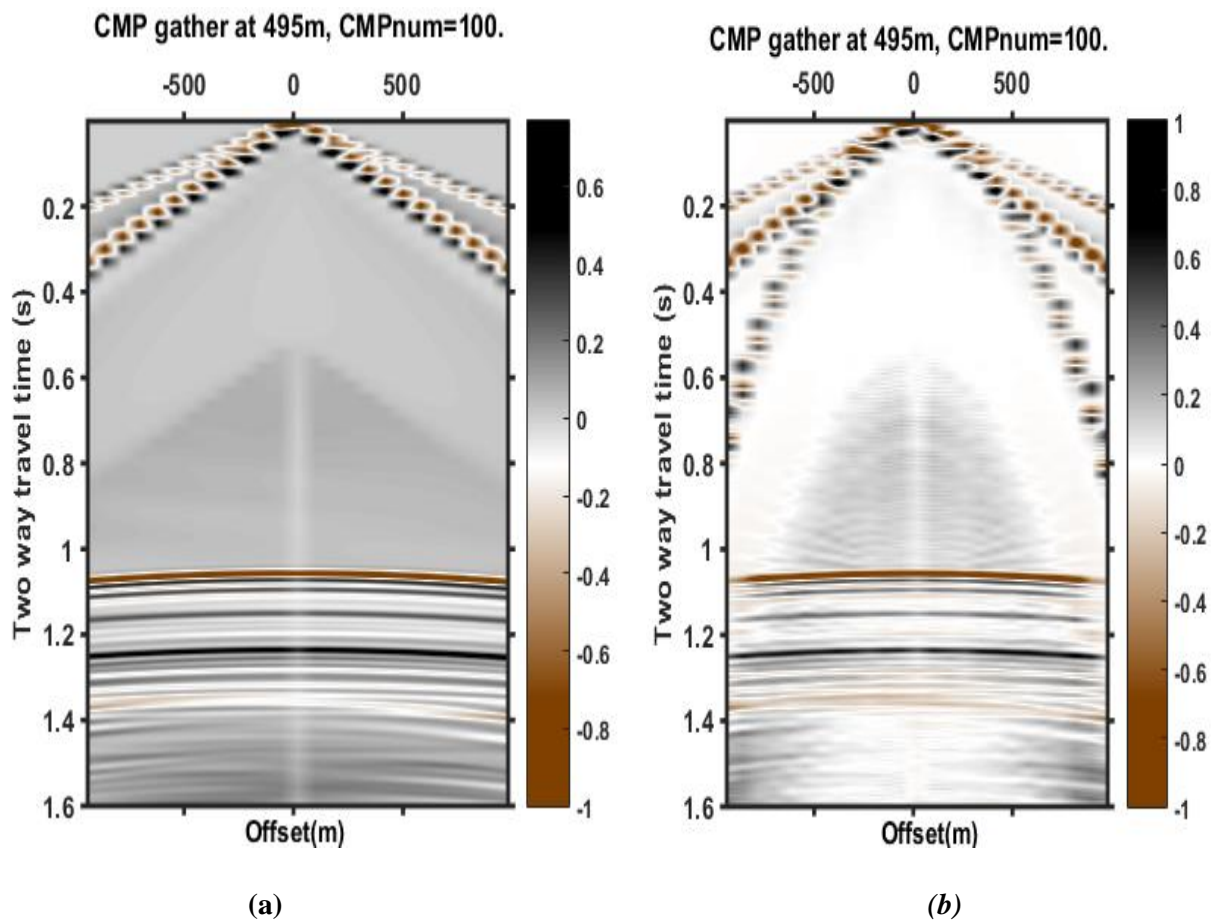


Figure 6.24 CMP gather 100 (a) before and (b) after the radon transform.

The following panel, named “**Deconvolution**” (Figure 6.25) applies spiking or predictive deconvolution to the data with the use of the functions **spiking** and **predictive** (Sacchi, 2008). The inputs of the functions can be directly inserted to the same panel. An example is given again for CMP 100 before and after the application of Spiking and predictive deconvolution in Figure 6.26.

DECONVOLUTION

☒ **Spiking**
 Operator Length:
 Prewhitening:

☒ **Predictive**
 Operator Length:
 Prediction distance:
 Prewhitening:

Figure 6.25 Spiking and predictive deconvolution function panel.

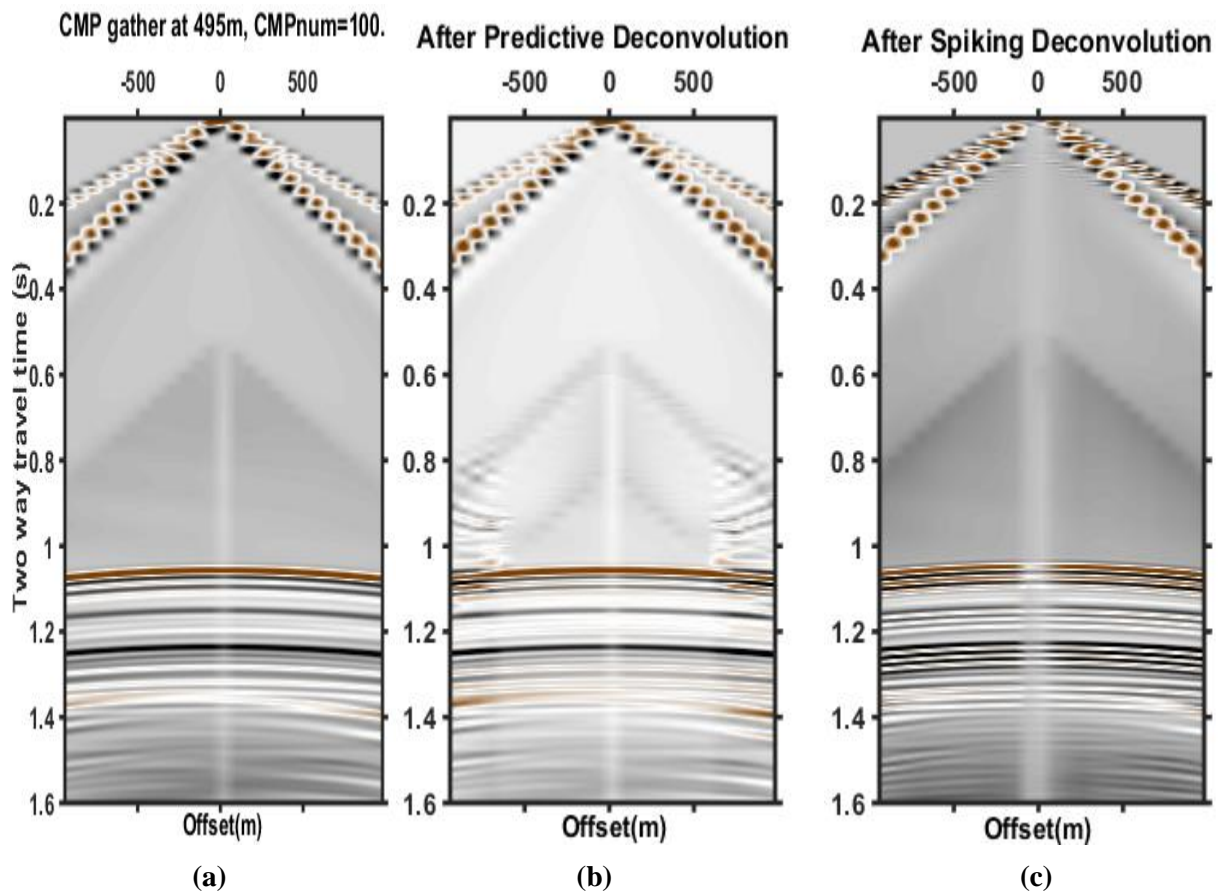


Figure 6.26 CMP gather 100 (a) before, (b) after the predictive and (c) after spiking deconvolution.

The panel “**Geometrical Spreading**” (Figure 6.27) applies spherical divergence correction to the data after loading the suitable .m file, containing the GS matrix. The GS matrix is a matrix containing the product of RMS velocities and time of the synthetic data. An example for CMP 100 is given in Figure 6.28.

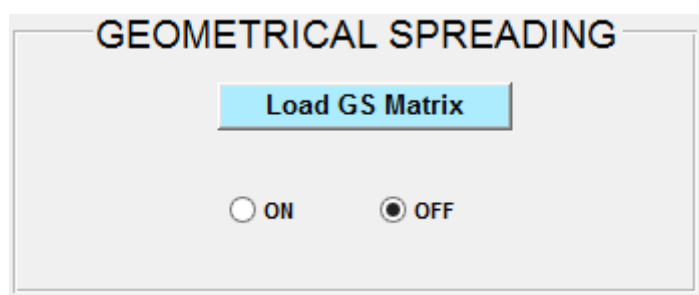


Figure 6.27 Geometrical Spreading function panel.

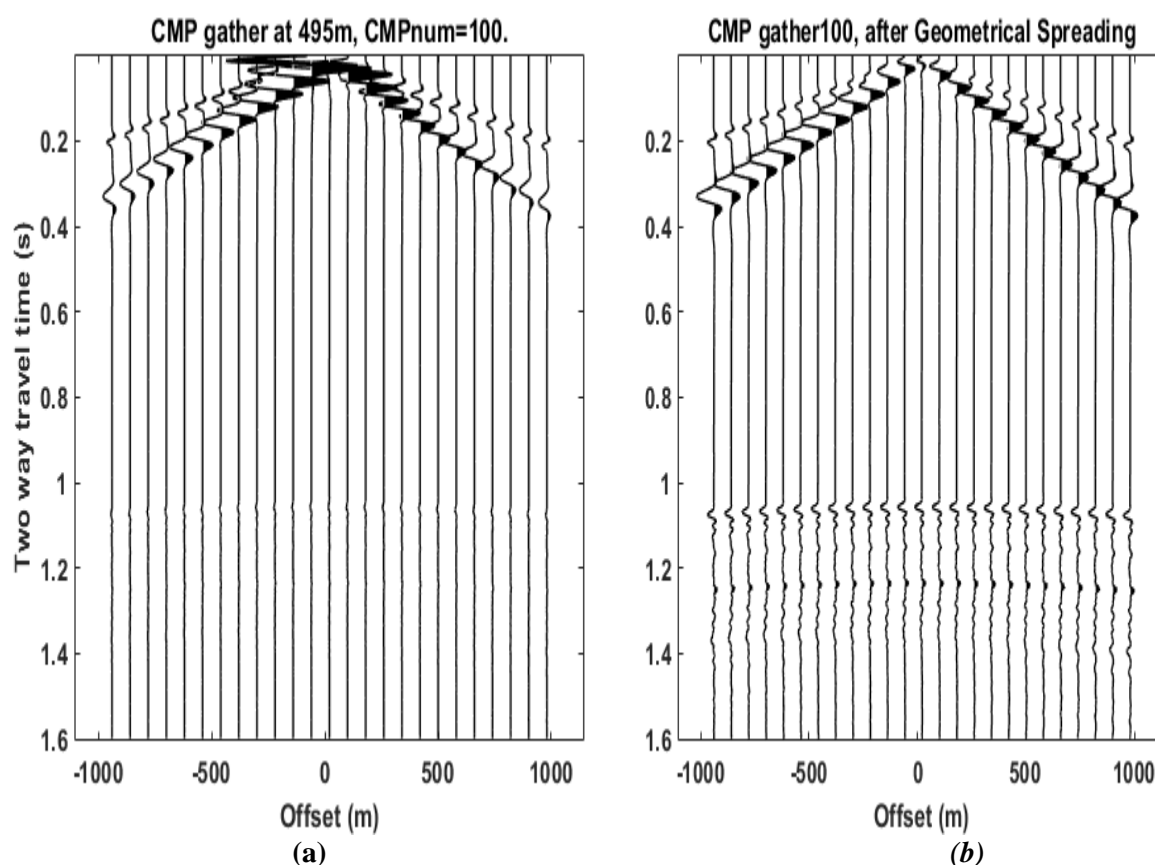


Figure 6.28 CMP gather 100 (a) before and (b) after geometrical spreading correction.

Following, “**Nmo Correction**” panel (Figure 6.29) applies nmo correction to the cmp gathers giving the desirable stretch factor as input. The panel uses the function nmo (Sacchi, 2008). An example for CMP 100 is given in Figure 6.30.

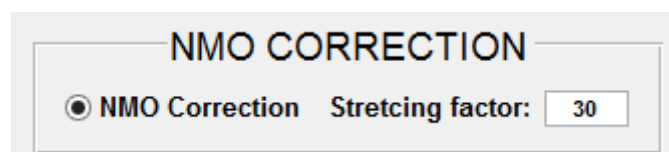


Figure 6.29 NMO correction function panel.

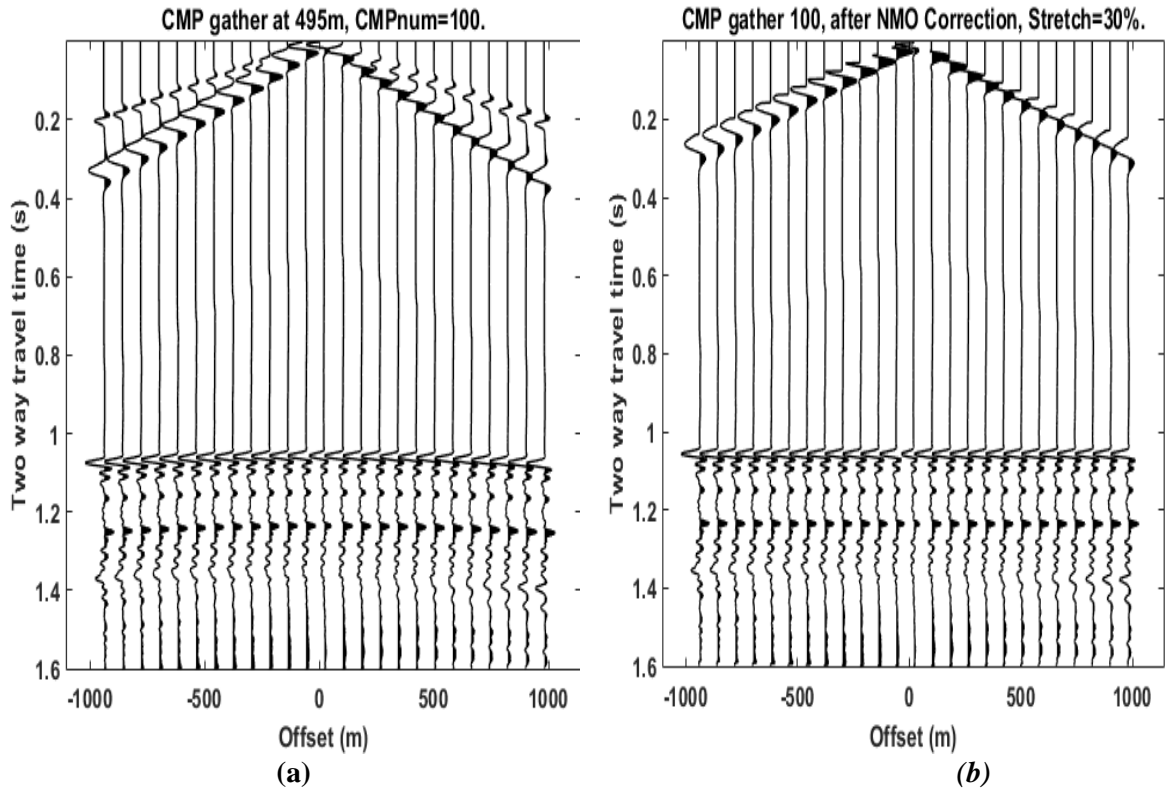


Figure 6.30 CMP gather 100 (a) before and (b) after nmo correction.

6.3 Stack section

In the “**Stack Section**” panel (**Figure 6.31**), all the CMP gathers of the model are read (or loaded, if they have been previously read) and summed in order to create the stack section of the model. The stack section panel gives to user the ability to apply different processing schemes on the pre-stacked and the post-stacked data. A partial stack of the data is also available by giving the desired initial and final traces of the cmp gather. In **Figure 6.32** an example is given for the full stack section of the model, before and after the post stack processing.

STACK SECTION

Max Fold 48

☐ Full Stack
 ☒ Partial Stack

Stack CMPs from trace No. to No.

☒ Gain
 ☒ Pre-Stack

Time Window:

☐ Wigb
☒ Pcolor

Figure 6.31 Stack section function panel.

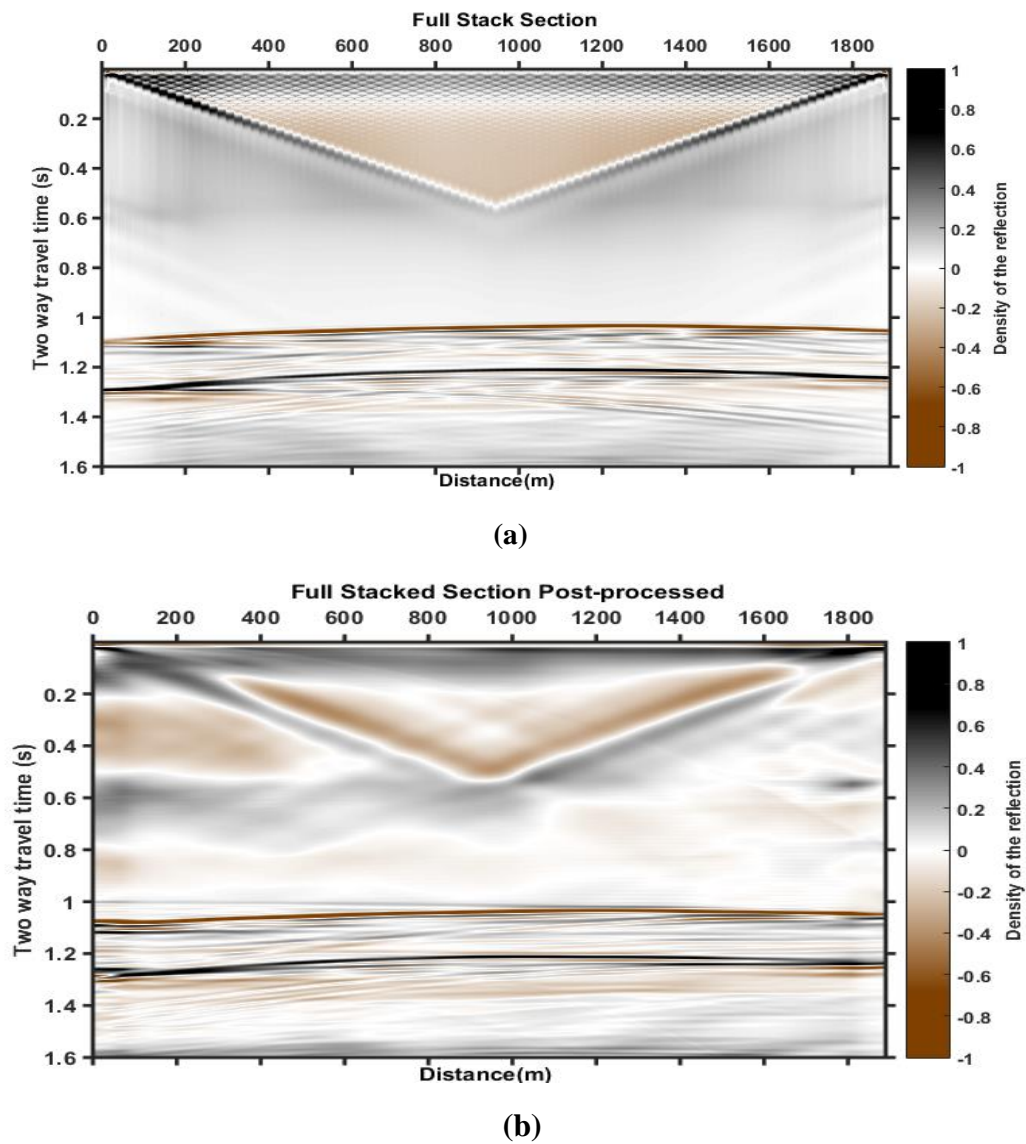


Figure 6.32 Full stack section (a) before and (b) after post-processing.

6.4 Migration

The final panel is the “**Migration**” panel (**Figure 6.33**). However, before the application of the migration, the velocity values should be interpolated. By pressing the Velocity *.mat button the Velocity analysis matrix is loaded and the velocity values are interpolated with the use of the Matlab function griddata. After loading the matrix a menu pops up, asking for the desired interpolation method (**Figure 6.33**). The results of the velocity models for linear interpolation are given in **Figures 6.34** and **6.35**. Finally, nine different migration algorithms have been embodied to the GUI, corresponding to different migration techniques. The functions that were used for the migration algorithms are, `kirk_mig` (Margrave, 1996), `ps_migt` (Ferguson, 1996), `fd15mig` (Margrave, 2000), (Margrave and Bancroft, 1996), `psmig` (Xinxiang, 1996), `splitstepf_mig` (Margrave, 2000), `psnps_mig` (Margrave, 1996) and `pspi_stack_tmig_rms` (Margrave, 2014). Indicatively, the PSPI and Vertical velocity Fourier migrations are applied to the data and plotted in **Figures 6.36** and **6.37**.

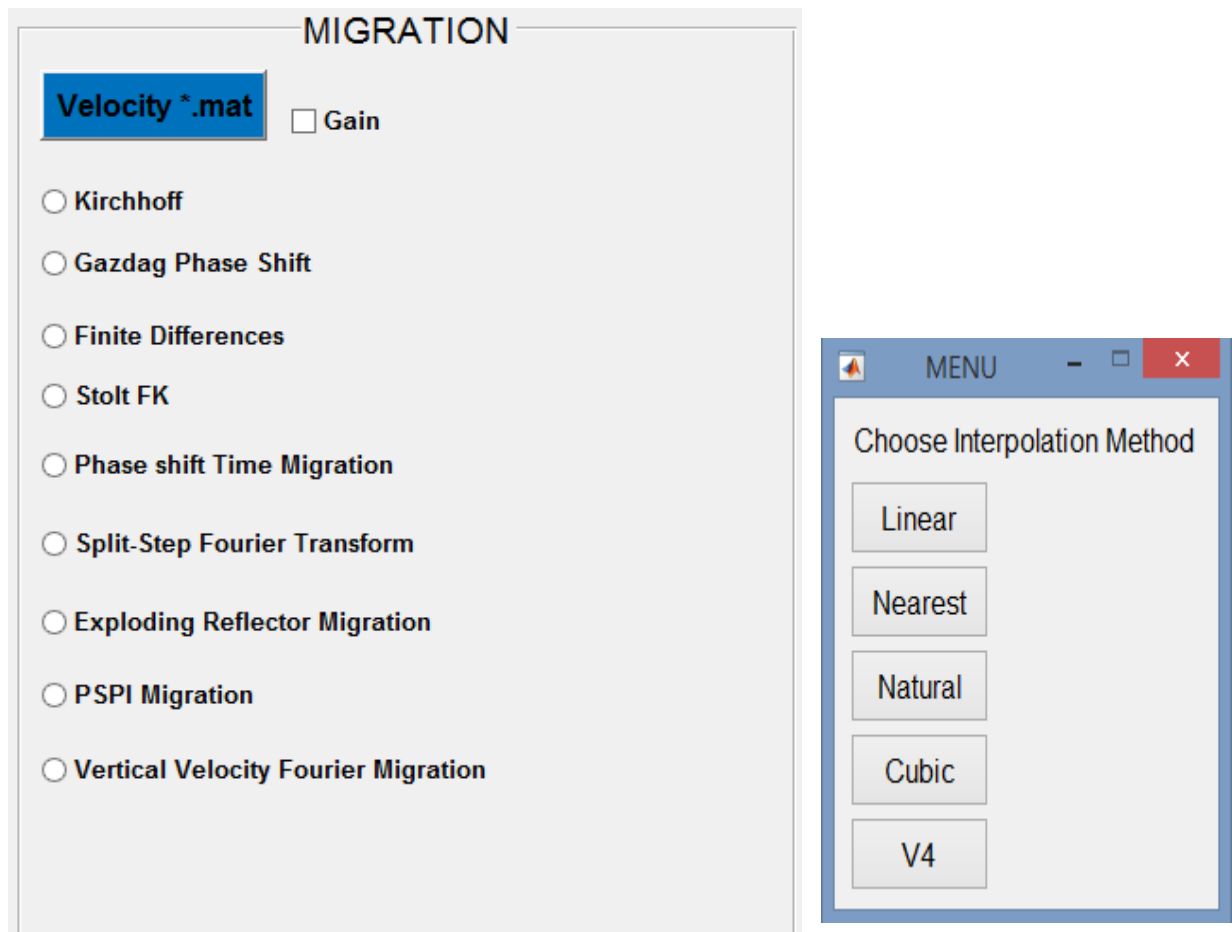


Figure 6.33 Migration function panel and interpolation method menu.

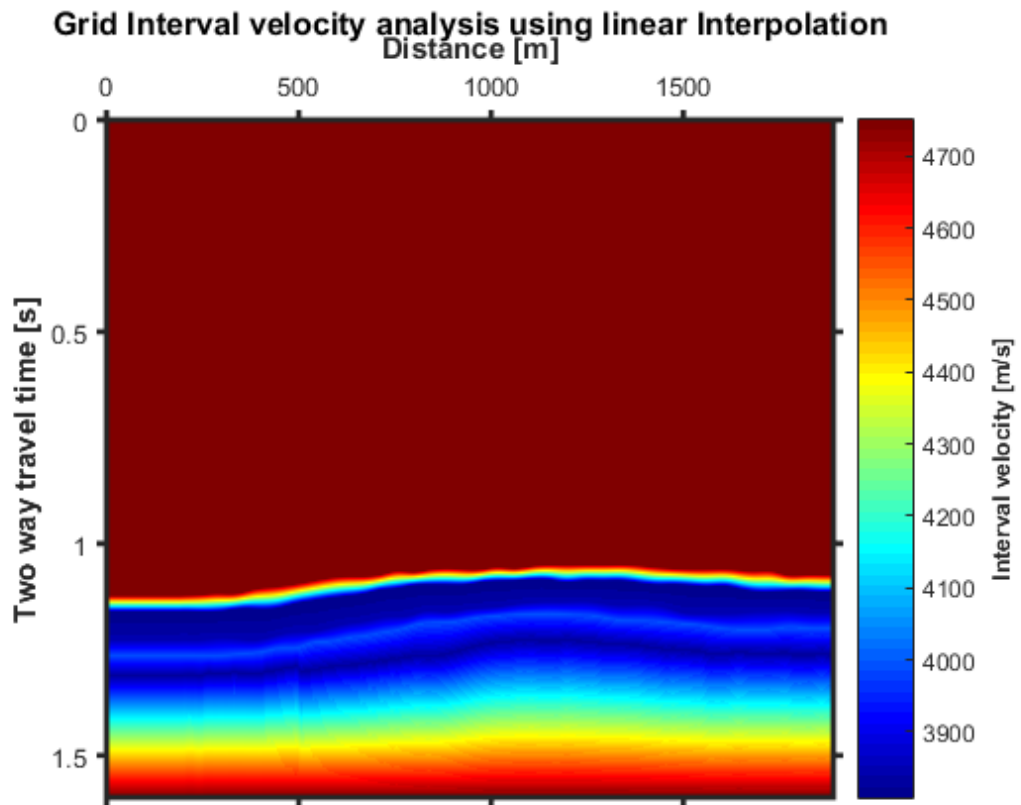


Figure 6.34 Interval velocity model after linear interpolation.

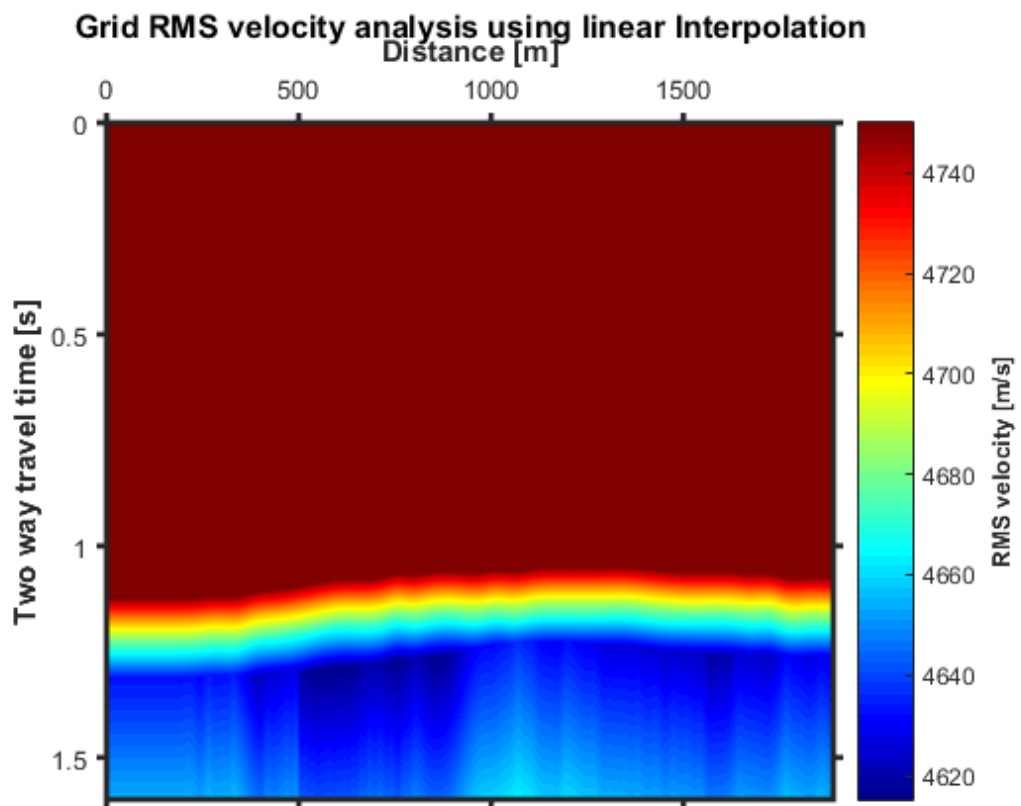


Figure 6.35 RMS velocity model after linear interpolation.

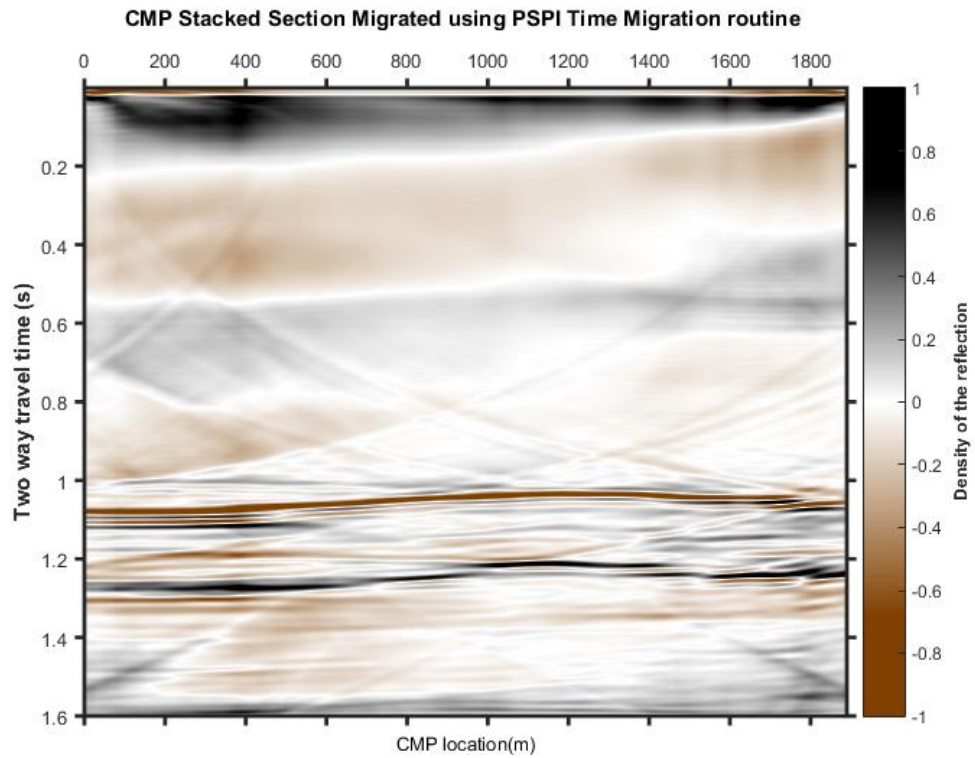


Figure 6.36 Migrated section using the PSPI time migration.

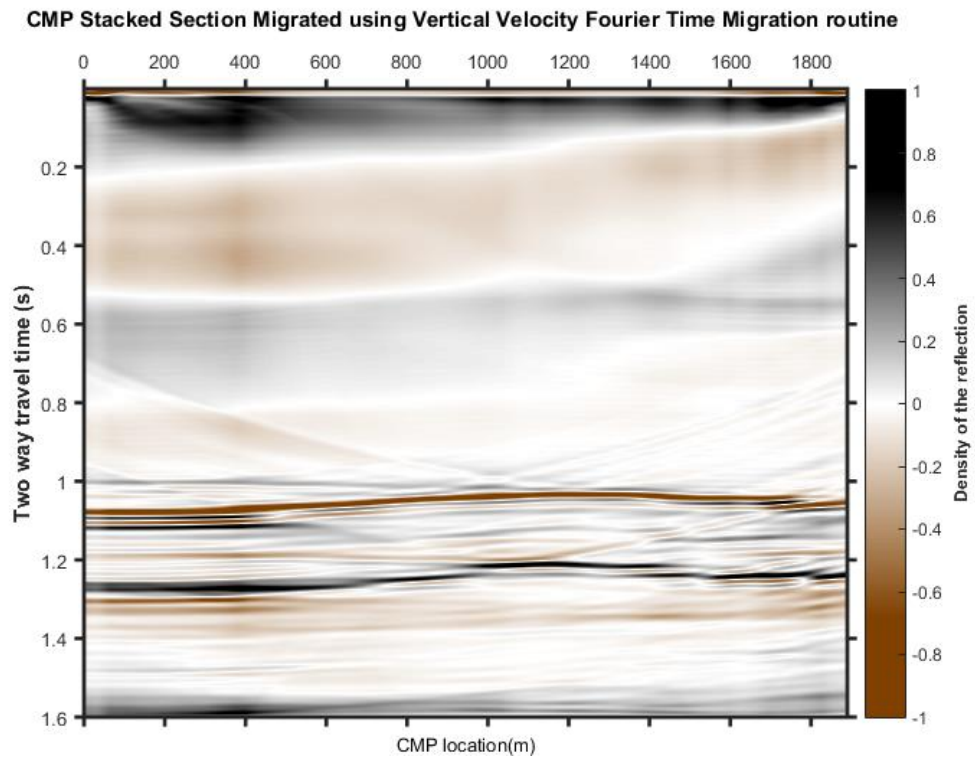


Figure 6.37 Migrated section using the vertical velocity Fourier transform.

6.5 Plotting tools

In this final part the different plotting features of the GUI are analysed. The “COLORED WIGGLE” panel (**Figure 6.38**) allows the wiggle plots to be colorized. For the colored wiggle the function wiggle was used (Portugal, 2012). If the colored option is chosen the wiggle plot will be presented with blue color for the negative amplitudes and red color for the positive amplitudes as shown in **Figures 6.39** and **6.40**.

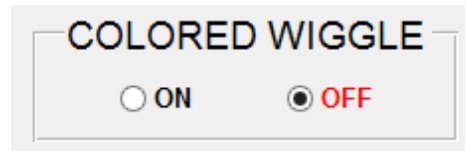


Figure 6.38 Wiggle type selection panel.

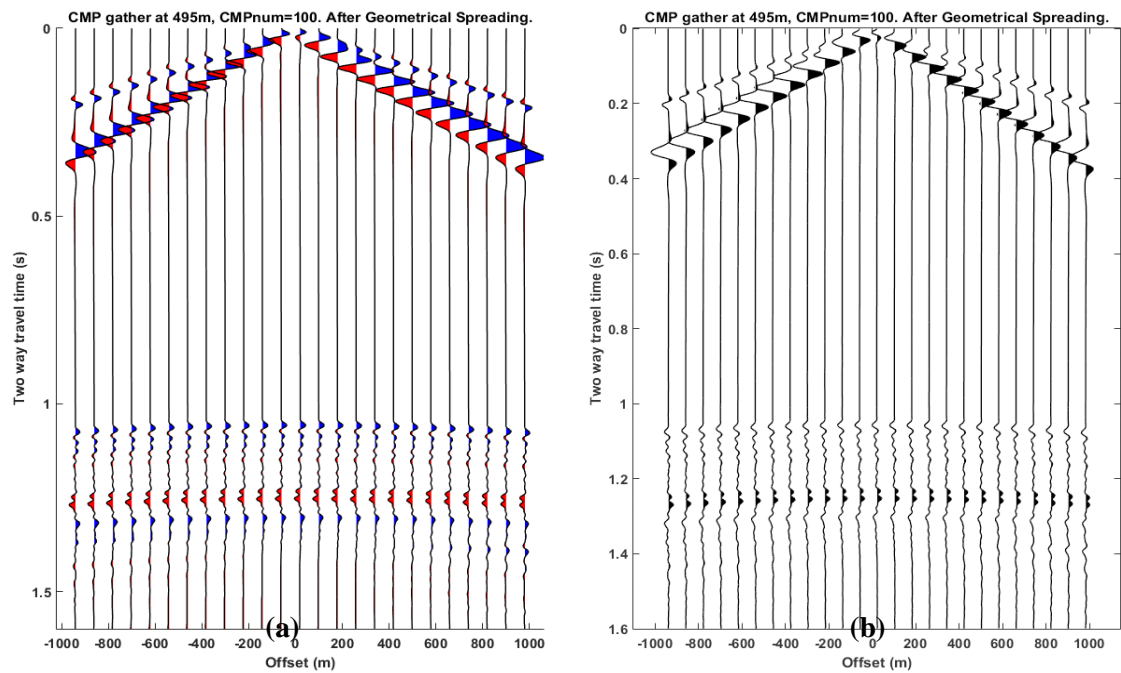


Figure 6.39 Wiggle plot of CMP gather 100 (a) with and (b) without colorized amplitudes.

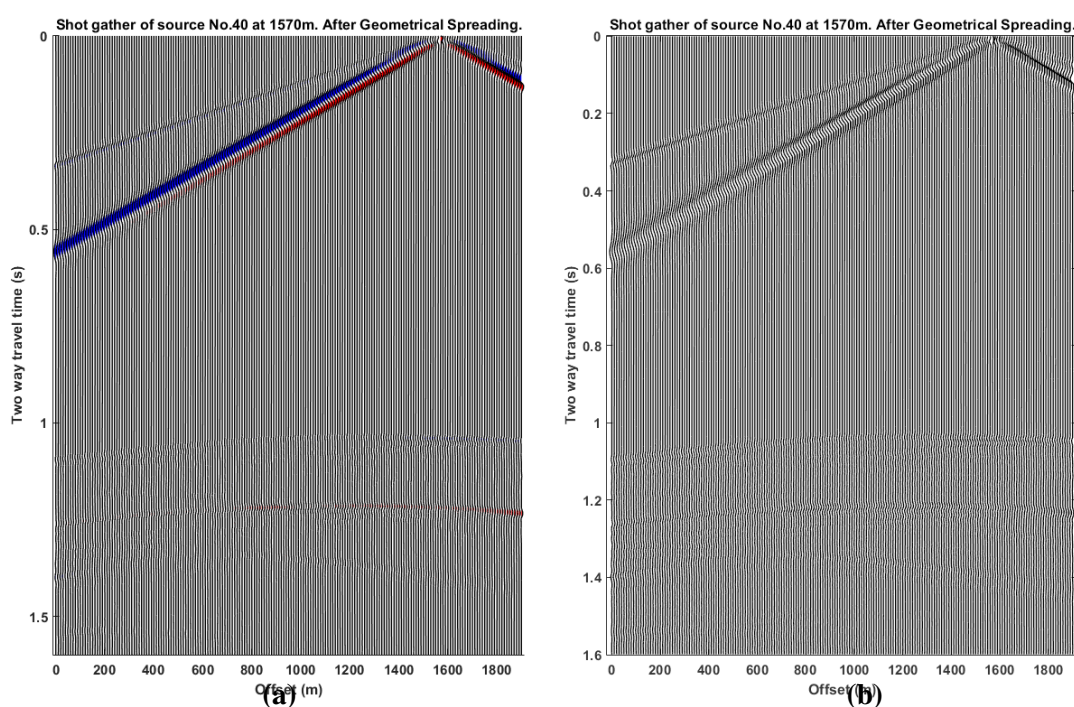


Figure 6.40 Wiggle plot of shot gather 40 (a) with and (b) without colorized amplitudes.

The “COLORMAP” panel allows the data to be plotted in seven different seismic colors as shown in **Figure 6.41**. As an example shot gather 40 is plotted with all the different color options in **Figure 6.42**.

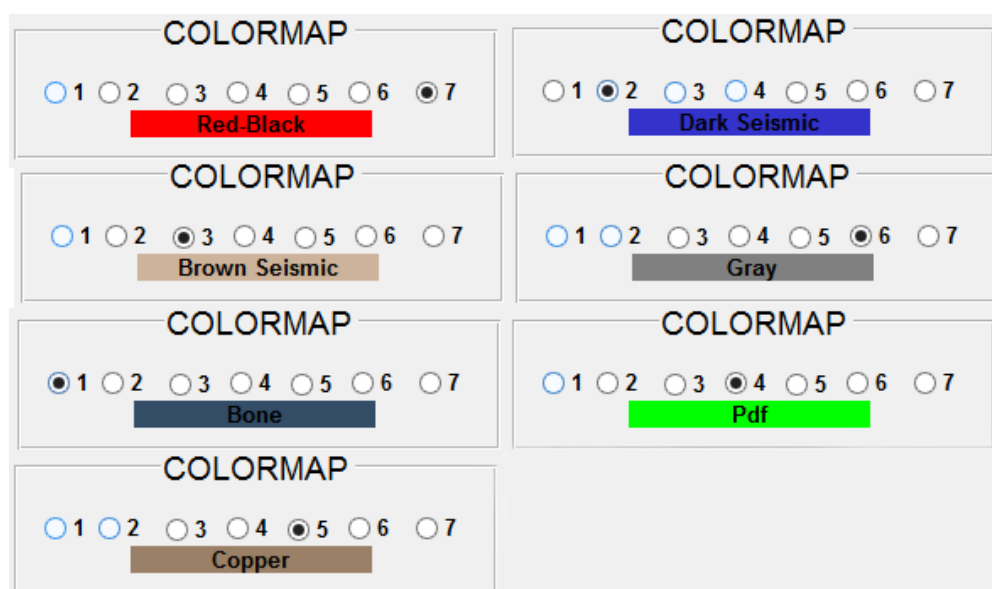


Figure 6.41 Available seismic colors selection.

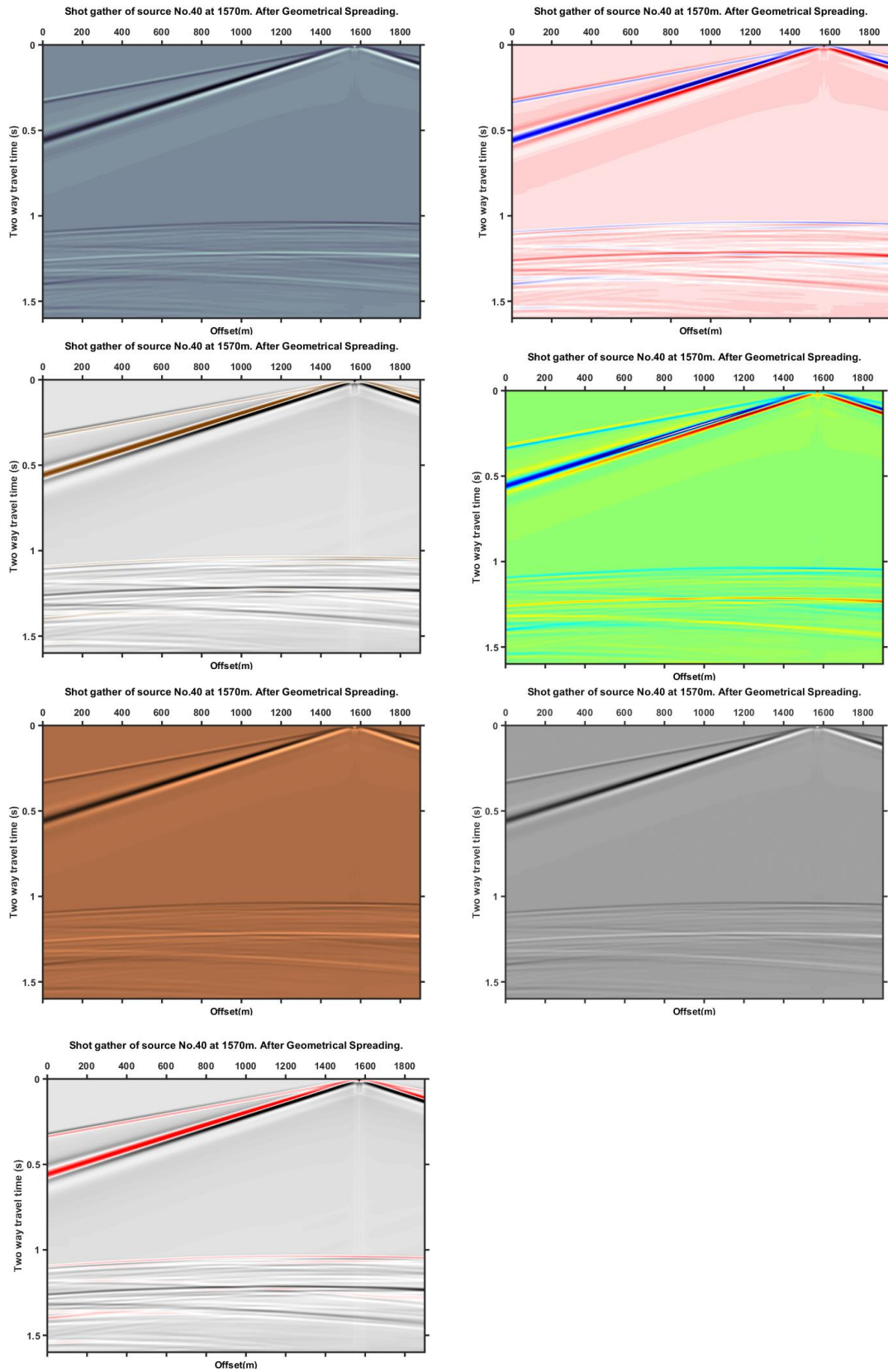


Figure 6.42 Representation of all the available seismic colors for shot gather 40.

7 AVO Analysis Application

According to the AVO theory presented on chapter 4, changes in the AVO responses can be directly correlated to changes in Poisson's ratio, which indicates pore fluid variation, especially gas existence. The characteristically low V_P/V_S ratio of gas sands should allow their differentiation from other low-impedance layers, such as coals and porous brine sands. In the case of the gas-saturated sediment, Poisson's ratio and P-wave velocity should be lower than the rest of the layers. Based on the reasoning above, we applied AVO analysis to identify the fluid type of the medium below the cap rock formation. In this study, the following AVO analysis flow was adopted.

- 1) Ray tracing and AVA analysis.
- 2) Rock Physics of AVO.
- 3) Far versus Near Stack attributes.
- 4) AVO cross-plot analysis.
- 5) AVO attribute analysis using P and G attributes.
- 6) Detailed investigation of distance to amplitude analysis.
- 7) AVO inversion of elastic parameters.

7.1 Ray tracing

Ray tracing is a necessary procedure for the transformation of the seismic data from offset to the angle domain. The algorithm of ray tracing in a $v(z)$ medium, which was described in chapter 4.2, was implemented by using bisection method in order to approximate the root of the ray parameter equation. In Matlab, this was achieved using Matlab's built-in function **fzero**. Fzero function first finds an interval containing the scalar where the function values of the interval endpoints differ in sign, then searches that interval for a zero. The medium consists of 6 layers with elastic parameters as described in **Table 8**. The calculated ray parameters are then used to calculate traveltime, reflectivity coefficients and incidence angles for each interface.

Formation	P-Velocity (m/	S-Velocity (m/s)	Density (g/cc)
Cap Rock	4750	3100	3.6
Sand A1	3809	2396	2.238
Sand A2	3846	2143	2.357
Sand B	3989	2266	2.389
Sand C	3830	2128	2.353
Bed Rock	4750	2900	2.7

Table 8. The elastic parameters of the model.

As an example the raytracing algorithm is applied for source and receiver offsets 100, 500 and 1000 m respectively as shown in **Figure 7.1** and the results of reflectivity and incidence angle values are shown in **Table 9**.

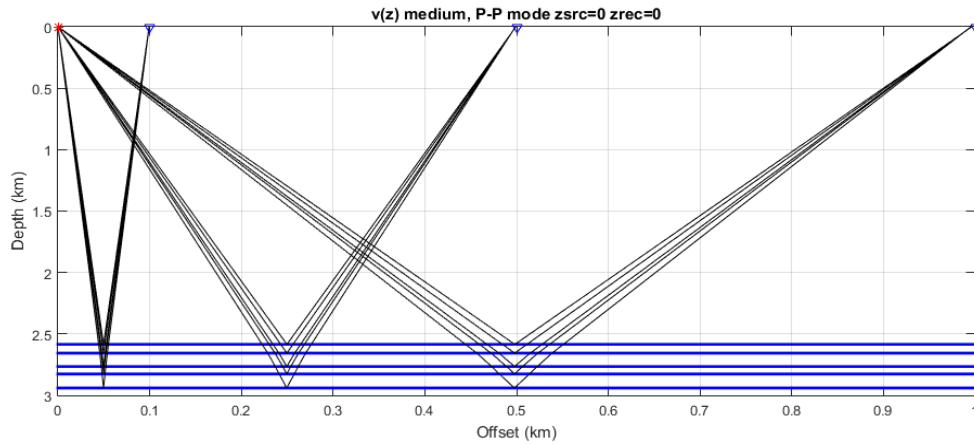


Figure 7.1 Raytracing procedure demonstration for offsets 100 m, 500m and 1000m. Red asterisk denotes shot location, blue triangles denote receiver locations.

Offset	Reflectivity			Angle of Incidence (°)		
	100 m	500 m	1000 m	100 m	500 m	1000 m
Layer 1-2	-0.160	-0.157	-0.146	1.08	5.38	10.66
Layer 2-3	0.007	0.008	0.011	0.84	4.17	8.27
Layer 3-4	0.024	0.024	0.023	0.83	4.14	8.21
Layer 4-5	-0.028	-0.028	-0.027	0.83	4.15	8.24
Layer 5-6	0.175	0.173	0.168	0.77	3.82	7.58

Table 9. Reflectivity coefficient and angle of incidence values for source- receiver offsets 100, 500 and 1000m.

Both traveltimes and incidence angle can be utilized to create a synthetic seismogram shown in **Figure 7.2** by convolving the reflectivity with a 20 Hz Ricker wavelet.

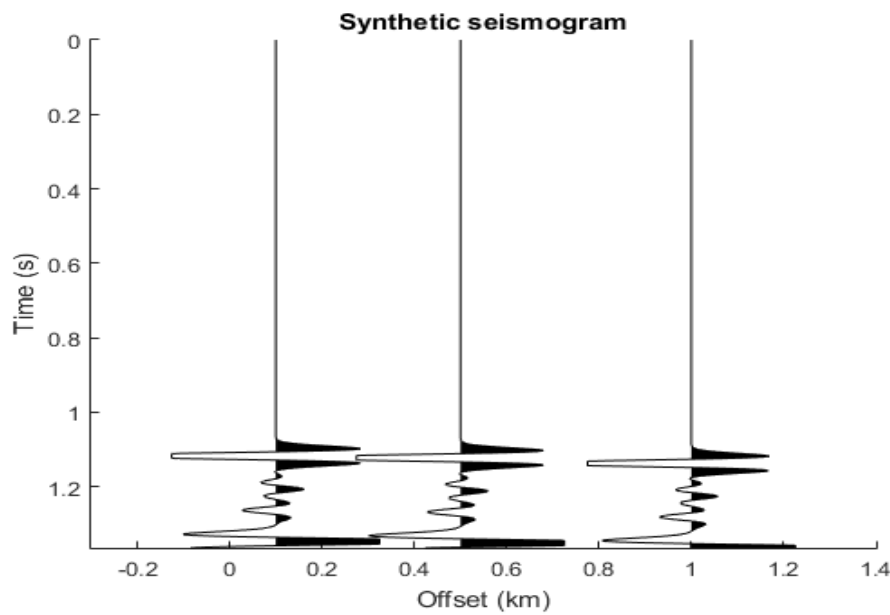


Figure 7.2 Synthetic seismogram for offsets 100 m, 500m and 1000m.

Similarly, the raytracing algorithm was applied to the whole model, for offsets 10m-1890m with a 10m interval. The raypaths within the medium are plotted in **Figure 7.3**, along with the traveltimes for each medium on **Figure 7.4**. Reflectivity computed based on Zoeppritz's work (1919) for solid – solid interface. The reflectivity series was again convolved with a 20 Hz Ricker wavelet and the result is plotted on **Figure 7.5**. The medium on each side of a given interface is considered perfectly elastic.

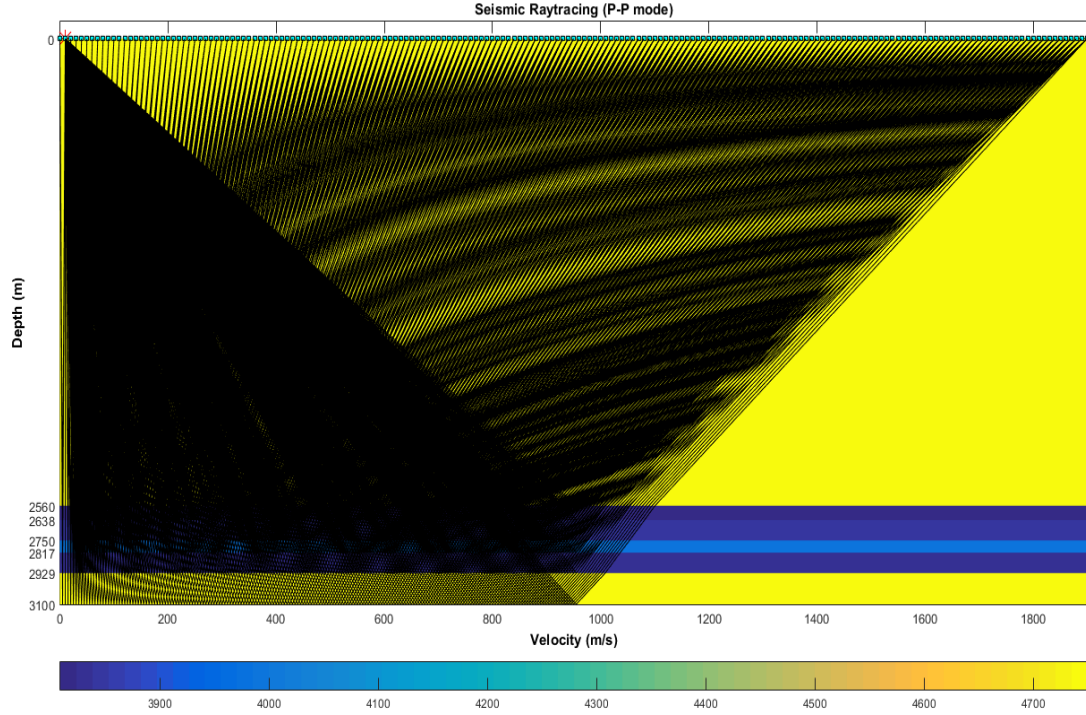


Figure 7.3 Raypaths within the medium for all interfaces. Red asterisk denotes shot location, blue triangles denote receiver locations.

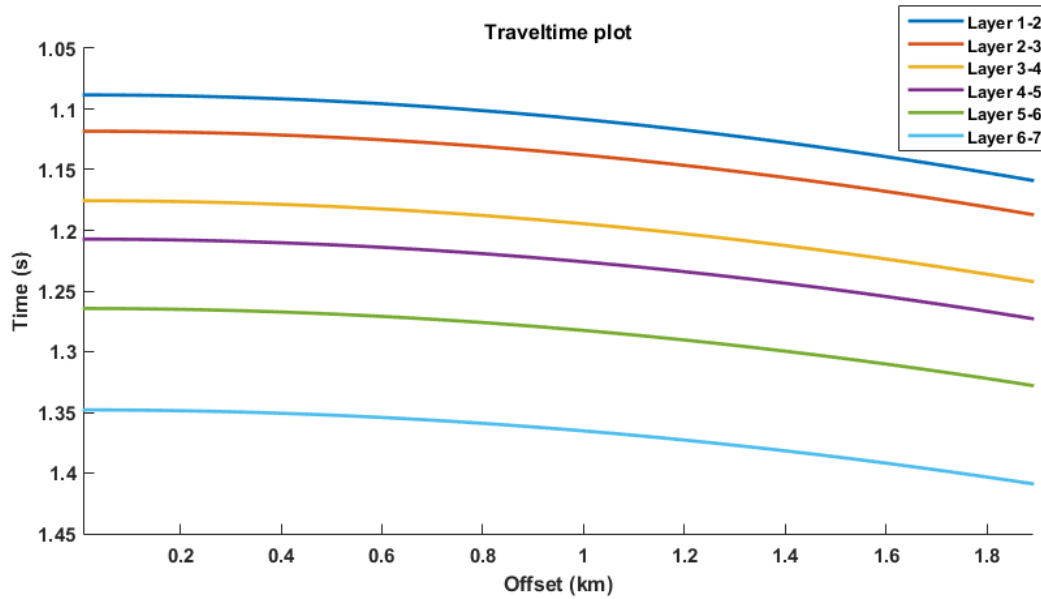


Figure 7.4 Traveltime plot calculated from the ray parameters obtained from ray tracing.

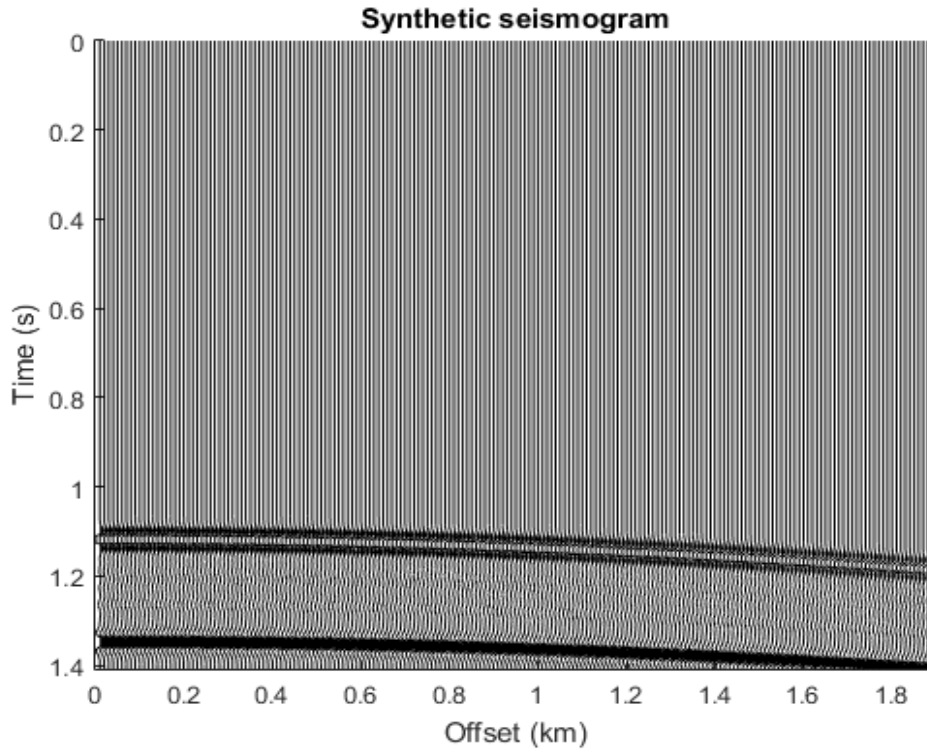


Figure 7.5 Synthetic seismogram created by convolving the reflectivity calculated from incidence angle with 20 Hz Ricker wavelet.

Judging from **Figure 7.5** the shallower interface between the overburden and the reservoir, presents highly negative amplitudes, while the deeper interface presents highly positive amplitudes. The intermediate interfaces have low amplitudes and are not easily observed. This behaviour can be confirmed, by analysing the convolved synthetic trace, separately, for each layer (**Figure 7.6**).

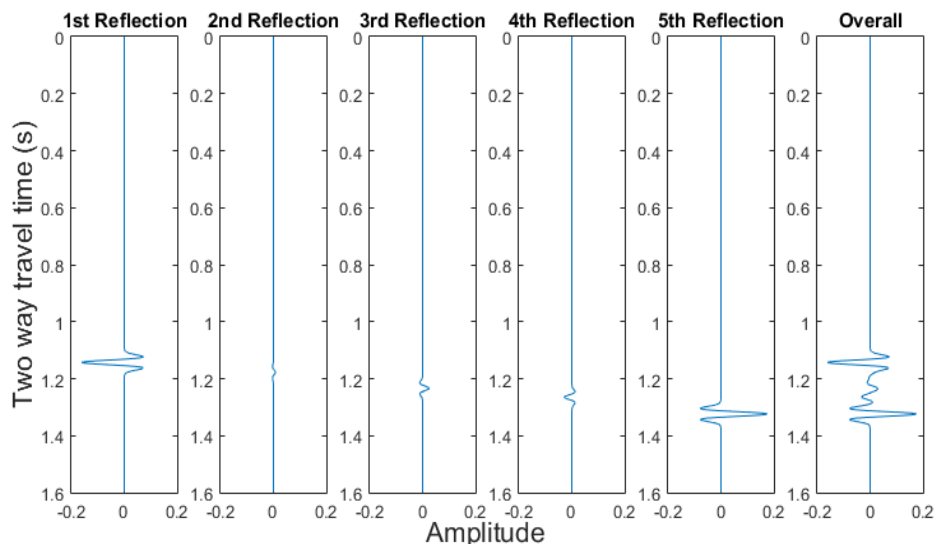


Figure 7.6 Reflectivity series of each layer convolved with a 20 Hz Ricker wavelet, along with the overall synthetic trace.

7.2 Rock Physics of AVO

Rock Physics represents the link between geologic reservoir parameters (e.g., porosity, clay content, sorting, lithology, saturation) and seismic properties (e.g., V_P/V_S , density, elastic moduli). Rock physics models can be used to interpret observed sonic and seismic velocities in terms of reservoir parameters. These models can also be used to estimate expected seismic properties from observed reservoir properties in order to interpret the seismic response (AVO) away from the well.

A typical task in a Rock Physics study is to calculate AVO attributes from the well logs and cross-plot various attributes from selected geologic units. These cross-plots are used to:

- understand how the rock properties are related
- determine the rock properties in various lithologies in the area
- determine the sensitivity of various attributes to fluid effects
- contribute velocity constraints such as mudrock line values to AVO analysis of seismic data.
- contribute to interpretation of attribute sections

Using the function **logsyn** in Matlab the elastic parameters of the model were converted to synthetic logs. Synthetic log for P sonic, S sonic, density and Poisson's ratio were estimated as shown in **Figure 7.7**.

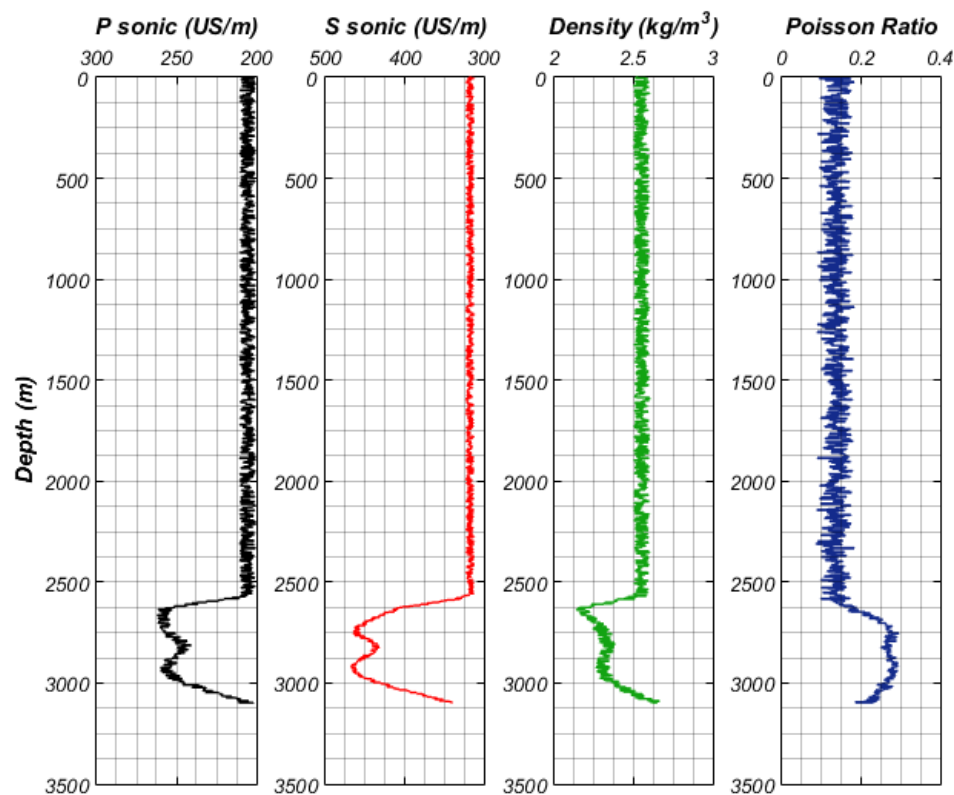


Figure 7.7 P sonic, S Sonic, and density synthetic log from the lithology model

The synthetic logs were then used for the crossplots of Vp-Vs, Vp/Vs-Vp, Vp/Vs-Vs and Vp/Vs-Poisson's Ratio as shown in **Figure 7.8**.

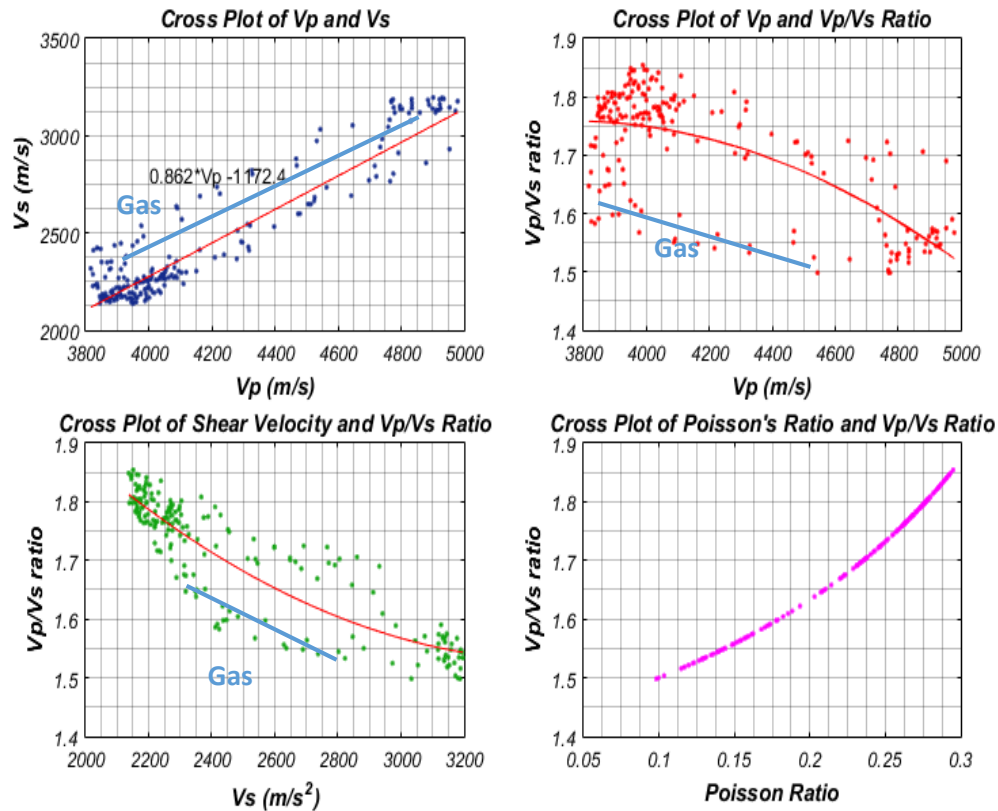


Figure 7.8 Cross plot of physical rock properties from the lithology model.

The crossplot of Vp-Vs shows a positive indicator of gas presence, since there are data points deviating from the mudrock line. Specifically, those data points have a trend slightly shifted upwards of the mudrock line. This behaviour as presented in **Figure 4.12** of chapter 4 is an indicator of gas saturation. The gas presence is also confirmed by the low Vp/Vs ratios of data points in the Vp/Vs-Vp and Vp/Vs-Vs crossplots, which are deviating from the basic trend line.

7.3 AVO crossplot analysis

AVO crossplots are a simple and elegant way of representing AVO data. Offset variations in amplitude for reflecting interfaces are represented as single points on a crossplot of intercept and gradient. The advantage of this type of plot is that a great deal of information can be presented and trends can be observed in the data that would be impossible to see with a standard offset (or angle) versus amplitude plot. The crossplot is an ideal way of examining differences in AVO responses that may be related to lithologic or fluid-type variations.

Commonly used techniques for revealing these differences include color-coding samples from the crossplot and using this as an overlay to a seismic display or creating linear combinations of intercept (R_0) and gradient (G).

Before applying the AVO crossplot analysis the reflection coefficients of the model are calculated using Hiltermann, Shuey, Bortfeld and Aki Richard approximations with the function **ava_approximation** [E. Rietsch, 2003]. The reflection coefficients are plotted against the angle of incidence (AVA response) for the different approximations (**Figure 7.9**).

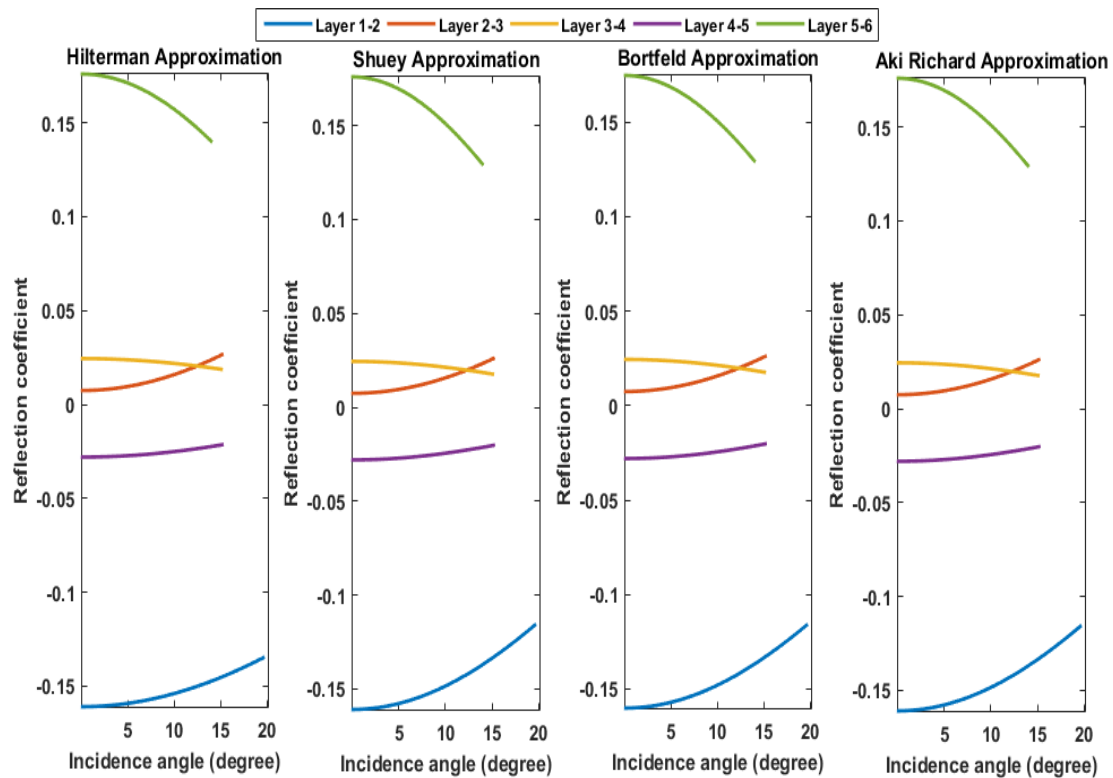


Figure 7.9 Reflection coefficients versus angle of incidence, using Hiltermann, Shuey, Bortfeld and Aki-Richard approximations for the five different layers of the model.

The Hiltermann approximation gives more pessimistic values for the reflection coefficients, compared to the other methods, but is considered more reliable since it takes into account the Poisson's ratio of each interface. Thus, the AVA response is plotted again using only the Hiltermann approximation in **Figure 7.10**.

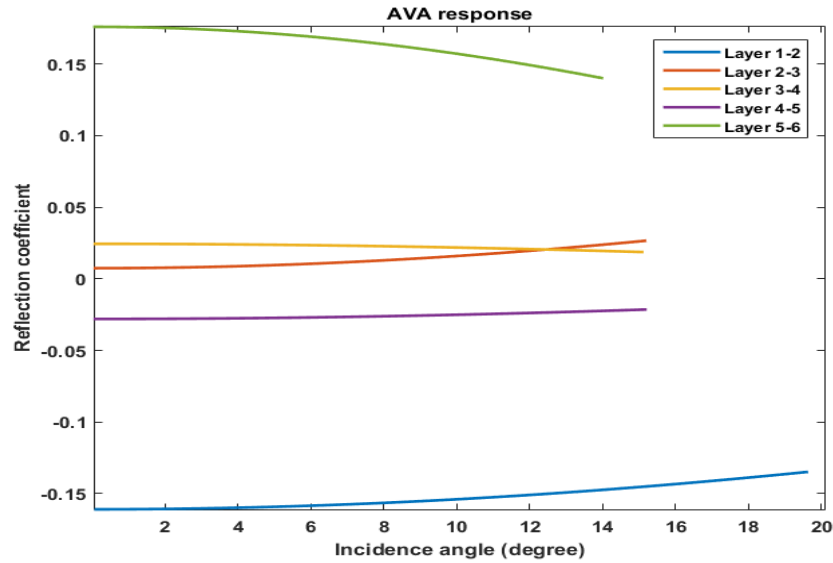


Figure 7.10 AVO response using Hilterman approximation for the five interfaces of the model.

Comparing **Figure 7.10** with the **Figure 4.13** of AVO classification each medium of the model can be categorized to an AVO class as shown in **Table 10**.

Medium	AVO class
1: Layers 1-2	IV
2: Layers 2-3	Flatspot
3: Layers 3-4	II
4: Layers 4-5	IV
5: Layers 5-6	I

Table 10. AVO classification of the model's interfaces.

In **Figure 7.11** the reflection coefficients are plotted against the square sin of the angle of incidence, giving the same results with **Figure 7.10**, but in a more linear form.

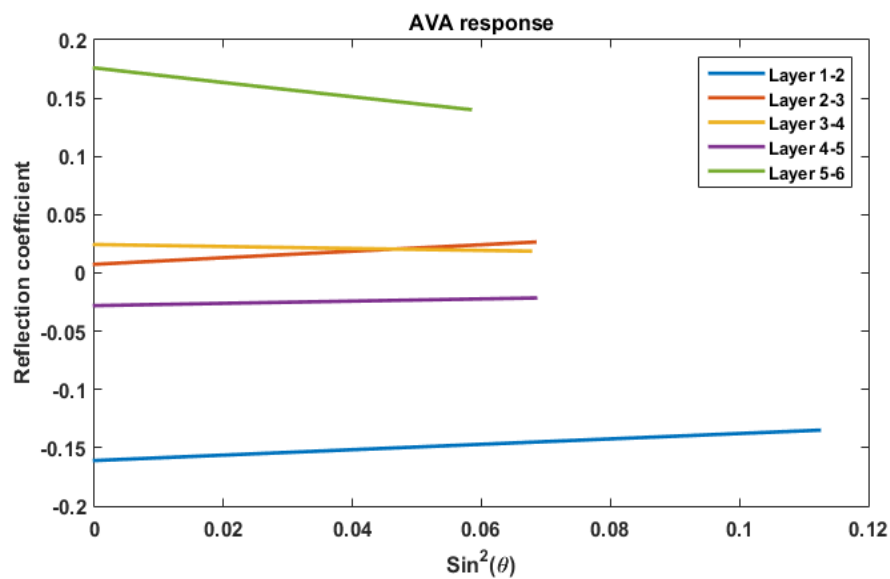


Figure 7.11 Reflection coefficients versus the square sin of the angle of incidence for the five interfaces of the model.

Finally, the crossplot of AVO gradient and intercept is presented in **Figure 7.12**. The background trend was plotted with the assumption that the ratio $V_p/V_s=2$. However as it was mentioned in **chapter 4.7**, the background trend will deviate for different values of V_p/V_s ratios. In our model the V_p/V_s ratio derives 1.6. Thus, using equation (4.27) the gradient of the

background trend was calculated as: $B = \frac{4}{5} \left(1 - 9 \cdot \left(\frac{1}{1.6} \right)^2 \right) \cdot A \Rightarrow B = -2 \cdot A$. The new crossplot with the shifted background trend is presented in **Figure 7.13**.

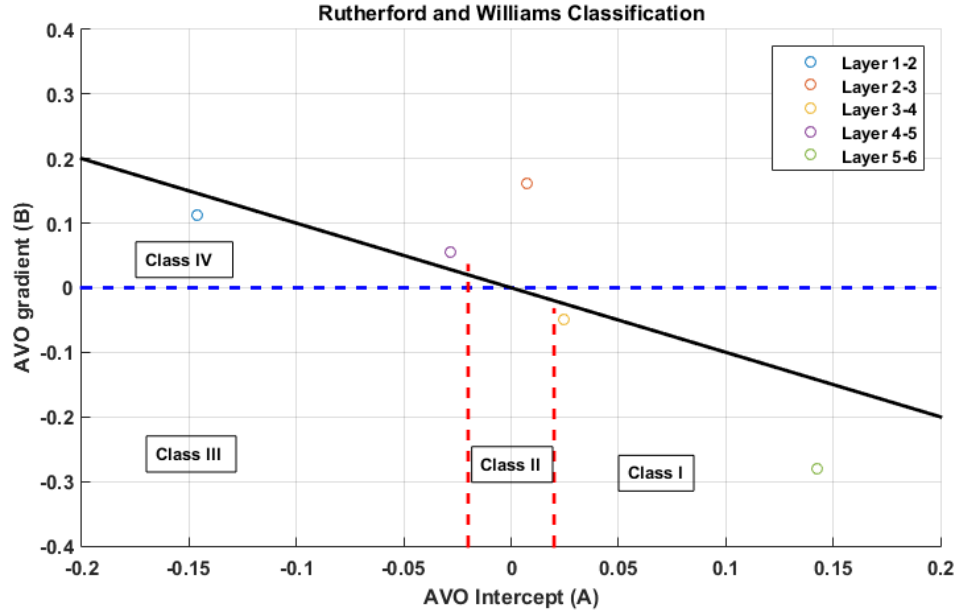


Figure 7.12 Crossplot of AVO gradient (B) and AVO intercept (A).

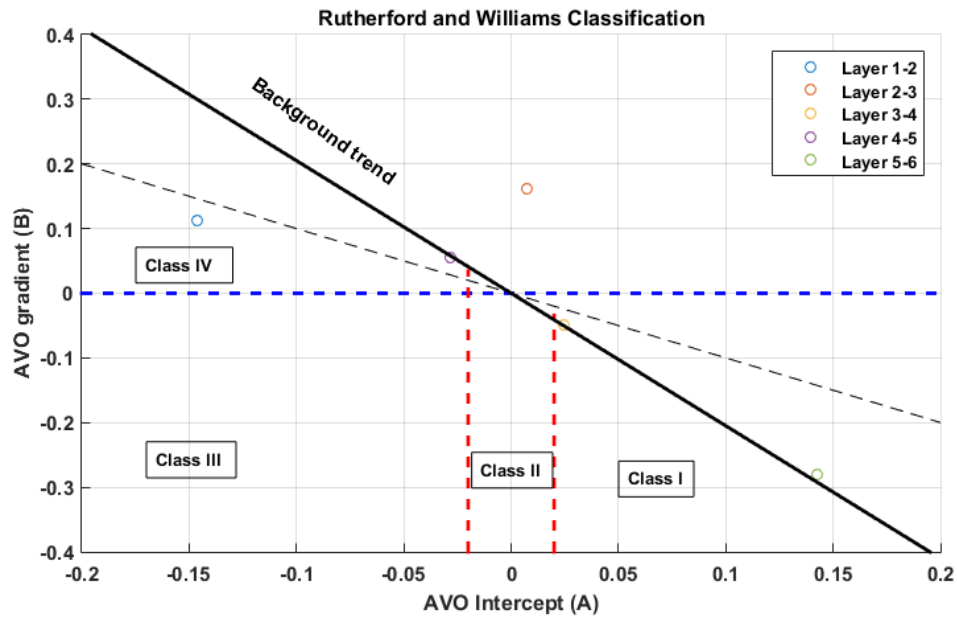


Figure 7.13 Crossplot of AVO gradient (B) and AVO intercept (A), after shifting the background trend. The initial background trend is plotted with dashed line, while the final background trend with continuous line.

As it can be observed in **Figure 7.13** the gas anomaly is evident, with the point corresponding to the first medium being plotted to the left of the background trend. The gas anomaly belongs to class IV, which confirms the results from the reflection coefficient curves. The points that are plotted to the right part of the trend act as the base of the saturated layers, as shown in **chapter 4.7**. Thus, the medium just below the gas saturated layer is plotted to the right of the background trend. All the other points are plotted on the background trend, which means that they are not related with gas.

7.4 Near Far Stack

In **chapter 4.5** the significance of near and far stacks, in gas detection, was underlined. However, the application of this technique in the synthetic data was a bit difficult, due to the fluctuation of the CMP gather's fold (see **Figure 5.36**). In order to balance the output of the far and near stacks, different size of traces intervals were used. Specifically, for the far stack the traces 24-48 were used, while for the near stack only the traces 1-24. The results are presented graphically in **Figures 7.14-7.17**.

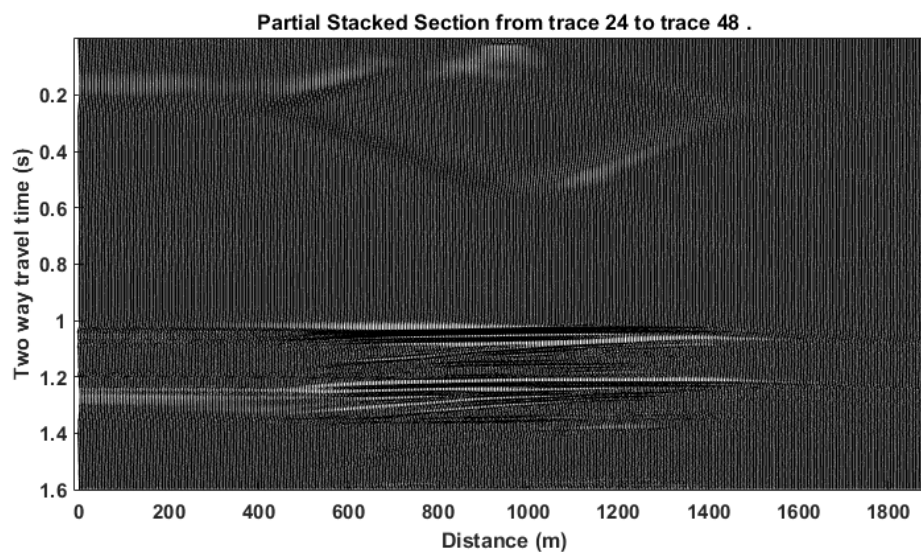


Figure 7.14 Wiggle plot of Far stacked section of traces 24-48.

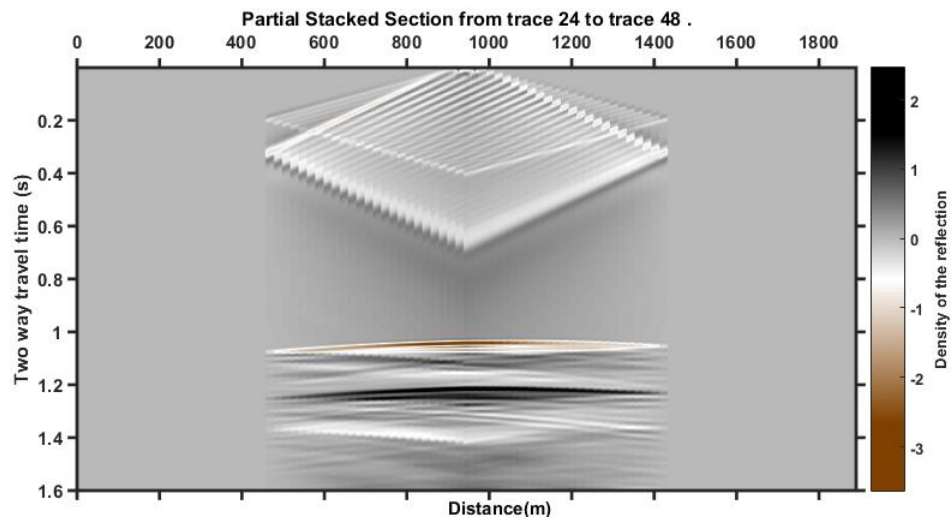


Figure 7.15 Color plot of Far stacked section of traces 24-48.

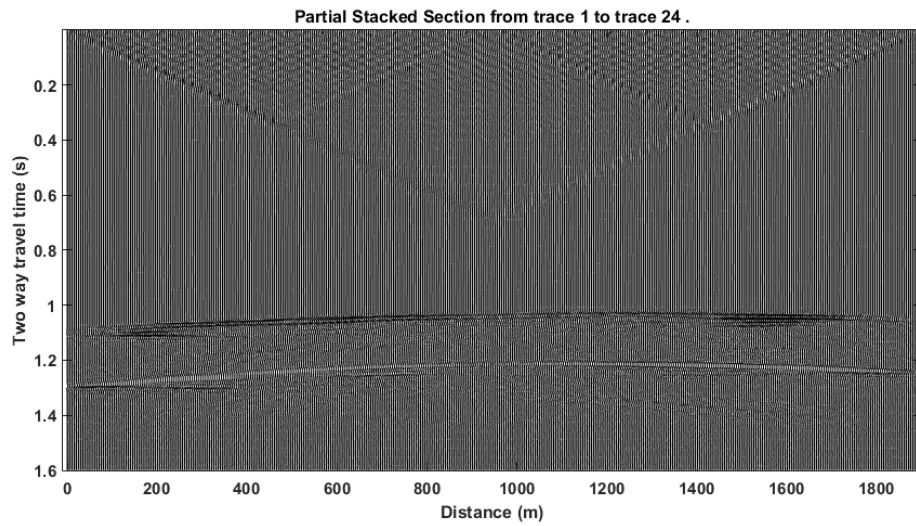


Figure 7.16 Wiggle plot of Near stacked section of traces 1-24.

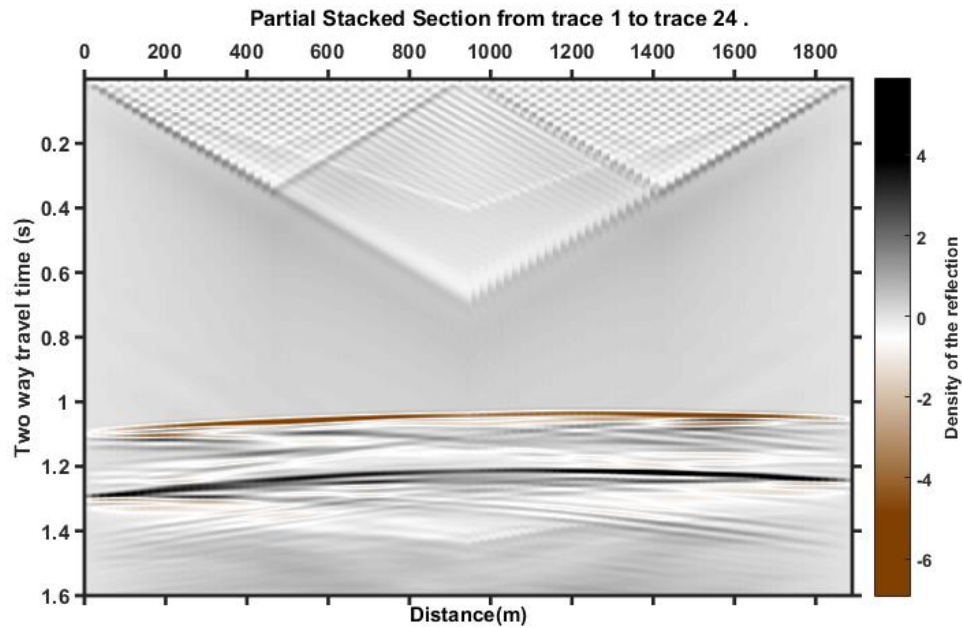


Figure 7.17 Color plot of Near stacked section of traces 1-24.

As it was mentioned in **chapter 4.5**, the far stack minus the near stack (FN) is a "rough" estimate of an AVO gradient, since the difference between far and near will manifest the significant negative gradient that is present. This theory is confirmed by the subtraction of far and near stack sections of the synthetic data in **Figure 7.18**. The shallower interface presents an evident reversal in polarity and a significant decrease in amplitude with offset which indicate the gas presence in this layer.

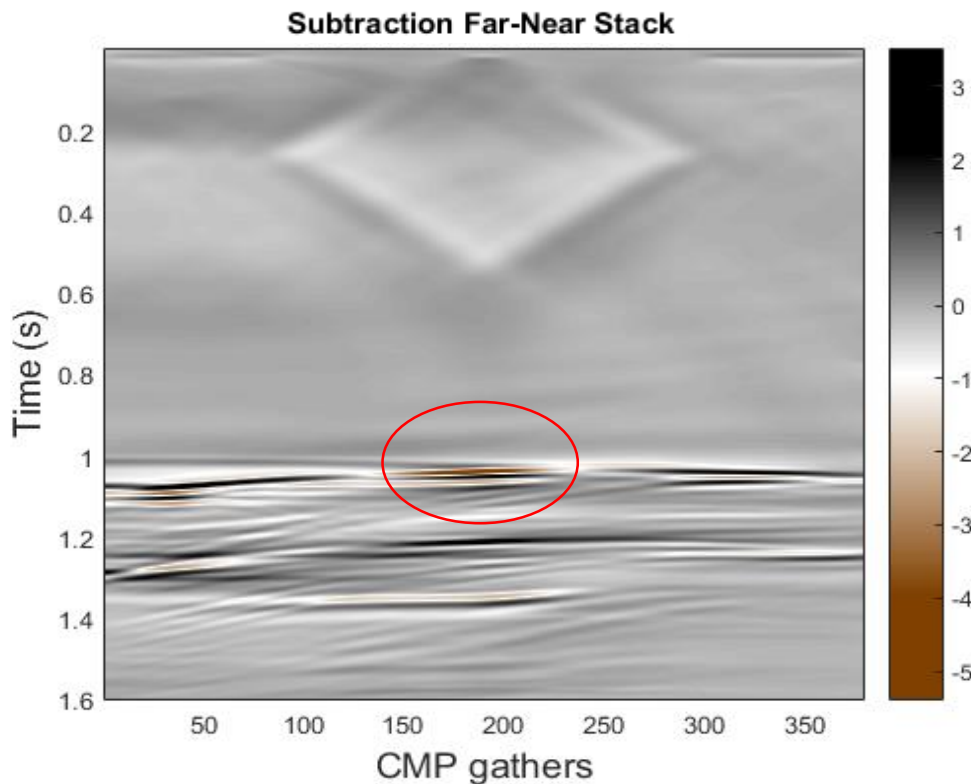


Figure 7.18 Far stack minus near stack of synthetic data .

Furthermore, the crossplotting of Near versus Far minus Near stack in **Figure 7.19** gives almost the same results with the gradient versus intercept crossplot. The shallower interface is plotted on the left part of the plot, separately from the other interfaces, which again confirms the gas presence in the specific medium.

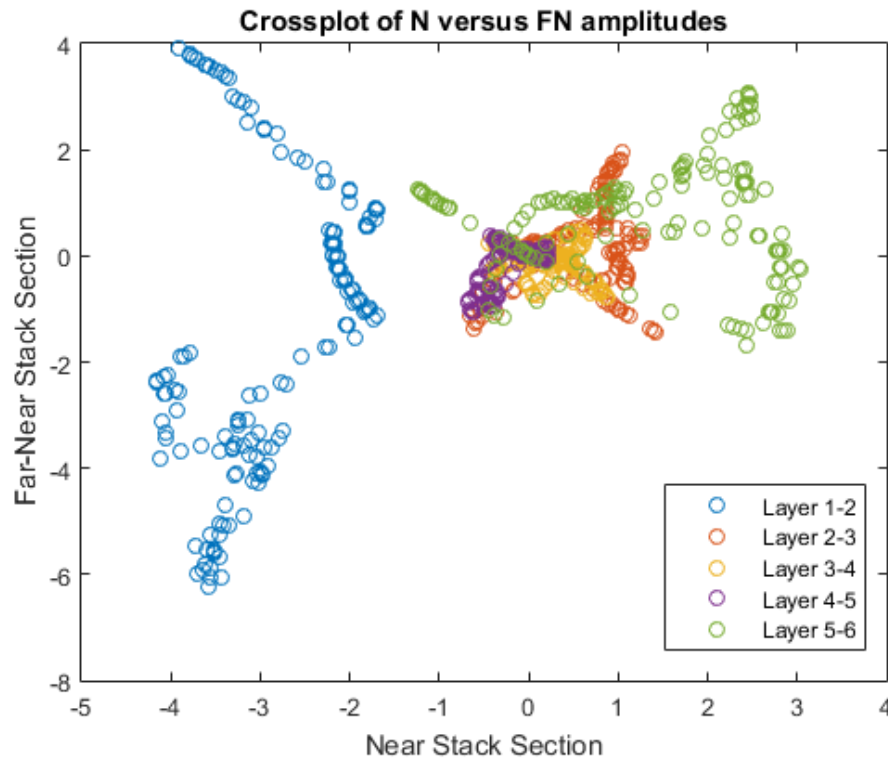


Figure 7.19 Crossplot of Near versus Far minus Near stack.

7.5 PG crossplot

For the creation of a PG crossplot, a random CMP gather is chosen and for each of its traces a line of observations is chosen. The selected line extends vertically from a particular point on the surface to some pre-selected depth of interest. Of course, the depth at this point, is expressed in two-way, acoustic travel time. The chosen travel time values correspond to possible reflectors locations. After finding the amplitude values for each trace at the specific chosen time, they are plotted against the square sin of the angle of incidence and fitted in straight lines. The crossplot of the straight line's slope and intercept is called PG crossplot. As an example, the CMP gather 200 is shown in **Figure 7.20** after NMO correction, with the travel time of each reflector plotted with a different colored straight line. Also, the graph **Figure 7.22** plots the amplitude for each trace at the selected time against the $\sin^2\theta$ of the angle of incidence for the specific offset. The values are best-fitted to first order polynomials, the first term of which corresponds to the P value and the second to the G value of the PG crossplot.

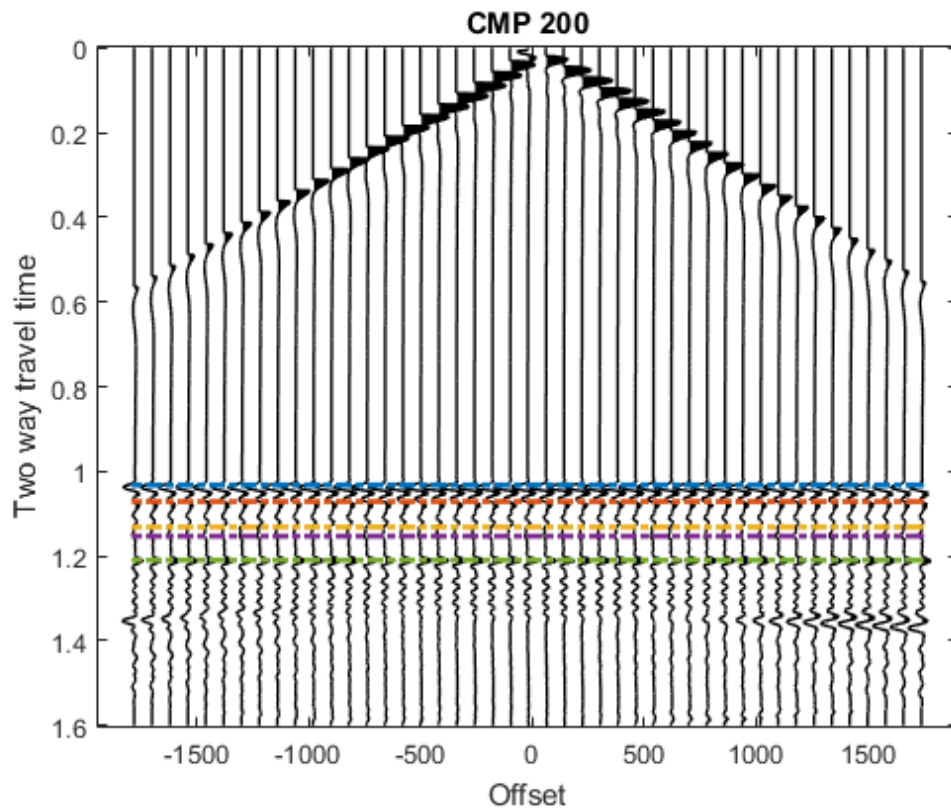


Figure 7.20. CMP 200 NMO corrected. The colours correspond to travel times for different reflectors.

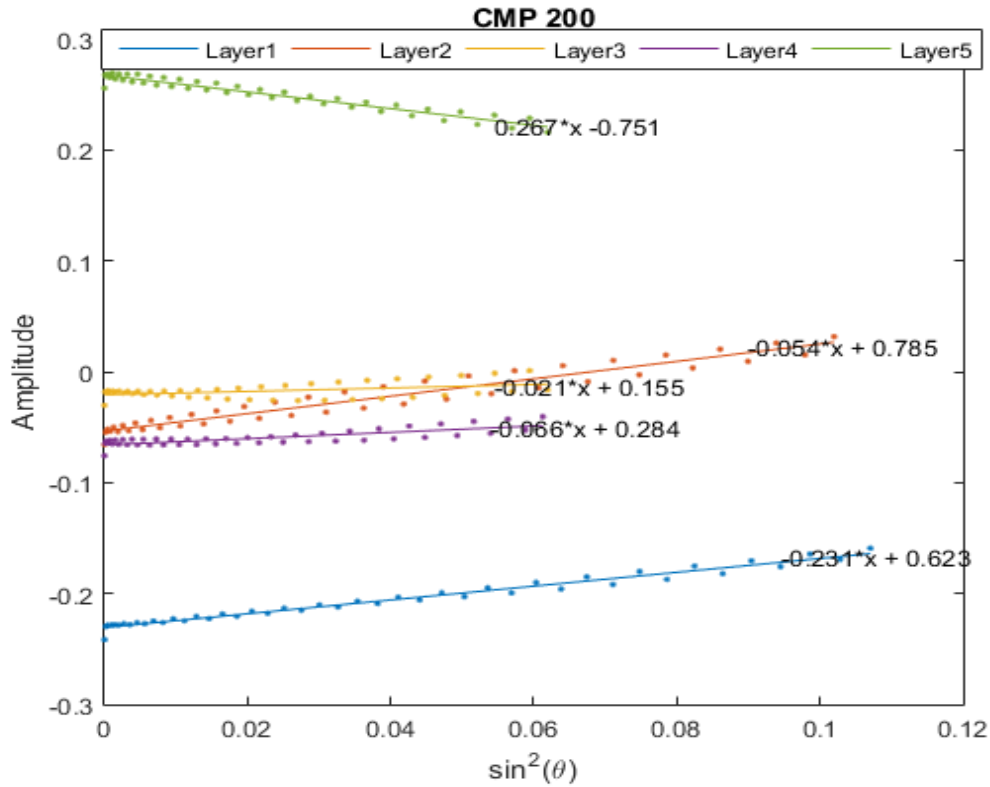


Figure 7.21 Amplitude versus $\sin^2\theta$ plot for cmp gather 200.

Comparing **Figures 7.11** and **7.21** we can see that both the synthetic data and the ray tracing algorithm gave similar results of AVO response, as shown in **Figure 7.22**.

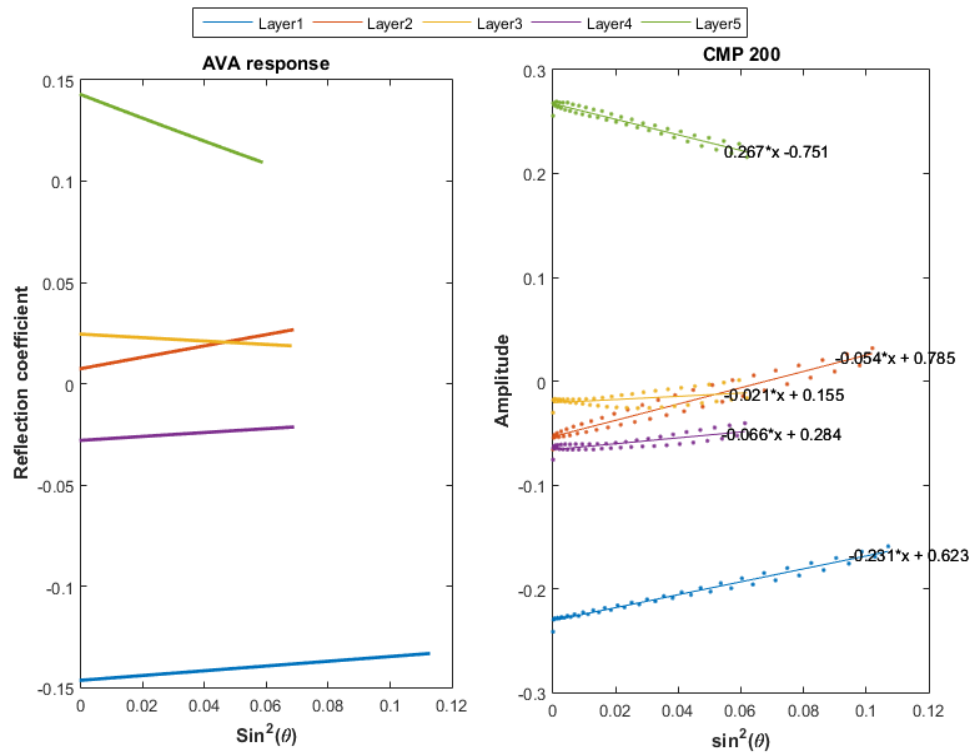


Figure 7.22 Comparison of AVO response using raytracing results and synthetic data of CMP 200.

The same procedure is repeated for all the CMP gathers. In **Figure 7.23** the results for the CMP gathers 50,150,250 and 350 are demonstrated. Observing **Figure 7.23**, we can see that the amplitude-offset trend of the intermediate reflectors is not accurately matched due to the low amplitude values. However, the response for the top and bottom layers of the reservoir is precisely matched in every CMP gather. Furthermore, the correlation between the amplitude and the offset becomes more pronounced in the intermediate cmp gathers (e.g 150, 250) than in the near or far (e.g 50, 350). As a result, the slope of the amplitude-offset trend for the near or far stacks deviates from the corresponding trend of the intermediate cmp gathers.

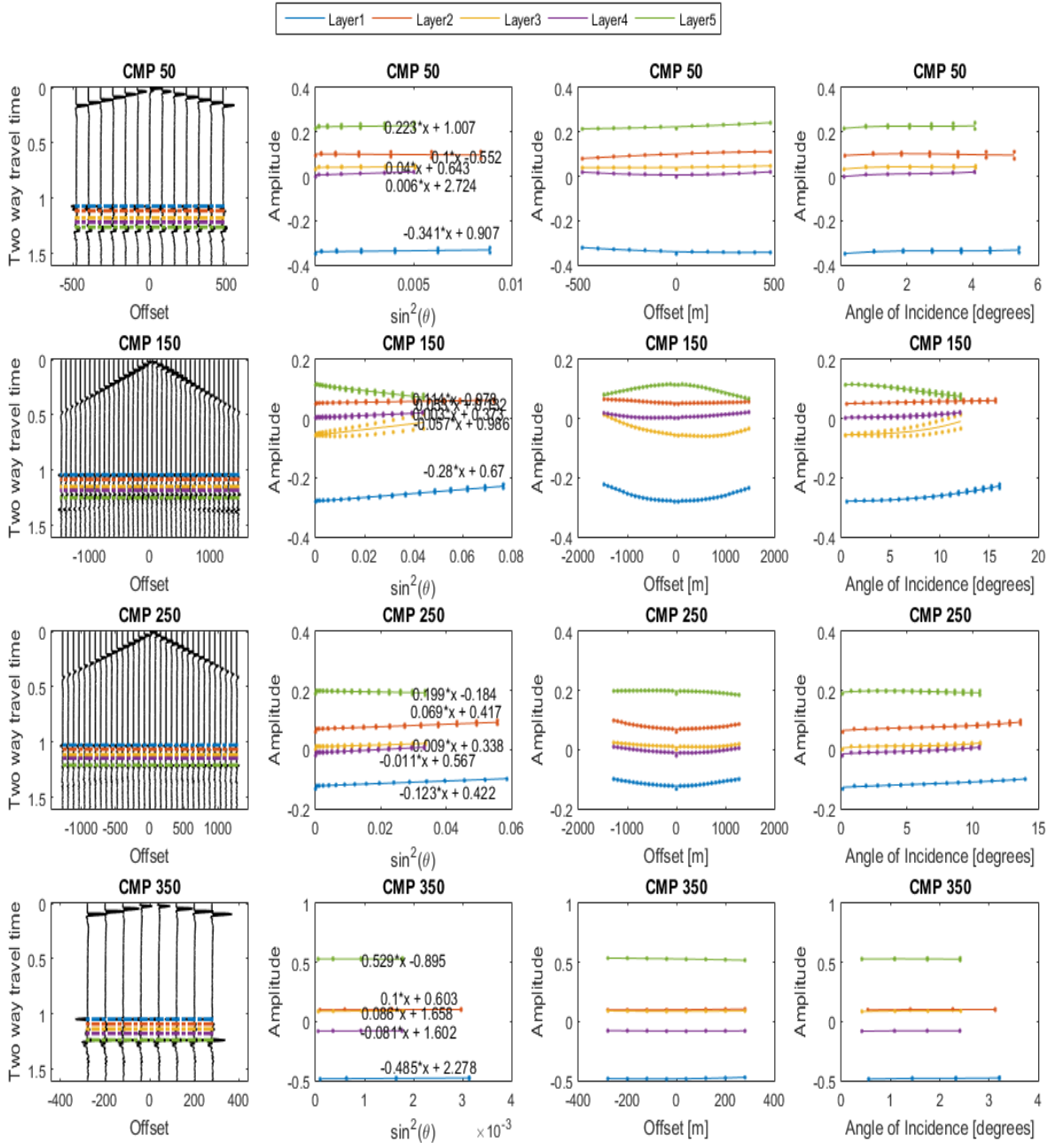


Figure 7. 23 Amplitude variation with offset, $\sin^2(\theta)$ and angle of incidence for random CMP gathers. The colours correspond to travel times for different reflectors.

Finally, after fitting the Amplitude- $\sin^2\theta$ plots to first order polynomials, the P and G values are extracted for all the 379 CMP gathers. In **Figure 7.24** the PG crossplot for the CMP gathers 150-300 is presented, where the amplitudes were stronger. Looking at **Figure 7.24**, we can observe some data points deviating from the rest of the population which can be attributed to the gas anomaly. In order to confirm the above assumption the PG crossplot is plotted again in **Figure 7.25**, but this time, with different color for each reflector of the model. It is obvious now that the PG crossplot has accurately indicated the existence of gas in the medium.

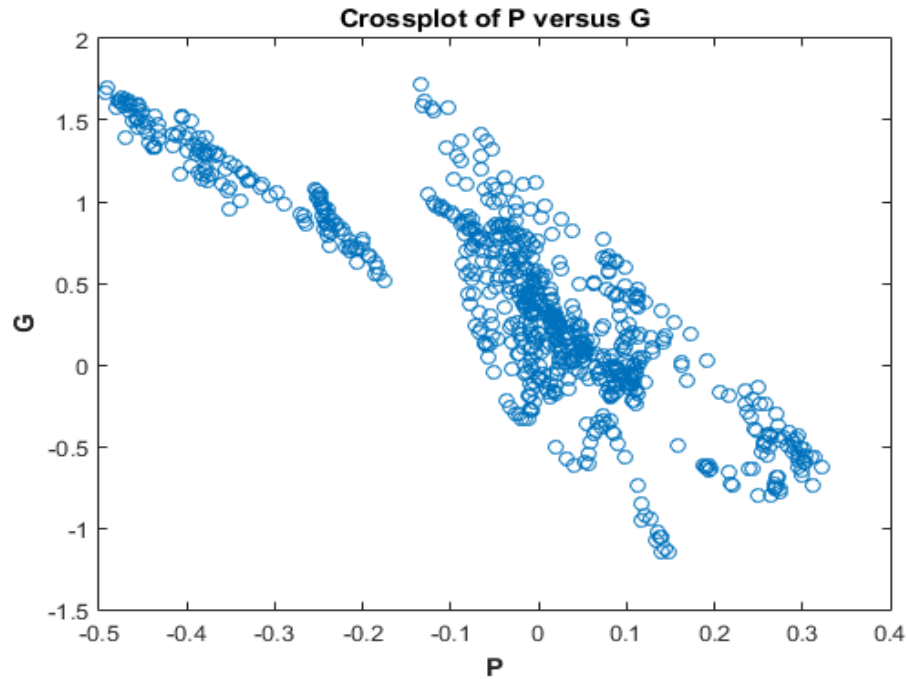


Figure 7.24 PG crossplot of CMP gathers 150-300.

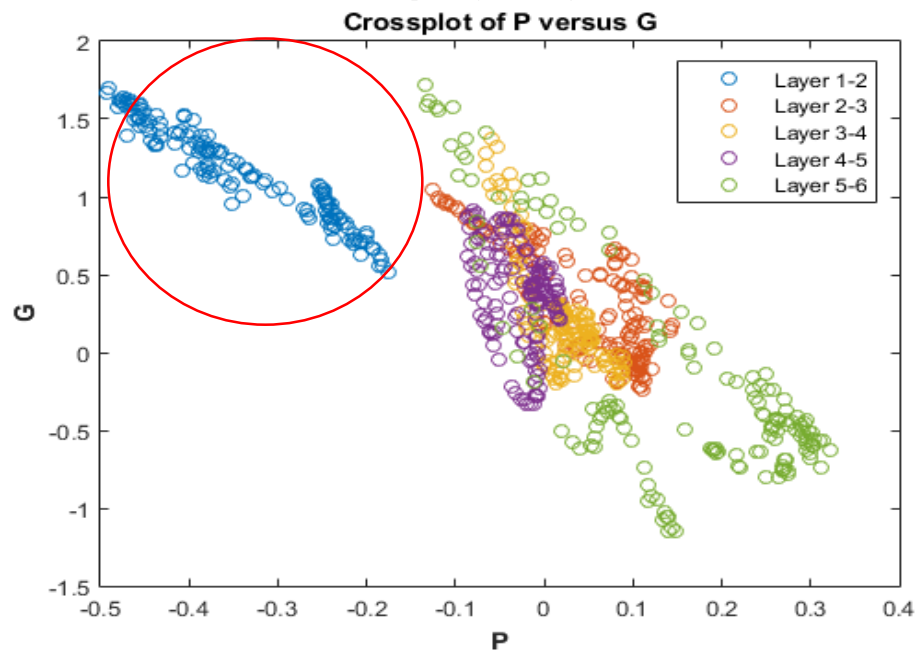


Figure 7.25 PG crossplot of CMP gathers 150-300, different colors represent the different reflectors. The red circle indicates the gas anomaly.

7.6 Detailed investigation of distance to amplitude analysis.

This part of the AVO flow analysis is comprised of the detailed investigation of distance to amplitude analysis. The CMP gathers are now stacked and the behavior of the amplitude over distance for the whole stacked section is examined. A part of the stacked section is chosen for this purpose, consisting of CMP gathers 150-300, which corresponds to a part of the seismic line at 750-1500 m, where the correlation between amplitude and offset is more intense. The stacked section is plotted in **Figure 7.26**, with the two-way travel time of each reflector, represented with different color. In **Figure 7.27** a closer depiction of **Figure 7.26** is presented. Judging from **Figure 7.27**, although, the travel times of the top and bottom reflectors have been accurately matched, there is still a mismatch for the intermediate reflectors, since these reflections are not easily distinguishable.

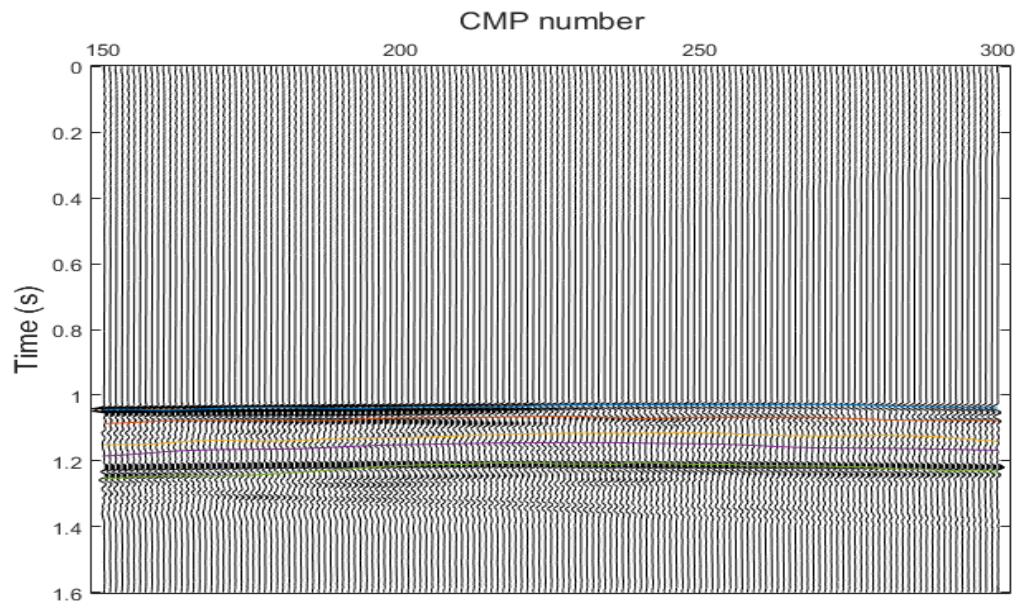


Figure 7.26 Stacked section of CMP gathers 150-300. The colours correspond to travel times for different reflectors.

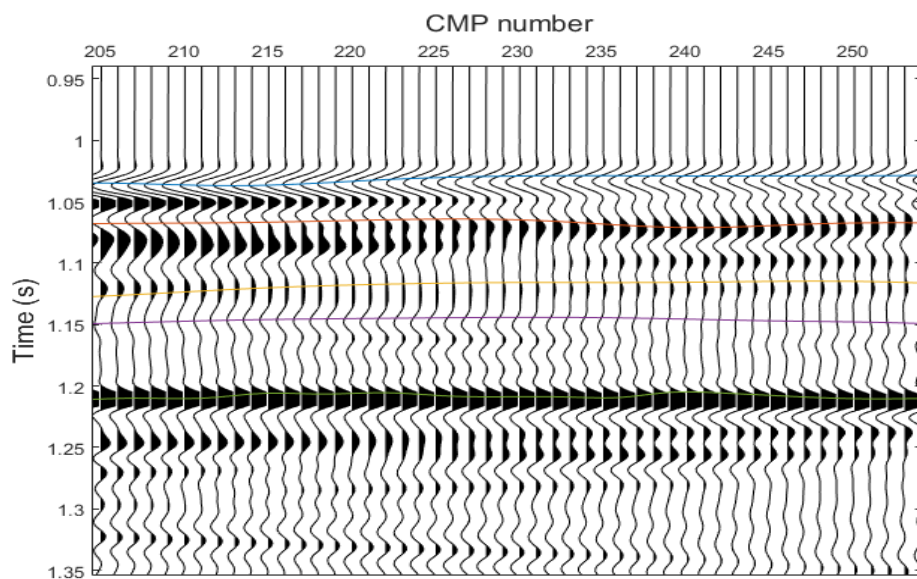


Figure 7.27 A Closer depiction of Figure 7.26, showing the travel time of each reflector.

In **Figure 7.28** the amplitude of each reflector is plotted against the corresponding CMP number for the selected travel time and a trend line is fitted to the data points. In **Figure 7.29**, a comparison between **Figures 7.28** and **7.11** is carried out, as in the previous section. We can see that both the stacked section of the synthetic data and the ray tracing algorithm gave similar results of AVO response, separating clearly each layer to its proper AVO class.

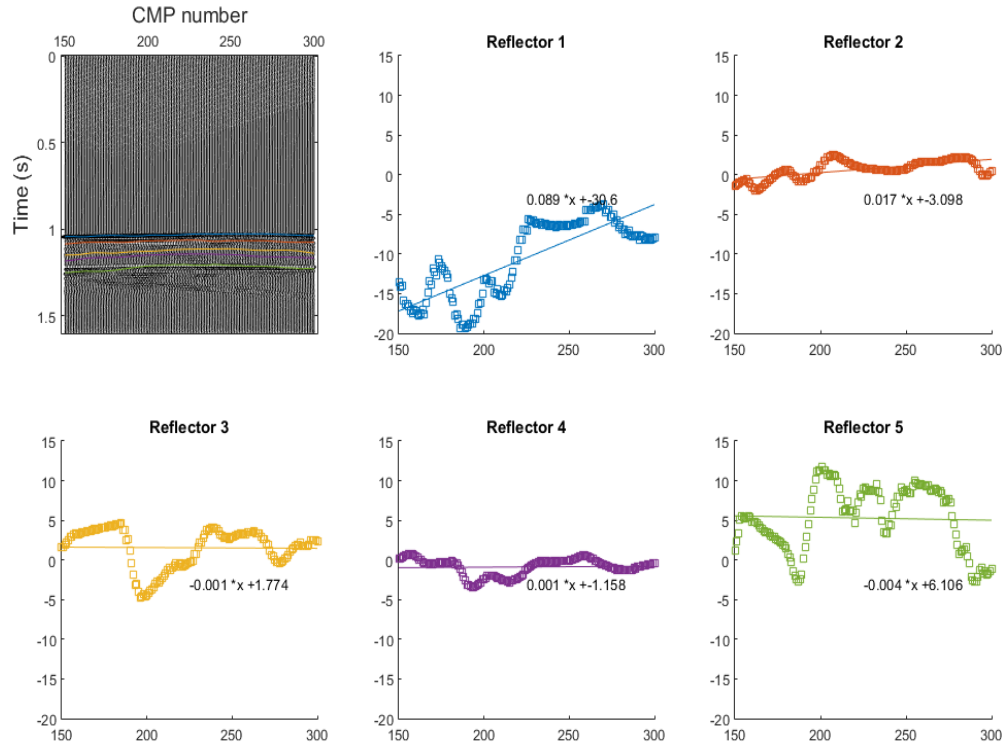


Figure 7.28 Amplitude versus CMP number of each reflector.

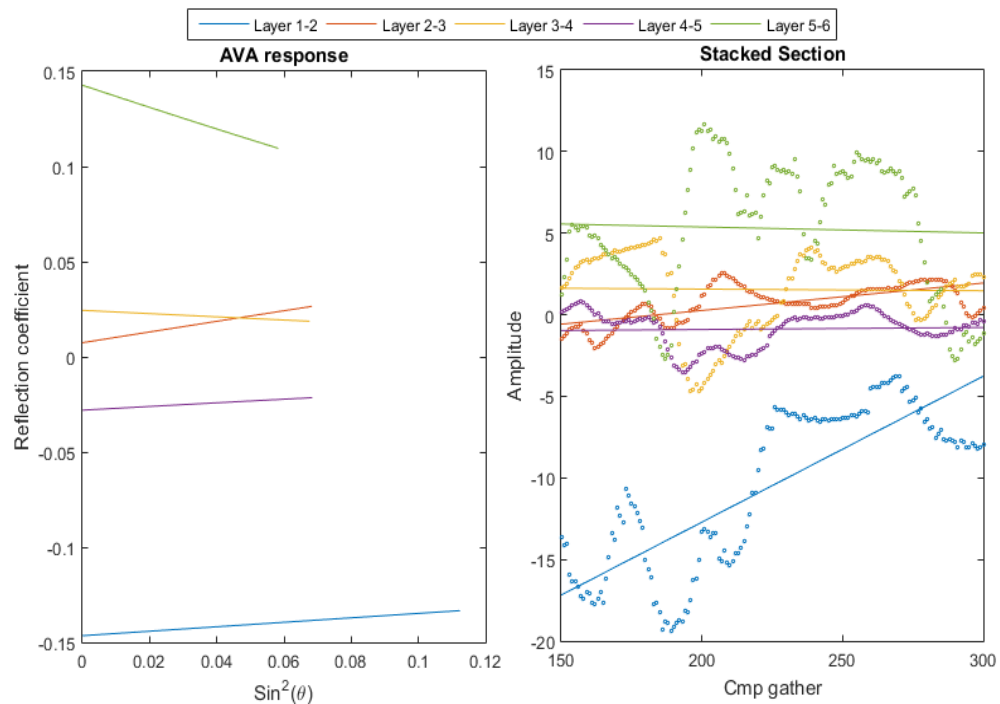


Figure 7.29 Comparison of AVO response using raytracing results and the stacked section of the synthetic data.

7.7 AVO inversion of elastic parameters

In the final part of the AVO flow analysis, AVO inversion is applied to the elastic parameters of the model, using Shuey's (1985) approximation to the exact expression of the particle displacement reflection and transmission coefficients (the relative displacement amplitudes). Since, we are only using 2-term approximation, which is valid only for incidence angle below 30 degree, the maximum incidence angle used in the inversion is set to 25 degree. The algorithm of the avo inversion is given as inputs, the desired error tolerance, the angles of incidence (lower than 25°) and the reflection coefficients of the model along with an initial assumption for the poisson's ratio of the upper and lower layers. A repetitive loop is then applied, where the partial derivative of the reflection coefficient is calculated, using its Jacobian matrix with the function **derive_avo** (Mudianto, 2007). Then, an increment parameter for the Poisson's ratio is calculated with the function **marquardt** (Mudianto, 2007). The function applies a least squares inversion algorithm, using Marquardt – Levenberg optimization method (Lines and Treitel, 1984). The inverted value of the Poisson's ratio derives as the sum of the initially assumed value of Poisson's ratio plus the increment parameter. The error tolerance is then checked for every loop. Finally, knowing the inverted values of the Poisson's ratio, the inverted values of P-wave and S-wave velocities can be easily approximated, with the use of equations 5.1 and 5.8. Inversion result (Poisson's ratio, P-wave velocity and S-wave velocity for each interface) is then plotted on **Figures 7.30-7.32**, along with the true model.

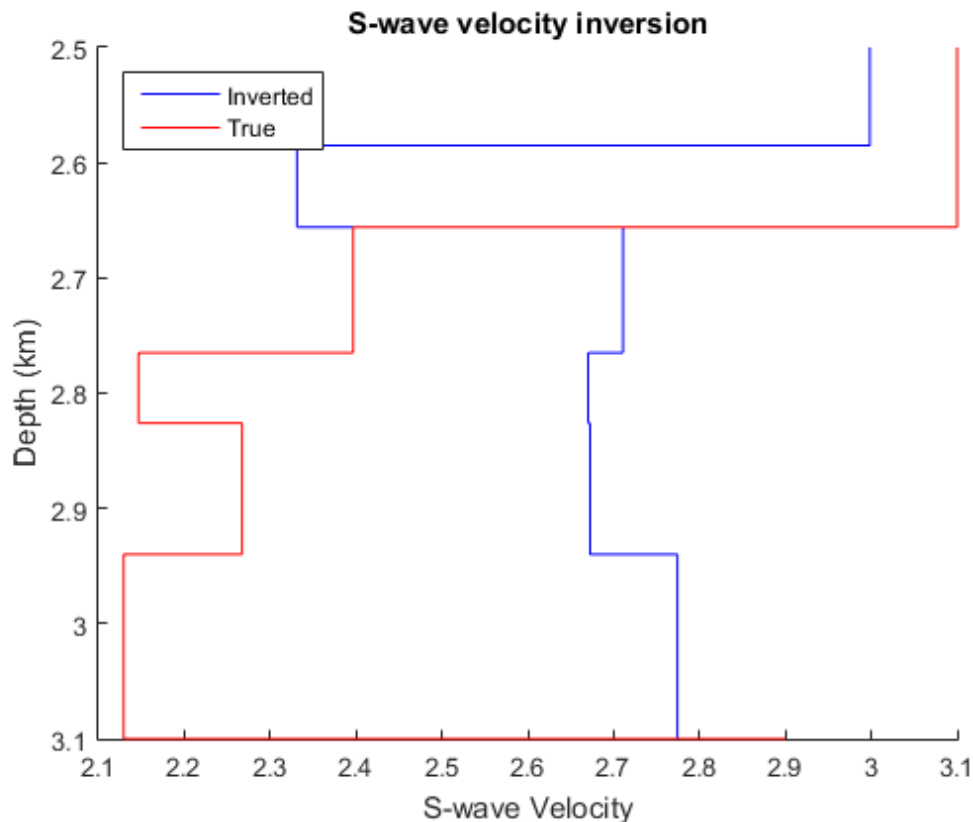


Figure 7.30 S-wave velocity for true (red) and inverted (blue) models.

The matching between the true and inverted data is not pretty accurate for the P-wave and S-wave velocities with the deviation ratio ranging from 10%-15%. Despite the deviation of the values, the behaviour of the elastic parameters through depth is pretty similar for the true and inverted data. Great differences are observed especially for the top and bottom formations where the changes of the elastic parameters are more abrupt. The deviation of the true and inverted values for the Poisson's ratio are even higher with a deviation percentage of about 20%. These deviations can be attributed to the several assumptions and simplifications made initially for the calculation of the model's elastic parameters.

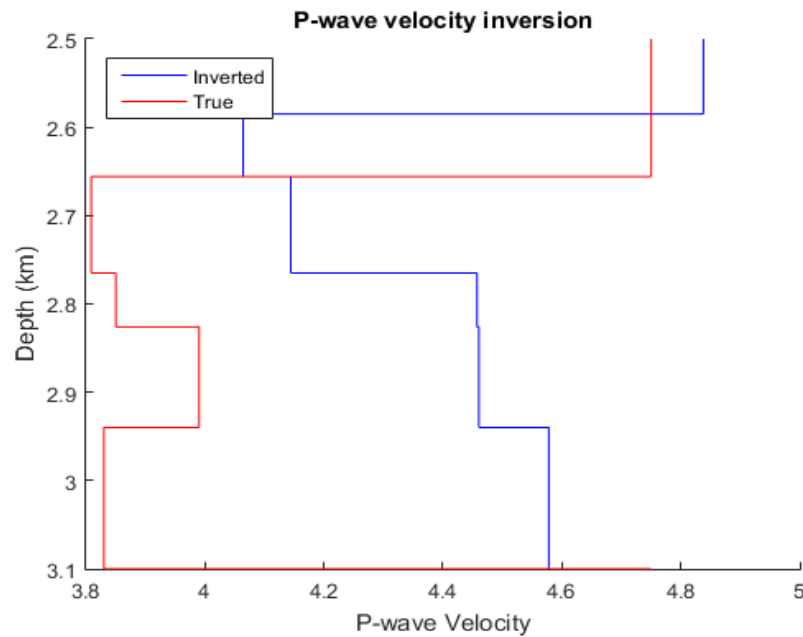


Figure 7.31 P-wave velocity for true (red) and inverted (blue) models.

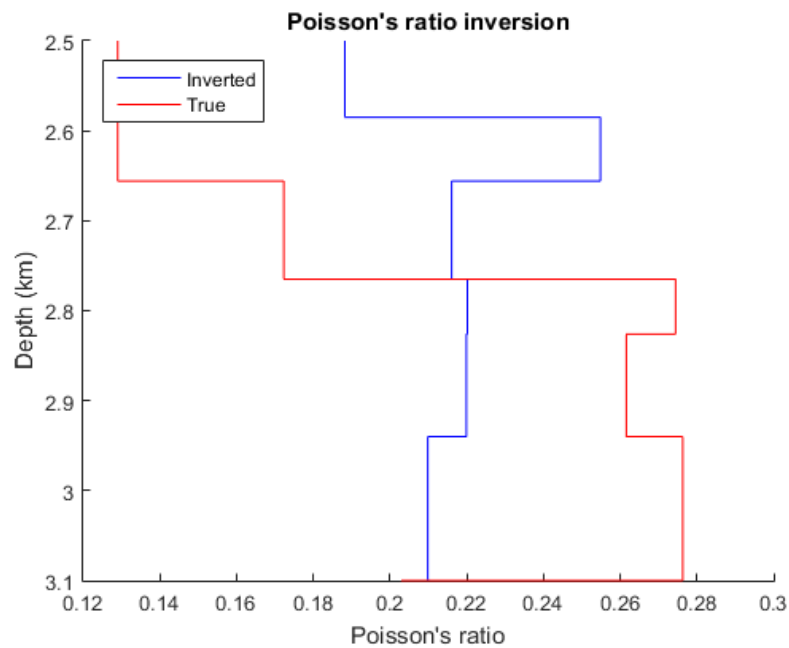


Figure 7.32 Poisson's ratio for true (red) and inverted (blue) models.

8 Summary and Conclusion

This study was focused on an integrated approach of gas detection in the sandstone reservoir of Prinos oil field, located in the northern Aegean Sea. The rock properties variation with depth in the study area, were inferred from real well seismic logs (Fronimos, 1998). The geological structure of the model was based on an East-West 2D geological plan of Prinos basin (Michelakis, 2010). Furthermore, the top layer of the reservoir was considered to be 50% saturated with gas, so, its elastic parameters were accordingly adjusted. The above information were given as input to a synthetic data simulator (Applied Geophysics Laboratory of the Technical University of Crete) in order to build low frequency synthetic seismograms. Additionally, a signal processing graphical interface was build, in order to properly process the synthetic data before the application of the AVO analysis. Finally, an analytical AVO analysis flow was adapted for the processed seismic data which managed to successfully detect the presence of gas in the gas saturated layer.

Despite the major limitations and simplifications that the model was based on (Gassmann fluid replacement model, mudrock line and Lindseth density correlation), it still provides a robust approach. The AVO signature is not dependent on the properties of the reservoir alone but also on the overburden through which the seismic pulse propagates. As a result, fluid replacement modeling needs to take into account not just the properties of the reservoir but the cap rock as well. However, despite these simplistic assumptions and limitations the following conclusions can be arrived at:

- Combined with rock physical property analysis, petrophysical analysis, and geological information, AVO modeling provides useful information in interpretation and thus increases certainty in gas detection and reservoir characterization. It emphasizes the influence of petrophysical rock properties on seismic rock properties.
- Cross-plotting of rock properties indicate that reservoir sandstone is of high impedance encased with in low impedance shale. Large drop in Poisson's ratio for gas charged reservoir sand allow utilization of AVO technique to characterize the reservoir.
- The AVO anomaly in the target zone in the present case has been classified as class IV anomaly on the basis of highly negative intercept and highly positive gradient computed from the model.
- The results taken from AVO analysis on the synthetic gathers show good correlation with the results taken from the raytracing algorithm.
- Cross-plot of Intercept versus Gradient from AVO analysis shows marked separation of anomalous points from background trend (shale/wet sand) which has been identified as calss IV AVO anomaly.
- AVO modeling may be used as a complimentary tool with 3D seismic in reservoir monitoring during production since the effects of changing saturation are less visible on the stacked seismic data compared to the changes in the reflection coefficient as a function of offset in the prestack domain

9 References

- [1] Abdullatif, A. A. & Mousa W. A., (2011). *Processing of Seismic Reflection Data Using MATLABTM*.
- [2] Aki, K. and Richards, P. (1980). Quantitative seismology.
- [3] Almutlaq, M., & Margrave, G. (2010). Tutorial: AVO inversion. *Crewes.Org*, 22, 1–23.
- [4] Arthur, J. M., & Lawton, D. C. (2011). Multicomponent AVO analysis of a single thinning bed, 23(1996), 1–15.
- [5] Avseth, P. (2010). Explorational Rock Physics – The Link Between Geological Processes and Geophysical Observables. *Petroleum Geoscience*, pp.403-426.
- [6] Avseth, P., Mukerji, T. and Mavko, G. (2005). Quantitative seismic interpretation. Cambridge, UK: Cambridge University Press.
- [7] Bagaini, C., Bunting, T., & El-emam, A. (2010). Land Seismic Techniques for High-Quality Data, 28–39.
- [8] Bhardwaj, B. M., Jambhekar, C. V., & Kandpal, M. C. (1985). Detection of gas in sandstone reservoirs using AVO analysis in Cambay Basin.
- [9] Carcione, J. M., Ursin, B. and Nordskag, J. I. (2007). Cross-property relations between electrical conductivity and the seismic velocity of rocks.
- [10] Castagna, J. P. (1985). Relationships between compressional-wave and shear-wave velocities in clastic silicate rocks. *Geophysics*, 50(4), 571.
- [11] Castagna, J. P., & Swan, H. W. (1997). Principles of AVO crossplotting. *The Leading Edge*, 16(4), 337.
- [12] Castagna, J. P., M. L. Batzle, and T. K. Kan, (1993), Rock physics – The link between rock properties and AVO response, in J. P. Castagna and M. Backus, eds., Offset-dependent reflectivity – Theory and practice of AVO analysis: Investigations in Geophysics 8, 135–171.
- [13] Castagna, J. P., Swan, H. W., & Foster, D. J. (1998). Framework for AVO gradient and intercept interpretation. *Geophysics*, 63(3), 948.
- [14] Chiburis, E., Leaney, S., Skidmore, C., Franck, C., & Mchugo, S. (1993). Hydrocarbon detection with AVO. *Oilfield Review*, 5(1), 42–50.
- [15] Dvorkin, J. P. (2008). Seismic Reflections of Rock Properties

- [16] Fatti, J. L., Smith, G. C., Vail, P. J., Strauss, P. J., & Levitt, P. R. (1994). Detection of gas in sandstone reservoirs using AVO analysis : A 3-D seismic case history using the Geostack technique, *59*(9), 1362–1376.
- [17] Feng, H., & Bancroft, J. C. (2006). AVO principles, processing and inversion. *CREWES Research Report — Volume 18 (2006)*, *18*, 1–19.
- [18] Fronimos P. (1998). Examination of horizontal well's location with the use of geophysical loggings. *Logging While Drilling*.
- [19] Guo, Q. (2014). Tuning, Avo, and Flat-Spot Effects in a Seismic Analysis of North Sea.
- [20] Han, D., Nur, a, & Morgani, D. (1986). De-hua Han*, A. Nur*, and Dale Morgani. *Geophysics*, *51*(11), 2093–2117.
- [21] Hato, M. H., Namori, T. I., Ahar, A. B., & Atsuoka, T. M. (2004). Application of AVO Analysis to Seismic Data for Detection of Gas below Methane Hydrate Stability Zone in Nankai Trough Area, *54*(1), 105–113.
- [22] Hsu, K.J., (1972). Origin of saline giants: a critical review after the discovery of the Mediterranean evaporite. *Earth-Science Review*, v. 8, pp.371-396.
- [23] K. O. Friedrichs and H. Lewy, “Über die Eindeutigkeit und das Abhängigkeitsgebiet der Lösungen beim Anfangswertproblem hearer hyperbolischer Differentialgleichungen,” *Math. Ann.* 98, 192-204 (1928).
- [24] Kiomourtzi, P., Pasadakis, N. and A. Zelilidis, (2007). Geochemical Characterization of Satellite Hydrocarbon Formations in Prinos-Kavala Basin (North Greece). *Bull. Geol. Soc. Greece*, vol. XXXX, n., pp.839-850.
- [25] Lee, M. W. (2015). Elastic velocities of partially gas-saturated unconsolidated sediments Elastic velocities of partially gas-saturated unconsolidated sediments.
- [26] Lines, L.R., and Treitel, (1984). A review of least-squares inversion and its application to geophysical problems: *Geophysical Prospecting*, *32*, 159-186.
- [27] Macleod, M. (n.d.). *Shear Waves Shine Brightly*, 2–15.
- [28] Margrave, G. F. (2000). New seismic modelling facilities in Matlab. *Report*, *12*, 1–45.
- [29] Mavko, G. The Rock Physics of AVO, Stanford Rock Physics Laboratory 302–326.
- [30] Michelakis M. (2010). 3D stromatographical simulation of the Prinos basin's hydrocarbon reservoir.
- [31] Murdianto B.S. (2007). Velocity Interpolation, Raytracing in V (z) Medium , AVO / AVA Inversion , Acoustic Wave Finite Difference Modeling and Migration.
- [32] N. Rigakis, N. Roussos, E. Kamberis, P. Proedrou. (2001). Hydrocarbon gas

- accumulations in Greece and their origin 9 International congress of the geological society of Greece with emphasis on the contribution of geosciences to development. Volume XXXIV, No 3, Athens, 2001
- [33] Nainggolan H. (2011). Seismic Forward Modelling for Synthetic P-P & P-S Reflection (Reviewed and Implemented by Matlab).
- [34] Nieto, C. E., & Stewart, R. R. (2001). Angle of incidence estimation for converted-waves, *13*(2).
- [35] Norwegian University of Science and Technology (1999). Avo theory.
- [36] P. D. Lax and B. Wendroff, "Difference schemes for hyperbolic equations with high order accuracy," *Comm. Pure and Applied Math.* 17, No. 3, 381-398 (1964).
- [37] Pelletier, H. (2009). AVO Crossplotting II : Examining Vp / Vs Behavior. *Frontiers & Innovation Conference*, (1998), 105–110.
- [38] Pelletier, H. (2009). AVO Crossplotting II : Examining Vp / Vs Behavior. *Frontiers & Innovation Conference*, (1998), 105–110.
- [39] Pollak, W.H., (1979). Structural and lithological development of the Prinos-Kavala basin, sea of Thrace, Greece.
- [40] Proedrou, P., (1979). The Evaporite formation in the Nestos-Prinos graben in the northern Aegean sea.
- [41] Proedrou, P., (2001). South Kavala gas field-Taphrogenetic Prinos basin. *Bull. Geol. Soc. Greece*, vol. XXXIV, n.3, pp.1221-1228.
- [42] Proedrou, P., and C.M., Papaconstantinou, (2004). Prinos basin – A model for oil exploration. *Bull. Geol. Soc. Greece*, vol. XXXVI, n.1, pp.327-333.
- [43] Proedrou, P., and T. Sidiropoulos, (1992). Prinos field – Greece, Aegean basin, structural traps. *Treatise of petroleum Geology atlas of oil and gas fields*, AAPG, pp.275-291.
- [44] Russell B. and Hampson D. (2006). *The old and the new in seismic inversion*.
- [45] Rutherford, R., & Williamss, R. H. (1989). Amplitude-versus-offset variations in gas sands, *54*(2).
- [46] Simm R., White R. and Uden R. (2000). The anatomy of AVO crossplots.
- [47] Vafidis, A., Abramovici, F., and Kanasewich, E. R., (1992), Elastic wave propagation using fully vectorized high order finite-difference algorithms: *Geophysics*, 57, 218-232.
- [48] Vafidis, A., Abramovici, F. and Kanasewichm E.R. (1992). Elastic wave propagation using fully vectorised high-order finite-difference algorithms. *Geophysics* 57, 218-232.

- [49] Walker, R.G., and E. Mutti, (1973). Turbidite facies and facies associations, in G.V. Middleton and A.H. Bouma, eds, *Turbidites and deep water sedimentation: SEPM Pacific Section Short Course*, Anaheim, California, pp.119-157.
- [50] Xu, Y., & Technologies, R. (n.d.). Angle-dependent amplitude and AVO / AVA analysis with PSDM.
- [51] Young, R., & LoPiccolo, R. (2005). AVO analysis demystified. *Hart's E & P*, 78(10), 77–81.
- [52] Zhang, H., & Brown, R. J. (2001). A review of AVO analysis. *CREWES Research Report*, 13(1), 357–380.

Matlab Codes:

- [53] Abdulatif A. A. and Mousa W. A., (2011)
- [54] Margrave G.F, (2013), CREWES Matlab Library, <http://www.crewes.org/>
- [55] Rietsch E. (2003). *Quantitative Seismic Interpretation*.
- [56] Technical University of Crete. Applied Geophysics Lab.
- [57] Tzanis A. National and Kapodistrian University of Athens, (2005).
- [58] University of Alberta, Seismic Lab, (2008). Signal Analysis and Imaging Group. <http://www-geo.phys.ualberta.ca/saig/SeismicLab>.

Appendix A

Matlab Codes:

AVA inversion

```
% run AVA inversion for each interface
% initial model : Poisson's ratio for upper and lower layer
% max. incidence angle is set to 25 deg. since we're using 2-term
Shuey
% approximation
pois1 = 0.4; pois2 = 0.2; thetamax = 25;
disp('Starting AVA inversion using Shuey's (1985) approximation');
disp(sprintf('Maximum incidence angle is set to %d
degree',thetamax));
disp('=====');
% stopping criteria
stop = 1e-4;
for k = 2:2:nint
    ao = refl(k,1);
    fprintf('Running AVA inversion for layer %d and %d\n',k,k+1);
    fprintf('True parameters for these layers :\n');
    fprintf('ao = %0.3f\n',ao);
    fprintf('Poisson's ratio for upper layer = %0.3f\n',pois(:,k));
    fprintf('Poisson's ratio for lower layer = %0.3f\n',pois(:,k+1));
    itheta = find(theta(k,:) <= thetamax);
    thetan = theta(k,1:length(itheta)); % incidence angle
    Robs = refl(k,1:length(itheta)); % observation data, from forward
modeling
    poisson = [pois1 pois2];
    p = [ao poisson]'; thetan = thetan';
    Rcal = shuey(ao,poisson,thetan);
    a = deriv_avo(ao,poisson,thetan); % jacobian matrix
    beta = 1e-5; % damping factor, to prevent singular matrix
    delta = marquardt(Robs,Rcal,a,p,beta); % parameter increment
    p = p+delta; % update initial model
    poisr(k-1) = p(2); poisr(k) = p(3);
    error = sum((Robs-Rcal).^2); % sum of squared errors
    % iterative computation
    count=0;
    while stop < error % stop iteration if error < stopping criteria
        ao = p(1); poisson = [p(2) p(3)];
        Rcal = shuey(ao,poisson,thetan);
        a = deriv_avo(ao,poisson,thetan);
        delta = marquardt(Robs,Rcal,a,p,beta);
        p = p+delta;
        poisr(k-1) = p(2); poisr(k) = p(3);
        error = sum((Robs-Rcal).^2);
        count = count+1; % update no. of iteration
    end
    pois1 = p(2); pois2 = p(3);
```

```

% display result
fprintf('Inversion result for these layers :\n',k,k+1);
disp(sprintf('ao = %0.3f',p(1)));
disp(sprintf('Poisson's ratio for upper layer = %0.3f',p(2)));
disp(sprintf('Poisson's ratio for lower layer = %0.3f',p(3)));
disp(sprintf('Sum of squared errors = %0.5f',error));
disp(sprintf('No. of iterations = %d\n',count));
end
if ~mod(length(poissr),2)
poissr(end+1)=p(2);
end
% plot result
figure;drawvint(z(:,2:length(z)),poissr);drawvint(z(:,2:length(z)),po
is(:,2:length(z)),'r');flipy;
ymin = min(z(:,2:length(z))); ymax = max(z(:,2:length(z)));
xmin = 0.2; xmax = 0.5;
axis([xmin xmax ymin ymax]);
xlabel('Poisson's ratio');ylabel('Depth (km)');
legend('Inverted','True','Location','NorthWest');

```

AVO classification

```

clear all;
clc;
close all

vp = [4.75,4.75,4.14*0.92,3.85,3.99,3.83,4.75]';

vs=(vp'-1.36)/1.16;
vs(3)=(4.14-1.36)/1.16;
vs(1)=3.1;
vs(2)=3.1;
vs(end)=2.9;

rho=(vp'*1000/0.3048-3460)/0.308./(vp'*1000/0.3048);
rho(1)=2.6;
rho(2)=2.6;
rho(end)=2.9;

v = vp';
z = [0 2.585 2.656 2.765 2.826 2.94 3.1];

h = diff(z);
D = 0.01:0.01:1.89;

ratio=min(vp./vs');

pois = (vs.^2-0.5*v.^2)./(vs.^2-v.^2);

% number of traces and number of interfaces
ntrace = length(D);
nint = min([length(h) length(v)]);

```

```

% find ray parameters using MATLAB command : fzero
disp('Calculating ray parameters...');
figure;
for j = 1:ntrace
    offset = D(j);
    for i = 1:nint
        hh = h(1:i);
        vv = v(1:i);
        er = 0.0001;
        x = min(1./vv) - er;
        if D(j)>0
            p(i,j) = fzero('fun_ray', [-er x], [], offset, hh, vv);
        else
            p(i,j) = fzero('fun_ray', [er -x], [], offset, hh, vv);
        end
        theta(i,j) = (asin(p(i,j)*vv(i)))*180/pi;

% calculate traveltime based on ray parameters
t(i,j) = 2*sum(hh./(vv.*sqrt(1-p(i,j)^2*vv.^2)));

    end
end

angles=theta;

for i=1:size(angles,2)
    [refl,coeff]=ava_approximation(vp,vs',rho',angles(:,i)', 'two-term');
    a(:,i)=refl(:,1);
    b(:,i)=coeff(:,1);
    c(:,i)=coeff(:,2);
end

figure;
for i=2:size(angles,1)
    plot(angles(i,:),a(i,:))
    hold on;
end
xmin = min(min(angles)); xmax = max(max(angles));
ymin = min(min(a)); ymax = max(max(a));
axis([xmin xmax ymin ymax]);
xlabel('Incidence angle (degree)');ylabel('Reflection coefficient');
title('AVA response');legend(...'Layer 1-2',
'Layer 1-2','Layer 2-3','Layer 3-4','Layer 4-5','Layer 5-
6');%,'Layer 6-7');
preppfig

figure;
for i=2:size(angles,1)
    plot(sind(angles(i,:)).^2,a(i,:))
    hold on;
end

xlabel('Sin^2(\theta)');ylabel('Reflection coefficient');

```



```

title('AVA response');legend(...'Layer 1-2',
'Layer 1-2','Layer 2-3','Layer 3-4','Layer 4-5','Layer 5-
6');%,'Layer 6-7');
preppfig

figure;
for i=2:size(b,1)
scatter(b(i,:),c(i,:));
hold on;
end
grid on;

hold on;
plot([-0.2 0.2],[0 0],'--b')
hold on;
plot([-0.02 -0.02],[-0.4 0.0342],'--r')
hold on;
plot([0.02 0.02],[-0.4 -0.0342],'--r')
hold on;
plot([-0.2,0.2],[4/5*(1-9*(1/ratio)^2)*(-0.2),4/5*(1-
9*(1/ratio)^2)*0.2],'--k')

legend('Layer 1-2','Layer 2-3','Layer 3-4','Layer 4-5','Layer 5-
6');%,'Layer 6-7');
xlabel('AVO Intercept (A)');
ylabel('AVO gradient (B)');
title('Rutherford and Williams Classification');
figure1=gcf;

h = text(-0.15,0.22, 'Background trend','FontSize',10);
set(h, 'rotation', -35)

annotation.figure1,'textbox',...
[0.49 0.2 0.09 0.04],...
'String',{'Class II'},...
'FitBoxToText','on','FontWeight','bold');

annotation.figure1,'textbox',...
[0.6 0.18 0.08 0.04],...
'String','Class I',...
'FitBoxToText','on','FontWeight','bold');

annotation.figure1,'textbox',...
[0.2 0.2 0.09 0.04],...
'String','Class III','FontWeight','bold');

annotation.figure1,'textbox',...
[0.2 0.45 0.09 0.04],...
'String','Class IV',...
'FitBoxToText','on','FontWeight','bold');
ylim([-0.4 0.4])

```

Common Offset gather creation

```

count=0;
rec=0;

dx1=dx; % Keep the coordinate of the receivers

for k=1:sourceinterval:SourceNum

count=count+1;

sx1(count)=segy.sx(k); % Keep the coordinate of the shot

idx = find( sx1(count)-dx1 == offsett ); % Keep the
indexes of the requested offset

if ~isempty(idx)

    rec=rec+1;

[h, t, shot] = SEGY_ReadShotGather(segy, k); % Read all
traces for each shot

common_offset(1:handles.max_length_def,rec)=shot(1:handles
.max_length_def,idx); % Keep the desired trace
sx2(rec)=segy.sx(k);
end
end

fprintf('\n%d Common offset gathers have been found with
offset= %d\n',rec,offsett);

```

Digitize function

```

function varargout = digitize(varargin)

global check_flag

%DIGITIZE digitize data from image.
% DIGITIZE with no input or output arguments allows the user to
% select an image file to load;only IMREAD-compatible image
% files are supported. The function then prompts the user
% to graphically identify the location of the origin and the X-
% and Y- axes of the plot. The user may then graphically select
% an arbitrary number of data points from anywhere on the image
% using the left mouse button. Data acquisition is terminated
% by clicking the RIGHT mouse button. The function then prompts
% the user to save the acquired data to file.
%
% ACQDATA = DIGITIZE with one output argument returns the X- and
% Y- values of the graphically selected data in the array ACQDATA.

```

```

% The user is not prompted to save the data to file.
%
% DIGITIZE(FILENAME) with one input argument FILENAME is used to
% directly specify the image file to load. As above, the user is
% prompted to graphically set up the coordinate system and select
% target data points.
%
% See also IMREAD, IMFINFO.

% Author(s): A. Prasad
% Edited by Choustoulakis E., 2015
% Original version created by J.D.Cogdell

% Check for proper number of input arguments
error(nargchk(0,1,nargin));

% Checks if there is any open figure and ask user to close it
if ~isempty(findall(0,'Type','Figure'))
CloseOpenFigures = questdlg(...
    'All open figures will close ', ...
    'Close Open Figures',...
    'OK','Cancel','OK');
switch CloseOpenFigures,
    case 'OK',
        close all
    case 'Cancel',
        return
    exit
end % CloseOpenFigures
end

figure_flag=1;

while figure_flag==1
% Identify image filename
if (nargin == 0),
    [filename, pathname] = uigetfile( ...
        {'*.jpg;*.tif;*.gif;*.png;*.bmp', ...
        'All MATLAB Image Files (*.jpg,*.tif,*.gif,*.png,*.bmp)';
    ...
        '*.jpg;*.jpeg', ...
        'JPEG Files (*.jpg,*.jpeg)'; ...
        '*.tif;*.tiff', ...
        'TIFF Files (*.tif,*.tiff)'; ...
        '*.gif', ...
        'GIF Files (*.gif)'; ...
        '*.png', ...
        'PNG Files (*.png)'; ...
        '*.bmp', ...
        'Bitmap Files (*.bmp)'; ...
        '.*', ...
        'All Files (*.*)'}, ...
        'Select image file');
    if isequal(filename,0) | isequal(pathname,0)
        check_flag=1;
        return

```

```

        else
            check_flag=0;
            imagename = fullfile(pathname, filename);
        end
elseif nargin == 1,
    imagename = varargin{1};
    [path, file,ext] = fileparts(imagename);
    filename = strcat(file,ext);
end

% Read image from target filename

pic = imread(imagename);
image(pic)

FigName = ['IMAGE: ' filename];

set(gcf,'Units','normalized', ...
'Position',[0 0.125 1 0.85], ...
'Name', FigName, ...
'NumberTitle','On', ...
'MenuBar','None')

set(gca,'Units','normalized','Position',[0 0 1 1]);

% dimensions

prompt = {'Enter the MAXIMUM X axis value',...
'Enter the MAXIMUM Z axis value'};
tit     = 'X-Y';
lin     = 1;
df      ={'1900','3100'};
xv      = inputdlg(prompt,tit,lin,df);

if isempty(xv)
    figure_flag=1;
    if ~isempty(findall(0,'Type','Figure'))
        close(FigName)
    end

else
    X=str2num(xv{1});
    Z=str2num(xv{2});
    figure_flag=0;
end
end
% INSTRUCTIONS

msg{1}=['PICKING POINTS'];
msg{2}=['=> Press RIGHT mouse click to SELECT a
point of the figure'];
msg{3}=['=> Press LEFT mouse click to ZOOM'];

```

```

msg{4}=['=> Press DOUBLE-LEFT mouse click to
UNZOOM...'];
msg{5}=['=> Press BACKSPACE to DELETE last
point'];
msb=msgbox(msg,'Help about picking
procedure','help');
set(msb,'WindowStyle','modal');
uiwait(msb);

% Determine location of origin with mouse click

origin_flag=1;

while origin_flag==1
OriginButton = questdlg('Select the ORIGIN (Xo,Yo) of the axes with
RIGHT mouse button click', ...
    'DIGITIZE: user input required', ...
    'OK','Cancel','OK');
switch OriginButton,

    case 'OK',
        drawnow
        [Xopixels,Yopixels] = ginput2(1);
        h1=line(Xopixels,Yopixels,...
            'Marker','o','Color','g','MarkerSize',14);
        h2=line(Xopixels,Yopixels,...
            'Marker','x','Color','g','MarkerSize',14);

    case 'Cancel',

        close(FigName)
        return
end % switch OriginButton

% Prompt user for X- & Y- values at origin
prompt={'Enter the X value at the origin',...
    'Enter the Y value at the origin:'};
def={'0','3100'};
dlgTitle='DIGITIZE: user input required';
lineNo=1;
answer=inputdlg(prompt,dlgTitle,lineNo,def);
if (isempty(char(answer{:}))) == 1,
    origin_flag=1;
    set(h1,'Visible','off');
    set(h2,'Visible','off');
else
    OriginXYdata = str2num(char(answer{:}));
    origin_flag=0;
end
end

x_flag=1;
while x_flag==1

% Define X-axis

```

```

XLimButton = questdlg(...
    'Select a point on the X-axis with RIGHT mouse button click ',
    ...
    'DIGITIZE: user input required', ...
    'OK','Cancel','OK');
switch XLimButton,
    case 'OK',

        drawnow
        [XAxisXpixels,XAxisYpixels] = ginput2(1);

        h1=line(XAxisXpixels,XAxisYpixels,...
            'Marker','*','Color','b','MarkerSize',14);
        h2=line(XAxisXpixels,XAxisYpixels,...
            'Marker','s','Color','b','MarkerSize',14);

    case 'Cancel',
        close(FigName)
        return
end % switch XLimButton

% Prompt user for XLim value
prompt={'Enter the X value at the selected point'};
def={'1900'};
dlgTitle='DIGITIZE: user input required';
lineNo=1;
answer=inputdlg(prompt,dlgTitle,lineNo,def);
if (isempty(char(answer{:})) == 1),
    x_flag=1;
    set(h1,'Visible','off');
    set(h2,'Visible','off');
else
    x_flag=0;
    XAxisXdata = str2num(char(answer{:}));
end
end

    scalefactorXdata = XAxisXdata - OriginXYdata(1);

% Rotate image if necessary
% note image file line 1 is at top
th = atan((XAxisYpixels-Yopixels)/(XAxisXpixels-Xopixels));
% axis rotation matrix
rotmat = [cos(th) sin(th); -sin(th) cos(th)];

% Define Y-axis
y_flag=1;
while y_flag==1

YLimButton = questdlg(...
    'Select a point on the Y-axis with RIGHT mouse button click',
    ...
    'DIGITIZE: user input required', ...
    'OK','Cancel','OK');
switch YLimButton,

```

```

    case 'OK',

        drawnow
        [YAxisXpixels,YAxisYpixels] = ginput2(1);

        h1=line(YAxisXpixels,YAxisYpixels,...
            'Marker','*', 'Color','b', 'MarkerSize',14);
        h2=line(YAxisXpixels,YAxisYpixels,...
            'Marker','s', 'Color','b', 'MarkerSize',14);

    case 'Cancel',
        close(FigName)
        return
end % switch YLimButton

% Prompt user for YLim value
prompt={'Enter the Y value at the selected point'};
def={'1800'};
dlgTitle='DIGITIZE: user input required';
lineNo=1;
answer=inputdlg(prompt,dlgTitle,lineNo,def);
if (isempty(char(answer{:})) == 1),
    y_flag=1;
    set(h1,'Visible','off');
    set(h2,'Visible','off');
else
    y_flag=0;
    YAxisYdata = str2num(char(answer{:}));
end
end

    scalefactorYdata = YAxisYdata - OriginXYdata(2);

% Complete rotation matrix definition as necessary
delxyx = rotmat*[(XAxisXpixels-Xopixels);(XAxisYpixels-Yopixels)];
delxyy = rotmat*[(YAxisXpixels-Xopixels);(YAxisYpixels-Yopixels)];
delXcal = delxyx(1);
delYcal = delxyy(2);

% Commence Data Acquisition from image
msgStr{1} = 'Click with RIGHT mouse button to ACQUIRE';
msgStr{2} = 'Click with LEFT mouse button to ZOOM IN';
msgStr{3} = 'DOUBLE Click LEFT mouse button to ZOOM OUT';
msgStr{4} = 'Press BACKSPACE to CANCEL last point';
msgStr{5} = 'Press ESC to STOP';
titleStr = 'Ready for data acquisition';
uiwait(msgbox(msgStr,titleStr,'warn','modal'));
drawnow

numberformat = '%6.2f';
nXY = [];
ng = 0;

flag=1;
counter=0;

```

```

while flag==1
    counter=counter+1;
while 1,

    n = 0;
col=rand(1,3);

% %%%%%%%%%%%%% DATA ACQUISITION LOOP
% %%%%%%%%%%%%%

while 1

    [x,y, buttonNumber] = ginput2(1,'KeepZoom');
    xy = rotmat*(x-Xopixels);(y-Yopixels)];
    delXpoint = xy(1);
    delYpoint = xy(2);

    if buttonNumber == 3

        h=line(x,y,'Marker','.', 'Color',col,'MarkerSize',16);
        x = OriginXYdata(1) +
delXpoint/delXcal*scalefactorXdata;
        y = OriginXYdata(2) +
delYpoint/delYcal*scalefactorYdata;
        n = n+1;
        xpt(n) = x;
        ypt(n) = y;
        ng = ng+1;
        nXY(ng,:) = [n x y];

    elseif buttonNumber == 8

        set(h,'Visible','off')
        n=n-1;
        ng=ng-1;
        xpt(end)=[];
        ypt(end)=[];
        nXY(end,:)=[];

    else

        if buttonNumber ~= [1,2,3,8]
            query = questdlg('STOP digitizing and save data?', ...
                'DIGITIZE: confirmation', ...
                'YES', 'NO', 'NO');
            drawnow
            switch upper(query),
                case 'YES',
                    %disp(sprintf('\n'))
                    break
                case 'NO',

            end % switch query
        end

```

```

        end
    end
    % %%%%%%%%%%%%% DATA ACQUISITION LOOP
    %%%%%%%%%%%%%
    cncl=0;

    [writefname, writepname] = uiputfile('*.mat','Save data as');
    if (writefname == 0) & (writepname == 0),
        cncl=1;
    end

    if cncl~=1
        writepname = fullfile(writepname, writefname);

        writedata = [ypt' xpt'];
        writedata = writedata(writedata(:,1)>0 & writedata(:,1)<Z &
writedata(:,2)>0 & writedata(:,2)<X,:);
        [z_column,Indexes]=sort(writedata(:,2));
        writedata=writedata(Indexes,:);

        writedata=[writedata(1,1) -5; writedata; writedata(end,1) X+5;
Z+5 X+5; Z+5 -5; writedata(1,1) -5];

        eval(['Layer' num2str(counter) '= writedata']);

        save(writepname,['Layer' num2str(counter)]);
    end

    question = questdlg('Do you want to draw another layer ?',
...
                        'LAYER: drawing', ...
                        'YES', 'NO', 'YES');
    drawnow
    switch upper(question),
    case 'YES',
        flag=1;
        break;
    case 'NO',
        flag=0;
        break;
    end % switch query

end
end
close all
end
Excel creation

% Excel Creation
ExcelButton = questdlg(...
    'Do you want to create an excel velocity file?', ...
    'EXCEL: Creation', ...
    'OK','Cancel','OK');

```

```

switch ExcelButton,
    case 'OK',

        cncl=0;

        [writefname, writepname] = uiputfile({'*.xlsx'; '*.xls'}, 'Save
data as');
        if (writefname == 0) & (writepname == 0),
            cncl=1;
        end

        if cncl~=1
            writepfname = fullfile(writepname, writefname);
        end

        fprintf('Please WAIT as the data is being saved...\n')
        fprintf(['Do NOT OPEN ', writefname, ' file yet...\n\n'])

        wb = waitbar(0, 'Initializing waitbar...');

        B={'Layer', 'X position', 'Z Depth', 'Time [s]', 'Vint
[m/s]', 'Vrms - Time [m/s]'};

        xlswrite(writepfname, B, 1, 'A1')

        canc=0;

        for l=1:length(xlength)

            wbtxt{1}=['WRITING EXCEL DATA. DATA ', num2str(l), ' OF
', num2str(length(xlength)), '. Please wait...'];

            perc=l/length(xlength);
            wb =waitbar(perc, wb, wbtxt);
            if ~ishandle(wb)
                canc=1;
                break
            end
            xlswrite(writepfname, Layer_name(l), 1, ['A', num2str(l+1)])
            xlswrite(writepfname, xlength(l), 1, ['B', num2str(l+1)])
            xlswrite(writepfname, Depth(l), 1, ['C', num2str(l+1)])
            xlswrite(writepfname, time_conv(l), 1, ['D', num2str(l+1)])
            xlswrite(writepfname, Vint(l), 1, ['E', num2str(l+1)])
            xlswrite(writepfname, Vrms_time(l), 1, ['F', num2str(l+1)])
            fprintf([num2str(round(l/length(xlength)*100)), '%% of the data has
been saved to ', writefname, '..\n']);
        end
        close(wb)

        if canc==1
            fprintf('\nEXCEL CREATION HAS BEEN CANCELED\n');

        else
            fprintf('\nEXCEL CREATION HAS FINISHED\n');
            fprintf(['You can now OPEN ', writefname, '\n']);
        end
    end

```

```

end
end

return

```

Geometrical Spreading

```

time_interval=2*Model_Parameters.dt*1000; % The sampling dt is
converted to two way travel time in seconds

k=0;

for i=1:length(x) % for all the distance intervals

for j=1:ln % for all the layers
    k=k+1;
    if j==1
        time_new{i}=(0:time_interval:time_cmp(j,i)*1000); % the first
value of the time array will be zero and the next will be the first
value of "time_cmp"
        Vrms_cmp{i}=repmat(Vrms_time(k),1,length(time_new{i})); % the
first value of the Vrms array will be the Vrms of the first layer and
will be repeated for the rest of the array
        elseif j==ln

new_time_array=(time_new{i}(end)+time_interval:time_interval:t_max);
% the final value of time array will be equal to the time length
        Vrms_cmp{i}=[Vrms_cmp{i},
repmat(Vrms_time(k),1,length(new_time_array))];
        time_new{i}=[time_new{i},new_time_array];

    else

new_time_array=(time_new{i}(end)+time_interval:time_interval:time_cm
p(j,i)*1000);% the same procedure is being repeated and the new
arrays are jointer
        Vrms_cmp{i}=[Vrms_cmp{i},
repmat(Vrms_time(k),1,length(new_time_array))];
        time_new{i}=[time_new{i},new_time_array];
    end

end

GV{i}=time_new{i}'.*Vrms_cmp{i}.'/1000; % For each distance interval
the GV value is calculated as the product of time and vrms
end

```

PG Crossplots of Synthetic Data

```

clc
clear
load CMP_correctedd
load Time_Vel_Spreading
load CMP_final_preprocessed_1_10

```

```

load CMP_partial_24_48
for i=1:size(CMP_corrected,2)
Stack(:,i)=sum(CMP_corrected{i},2);
end

col=lines(5);
off=0.021;
figure;
subplot(2,3,1)
hold on;
mwigb(Stack(:,150:300),2,(150:300),(0:0.001:1.6));
xlabel('CMP number','FontSize',14)
ylabel('Time (s)','FontSize',14)
hold on;
for i=2:6
p= polyfit((1:379),Time_Vel_Spreading{1}(i,2:end-1)-off,3);
yfit(i-1,:)= polyval(p,(1:379));
Time100=Time_Vel_Spreading{1}(i,150:300);
plot((150:300),Time100-off,'color',col(i-1,:))
hold on;
end

col=lines(5);
l=0;

for cmpcol=150:300
l=l+1;
Time=Time_Vel_Spreading{1}(:,cmpcol+2);
Vrms=Time_Vel_Spreading{2}(:,cmpcol+2);
Times=round((Time(2:end-1))*1000)';
Times=Times+1;
col=lines(length(Times));
k=0;
for i=Times
k=k+1;
amplitude(k,cmpcol)=Stack(i,cmpcol);
plot(cmpcol,amplitude(k,:),'.','color',col(k,:));
p= polyfit(x,amplitude(k,:),1);
yfit= polyval(p,x);
hold on;
ger(k)=plot(x,yfit,'color',col(k,:));

if p(1)<0
text(x(2),yfit(1),[num2str(round(p(2)*1000)/1000),'*x
',num2str(round(p(1)*1000)/1000)])
else
text(x(2),yfit(1),[num2str(round(p(2)*1000)/1000),'*x +
',num2str(round(p(1)*1000)/1000)])
end
hold on;

end
end
xlabel('CMP number');
ylabel('Amplitude');

```

```

title(['CMP ', num2str(cmpcol)]);
col={'o', '.', 'd', 's', '*'};

figure;

for i=1:5
    subplot(2,3,i+1)
    hold on;
    if i==2
        q= polyfit((150:300),amplitude(i+1,150:300),1);
        qfit(i,:) = polyval(q,(150:300));
        hf(i)=plot((150:300),amplitude(i+1,150:300),'s','color',col(i,:));
    hold on;
    plot((150:300),qfit(i,:), '-','color',col(i,:))
    hold on;
    elseif i==3
        q= polyfit((150:300),amplitude(i-1,150:300),1);
        qfit(i,:) = polyval(q,(150:300));
        hf(i)=plot((150:300),amplitude(i-1,150:300),'s','color',col(i,:));
    hold on;
    plot((150:300),qfit(i,:), '-','color',col(i,:))
    hold on;
    else
        q= polyfit((150:300),amplitude(i,150:300),1);
        qfit(i,:) = polyval(q,(150:300));
        hf(i)=plot((150:300),amplitude(i,150:300),'s','color',col(i,:));
    hold on;
    plot((150:300),qfit(i,:), '-','color',col(i,:))
    hold on;
end
text(225,-3,[num2str(round(q(1)*1000)/1000), ' *x
+',num2str(round(q(2)*1000)/1000)]);
title(['Reflector ', num2str(i)]);
ylim([-20 15])
end

figure;

for i=1:5
    if i==2
        hold on;
        q= polyfit((150:300),amplitude(i+1,150:300),1);
        fre(i,1)=q(1);fre(i,2)=q(2);
        qfit(i,:) = polyval(q,(150:300));
        hf(i)=plot((150:300),amplitude(i+1,150:300),'o','color',col(i,:),
), 'MarkerSize',2);
    hold on;
    plot((150:300),qfit(i,:), '-','color',col(i,:), 'LineWidth',0.5)
    elseif i==3
        hold on;
        q= polyfit((150:300),amplitude(i-1,150:300),1);

```

```

fre(i,1)=q(1);fre(i,2)=q(2);
qfit(i,:) = polyval(q,(150:300));
hf(i)=plot((150:300),amplitude(i-
1,150:300),'o','color',col(i,:), 'MarkerSize',2);
hold on;
plot((150:300),qfit(i,:), '-','color',col(i,:), 'LineWidth',0.5)
    else
        hold on;
q= polyfit((150:300),amplitude(i,150:300),1);
fre(i,1)=q(1);fre(i,2)=q(2);
qfit(i,:) = polyval(q,(150:300));
hf(i)=plot((150:300),amplitude(i,150:300),'o','color',col(i,:),
'MarkerSize',2);
hold on;
plot((150:300),qfit(i,:), '-','color',col(i,:), 'LineWidth',0.5)
    end
end
title('Stacked Section');
xlabel('Cmp gather');
ylabel('Amplitude');
ylim([-20 15])

met=0;

for cmpcol=(150:300)
met=met+1;
Time100=Time_Vel_Spreading{1}(:,cmpcol+1);
Vrms100=Time_Vel_Spreading{2}(:,cmpcol+1);
Times=round((Time100(2:end-1)-off)*1000)';
Times=Times+1;
hh=h{cmpcol};
ind=abs(hh)/10;
idx=find(ind==0);
ind(idx)=1;
angles=theta(:,ind);
k=0;
col=lines(length(Times));
for i=Times
    k=k+1;
amplitude{k}=CMP_corrected{cmpcol}(i,:);
x=sind(angles(k,:)).^2;
p = polyfit(x,amplitude{k},1);
PG(met,:)=[p(1) p(2)];
if k==1
PG1(met,:)=[p(1) p(2)];
elseif k==2
PG2(met,:)=[p(1) p(2)];
elseif k==3
PG3(met,:)=[p(1) p(2)];
elseif k==4
PG4(met,:)=[p(1) p(2)];
else
PG5(met,:)=[p(1) p(2)];
end
end
end
end

```


Raytracing Algorithm

```
% This script creates synthetic seismogram. Traveltimes are
% calculated
% using raytracing and amplitudes are calculated using Zoeppritz's
% equation. AVA inversion is run on synthetics to get elastic
% parameters
% (Poisson's ratio) using Shuey's (1985) approximation.

clc;
clear all;
close all

v = [4.75,4.75,4.14*0.92,3.85,3.99,3.83 4.75];
z = [0 2.585 2.656 2.765 2.826 2.94 3.1];
h = diff(z);
D = (0.01:0.01:1.89);

vs=(v-1.36)/1.16;
vs(3)=(4.14-1.36)/1.16;
vs(1)=3.1;
vs(2)=3.1;
vs(end)=2.9;

rho=(v*1000/0.3048-3460)/0.308./(v*1000/0.3048);
rho(1)=2.6;
rho(2)=2.6;
rho(end)=2.9;

pois = (vs.^2-0.5*v.^2)./(vs.^2-v.^2);

% number of traces and number of interfaces
ntrace = length(D);
nint = min([length(h) length(v)]);

% find ray parameters using MATLAB command : fzero
disp('Calculating ray parameters...');
for j = 1:ntrace
    offset = D(j);
    for i = 1:nint
        hh = h(1:i);
        vv = v(1:i);
        er = 0.0001;
        x = min(1./vv) - er;
        if D(j)>0
            p(i,j) = fzero('fun_ray',[-er x],[],offset,hh,vv);
        else
            p(i,j) = fzero('fun_ray',[er -x],[],offset,hh,vv);
        end
        theta(i,j) = (asin(p(i,j)*vv(i)))*180/pi;

% calculate traveltime based on ray parameters
```

```

t(i,j) = 2*sum(hh./(vv.*sqrt(1-p(i,j)^2*vv.^2)));

end
end
disp('Ray parameter calculation completed');

% plot traveltimes

figure
hold on
for i = 1:nint
    plot(D,t(i,:)); axis ij;
    axis([min(D) max(D) 0 1.25*max(max(t))]);
    title('Traveltimes plot');
    xlabel('Offset (km)');ylabel('Time (s)');
end
hold off
prepfig

% source and receiver depths
zsrc = z(:,1); zrec = zsrc;
figure;

col=copper(length(z)-1);
for i=2:length(z)
    plot([0,1.9],[z(i),z(i)],'-','color','b','LineWidth',2)
    hold on;

end

%figure;
flipy;

% trace the rays, iterate over each layer
disp('Tracing rays...');
for k = 1:length(z)
    zd = z(:,k);
    [t2,p2] = traceray_pp(v,z,zsrc,zrec,zd,D,10,-1,10,1,1,2);
end
title(['v(z) medium, P-P mode zsrc=' num2str(zsrc) ' zrec='
num2str(zrec)])
line(D,zrec*ones(size(D)),'color','b','linestyle','none','marker','v')
line(0,zsrc,'color','r','linestyle','none','marker','*')
grid;xlabel('Offset (km)');ylabel('Depth (km)');
disp('Ray tracing completed');
%prepfig;

% create zeros matrix for spike's location
tmax = max(max(t)); dt = 0.001;
ta = (0:dt:tmax);
spikes = zeros(length(ta),ntrace);

% put spikes into location

```

```

disp('Creating synthetics...');
for i = 1:nint
    for j = 1:ntrace
        ir(i,j) = fix(t(i,j)/dt+0.1)+1;
        refl(i,j) = zoeppritz(rho(:,i),v(:,i),vs(:,i),...
            rho(:,i+1),v(:,i+1),vs(:,i+1),1,1,1,theta(i,j)));
        refl(i,j) = real(refl(i,j));
        if i==2 || i==nint-1
            refl(i,j)=-refl(i,j);
        end
        spikes(ir(i,j),j) = spikes(ir(i,j),j)+refl(i,j);
    end
end

% convolve spikes with 25Hz ricker wavelet
[w,tw] = ricker(0.001,20);
for i = 1:ntrace
    seis(:,i) = convz(spikes(:,i),w);
end
disp('Synthetics done');

% plot synthetics
figure;plotseis(seis,ta,D,1,2,1,1,'k');
title('Synthetic seismogram');set(gca,'axislocation','bottom');
xlabel('Offset (km)');ylabel('Time (s)');
%prepfig

% plot AVO response
xmin = min(min(theta)); xmax = max(max(theta));
ymin = min(min(refl)); ymax = max(max(refl));
figure;plot(theta(1,:),refl(1,:),...
theta(2,:),refl(2,:), 'r',theta(3,:),...

refl(3,:), 'k',theta(4,:),refl(4,:), 'g',theta(5,:),refl(5,:), 'c',theta(6,:),refl(6,:), 'b');
axis([xmin xmax ymin ymax]);
xlabel('Incidence angle (degree)');ylabel('Reflection coefficient');
title('AVA response');legend('Layer 1-2',...
'Layer 2-3','Layer 3-4','Layer 4-5','Layer 5-6','Layer 6-7');

```

Record's Length Calculation

```

k=0;
for i=1:size(Source.positions,1) % For all the shots number
    for j=1:size(Receivers.positions{i},1) % Take the positions of all
        the receivers at each shot
        dist(j)=abs(Source.positions(i,2)-Receivers.positions{i}(j,2)); %
        Save in varriable dist all the distances between each shot and
        receivers
    end
    The varriable "dist" has length equal to the number of the
    receivers,

```

```

[Dist_max(i),Rec_Ind(i)]=max(dist); % Keep the max distances between
shot and receiver for each shot in an array "Dist_max" along with
the No of the receiver "Rec_Ind"
end

[Dist_max,Sourc_Ind]=max(Dist_max); % Keep the overall max distance
between shot and receiver "Dist_max" along with the No of the source
with the max distance

Rec_Indx=Rec_Ind(Sourc_Ind); % Pass the No of the source to the
previous Rec_Ind array in order to find the number of the receiver
with the max distance from the particular source

Sourc_dist=Source.positions(Sourc_Ind,2); % Take the ds position of
the specific source

Rec_dist=Receivers.positions{Sourc_Ind}(Rec_Indx,2); % Take the dx
position of the specific receiver

leng=length(Model_Parameters.BodyVertex); % Number of the layers

for m=1:leng % Calculate the mean value of depth for each layer
    mean_z(m)=mean(Model_Parameters.BodyVertex{m}(:,1));
end

% If mn=1 the "import" menu had been chosen previously and the
values of interval velocities, max distance and max depth are stored
as Vp,X and Z

%If mn~=1 the menu cretae had been chosen previously and the same
values are stored now as Model_Parameters.Vp, X_depth and Z_depth

if mn==1
    mean_z=[0 mean_z];
    P_velocity=Vp;
    X_length=X;
    Zmax=Z;
else
    mean_z=[0 mean_z];
    P_velocity=Model_Parameters.Vp;
    X_length=X_depth;
    Zmax=Z_depth;
end

% Here the ratio of each layer is calculated compared to the rest of
the model

Layers_Volume=diff(mean_z);

for i=1:length(mean_z)-1
    Z_ratio_max=mean_z(i+1); % For each iteration the max depth
increases as the ray reaches to the rest of the layers
    z_ratio{i}=Layers_Volume(1:i)/Z_ratio_max;
end

Vmean=P_velocity(1:end-1)*z_ratio{end}';

```

```

% The average Interval velocity for the last layer is calculated

% Representation of record length's calculation plot
figure('color','w');
plot(Sourc_dist,0,'hr','MarkerSize',10,'MarkerFaceColor','k');
hold on;
plot(Rec_dist,0,'vk','MarkerSize',7,'MarkerFaceColor','r');
hold on;
col=lines(length(mean_z)-1);

for i=1:length(mean_z)-1

plot([0,X_length],[mean_z(i+1),mean_z(i+1)],'color',col(i,:), 'LineWidth',2)
    hold on;
end

plot([Sourc_dist,Rec_dist],[10,10],'k','LineWidth',2)
hold on;
plot([Sourc_dist,Dist_max/2],[0,mean_z(end)],'k','LineWidth',2)
hold on;
plot([Rec_dist,Dist_max/2],[0,mean_z(end)],'k','LineWidth',2)
hold on;
set(gca,'YDir','reverse');

% plot axis values
x1=Dist_max/2;
x2=Dist_max/4;
y2=mean_z(end)/2;
x3=3*Dist_max/4;
y3=mean_z(end)/2;

d1=Dist_max;
d2=round(sqrt((mean_z(end))^2+(Dist_max/2)^2));
d3=d2;

text(x1,10,['d1= ', num2str(d1),' m'], 'FontSize',
12,'color','k','VerticalAlignment','top');

if Sourc_dist-Rec_dist>0
text(x2,y2,['d2= ', num2str(d2),' m'], 'FontSize',
12,'color','k','HorizontalAlignment','right','VerticalAlignment','bottom');
text(x3,y3,['d3= ', num2str(d3),' m'], 'FontSize',
12,'color','k','HorizontalAlignment','right','VerticalAlignment','top');
else
text(x2,y2,['d2= ', num2str(d2),' m'], 'FontSize',
12,'color','k','HorizontalAlignment','left','VerticalAlignment','bottom');
text(x3,y3,['d3= ', num2str(d3),' m'], 'FontSize',
12,'color','k','HorizontalAlignment','left','VerticalAlignment','top');
end
set(gca,'YDir','reverse');

```

```

V_mean=round(Vmean);
time=round((d2/V_mean+d3/V_mean)*1000); % Time calculated using the
Vrms value
%time=round(sqrt(d2^2+d3^2+d1^2)*1000/V_mean); % Time calculated
using the Vrms value

%Rounding the time to its nearest order of magnitude
order_magnitude = floor(log(abs(time))./log(10))-1;
time_int=time;
time=round(time/10^order_magnitude)*10^order_magnitude+300;
title(['Mean Vp= ',num2str(V_mean),' [m/s]', ' Time = ',
num2str(time_int),' [ms]'], 'FontWeight','bold');

```

Rock Physics

```

figure;
set(gcf, 'color', 'white');
% Plot P wave velocity
subplot(1,4,1);
stairs(vp,zlayer, 'LineWidth',2.5, 'Color',[0.07843 0.1686
0.549]);
ylabel('Depth (m)', 'FontWeight','bold', 'Color','black');
title('V_{p} (m/s)', 'FontWeight','bold');
set(gca, 'XMinorGrid', 'on', 'YMinorGrid', 'on', 'YDir', 'reverse', 'Y
Color','k',...
'XAxisLocation','top', 'XColor','k', 'FontWeight',...
'demi', 'FontAngle','italic');
ax=gca;
ax.MinorGridLineStyle='-';
ylim([2500 3100]);
% Plot S wave velocity
subplot(1,4,2);
stairs(vs,zlayer, 'LineWidth',2.5, 'Color',[1 0 0]);
title('V_{s} (m/s)', 'FontWeight','bold');
set(gca, 'XMinorGrid', 'on', 'YMinorGrid', 'on', 'YDir', 'reverse', 'Y
Color','k',...
'XAxisLocation','top', 'XColor','k', 'FontWeight',...
'demi', 'FontAngle','italic');
ax=gca;
ax.MinorGridLineStyle='-';
ylim([2500 3100]);
% Plot Density
subplot(1,4,3);
stairs(ro,zlayer, 'LineWidth',2.5, 'Color',[0.07059 0.6392
0.07059]);
title('Density (kg/m^3)', 'FontWeight','bold');
set(gca, 'XMinorGrid', 'on', 'YMinorGrid', 'on', 'YDir', 'reverse', 'Y
Color','k',...
'XAxisLocation','top', 'XColor','k', 'FontWeight',...
'demi', 'FontAngle','italic');
ax=gca;
ax.MinorGridLineStyle='-';

```

```

ylim([2500 3100]);
xlim([2 3]);
% Plot Poissons Ratio
subplot(1,4,4);
stairs(pois,zlayer,'LineWidth',2.5,'Color',[0.2 0.1 0.9]);
title('Poisson's Ratio','FontWeight','bold');
set(gca,'XMinorGrid','on','YMinorGrid','on','YDir','reverse','Y
Color','k',...
'XAxisLocation','top','XColor','k','FontWeight',...
'demi','FontAngle','italic');
ax=gca;
ax.MinorGridLineStyle='-';
ylim([2500 3100]);

% Plot Geology Model
fId=figure('units','normalized','outerposition',[0 0 1
1],'color','w');

%writerObj = VideoWriter('Test.avi'); % Name it.
%writerObj.FrameRate = 20; % How many frames per second.
%open(writerObj);

%color = load('mycmap.txt');
pcolor(xx,zz,repmat(vlayer,1,nx)); shading flat; hold on
colormap(parula); colorbar ('horz');
axis([0 xmax zmin-0.03*zmax zmax])
set(gca,'YDir','reverse','XaxisLocation','bottom',...
'Ytick',zlayer,'FontWeight','demi','PlotBoxAspectRatioMode','Ma
nual',...
'PlotBoxAspectRatio',[2.4 1.2 1],'Position',[0.04 0.30 0.90
0.60]);
% Plot Source-Receiver Group
plot(xs,zs,'r*','markersize',12); hold on
plot(xr,zr,'sk','markersize',4,'markerfacecolor','c'); hold on
xlabel('Velocity (m/s)','FontWeight','bold','Color','black');
ylabel('Depth (m)','FontWeight','bold','Color','black');

figure;
for i=1:ns
tm = load(['time_shot',num2str(i),'.mat']); tt = tm.twt;
plot(xx(2:nlayer,:),tt(2:nlayer,:,i),'b.');
```

hold on

xlabel('Horizontal Position
(m)','FontWeight','bold','FontAngle','normal','Color','black');

ylabel('Time
(s)','FontWeight','bold','FontAngle','normal','Color','black');

title('Traveltime','FontWeight','bold');

set(gca,'Ydir','reverse');

set(gcf,'color','white');

end

% Plot Reflection Coefficient

figure;

for i=1:ns

reflz = load(['reflz_shot',num2str(i),'.mat']); reflz =

reflz.rcz;


```

refls = load(['refls_shot',num2str(i),'.mat']); refls =
refls.rcs;
reflt = load(['reflt_shot',num2str(i),'.mat']); reflt =
reflt.rct;
theta = load(['teta_shot',num2str(i),'.mat']); angle =
theta.angle;
%Reflection Coefficient of Zoeppritz
for j=1:nlayer
subplot(1,3,1)
plot(abs(angle(j,:,i)),reflz(j,:,i),'.'); hold on
xlabel('Incidence Angles
(degree)','FontWeight','bold','Color','black');
ylabel('Reflection
Coefficient','FontWeight','bold','Color','black');
grid on; title('Rpp
Zoeppritz','FontWeight','bold','Color','black')
set(gca,'YColor','k','XColor','k'); hold on

%Reflection Coefficient of Shuey
subplot(1,3,2)
plot(abs(angle(j,:,i)),refls(j,:,i),'.'); hold on
xlabel('Incidence Angles
(degree)','FontWeight','bold','Color','black');
grid on; title('Rpp Shuey','FontWeight','bold','Color','black')
set(gca,'YColor','k','XColor','k'); hold on

%Reflection Coefficient of Thomsen
subplot(1,3,3)
plot(abs(angle(j,:,i)),reflt(j,:,i),'.'); hold on
xlabel('Incidence Angles
(degree)','FontWeight','bold','Color','black');
grid on; title('Rpp
Thomsen','FontWeight','bold','Color','black')
set(gca,'YColor','k','XColor','k'); hold on
set(gcf,'color','white');
end
end

for i=1:ns
refls = load(['refls_shot',num2str(i),'.mat']); refls =
refls.rcs;
theta = load(['teta_shot',num2str(i),'.mat']); angle =
theta.angle;
Rt = load(['intercept_shot',num2str(i),'.mat']); Rt = Rt.AA;
Gt = load(['gradient_shot',num2str(i),'.mat']); Gt = Gt.BB;
Ro(1:nlayer,:,i) = Rt(1:nlayer,:,i);
Go(1:nlayer,:,i) = Gt(1:nlayer,:,i);
Rc(1:nlayer,:,i) = refls(1:nlayer,:,i);
inc(1:nlayer,:,i) = angle(1:nlayer,:,i);
end
Rp = reshape(Ro,nr*ns*nlayer,1);
G = reshape(Go,nr*ns*nlayer,1);
R = reshape(Rc,nr*ns*nlayer,1);
teta = reshape(inc,nr*ns*nlayer,1);
% Plot Attributes
figure;

```

```

% Rp-G Cross Plot
subplot(1,2,1)
for i=1:nlayer
plot(Ro(i,:),Go(i,:),'.','MarkerSize',10); hold on
end
%plot(R,G,'m.');
```

$$\text{hold on}$$

```

xlabel('R','FontWeight','bold','Color','black');
ylabel('G','FontWeight','bold','Color','black');
grid on; title('R-G Cross
Plot','FontWeight','bold','Color','black')
set(gca,'YColor','k','XColor','k'); hold on
legend('Layer1','Layer2','Layer3','Layer4','Layer5','Layer6','L
ayer7');
```

$$\text{hold on}$$

```

% R-sin^2(teta) Cross Plot
subplot(1,2,2)
for i=1:nlayer
plot((sin(inc(i,:)).^2),Rc(i,:),'.'); hold on
end
xlabel('sin^2(teta)','FontWeight','bold','Color','black');
ylabel('R(teta)','FontWeight','bold','Color','black');
grid on; title('R-sin^2(teta) Cross
Plot','FontWeight','bold','Color','black')
set(gca,'YColor','k','XColor','k'); hold on
set(gcf,'color','white');
legend('Layer1','Layer2','Layer3','Layer4','Layer5','Layer6','L
ayer7');
```

$$\text{hold on}$$

```

%=====
=====
% AVO Modelling
%=====
=====
fprintf('---> Starting AVO Modelling ...\n');
% Make wavelet ricker (f = 2 Hz)
dt = 0.001; f = 20;
[w,tw] = ricker(dt,f);
% Create zeros matrix for spike's location
tmax = max(tt(:));
tr = 0:dt:tmax; nt = length(tr);
t = tt(2:nlayer,:);
%t = t(:,all(~isnan(t)));
t(:,all(isnan(t)))=0;
%t(:,2)=[];
% Take reflectivity into spike location
spikes = zeros(nt,nray);
rcz = real(reflz(2:nlayer,:));
for k=1:nlayer-1
for j=1:nray-1
ir(k,j) = fix(t(k,j)/dt+0.1)+1;
spikes(ir(k,j),j) = spikes(ir(k,j),j) + rcz(k,j);
end
end
% Convolve spikes with wavelet ricker
for j=1:nray
seisz(:,j) = convz(spikes(:,j),w);
end

```

```

ampz=reshape(seisz,length(tr),nr,ns);
for i=1:ns
ampz_shot(:,:,i) = ampz(:,:,i);
save(['ampz_shot',num2str(i),'.mat'],'ampz_shot');
end
% CMP Stacked
Stacked = zeros(nt,nr);
for i=1:ns
files = load(['ampz_shot',num2str(i),'.mat']);
files = files.ampz_shot;
Stacked = Stacked + files(:,:,i);
end
% Save Seismic Data
save(['seis','.mat'],'Stacked');
% Plot AVO
figure;
wig(xr,tr,Stacked,'black'); hold on
xlabel('Offset (m)','FontWeight','bold','Color','black');
ylabel('Time (s)','FontWeight','bold','Color','black');
title('Synthetic
Seismogram','FontWeight','bold','Color','black');
axis tight
set(gca,'YColor','k','XColor','k'); hold on
set(gcf,'color','white');
fprintf(' AVO Modelling has been computed...[OK]\n');

%=====
% Seismogram Synthetic
%=====
% Create Smooth Synthetic Log From Elastic Data Set
[pson,sson,spson,rlog,zlog] = logsyn(vp,vs,ro,zlayer,1000);
vplog = 1.0e6./pson; vslog = 1.0e6./sson;
rholog = 0.31.*(vplog).^0.25; vpv = vplog./vslog;
poisson = (vslog.^2-0.5*vplog.^2)./(vslog.^2-vplog.^2);
% Plot Synthetic Data Log

% Plot Rock Properties
figure;
% Cross Plot P and S wave velocity
subplot(2,2,1);
plot(vplog(800:1000),vslog(800:1000),'.','Color',[0.07843
0.1686 0.549]);
%p = polyfit(vplog(400:500),vslog(400:500),1);
%yfit = polyval(p,vplog(400:500));
hold on;
plot(vplog(800:1000),(vplog(800:1000)-1360)/1.16,'r');
%plot(vplog(400:500),yfit,'r');
%text(4400,2800,[num2str(round(p(2)*1000/1000)), '*x
+',num2str(round(p(1)*1000/1000)'])
text(4000,2800,[num2str(0.862), '*Vp -',num2str(1172.4)])
xlabel('Vp (m/s)','FontWeight','bold','Color','black');
ylabel('Vs (m/s)','FontWeight','bold','Color','black');
title('Cross Plot of Vp and
Vs','FontWeight','bold','Color','black');

```

```

set(gca, 'XMinorGrid', 'on', 'YMinorGrid', 'on', 'YColor', 'k', ...
'XAxisLocation', 'bottom', 'XColor', 'k', ...
'FontWeight', 'demi', 'FontAngle', 'italic');
ax=gca;
ax.MinorGridLineStyle='-';

% Plot S Sonic Log
subplot(2,2,2);
plot(vplog(800:1000),vpvs(800:1000),'.','Color',[1 0 0]);
p = polyfit(vplog(800:1000),vpvs(800:1000),2);
yfit = polyval(p,vplog(800:1000));
hold on;
plot(vplog(800:1000),yfit,'r');
%text(4400,1.7,[num2str(round(p(2)*1000/1000)), '*Vp
+',num2str(round(p(1)*1000)/1000)])
xlabel('Vp (m/s)', 'FontWeight', 'bold', 'Color', 'black');
ylabel('Vp/Vs ratio', 'FontWeight', 'bold', 'Color', 'black');
title('Cross Plot of Vp and Vp/Vs
Ratio', 'FontWeight', 'bold', 'Color', 'black');
set(gca, 'XMinorGrid', 'on', 'YMinorGrid', 'on', 'YColor', 'k', ...
'XAxisLocation', 'bottom', 'XColor', 'k', ...
'FontWeight', ...
'demi', 'FontAngle', 'italic');
ax=gca;
ax.MinorGridLineStyle='-';
% Plot Density Log
subplot(2,2,3);
plot(vslog(800:1000),vpvs(800:1000),'.','Color',[0.07059 0.6392
0.07059]);
p = polyfit(vslog(800:1000),vpvs(800:1000),2);
yfit = polyval(p,vslog(800:1000));
hold on;
plot(vslog(800:1000),yfit,'r');
%text(2.52,1.7,[num2str(round(p(2)*1000/1000)), '*Vp
+',num2str(round(p(1)*1000)/1000)])
xlabel('Vs (m/s^2)', 'FontWeight', 'bold', 'Color', 'black');
ylabel('Vp/Vs ratio', 'FontWeight', 'bold', 'Color', 'black');
title('Cross Plot of Shear Velocity and Vp/Vs
Ratio', 'FontWeight', 'bold', 'Color', 'black');
set(gca, 'XMinorGrid', 'on', 'YMinorGrid', 'on', 'YColor', 'k', ...
'XAxisLocation', 'bottom', 'XColor', 'k', ...
'FontWeight', 'demi', 'FontAngle', 'italic');
ax=gca;
ax.MinorGridLineStyle='-';
subplot(2,2,4);
plot(poisson(800:1000),vpvs(800:1000), 'm. ');
xlabel('Poisson Ratio', 'FontWeight', 'bold', 'Color', 'black');
ylabel('Vp/Vs ratio', 'FontWeight', 'bold', 'Color', 'black');
title('Cross Plot of Poisson's Ratio and Vp/Vs
Ratio', 'FontWeight', 'bold', 'Color', 'black');
set(gca, 'XMinorGrid', 'on', 'YMinorGrid', 'on', 'YColor', 'k', ...
'XAxisLocation', 'bottom', 'XColor', 'k', ...
'FontWeight', 'demi', 'FontAngle', 'italic');
set(gcf, 'color', 'white');
ax=gca;
ax.MinorGridLineStyle='-';

```

```

% Integrate Depth and Velocity To Get Two-Way Time
tstart = 0; tracenum = 10;
[tz,zt] = sonic2tz(spson,zlog,-100,tstart);
tzobj = [zt tz];
vins = vplog; dens = rholog; z = zlog;
% Determine Ricker Wavelet
dt = 0.001; f = 20;
[w,tw] = ricker(dt,f);
[theo,tlog,rsc,pm,p] =
seismogram(vins,dens,z',w,tw,tzobj,0,0,1);

% Compare AVO Data Estimation
rseis = load(['seis','.mat'],'Stacked'); num = 1:191;
rseis = rseis.Stacked; seis = rseis(:,num);

[seisr,zp,dzp,tz,zt]=seis2z(seis,tr,vp,zlayer,vs,1,min(zlayer),
max(zlayer));

figure;
set(gcf,'color','white');
% Plot P Sonic Log
subplot(1,4,1);
stairs(pson,zlog,'LineWidth',1,'Color',[0.07843 0.1686 0.549]);
xlabel('P sonic (US/m)','FontWeight','bold','Color','black');
ylabel('Depth (m)','FontWeight','bold','Color','black');
set(gca,'XMinorGrid','on','YMinorGrid','on','YDir','reverse','X
Dir','reverse','YColor',...
'k','XAxisLocation','top','XColor',...
'k','FontWeight','demi','FontAngle','italic');
ax=gca;
ax.MinorGridLineStyle='-';
% Plot S Sonic Log
subplot(1,4,2);
stairs(sson,zlog,'LineWidth',1,'Color',[1 0 0]);
xlabel('S sonic (US/m)','FontWeight','bold','Color','black');
set(gca,'XMinorGrid','on','YMinorGrid','on','YDir','reverse','X
Dir','reverse','YColor','k',...
'XAxisLocation','top','XColor','k','FontWeight',...
'demi','FontAngle','italic');
ax=gca;
ax.MinorGridLineStyle='-';
% Plot Density Log
subplot(1,4,3);
stairs(rlog,zlog,'LineWidth',1,'Color',[0.07059 0.6392
0.07059]);
xlabel('Density (kg/m^3)','FontWeight','bold','Color','black');
set(gca,'XMinorGrid','on','YMinorGrid','on','YDir','reverse','Y
Color','k',...
'XAxisLocation','top','XColor','k','FontWeight',...
'demi','FontAngle','italic');
ax=gca;
ax.MinorGridLineStyle='-';

subplot(1,4,4);
stairs(poisson,zlog,'LineWidth',1,'Color',[0.07843 0.1686
0.549]);

```

```

xlabel('Poisson Ratio','FontWeight','bold','Color','black');
ylabel('Depth (m)','FontWeight','bold','Color','black');
title('Poisson Ratio','FontWeight','bold','Color','black');
set(gca,'XMinorGrid','on','YMinorGrid','on','YDir','reverse','Y
Color','k',...
'XAxisLocation','bottom','XColor','k',...
'FontWeight','demi','FontAngle','italic');
ax=gca;
ax.MinorGridLineStyle='-';

figure;
wig(1:191,zp',seisr,'blue'); hold on
xlabel('Trace Number','FontWeight','bold','Color','black');
title('AVO Estimation','FontWeight','bold','Color','black');
axis tight
set(gca,'YDir','reverse','YColor','k',...
'XAxisLocation','bottom','XColor','k',...
'FontWeight','demi','FontAngle','italic');
ax=gca;
ax.MinorGridLineStyle='-';
set(gcf,'color','white');

```

Spline Layers

```

function [] = Spline_layers

global figm fign Model_Parameters...
    record_length X_length P_velocity Zmax...
    depth_layer time time_layer z_ratio...
    record_length_flag time_fin

    record_length_flag=0;
    spline_flag=1; % While spline_flag=1 the user will be asked to give
    record length and spline interval

    while spline_flag==1
        spline_flag=0;

    % Give the record length and the spline interval
        prompt = {'Enter the record length (ms)' 'Enter the
    SPLINE interval value'};
        tit    = 'RECORD LENGTH - SPLINE DEFINITION';
        lin    = 1;
        df     = {num2str(time) '50'};
        xv     = inputdlg(prompt,tit,lin,df);

        if isempty(xv);
            record_length_flag=1;
            return;
        else
            for j=1:size(xv,2);
                if isempty(xv{j});

```

```

                                spline_flag=1;
                                end
                                end
                                end
                                end

    record_length=str2num(xv{1}); %Reads record length and spline
    interval given by user
    intv=str2num(xv{2});
    X=X_length; % The max length of the
    x=(0:intv:X); % Splits the distnace according to the given
    interval value
    ln=size(Model_Parameters.BodyVertex,2); % ln equals to the
    number of the layers
    layers=Model_Parameters.BodyVertex; % layers contains the
    coordinates for each layer

    % Plot layers with spline intervals
    figure('color','w');

    col=copper(ln);

    for i=1:ln

        layers{i}(end,:)=[]; % The last three values are deleted since
        they have no physical meaning
        layers{i}(end,:)=[];
        layers{i}(end,:)=[];

        [A,B]=unique(layers{i}(:,2)); % Only the unique z values are
        kept in order to apply spline
        B=sort(B);
        Layer{i}=layers{i}(B,:); % The "Layer" cell array contains in
        each of its cells the corresponding layers: e.g Layer{1}=[Z X] of
        layer 1
        clear A B;
        depth_layer{i}=spline(Layer{i}(:,2)',Layer{i}(:,1)',x); % Apply
        spline with increment x: "depth_layer" cell array

        plot(Layer{i}(:,2),Layer{i}(:,1),'color',col(i,:)) %plot the
        results
        hold on;
        plot(x,depth_layer{i},'.','color',col(i,:));
        hold on;
        end

        title('Digitized Layers');
        xlabel('Length (m)','FontWeight','bold');
        ylabel('Depth (m)','FontWeight','bold');
        set(gca,'YDir','Reverse')
        xlim([0,X]);
        ylim([0,Zmax]);

        figm=gcf; %keep the figure

```



```

% Load Interval velocities

vint=P_velocity; % Vint contains the interval velocities for each
layer
depths=cell2mat(depth_layer);
depths2=reshape(depths,[length(x) ln]);
depth_final=depths2';
depth_final=[zeros(1,size(depth_final,2));depth_final];
depth_diff=diff(depth_final);

for i=1:length(x)
time_jnk=2*depth_diff(:,i)./vint(1:end-1)';
time_final(:,i)=cumsum(time_jnk);
end

time_final=[zeros(1,length(x)); time_final ;
(record_length/1000)*ones(1,length(x))];
depth_final=[depth_final; Zmax*ones(1,length(x))];

figure('color','w');

for i=1:ln % for all the layers
plot(x,time_final(i+1,:),'.-','color',col(i,:));
hold on;
end

title('Digitized Layers');
xlabel('Length (m)','FontWeight','bold');
ylabel('Time (s)','FontWeight','bold');
set(gca,'YDir','Reverse')
xlim([0,X]);
ylim([0,record_length/1000]);

fign=gcf;
Z=Zmax;
t_max=record_length;

k=0;
for i=1:length(x) % For the whole length of the spline array
    for j=1:ln+2 % For all the layers
        k=k+1;
Vint(k)=vint(j);
Depth(k)=depth_final(j,i);
Layer_name(k)={strcat('Layer',num2str(j))};
xlength(k)=x(i);
time_conv(k)=time_final(j,i);
    end
end

time_cmp=time_final;
vint_cmp=reshape(Vint,[ln+2,length(x)]);

% Calculate Vrms using Time

```

```
for i=1:length(x)
    vel_rms_cmp(:,i)=vint2vrms(vint_cmp(:,i),time_cmp(:,i)); %Calculate
    Vrms using Time
end

vel_rms_cmp=[Vint(1)*ones(1,length(x)); vel_rms_cmp];
Vrms_time=reshape(vel_rms_cmp,1,length(x)*(ln+2));

Velocity_analysis=[xlength' Depth' time_conv' Vint' Vrms_time'];
```

Appendix B

List of Figures

Chapter 2

- Figure 2.1** Prinos – Kavala Basin. Prinos field, Prinos North field, Epsilon field and South Kavala gas field are the only productive hydrocarbon fields in Greece. The oil generation and the migration paths are shown (improved version published after Kioumourtzi et al., 2007). 2
- Figure 2.2** Simplified cross section of the Prinos basin parallel to the long axis. The roll-over syngenetic faulting formed the dome-like anticlines. Depths in kilometres below mean sea level. Figure from Proedrou and Sidiropoulos (1992). 3
- Figure 2.3.** Generalized chronostratigraphic column of Prinos basin. Figure from Proedrou and Sidiropoulos (2004). 4
- Figure 2.4** NW-SE seismic section across the Prinos basin. The anticlinal structure with the downthrown faults are well illustrated from the seismic reflectors [Stuart Harker 2004-2008]. 6

Chapter 3

- Figure 3.1** The differencing star for the modified Lax-Wendroff scheme. 10
- Figure 3.2** The domains of dependence on the plane x - z : a square for Lax-Wendroff scheme and a circle for the simplest ($\rho(x,z)-\mu(x,z)=1$) SH wave equation. 14

Chapter 4

- Figure 4.1** Reflection and transmission at an interface for an incident P-wave. 16
- Figure 4.2** Notation for the sixteen possible reflection/transmission coefficients for P-SV waves at an interface between two different solid half-spaces. Short arrows show the direction of particle motion (from Aki and Richards, 1980). 17
- Figure 4.3** (a) shows AVO response and (b) shows transform of (a) in AVA (amplitude versus angle) response [NTNU, AVO theory, 2004]. 20
- Figure 4.4** A plot of constant angle curves superimposed on constant offset traces. 21
- Figure 4.5** Schematic illustration of class II and class IIp and definitions of parameters used in equation (4.22). The angle ϑ_p is the angle of polarity change. Separation of near and far stack away from the angle of phase reversal will increase the dynamic range of the FN attribute. (Modified from Ross and Kinman, 1995.) 27
- Figure 4.6** A basic AVO analysis after appropriate geometric corrections the individual traces for one gather are displayed in the panel on the left; the colours correspond to different reflectors. A graph may be constructed at any point in time (e.g. t_1 , t_2 or t_3) to analyse the amplitude variation with offset of the traces at that time; the graph at the right shows one such plot for time t_2 . The gray line is a least-squares, best-fit to the natural distribution; values for P and G are extracted from analysis of the best-fit line. Triangle shows the average amplitude of all of the traces at t_2 28
- Figure 4.7** On the left, a cross-plot shows P versus G for every time sample for every gather in a volume of seismic data. The data have been normalized to constrain P and G to the same range of values. On the right, the same cross-plot has been color-coded to show the stacked amplitude of each point; light to dark blues are low to high amplitude troughs, and pink to dark reds are low to high amplitude peaks. The three regions denoted 1, 2 and 3 are defined by the three AVO classes of Rutherford and Williams. 29
- Figure 4.8** Zoeppritz P-wave reflection coefficients for a shale/gas-sand interface for a range of R_0 values. The Poisson's ratio and density of the shale were assumed to be 0.38 and 2.4 g/cm³, respectively. The Poisson's ratio and density of the gas sand were assumed to be 0.15 and 2.0 g/cm³, respectively (Rutherford and Williams, 1989). 30

Figure 4.9 This newer classification is identical to that of Rutherford and Williams (1989) for Class I (high-impedance-contrast) and Class II (low-impedance-contrast) sands. However, it differs in that Class III (low-impedance-contrast) is subdivided into two classes, III and IV. The Class IV sands are highly significant in that they exhibit AVO behaviour contrary to established rules of thumb and occur in many basins throughout the world, including the Gulf of Mexico (Castagna and Swan, 1997). (Numbers in the corners are quadrant numbers).....	31
Figure 4.10 Zero-offset reflection coefficient (A) versus the AVO gradient (B) assuming constant V_P/V_S and Gardner's relation. The background trend rotates counter clockwise as V_P/V_S increases.....	32
Figure 4.11 Deviations from the background petrophysical trends, as would be caused by hydrocarbons or unusual lithologies, cause deviations from the background A versus B trend. This figure shows brine sand-gas sand tie lines for shale over brine-sand reflections falling along a given background trend. In general, the gas sands exhibit more negative As and Bs than the corresponding brine sands (assuming the frame properties of the gas sands and the brine sands are the same). Note that the gas sands form a distinct trend which does not pass through the origin.	33
Figure 4.12 Diagrammatic crossplot of P-wave velocity against S-wave velocity [Stanford Rock Physics Laboratory].....	34
Figure 4.13 The four usual AVO classifications defined by Rutherford, et al. (1989) and Castagna, et al. (1998), and typical flatspot behaviour.	35
Figure 4.14 Rutherford and Williams AVO classes, originally defined for gas sands (classes I, II and III), along with the added classes IV (Castagna and Smith, 1994) and IIP (Ross and Kinman, 1995). Figure is adapted from Castagna et al. (1998).	37

Chapter 5

Figure 5.1 Schematic of overall field setup for a seismic survey [Park Seismic].	38
Figure 5.2 Major types of seismic waves based on propagation characteristics [Park Seismic].	38
Figure 5.3 A field record and interpretation of different seismic events based on the arrival pattern [Park Seismic].	39
Figure 5.4 Illustration of active versus passive waves and inline versus offline waves.	39
Figure 5.5 Convolution seismic data model. A seismic pulse is convolved with the reflection coefficient log (reflectivity function) to get a seismic trace. The reflection coefficient log is related to the geological section of the subsurface through the reflection coefficient of each geological boundary and the two-way travel time [Mousa, Al-Shuhail, 2011].	40
Figure 5.6 3-D geological model representation of Prinos basin [Michelakis 2010].	41
Figure 5.7 Geological plan of Prinos basin with East-West orientation.	42
Figure 5.8 2-D representation of the East-West geological plan.	42
Figure 5.9 Picking procedure for the layers' digitization.	43
Figure 5.10 Digitized layers after applying spline procedure with spline interval equal to 5m.	43
Figure 5.11 Layer representation versus depth using the "area" function.....	44
Figure 5.12 The simplified geological model of Prinos' basin East-West plan. The model consists of six formations, Evaporites, sand A1, sand A2, sand B, sand C and the Basal formation.	45
Figure 5.13 Different models of the P-wave velocity as a function of porosity and real data (circles), corresponding to the shaly section of the well.	47
Figure 5.14 Different models of the P-wave velocity as a function of porosity and real data (crosses), corresponding to the sandy section of the well.	48
Figure 5.15 P-wave velocity as a function of porosity corresponding to different models of the reservoir (sandstone saturated with oil). The harmonic average is the time-average equation.....	48
Figure 5.16 P-wave velocity as a function of porosity using Geomteric, Raymer and Gassmann curve fitting.	49
Figure 5.17 V_p versus V_s crossploting from shale and sandstone formations [Castagna, Batzlek and Kan, 1993].....	50

Figure 5.18 Effect of gas/water or oil/water saturation on velocity. Solid curves are for gas, dashed for oil. a) P-wave velocity versus saturation and b) reflection coefficient for gas/oil sands overlain by shale. [Sheriff and Geldart, 1995]	52
Figure 5.19 P-wave velocity versus gas saturation at 3050 m.	52
Figure 5.20 Percentage P-wave velocity drop versus gas saturation at 3050m.....	52
Figure 5.21 Gas saturation effect on P-wave and S-wave velocity. [Caldwell, Christie, Engelmark, Kristiansen, Macleod, McHugo and Ozdemir, 1999]	53
Figure 5.22 Initial model parameters.	54
Figure 5.23 Representation of the layers import in the simulator. a) The background evaporite horizon. b-e) The horizons sand A1, sand A2 , sand B and sand C respectively. f) To the bed evaporite horizon. .	57
Figure 5.24 Vp, Vs, density and Poisson's ratio versus depth for the Prinos basin.	57
Figure 5.25 The Source parameters introduction.	58
Figure 5.26 Introduction of the receiver's parameters.	58
Figure 5.27 The final setup of the experiment.....	58
Figure 5.28 Presentation of the record's length calculation procedure.	59
Figure 5.29 Prinos basin layers representation in time using the "area" function.....	59
Figure 5.30 An example of the time calculation for the first three layers of the reservoir.	60
Figure 5.31 The stacking chart plot of the seismic data.	61
Figure 5.32 The number of traces per shot.	61
Figure 5.33 A conventional seismic data processing flow [Mousa, Al-Shuhail, 2011].....	63
Figure 5.34 Two-sided common shot gather configuration with five receivers from each side of the shot record [Mousa, Al-Shuhail, 2011].	63
Figure 5.35 Common mid-point gather (CMP) configuration. Each of the shot-receiver combinations is centred around the same mid-point.	64
Figure 5.36 The fold (number of traces per CMP) versus the CMP numbers.	64
Figure 5.37 Representation of source wavelet, reflectivity series and their convolution in time.	65
Figure 5.38 Various displays for shot gather number 8.	66
Figure 5.39 Seismic data shot gather number 8: (a) before, (b) after applying amplitude correction gain method of Equation 5.11 with $a=3$ and (c) amplitude correction gain method of Equation 5.12 with $b=3$	67
Figure 5.40 Seismic data shot gather number 8: (a) before, (b) after applying the AGC using the RMS and (c) instantaneous based methods.....	68
Figure 5.41 The amplitude envelope gain in dB of the average trace for a) instantaneous ACG, b) RMS amplitude ACG, c) power gain correction with $a=3$ and d) exponential gain correction with $b=3$	69
Figure 5.42 Seismic data shot gather number 8: (a) before and (b) after applying geometrical spreading correction.....	70
Figure 5.43 The amplitude envelope gain in dB for the average trace before and after the application of geometrical spreading correction.....	71
Figure 5.44 Shot gather 8 (a) before applying spiking deconvolution (b) its autocorrelogram for window 0.2 s and (c) after applying spiking deconvolution.	72
Figure 5.45 PSD of the average trace of shot gather 8 before and after spiking deconvolution.	73
Figure 5.46 Shot gather 8 (a) before and (b) after applying predictive deconvolution with autocorrelation window 0.2 s and operator's length 0.08 s.	73
Figure 5.47 PSD of the average trace of shot gather 8 before and after predictive deconvolution.	74
Figure 5.48 Display of seismic data form left to right, before FX deconvolution, after FX deconvolution and estimated noise.	75
Figure 5.49 Shot gather number 8 (a) before and (b) after the application of fx deconvolution.	75
Figure 5.50 a) Seismic data shot gather number 8 after geometrical spreading b) Its $f - x$ and c) its $f - k$ magnitude spectra. The color bars in b) and c) indicate the magnitude values in dB.	76
Figure 5.51 Design of the polygonal zone band-pass filter.	77
Figure 5.52 Shot gather number 8 (a) before and (b) after the application of the f-k BPF.	77
Figure 5.53 CMP number 100 (a) before geometrical spreading (b) after geometrical spreading (c) in colored display.....	78

Figure 5.54 Velocity spectra of a hyperbolic reflectors.	79
Figure 5.55 Velocity interpolation results from 4 velocity locations. Red circle is the picked velocity, while blue line is the interpolated velocity using shape-preserving cubic interpolation.	80
Figure 5.56 Comparison between interpolated vrms (blue) and block constant vint (red) on 4 velocity analysis locations.	81
Figure 5.57 Interpolated vrms for all velocity analysis locations.	81
Figure 5.58 CMP gather number 150 (a) before and (b) after the NMO correction.	82
Figure 5.59 CMP gather number 150 NMO corrected for stretching (a) 50% and (b) 10%.	83
Figure 5.60 Parabolic Radon transform used on synthetic data for the elimination of multiples.	84
Figure 5.61 Parabolic Radon transform used on real seismic data for the elimination of multiples.	84
Figure 5.62 Parabolic Radon transform used on CMP gather 200 for multiple's elimination.	85
Figure 5.63 Different displays for the full stack section.	86
Figure 5.64 Full stack section of synthetic data.	86
Figure 5.65 Full stack section of synthetic data after post-stack application of FK filtering, Radon transform and spiking deconvolution.	87
Figure 5.66 (a) A point scatterer (secondary source), and (b) a curved reflector which is produced based on the point scatterer.	88
Figure 5.67 (a) An array of point scatterers positioned at different locations, and (b) its resultant curved reflectors interfering with each other.	89
Figure 5.68 Time migrated section using Kirchhoff migration routine.	90
Figure 5.69 Time migrated section using Stolt FK migration routine.	90
Figure 5.70 Time migrated section using finite differences migration routine.	91
Figure 5.71 Time migrated section using Gazdag phase shift migration routine.	91
Figure 5.72 Superposition of the reflectors on the migrated section.	92
Figure 5.73 Superposition of the interval velocity model on the migrated section.	92

Chapter 6

Figure 6.1 Display of the graphical user interface for the seismic processing.	93
Figure 6.2 Convert to SGY function panel.	93
Figure 6.3 Load SGY file function panel.	94
Figure 6.4 Load SGY file function panel.	94
Figure 6.5 Shot gathers plot function panel along with the menu prompt for the gain correction method.	95
Figure 6.6 Shot gather number 20 in wiggle display.	95
Figure 6.7 Shot gather number 20 in colored display.	96
Figure 6.8 Time function panel.	96
Figure 6.9 Shot gather number 20 for time interval (1s-1.4s).	96
Figure 6.10 Common Offset plot function panel.	97
Figure 6.11 Common Offset gather with offset 50 m in wiggle display.	97
Figure 6.12 Common Offset gather with offset 50 m in colored display.	98
Figure 6.13. Display of the Find CMPs panel.	98
Figure 6.14 Display of the CMP Plot function panel.	99
Figure 6.15 Common Midpoint Gather number 100 in wiggle display.	99
Figure 6.16 Common Midpoint Gather number 100 in colored display.	100
Figure 6.17 Fk filter function panel.	100
Figure 6.18 Design of the polygonal zone band-pass filter for CMP 100.	101
Figure 6.19 CMP gather 100 (a) before and (b) after the fk filtering.	101
Figure 6.20 FX deconvolution function panel.	102
Figure 6.21 Dialog box for FX deconvolution operator's selection.	102
Figure 6.22 Radon transform function panel.	102
Figure 6.23 Dialog box for Radon transform operator's selection.	103

Figure 6.24 CMP gather 100 (a) before and (b) after the radon transform.	103
Figure 6.22 Spiking and predictive deconvolution function panel.	104
Figure 6.26 CMP gather 100 (a) before, (b) after the predictive and (c) after spiking deconvolution. ..	104
Figure 6.27 Geometrical Spreading function panel.	105
Figure 6.28 CMP gather 100 (a) before and (b) after geometrical spreading correction.	105
Figure 6.29 NMO correction function panel.	105
Figure 6.30 CMP gather 100 (a) before and (b) after nmo correction.	106
Figure 6.31 Stack section function panel.	107
Figure 6.32 Full stack section (a) before and (b) after post-processing.	107
Figure 6.33 Migration function panel and interpolation method menu.	108
Figure 6.34 Interval velocity model after linear interpolation.	109
Figure 6.35 RMS velocity model after linear interpolation.	109
Figure 6.36 Migrated section using the PSPI time migration.	110
Figure 6.37 Migrated section using the vertical velocity Fourier transform.	110
Figure 6.38 Wiggle type selection panel.	111
Figure 6.39 Wiggle plot of CMP gather 100 (a) with and (b) without colorized amplitudes.	111
Figure 6.40 Wiggle plot of shot gather 40 (a) with and (b) without colorized amplitudes.	112
Figure 6.41 Available seismic colors selection.	112
Figure 6.42 Representation of all the available seismic colors for shot gather 40.	113

Chapter 7

Figure 7.1 Raytracing procedure demonstration for offsets 100 m, 500m and 1000m. Red asterisk denotes shot location, blue triangles denote receiver locations.	115
Figure 7.2 Synthetic seismogram for offsets 100 m, 500m and 1000m.	115
Figure 7.3 Raypaths within the medium for all interfaces. Red asterisk denotes shot location, blue triangles denote receiver locations.	116
Figure 7.4 Traveltime plot calculated from the ray parameters obtained from ray tracing.	116
Figure 7.5 Synthetic seismogram created by convolving the reflectivity calculated from incidence angle with 20 Hz Ricker wavelet.	117
Figure 7.6 Reflectivity series of each layer convolved with a 20 Hz Ricker wavelet, along with the overall synthetic trace.	117
Figure 7.7 P sonic, S Sonic, and density synthetic log from the lithology model.	118
Figure 7.8 Cross plot of physical rock properties from the lithology model.	119
Figure 7.9 Reflection coefficients versus angle of incidence, using Hilterman, Shuey, Bortfeld and Aki-Richard approximations for the five different layers of the model.	120
Figure 7.10 AVA response using Hilterman approximation for the five interfaces of the model.	121
Figure 7.11 Reflection coefficients versus the square sin of the angle of incidence for the five interfaces of the model.	121
Figure 7.12 Crossplot of AVO gradient (B) and AVO intercept (A).	122
Figure 7.13 Crossplot of AVO gradient (B) and AVO intercept (A), after shifting the background trend. The initial background trend is plotted with dashed line, while the final background trend with continuous line.	122
Figure 7.14 Wiggle plot of Far stacked section of traces 24-48.	123
Figure 7.15 Color plot of Far stacked section of traces 24-48.	124
Figure 7.16 Wiggle plot of Near stacked section of traces 1-24.	124
Figure 7.17 Color plot of Near stacked section of traces 1-24.	125
Figure 7.18 Far stack minus near stack of synthetic data	125
Figure 7.19 Crossplot of Near versus Far minus Near stack.	126
Figure 7.20. CMP 200 NMO corrected. The colours correspond to travel times for different reflectors.	127
Figure 7.21 Amplitude versus $\sin^2\theta$ plot for cmp gather 200.	128
Figure 7.22 Comparison of AVA response using raytracing results and synthetic data of CMP 200.	128

Figure 7.23 Amplitude variation with offset, $\sin^2(\theta)$ and angle of incidence for random CMP gathers. The colours correspond to travel times for different reflectors.	129
Figure 7.24 PG crossplot of CMP gathers 150-300.	130
Figure 7.25 PG crossplot of CMP gathers 150-300, different colors represent the different reflectors. The red circle indicates the gas anomaly.	130
Figure 7.26 Stacked section of CMP gathers 150-300. The colours correspond to travel times for different reflectors.	131
Figure 7.27 A Closer depiction of Figure 7.26, showing the travel time of each reflector.	131
Figure 7.28 Amplitude versus CMP number of each reflector.	132
Figure 7.29 Comparison of AVA response using raytracing results and the stacked section of the synthetic data.	132
Figure 7.30 S-wave velocity for true (red) and inverted (blue) models.	133
Figure 7.31 P-wave velocity for true (red) and inverted (blue) models.	134
Figure 7.32 Poisson's ratio for true (red) and inverted (blue) models.	134

Appendix C

List of Tables

Table 1. AVO classes, after Rutherford and Williams (1989), extended by Castagna and Smith (1994), and Ross and Kinman (1995).	37
Table 2. Summary of well log analysis for Prinos basin [Fronimos 1998], where R_t =formation's electrical resistivity, R_{xo} = resistivity of flushed zone, ϕ =porosity, F =formation's factor, S_w =water saturation, S_o =oil saturation, S_{xo} =water saturation of flushed zone, S_{or} =oil saturation of flushed zone and d_i =diameter of flushed zone.	45
Table 3. Material properties of a North Sea Well. K and μ are the bulk and shear moduli respectively, while ρ is the medium's density.....	47
Table 4. P-Velocity estimation using Gassmann's, Raymer's and Geometric curves.	49
Table 5. Shear velocity approximation using Mudrock, Castagna's and Han's empirical equations.	50
Table 6. Density estimation from P-velocity using Gardner and Lindseth approximations.....	51
Table 7. Elastic parameters for the 4-layer medium.	53
Table 8. The elastic parameters of the model.	114
Table 9. Reflectivity coefficient and angle of incidence values for source- receiver offsets 100, 500 and 1000m.....	115
Table 10. AVO classification of the model's interfaces.....	121